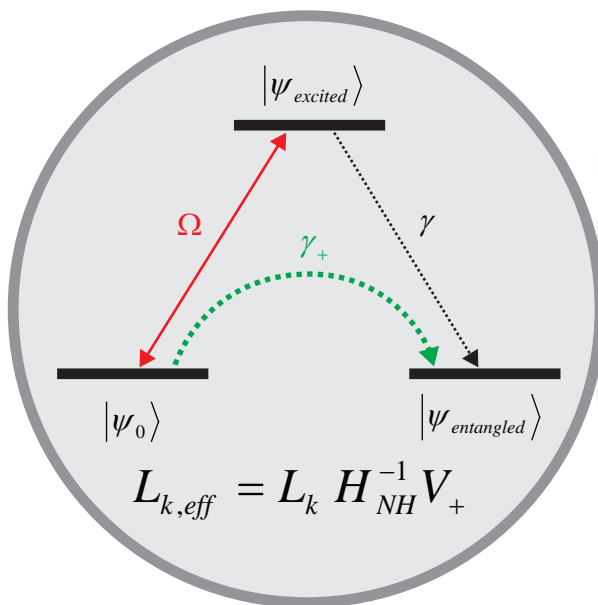




Dissipative preparation of entanglement in quantum optical and solid state systems



PhD thesis
Florentin Reiter

Theoretical Quantum Optics Group
The Niels Bohr Institute

Academic supervisor: Anders S. Sørensen

December 19, 2014

Dissipative preparation of entanglement in quantum optical and solid state systems

Florentin Reiter

This thesis is submitted in partial fulfilment of the requirements for the PhD degree at the University of Copenhagen.

Copyright © 2014 Florentin Reiter

Cover figures: Left: Effective decay into an entangled state, effective Lindblad operator. Right: Two ions getting dissipatively entangled through spontaneous emission and cooling by two auxiliary ions. Credit: Bertram/Motion Forge for NIST.

Abstract

Quantum mechanics is an immensely successful theory which is essential for the explanation of numerous phenomena in atomic physics, solid state physics, nuclear physics and elementary particle physics. Quantum theory also involves effects which have no analogy in the classical world. In particular, quantum entanglement is a correlation predicted by quantum mechanics, but not by classical physics. As an observable property it is indispensable for our understanding of nature. In addition, entangled states are important in quantum computation, quantum communication and quantum measurement protocols. Entangled states are, however, sensitive to interactions with the environment, which are present in any open system. Here, in particular decoherence, i.e. loss of coherence, and dissipation, i.e. loss of energy, destroy the desired correlations.

The novel approach of “dissipative quantum computing” and “dissipative state engineering” suggests to use the interaction with the environment to perform quantum information tasks. Here, decay processes are no longer undesirable, but play an integral part in the dynamics. Following this approach, we consider the dissipative preparation of two-particle and multi-particle entangled states in several concrete physical systems such as optical cavities, trapped ions, and superconducting qubits.

To study the dynamics of open quantum systems, we first develop an operator formalism which allows us to identify the effective interactions. Eliminating the decaying states from the dynamics of a weakly driven system, we derive an effective master equation which reduces the evolution to the ground states. We obtain simple expressions for the effective operators which can be directly applied to reach effective equations of motion for the ground states, as is demonstrated considering several widely used example systems.

Using this operator formalism we identify the effective interactions in the physical systems under consideration and engineer them to prepare a desired entangled target state. This state is then reached regardless of the initial state of the system and stabilized as the unique steady state of the dissipative time evolution. In this way, we develop theoretical schemes for the generation of two-particle entangled states in optical cavities, superconducting systems and trapped ions.

For optical cavities, we harness the natural decay processes of cavity photon loss and spontaneous emission to prepare the maximally entangled singlet state of the system. We analytically derive the optimal parameters, the error and the

speed of convergence of our protocols and find a qualitative improvement of the error as compared to previous methods.

A similar scheme is presented for two superconducting qubits in a circuit QED setup. Combining resonator photon loss, a dissipative process already present in the setup, with an effective two-photon microwave drive, we engineer an effective decay mechanism which prepares a maximally entangled state of two qubits. We find that high fidelities with the target state can be achieved both with state-of-the-art three-dimensional, as well as with the more commonly used two-dimensional transmon qubits.

For trapped ions, we present a theoretical scheme together with its experimental realization. In our scheme we combine unitary processes with added dissipation to deterministically produce a Bell state of two trapped-ion qubits in a continuous time-independent fashion. By continuously driving the system towards the steady state, the entanglement is stabilized and thus made robust against decoherence.

In addition, we consider the dissipative preparation of many-body entangled states. Here we consider a generic system of a number of atoms coupled to a harmonic oscillator. Adding sources of dissipation to the system, we engineer dissipative processes that prepare many-body Greenberger-Horne-Zeilinger (GHZ) or W states. Our assessment of the performance of the schemes shows a favorable scaling of the preparation time with the number of qubits. We propose an implementation of our schemes using trapped ions.

Our results show that dissipative preparation of entanglement is more than just a new conceptual approach, but is of practical relevance in concrete physical systems. This is confirmed by the experimental realization of one of our schemes using trapped ions. In addition, dissipation is found to offer a qualitative improvement of the error scaling of protocols for optical cavities. Finally, our schemes for dissipative preparation of multi-particle entanglement pave the way for the dissipative preparation of high-fidelity many-body entangled steady states. Our study can thus be seen as a step towards the long term goals of dissipative quantum computation and dissipative phase transitions.

Dansk resumé

Kvantemekanik er en uhyre succesrig teori, som er afgørende for forklaringen af mange fenomener i atomfysik, faststoffysik, kerne- og elementærpartikelfysik. Kvanteteori indebærer også effekter, der ikke har nogen analogi i den klassiske verden. Navnlige kvantesammenfiltring (quantum entanglement) der er en korrelation der forudsiges af kvantemekanikken, men ikke af klassisk fysik. Som en observerbar egenskab er den uundværlig for vores forståelse af naturen. Kvantefiltrede tilstande er desuden vigtige i kvanteberegning, kvantekommunikation og protokoller til kvantemåling. Kvantefiltrede tilstande er skrøbelige for interaktionen med omgivelserne, hvilket er til stede i ethvert åbent system. Her ødelægger især dekohærens, dvs. tab af kohærens, og dissipation, dvs. tab af energi, de ønskede korrelationer.

En ny metode, der kaldes "dissipativ kvanteberegning" og "dissipativ tilstandsforberedelse", foreslår at bruge samspillet med miljøet til at udføre kvanteinformationsopgaver. Her er henfaldsprocesser ikke længere uønskede, men spiller en essentiel rolle i dynamikken. Ved at følge denne fremgangsmåde, undersøger vi dissipativ forberedelse af to-partikel og flere-partikel kvantesammenfiltrede tilstande i flere konkrete fysiske systemer såsom optiske kaviteter, indfangede ioner og superledende qubits.

For at studere dynamikken i åbne kvantesystemer, udvikler vi først en operatorformalisme, der gør det muligt for os at identificere de effektive interaktioner. Ved at eliminere de henfaldende tilstande fra dynamikken i et svagt drevet system, udleder vi en effektiv master ligning, som reducerer udviklingen til grundtilstandene. Vi opnår simple udtryk for de effektive operatorer, der kan anvendes direkte til at nå effektive bevægelsesligninger for grundtilstandene hvilket demonstreres ved at betragte flere meget benyttede modelsystemer.

Ved hjælp af denne operatorformalisme identificerer vi de effektive interaktioner i de fysiske systemer under overvejelse og konstruerer dem så det forbereder en given ønsket kvantesammenfiltret tilstand. Denne tilstand kan derved opnåes uanset begyndelsestilstanden af systemet og stabiliseres som den unikke stationære tilstand af den dissipative tidsudvikling. På denne måde udvikler vi teoretiske skema til genereringen af to-partikel kvantesammenfiltrede tilstande i optiske kaviteter, superledende systemer og fangede ioner.

For optiske kaviteter, udnytter vi de naturlige henfaldsprocesser fra kavitetsfotontab og spontan emission til at forberede den maksimalt kvantesammen-

filtrede singlet-tilstand af systemet. Vi udleder analytisk de optimale parametre, fejlen og konvergenshastigheden af vores protokoller og finde en kvalitativ forbedring af fejlen sammelignet med tidligere metoder.

Et lignende skema præsenteres for to superledende qubits i et circuit QED opstilling. Ved at kombinere resonatorfotontab, en dissipativ proces der allerede er til stede i opstillingen, med en effektiv to-foton mikrobølgekilde, konstruerer vi en effektiv henfaldsmekanisme, som genererer en maksimalt kvantesammenfiltret tilstand af to qubits. Vi finder, at høje pålidelighed for den ønskede tilstand kan opnås både med state-of-the-art tredimensionale, samt med de mere almindeligt anvendte todimensionale transmon qubits.

For indfangede ioner, præsenterer vi et teoretisk skema sammen med dets eksperimentelle realisering. I vores skema kombinerer vi unitære processer med tilsat henfald til deterministisk at producere en Bell-tilstand af to fanget-ion qubits på en kontinuerlig tidsuafhængig måde. Ved kontinuerligt at drive systemet mod den stationære tilstand er kvantesammenfiltreringen stabiliseret og således gjort robust mod dekohærens.

Derudover betragter vi den dissipative generering af mange-legeme kvantesammenfiltrede tilstande. Her undersøger vi et generisk system af et antal atomer koblet til en harmonisk oscillator. Ved at tilføje kilder af dissipation til systemet, konstruerer vi dissipative processer der forbereder mange-legeme Greenberger-Horne-Zeilinger (GHZ) eller W tilstande. Vores vurdering af resultaterne af skema viser en gunstig skalering af forberedelsestiden med antallet af qubits. Vi foreslår en mulig metode til implementering med indfangede ioner.

Vores resultater viser, at dissipativ forberedelse af kvantesammenfiltrering er mere end en ny konceptuel tilgang, men har praktisk relevans i konkrete fysiske systemer. Dette bekræftes af den eksperimentelle realisering af en af vores skema med indespærrede ioner. Desuden finder vi at dissipation tilbyder en kvalitativ forbedring af fejl-skaleringen af protokoller for optiske kaviteter. Endelig baner vores fremgangsmåder for dissipative fremstilling af mange-partikel kvantesammenfiltrering vejen for den pålidelige dissipative fremstilling af mange-legeme kvantesammenfiltrede stationære tilstande. Vores undersøgelse kan ses som et skridt i retning af det langsigtede mål om dissipativ kvanteberegning og dissipative faseovergange.

Acknowledgements

Foremost, I would like to thank my advisor Anders S. Sørensen for giving me the chance to work with him and to be part of his group. I am grateful to him for sharing his knowledge and ideas with me, and for his appreciation of my ideas and his insightful comments on my work.

Furthermore, I would like to express my gratitude to Yiheng Lin, John Gaebler, and Dave Wineland from the National Institute of Standards and Technology in Boulder as the experimentalists who got interested in my theoretical work during the Gordon Research Conference on Quantum Science in August 2012, and soon thereafter realized it experimentally, together with Ting-Rei Tan, Ryan Bowler and Didi Leibfried. I very much enjoyed our collaboration and exchange.

I would like to thank the colleagues I had the chance to work with and to learn from during my PhD thesis. These are Michael Kastoryano, with whom I worked on the early schemes for cavity QED, David Reeb, who became a long-term contributor in the many-body project, as well as Lars Tornberg and Göran Johansson from Chalmers University Gothenburg, with whom we had a close collaboration on superconducting qubits. In addition, I had the pleasure to support the activities of the master students Marco Manzoni, Frederik Kerling, and Malte Dueholm. I am grateful to all members of the group over the years for creating a nice atmosphere.

Special thanks go to people who provided me valuable feedback during discussions or on manuscripts: to Emil Zeuthen, Sumanta Das, Eran Kot, Michael Wolf, Chris Pethick, and Bernhard Mehlhig on the effective operator formalism; to the Rempe group, in particular Tatjana Wilk, on cavity QED systems; to Jonas Bylander, Per Delsing, Gerhard Kirchmair, Shyam Shankar, and Steve Girvin on superconductors; and to Ben Lanyon, Rainer Blatt, and Jonathan Home on trapped ion systems.

This PhD project would not have been possible without the generous financial support from several funding agencies. I acknowledge support from the German Academic Exchange Service (DAAD), the Studienstiftung des deutschen Volkes, and a partial scholarship from the Niels Bohr Institute.

List of publications

The results presented in this thesis are covered by the following articles¹:

- F. Reiter, and A. S. Sørensen, Effective operator formalism for open quantum systems, *Phys. Rev. A* **85**, 032111 (2012).
- F. Reiter, M. J. Kastoryano, and A. S. Sørensen, Driving two atoms in an optical cavity into an entangled steady state using engineered decay, *New J. Phys.* **14**, 053022 (2012).
- M. J. Kastoryano, F. Reiter, and A. S. Sørensen, Dissipative preparation of entanglement in optical cavities, *Phys. Rev. Lett.* **106**, 090502 (2011).
- F. Reiter, L. Tornberg, G. Johansson, and A. S. Sørensen, Steady-state entanglement of two superconducting qubits engineered by dissipation, *Phys. Rev. A* **88**, 032317 (2013).
- Y. Lin, J. P. Gaebler, F. Reiter, T. R. Tan, R. Bowler, A. S. Sørensen, D. Leibfried, and D. J. Wineland, Dissipative production of a maximally entangled steady state of two quantum bits, *Nature* **504**, 415 (2013).
- F. Reiter, D. Reeb, and A. S. Sørensen, Dissipative preparation of many-body entanglement, *to be submitted*.

Related publications by the author which are not included in this thesis:

- M. T. Manzoni, F. Reiter, J. Taylor, and A. S. Sørensen, A single photon transistor based on superconducting systems, *Phys. Rev. B* **89**, 180502 (2014).
- T. E. Lee, F. Reiter, and N. Moiseyev, Entanglement and Spin Squeezing in Non-Hermitian Phase Transitions, *Phys. Rev. Lett.* **113**, 250401 (2014).

¹Beginning with Ch. 3, each chapter corresponds to one of the listed articles, with the exception of Ch. 4 (second article and third article). Figures and text in the respective chapters may thus overlap with the listed articles, the publication and copyright of which is hereby acknowledged.

Contents

Abstract	iii
Dansk resumé	v
Acknowledgements	vii
List of publications	ix
1 Introduction	1
1.1 Outline of the thesis	3
2 Fundamentals	5
2.1 Quantum states	5
2.1.1 Pure states and observables	5
2.1.2 Mixed states and the density operator	6
2.1.3 Entanglement	7
2.2 Quantum-mechanical time evolution of closed systems	9
2.2.1 Time evolution of pure states: The Schrödinger equation	9
2.2.2 Time evolution of operators: The Heisenberg equation	10
2.2.3 Time evolution of the density operator: The von Neumann equation	10
2.2.4 Dark states	10
2.3 Quantum-mechanical time evolution of open systems	11
2.3.1 Decoherence	11
2.3.2 The master equation	12
2.4 Quantum information processing	14
2.4.1 Systems	14
2.4.2 Unitary preparation of entanglement and limitations	17
2.4.3 Dissipative quantum computation and state engineering	18
3 Effective dynamics of open quantum systems	21
3.1 Effective theories for open quantum systems	21
3.2 Effective operator formalism for open quantum systems	23
3.3 Derivation of the effective operator formalism	24
3.3.1 Projection-operator formalism	24

3.3.2	Non-Hermitian time evolution in the quantum jump picture	25
3.3.3	Perturbation theory in the interaction picture	25
3.3.4	Adiabatic elimination of the excited states	27
3.3.5	Non-perturbative ground-state coupling	29
3.3.6	Several perturbations or fields	31
3.3.7	General formalism	31
3.4	Examples	32
3.4.1	The two-level system	32
3.4.2	The three-level Raman system	33
3.4.3	Engineered decay	36
3.4.4	Dissipative state preparation	40
3.5	Comparison to other methods	41
3.6	Beyond perturbation theory	42
3.7	Reduction of the dynamics to rate equations	43
4	Dissipative preparation of entanglement in cavity QED	45
4.1	Cavity QED setup	46
4.2	Effective dynamics of the system	49
4.2.1	Complex energies and non-Hermitian time evolution of the excited states	49
4.2.2	Effective Hamiltonian and Lindblad operators	50
4.2.3	Effective propagators of the excited states	51
4.3	An entangling scheme using engineered spontaneous emission	53
4.3.1	Mechanism of the state preparation	53
4.3.2	Effective processes	54
4.3.3	Parameter analysis at weak driving	56
4.3.4	Derivation of the spectral gap for weak driving	57
4.3.5	Derivation of the static error	58
4.3.6	Improved error scaling as compared to unitary protocols	58
4.3.7	Time evolution for weak driving	60
4.4	How fast can two atoms be entangled by dissipation?	60
4.4.1	Effective processes in the presence of ground-state dressing	61
4.4.2	Derivation of the error and of the spectral gap in the presence of ground-state dressing	62
4.4.3	Beyond rate equations	63
4.4.4	Derivation of the recycling error and optimal reshuffling	64
4.4.5	Performance of the scheme at increased driving	66
4.4.6	Scaling of the dynamic error with the preparation time	66
4.5	Schemes for various experimental situations	68
4.5.1	A scheme for an identical driving phase of the atoms	68
4.5.2	A scheme using engineered cavity decay	71
4.5.3	A scheme with robustness to the driving phase	71
4.5.4	A scheme for cavity driving	72
4.6	Comparison of the presented schemes	72
4.6.1	Static error scaling with the cavity parameters	73
4.6.2	Dynamic error scaling with the speed of convergence	74
4.7	Summary and realization perspectives	75

5	Steady-state entanglement of two superconducting qubits	77
5.1	Setup: interactions of two coupled transmons	78
5.2	Mechanisms for the dissipative preparation of the singlet state . . .	81
5.2.1	Effective coherent driving of the dipole-forbidden transition $ 0\rangle \leftrightarrow 2\rangle$ by a two-photon process	84
5.2.2	Engineered decay processes and their effective Lindblad operators	86
5.3	Parameter and performance analysis	90
5.3.1	Error and speed of the protocol	90
5.3.2	Numerical results	92
5.3.3	Anharmonicity of the transmon	92
5.3.4	Experimental imperfections	93
5.4	Summary	95
6	Entangling two trapped ions by engineered dissipation	97
6.1	System	98
6.2	Entangling scheme	99
6.3	Experimental realization	100
6.3.1	Experimental Setup	100
6.3.2	Continuous implementation	101
6.3.3	Stepwise implementation	103
6.4	Theoretical analysis	104
6.4.1	Numerical model	104
6.4.2	Analytical model	105
6.4.3	Results	113
6.5	Summary	113
7	Dissipative preparation of many-body entanglement	115
7.1	Protocols for the dissipative preparation of GHZ and W states . . .	117
7.2	System	117
7.2.1	Dynamical model	117
7.3	Realization of the GHZ protocol	119
7.3.1	Setup	119
7.3.2	Preparing $ \text{GHZ}\rangle$: the Z pumping	120
7.3.3	Emptying $ \text{GHZ}_-\rangle$: the X pumping	126
7.4	Performance of the GHZ protocol	131
7.4.1	Scaling analysis for weak driving	131
7.4.2	Strong driving effects	133
7.4.3	Scaling analysis for strong driving	135
7.4.4	Numerical analysis and comparison	136
7.5	Realization of the W protocol	137
7.5.1	Setup	138
7.5.2	Transferring states to $n_1 \leq 1$ by the Z pumping	139
7.5.3	Emptying antisymmetric states: the A pumping	141
7.5.4	Preparation of $ W\rangle$ from $ 0\rangle^{\otimes N}$: the W pumping	144
7.6	Performance of the W protocol	147
7.6.1	Scaling analysis for weak driving	147
7.6.2	Strong driving effects	148

7.6.3	Scaling analysis for strong driving	149
7.6.4	Numerical analysis and comparison	150
7.7	Implementation in a system of trapped ions	151
7.8	Summary	151
8	Conclusion and Outlook	153
A	Wang-Schirmer scheme generalized to Λ-atoms	157
B	Effects from imperfect coupling of the atoms to the cavity	161
C	Spin-state fidelity measurement	163
D	Derivation of the effective operators for the many-body schemes	165
E	Scaling analysis of the GHZ protocol	173
E.1	Optimization of the parameters for Z pumping alone	173
E.2	Compartment model and effective rates	177
E.3	Transition matrix, stationary error, and GHZ preparation time	181
E.4	Analysis of the “dynamical problem”	183
E.5	GHZ scaling analysis for strong driving	187
F	Scaling analysis of the W protocol	191
F.1	Weak driving analysis	191
F.2	W scaling analysis for strong driving	196
	Bibliography	203

Introduction

The evolution of small systems, such as atoms, follows the rules of **quantum mechanics** [1]. Quantum mechanics describes their properties and dynamics and predicts their behavior, which can be observed in experiments. Over the past century, quantum theory has enabled the explanation of a many effects in nature, such as in atomic physics, solid state physics, nuclear and elementary particle physics, and has thus been essential in a large fraction of the knowledge we have about the world today. Remarkably, quantum theory allows for effects which have no analogy in classical physics. These effects are therefore counterintuitive, but even more important for our understanding of nature. In particular **quantum entanglement** [2] as the common knowledge shared by distant systems, has puzzled physicists since the first formulations of quantum mechanics. Early on, it has been argued that entanglement is incommensurable with our perception of the world [3]. It has, however, proven to be an indispensable for the explanation of certain experiments [4].

In parallel to quantum mechanics, another theory has been on a road of success: information theory [5]. Starting from cryptographic considerations, it has lead to what we call the “information society”, where information processing and transmitting devices such as computers and mobile phones are ubiquitous. In the need to shrink the building blocks of the devices further and further, commonly referred to as Moore’s law, information processing technology is rapidly approaching the quantum world. Here, technologies have been developed for the control and measurement of single quantum objects, in which information can be encoded. The combination of these advancements has given rise to the field of **quantum information science** [6].

Since then, impressive applications of quantum information have been proposed: Using the quantum superposition principle which permits a system to attain many possible states in parallel, algorithms for **quantum computing** [7] were developed for the search of large databases [8] and for the factorization of large prime numbers [9]. For such tasks quantum algorithms were shown to require significantly less time compared to their classical counterparts, providing an exponential speedup. In addition, **quantum cryptography** [10] was suggested for the secure transmission of information and has meanwhile become a commercial technique. **Quantum-enhanced measurements** [11] allow for an improved

sensitivity, e.g. in atomic clocks.

Such quantum information protocols are thought of and experimentally studied in a variety of physical systems, e.g. nuclear magnetic resonance in molecules [12], trapped ions [13], and superconducting systems [14], which all come with certain strengths and challenges.

Nearly independent of the concrete physical system under consideration, entanglement plays a key role in most quantum information tasks: Providing correlations which are stronger than what a classical device could ever offer, entanglement allows for the speed up in quantum information processing due to the parallel manipulation of different states and for improved measurements due to correlated sensing of a signal. The reliable and efficient preparation of entanglement has thus been one of the main tasks in quantum information science since the birth of the field. To date, entanglement is mostly generated by controlled interactions applied to a quantum system, so-called “quantum gates”. Unfortunately, however, entangled states suffer from couplings of the system with the surrounding environment, the so-called **quantum noise** [15]. Such interactions cause **decoherence** [16], which turns quantum states into classical ones, thereby removing the advantage over classical protocols. For this reason, quantum noise and **dissipation**, i.e., loss processes, have been thought of as purely detrimental processes which have to be avoided [17]. The possibilities to isolate a system are, however, limited.

As a way out of this difficult situation, it has been proposed to turn noise from an adversary into a resource by actively engineering the coupling of the system to the environment [18]. This principle has been formalized in the novel paradigm of **dissipative state preparation** [19] and **dissipative quantum computing** [20]. Here, the idea is that the coupling to the environment continuously drives the system towards a steady state. This state either contains the outcome of a computation, or is otherwise of interest for quantum information, such as an entangled state. Therefore, the question of whether the dissipative approach can in be applied in practice and thereby become an alternative to the methods used so far for quantum information processing is of high relevance.

In this thesis we explore the potential of the new approach by developing protocols for the dissipative preparation of entanglement. We begin by considering simple tasks and then move on to more advanced protocols. We study several concrete physical systems, thereby showing that the new approach is realistic. This claim is in particular supported by the experimental implementation of one of our dissipative protocols in trapped ions. Our theoretical assessment of our schemes shows that dissipative preparation of entanglement is promising and can have advantages over the previously used methods.

The work on dissipative preparation of entanglement presented in this thesis constitutes a step towards the long-term goal of dissipative quantum computation. Following this approach, wider classes of dissipative operations and quantum information tasks may be realized in a broad range of experimental systems.

1.1 Outline of the thesis

We start out by a discussion of the fundamental concepts used in this work in Chapter 2. Here, we address different types of quantum states and their properties, quantum mechanical time-evolution and relevant aspects of quantum information processing. Based on the discussion of quantum-mechanical time evolution we develop a method for the description of effective dynamics in open quantum systems in Chapter 3 which is used extensively in the following chapters. In Chapter 4 we present a scheme for the dissipative preparation of an entangled state of two atoms in an optical cavity. Our analysis of the properties of the scheme allows us to make conclusions about the performance of the protocol and the advantages over previous methods. Realization perspectives are also addressed in detail. In a similar manner, we discuss a scheme for the preparation of steady-state entanglement between two superconducting qubits in Chapter 5. In Chapter 6 we present a theoretical scheme for the dissipative preparation of an entangled state of two trapped ions, together with its experimental realization and the theoretical analysis of the experiment. We move on to many-body protocols in Chapter 7, where we consider the preparation of multi-particle entangled Greenberger-Horne-Zeilinger and W states by engineered dissipation. Our analysis shows that our protocols for the dissipative preparation of many-body entangled states exhibit a favorable polynomial scaling with the number of qubits. A conclusion and an outlook are given in Chapter 8.

Fundamentals

Quantum mechanics is an immensely successful theory. As we will see throughout this thesis, it describes systems ranging from microscopic single particles, such as trapped ions, to macroscopic solid state devices, such as superconducting circuits. In this section, we summarize basic concepts of quantum mechanics [1] and quantum information [6] which are helpful to understand the work covered in this thesis and its implications.

We will first, in Sec. 2.1, briefly review different kinds of quantum mechanical states. Among these are, most importantly, entangled states, the generation of which is the main objective of Chapters 4–7. Then, in Sec. 2.2, we will present quantum-mechanical equations of motion that describe the time evolution of closed systems. In Sec. 2.3 we discuss open systems. Here, we introduce the notions of decoherence and dissipation and present the master equation, which lays the foundation for the methods developed in Chapter 3. Then, in Sec. 2.4, we give a short account on state-of-the-art quantum information processing with special emphasis on the physical systems used in this work. In Sec. 2.4.2, we consider the preparation of entanglement by unitary methods and discuss their limitations. Finally, we give an overview over the development of the newly established field of dissipative quantum computation and dissipative state engineering which constitutes the framework for our studies in Chapter 4–7.

2.1 Quantum states

Below we give a brief introduction to several classes of quantum states. Here, we first discuss pure and mixed states and then address the states of composite quantum systems, in particular entangled states.

2.1.1 Pure states and observables

A **quantum state** contains the knowledge about a quantum-mechanical system. Quantum states can appear as either **pure** or **mixed** states. **Pure** quantum states can be written as a wave function, e.g. $|\psi\rangle$, which constitutes a vector of a Hilbert space. This vector can generally be expanded in terms of the states $|n\rangle$

in an orthonormal basis,

$$|\psi\rangle = \sum_n |n\rangle \langle n|\psi\rangle = \sum_n c_n |n\rangle. \quad (2.1)$$

Here, the coefficients $c_n = \langle n|\psi\rangle$ denote the projection of $|\psi\rangle$ on the basis vectors $|n\rangle$. From this representation we already notice an important implication of quantum mechanics: A quantum system can be in a superposition of states [2]. An instructive example for a **superposition state** is given by

$$|\psi\rangle = c_0|0\rangle + c_1|1\rangle \quad (2.2)$$

Here, the system is partly in one state $|0\rangle$ and partly in another state $|1\rangle$. The superposition collapses once the state is determined by a measurement. The probability to find the system in Eq. (2.1) in state $|n\rangle$ is given by $P_n = |c_n|^2$. Such a two-state system can be regarded as the elementary unit of quantum information, the so-called “quantum bit” or **qubit**. Other than a classical bit which can be in one of two states, 0 and 1, a qubit can also attain any superposition of $|0\rangle$ and $|1\rangle$. Moreover, while a single qubit can be in a superposition of two states, a register of N qubits can, due to the superposition principle, simultaneously be in 2^N states, as opposed to a classical register which only is in one of these 2^N states. This effect called quantum parallelism allows quantum computing and quantum simulation to outperform their classical counterparts.

Quantum-mechanical **observables** are measurable quantities that are represented by Hermitian operators. In some parts of this work, especially when heavier operator algebra is involved, it will be useful to denote the operators by “hats” [21]. The expectation value of an observable \hat{O} for a system being in a pure state $|\psi\rangle$ is given by

$$\langle \hat{O} \rangle = \langle \psi | \hat{O} | \psi \rangle. \quad (2.3)$$

An observable can be diagonal in a basis of state vectors $|n\rangle$, in which case one can write

$$\hat{O}|n\rangle = o_n|n\rangle. \quad (2.4)$$

Here, o_n are the eigenvalues of the operator \hat{O} . An important measure is the **fidelity** F , which determines the overlap of a state $|\psi\rangle$, typically the actual state of a system, and another state $|\phi\rangle$, typically the desired state,

$$F_\phi = |\langle \psi | \phi \rangle|^2. \quad (2.5)$$

We will use this quantity extensively throughout this work.

2.1.2 Mixed states and the density operator

The description of a system by a pure state is not always sufficient. In particular large systems and systems which are subject to decoherence (see Sec. 2.3 below), can be in a state that is not a pure state which can be described by a state vector.

These states are called mixed states, and are generally described by the **density operator**

$$\rho = \sum_i p_i |\psi\rangle_i \langle\psi|, \quad (2.6)$$

which consists of a sum of projectors onto pure states $|\psi\rangle_i$. A pure state $|\psi\rangle$ is expressed by a density operator consisting of a single projector

$$\rho = |\psi\rangle \langle\psi|. \quad (2.7)$$

The elements of the corresponding density matrix are given by

$$\rho_{mn} = \langle\psi_m|\rho|\psi_n\rangle. \quad (2.8)$$

While the diagonal entries ($n = m$) of the corresponding density matrix denote the **populations** of the system, the off-diagonal elements ($n \neq m$) are the **coherences**. For a pure superposition state $|\psi\rangle = \frac{1}{\sqrt{2}}(|0\rangle + |1\rangle)$ we have

$$\rho_{00} = \rho_{11} = \rho_{01} = \rho_{10} = \frac{1}{2}, \quad (2.9)$$

which means that the coherences are as large as the populations, whereas

$$\rho = \frac{1}{2}(|0\rangle\langle 0| + |1\rangle\langle 1|), \quad (2.10)$$

with $\rho_{01} = \rho_{10} = 0$ describes a completely incoherent “statistical mixture”. The expectation value of an observable for a system in a mixed state is given by

$$\langle\hat{O}\rangle = \text{Tr}(\rho\hat{O}) = \sum_n \langle n|\rho\hat{O}|n\rangle. \quad (2.11)$$

Note that the trace can be taken using any orthonormal basis $\{|n\rangle\}$. When using the density operator to describe a system in state ρ , the fidelity of a pure state $|\phi\rangle$ is obtained from

$$F_\phi = \text{Tr}(\rho|\phi\rangle\langle\phi|). \quad (2.12)$$

Here, $|\phi\rangle$ can, e.g., be the desired state of a protocol for state preparation. Such states are often entangled states, which we introduce in the section below.

2.1.3 Entanglement

So far, we have considered pure and mixed quantum states of individual systems, we now turn to pure states of composite systems. To begin with, we regard the quantum state of a joint system consisting of a subsystem 1 and a subsystem 2. In some cases, the state of such a composite system can be written as a product of the states of the individual subsystems,

$$|\psi\rangle = |\phi\rangle_1 \otimes |\chi\rangle_2, \quad (2.13)$$

where $|\phi\rangle_1$ denotes the state of subsystem 1 and $|\chi\rangle_2$ is the state of subsystem 2. Here, we refer to $|\psi\rangle$ as a “product state” or “separable state”. However, it is possible that the state of a composite system cannot be factored,

$$|\psi\rangle \neq |\phi\rangle_1 \otimes |\chi\rangle_2, \quad (2.14)$$

in which case the system is said to be in an **entangled state**. This can be seen for a singlet state of two qubits,

$$|S\rangle = \frac{1}{\sqrt{2}} (|0\rangle_1|1\rangle_2 - |1\rangle_1|0\rangle_2). \quad (2.15)$$

The counter-intuitive character of entanglement [2] can hardly be overestimated: Early on, it has been argued by Einstein, Podolsky, and Rosen (“EPR”) that the existence of such states would make quantum mechanics an incomplete theory [3]: As measurements on one system could not determine the state of another system at a distance without violating the concept of local realism, the actual state would need to be explained by local hidden variables which are outside the realm of quantum mechanics. Bases on theoretical work by Bell [22], the existence of a hidden variable theory was later on disproved experimentally [4]. The conclusion is that entanglement is indeed a non-local effect, meaning that distant systems can share common information. Such experiments were performed using bipartite entangled states of the form of Eq. (2.15), which are commonly referred to as **Bell states**,

$$|\psi^+\rangle = \frac{1}{\sqrt{2}} (|00\rangle + |11\rangle) \quad (2.16)$$

$$|\psi^-\rangle = \frac{1}{\sqrt{2}} (|00\rangle - |11\rangle) \quad (2.17)$$

$$|\phi^+\rangle = \frac{1}{\sqrt{2}} (|01\rangle + |10\rangle) \quad (2.18)$$

$$|\phi^-\rangle = \frac{1}{\sqrt{2}} (|01\rangle - |10\rangle) \quad (2.19)$$

Similar experiments [23] have been carried out using tripartite, so-called **Greenberger-Horne-Zeilinger (GHZ)** states,

$$|\text{GHZ}\rangle = \frac{1}{\sqrt{2}} (|000\rangle + |111\rangle). \quad (2.20)$$

GHZ states constitute a class of entangled states for three qubits [24]. Another class of entangled three-body states is given by the so called **W states**,

$$|W\rangle = \frac{1}{\sqrt{3}} (|001\rangle + |010\rangle + |100\rangle). \quad (2.21)$$

Both classes can be generalized to N qubits, where they can be written as

$$|\text{GHZ}\rangle = \frac{1}{\sqrt{2}} (|0\rangle^{\otimes N} + |1\rangle^{\otimes N}) \quad (2.22)$$

$$|W\rangle = \frac{1}{\sqrt{N}} (|0\dots 01\rangle + |010\dots 0\rangle + \dots + |10\dots 0\rangle). \quad (2.23)$$

Beside fundamental questions, entangled states of the types in Eqs. (2.16)–(2.19) are also useful for quantum teleportation [25] and quantum cryptography [10]. Large entangled states, such as those in Eqs. (2.22)–(2.23) are of great interest in entanglement-enhanced quantum measurement schemes [11] and for quantum memories [26]. In addition, quantum computation takes advantage of large entangled states: As we already pointed out when discussing superposition states, the higher correlations of quantum mechanical states, in particular of entangled ones, allow for an improvement as compared to classical computation. Entangled states, e.g. GHZ states, can also be used to store logical qubits redundantly, which allows for quantum error correction schemes [27, 28] and fault-tolerant quantum computation (for a detailed account on these see Ref. [6]). The generation of high-fidelity entangled states is therefore crucial in many quantum information tasks. In Sec. 2.4.2 we will consider an example for the preparation of an entangled state by means of a unitary gates. Below we introduce the quantum-mechanical equation of motion which we will need to study the unitary time evolution of quantum-mechanical systems.

2.2 Quantum-mechanical time evolution of closed systems

Just like their classical counterparts, quantum systems evolve over time. Their time evolution is described by certain equations of motion, some of which we will present in the following. In the absence of measurements and decoherence (to be discussed in Sec. 2.3), the time evolution of closed quantum-mechanical systems is governed by the Schrödinger equation, the Heisenberg equation or the von Neumann equation discussed below. The dynamics of open systems leading to the master equation will then be addressed in Sec. 2.3. Examples for the time evolution of both, closed and open systems, are found in Sec. 3.4.

2.2.1 Time evolution of pure states: The Schrödinger equation

Quantum systems can be described in the Schrödinger picture, where states $|\psi\rangle$ are time-dependent and observables, such as the Hamiltonian of a system, \hat{H} , are time-independent. The dynamics is governed by the **Schrödinger equation**,

$$i\hbar \frac{d}{dt} |\psi\rangle = \hat{H} |\psi\rangle. \quad (2.24)$$

For a time-independent Hamiltonian this equation can be generally solved. The time evolution of the states then follows

$$|\psi(t)\rangle = \hat{U}(t) |\psi(0)\rangle = e^{-\frac{i}{\hbar} \hat{H} t} |\psi(0)\rangle. \quad (2.25)$$

Here, $\hat{U}(t)$ is the time evolution operator, which is found to be unitary, $\hat{U}^\dagger \hat{U} = \mathbb{1}$. Throughout this work we will refer to **unitary dynamics**, when the resulting time-evolution of the system is described by unitary operators. Also note that we will, for convenience of the notation, use $\hbar = 1$ in most places.

2.2.2 Time evolution of operators: The Heisenberg equation

As opposed to the Schrödinger picture, where states are time-dependent, it is also possible to regard the time evolution in a picture where the states are time-independent, but the operators representing the observables evolve over time. The dynamics is then governed by the **Heisenberg equation**,

$$i\hbar \frac{\partial}{\partial t} \hat{O} = [\hat{O}, \hat{H}] + i\hbar \frac{\partial \hat{O}}{\partial t}. \quad (2.26)$$

Here, the second term refers to a potential explicit time-dependence of the operator \hat{O} . Solving the Heisenberg equation, the time evolution of \hat{O} is found to be described by

$$\hat{O}(t) = \hat{U}^\dagger(t) \hat{O} \hat{U}(t) = e^{+\frac{i}{\hbar} \hat{H} t} \hat{O} e^{-\frac{i}{\hbar} \hat{H} t}, \quad (2.27)$$

again with a unitary time evolution operator $\hat{U}(t)$. Another physical picture is given by the interaction picture, which is useful for time-dependent perturbation theory. We will introduce it in Sec. 3.3.3.

2.2.3 Time evolution of the density operator: The von Neumann equation

For mixed states described by a density operator ρ the time-evolution is given by the **von Neumann equation**

$$\dot{\rho} = -i [\hat{H}, \rho] = \mathcal{L}(\rho) \quad (2.28)$$

which can be represented by a **Liouvillian superoperator** \mathcal{L} . In classical mechanics, \mathcal{L} represents a Liouville equation that describes the evolution of a system in phase-space. The von Neumann equation is the extension of this concept to the quantum-mechanical case, yielding a “Quantum Liouville” equation which governs the evolution of populations and coherences of a quantum system. As we will see below, the master equation which describes the dynamics of open quantum systems can also be represented by a Liouvillian operator.

2.2.4 Dark states

To conclude this section on unitary time evolution we introduce the notion of dark states. A **dark state** is an eigenstate of the dynamics as, e.g., given by the Schrödinger equation (2.24) which has eigenvalue zero,

$$i\hbar \frac{d}{dt} |D\rangle = \hat{H} |D\rangle = 0. \quad (2.29)$$

Dark states are thus stable under the interactions present in the system and do not evolve into other states. The latter criterion is in principle fulfilled for any eigenstate of the Hamiltonian,

$$\hat{H} |\psi\rangle = \lambda |\psi\rangle, \quad (2.30)$$

which only rephases, but does not couple to other states. As opposed to a dark state, a **bright state** is coupled by the Hamiltonian,

$$\hat{H}|B\rangle \neq 0, \quad (2.31)$$

and thus evolves over time. The concept of dark states is generalized to steady states in Sec. 2.3.2.

2.3 Quantum-mechanical time evolution of open systems

In the previous sections, we have introduced quantum-mechanical states and their time evolution. The dynamics have so far been assumed to be that of closed systems, leading to a purely unitary evolution. We will now turn to open quantum systems [29, 30], i.e. systems which interact with an environment. Here, we will briefly address the notion of decoherence and dissipation and then introduce the master equation which governs the dynamics of so-called Markovian open systems. Based on this description, a formalism for the effective dynamics of open quantum systems will be developed in Chapter 3.

2.3.1 Decoherence

In Sec. 2.1–2.2 we have made the implicit assumption that only the desired Hamiltonian of, e.g., a unitary gate operation acts on the system. This requires full isolation of the system from its environment, which has so far been considered a requirement for building a quantum computer [17]. In practice, perfect shielding from the outer world is, however, hard to achieve. Any real system is subject to irreversible dynamics, such as loss processes, e.g. by spontaneous emission of photons. Such processes are called **noise**, or **quantum noise** [15], and can lead to several unwanted effects, in particular decoherence and dissipation:

Generally, **decoherence** [16] is the transformation of a quantum-mechanical superposition state into a classical “statistical mixture”, accompanied by the loss of quantum-mechanical coherence. An example is given by

$$\rho_i = |\psi_i\rangle\langle\psi_i| = \frac{1}{2}(|0\rangle + |1\rangle)(\langle 0| + \langle 1|) \rightarrow \rho_f = \frac{1}{2}(|0\rangle\langle 0| + |1\rangle\langle 1|), \quad (2.32)$$

which describes the transformation of an initially pure superposition state $|\psi_i\rangle = \frac{1}{\sqrt{2}}(|0\rangle + |1\rangle)$, to a final state ρ_f , which is a classical statistical mixture of $|0\rangle$ and $|1\rangle$. Also referred to as “depolarization”, such a mapping from a pure quantum-mechanical state to a fully mixed, classical state constitutes a non-unitary process.

Dissipation, on the other hand, refers to changes of the occupation of the states of a system, typically due to loss of energy. We regard the example

$$|\psi_i\rangle = \frac{1}{\sqrt{2}}(|0\rangle + |1\rangle) \rightarrow |\psi_f\rangle = |0\rangle. \quad (2.33)$$

Here, a qubit $\{|0\rangle, |1\rangle\}$, initially encoded in a superposition, is projected onto its ground state by a decay process. As a consequence, the quantum information encoded in the qubit is lost.

Finally, “dephasing” denotes changes in the phases of a quantum state, i.e. the off-diagonal elements of the density matrix, and can be both of coherent unitary, and of decoherent origin. While an example for the latter is given by the process in Eq. (2.32), coherent dephasing, e.g.

$$|\text{GHZ}\rangle = \frac{1}{\sqrt{2}} (|000\rangle + |111\rangle) \rightarrow \frac{1}{\sqrt{2}} (|000\rangle + e^{i\phi}|111\rangle), \quad (2.34)$$

plays an important role in quantum-enhanced measurements. Here, the dephasing effect of, e.g., a magnetic field can be used for its detection. However, averaging over several dephasings with different ϕ will also result in non-unitary evolution and decoherence.

2.3.2 The master equation

In view of the above examples for non-unitary behavior due to the interaction with an environment discussed in the previous section, it is clear that the evolution of an open system cannot be accessed by any of the equations in the previous section which only describe unitary time evolution. However, since decoherence occurs in many physical settings, it is highly relevant to model the dynamics of an open quantum system. Here, keeping track of the evolution of both the system and its surrounding environment may be possible for very simple environments. This is, however, not realistic in more general cases, in particular since the most general environment may be given by the universe itself. Nevertheless, it turns out that it is possible to eliminate the environment, or: **reservoir**, from the dynamics. This truncation is very useful, as it allows one to derive an equation of motion that governs the evolution of a system alone, provided that the reservoir and the coupling to it fulfill certain requirements.

Here, the crucial assumptions are (1) a “Markovian” reservoir, meaning that the reservoir has a short correlation time in comparison to the characteristic timescale of the system, typically because it is considered large, and (2) the “Born approximation” which assumes the interaction between the system and the reservoir to be weak. These criteria define a reservoir which is “oblivious” with respect to its interaction with the system and are typically summarized as the **Born-Markov approximation** or the “Markov approximation of quantum optics”.

As can be shown, the dynamics of an open system weakly coupled to a Markovian reservoir is governed by a **master equation of Lindblad form** [31] which in the Schrödinger picture is given by

$$\dot{\rho} = -i [\hat{H}, \rho] + \sum_k \hat{L}_k \rho \hat{L}_k^\dagger - \frac{1}{2} \left(\hat{L}_k^\dagger \hat{L}_k \rho + \rho \hat{L}_k^\dagger \hat{L}_k \right) = \mathcal{L}(\rho) \quad (2.35)$$

Here, the Hamiltonian \hat{H} contains the coherent couplings of the system, and the **Lindblad operators** \hat{L}_k describe physical decay processes, e.g. $L_\gamma = \sqrt{\gamma}\sigma_- =$

$\sqrt{\gamma}|0\rangle\langle 1|$ in Eq. (2.33) and $L_\gamma = \sqrt{\gamma}\sigma_z = \sqrt{\gamma}(|1\rangle\langle 1| - |0\rangle\langle 0|)$ in Eq. (2.32). Note that, while the Hamiltonian has to be Hermitian for the time evolution to be trace-preserving, the Lindblad operators do not need to fulfill such a criterion and can model various different kinds of noise processes, e.g. cooling and heating through interaction with a nonzero temperature reservoir. In this work, we will, however, mostly consider decay processes due to interactions with a cold reservoir. As previously discussed for the von Neumann equation in Eq. (2.28), the master equation describes a Liouville-type time evolution in phase space, and can therefore be represented by a Liouvillian (super-)operator as defined in Eq. (2.35) above.

As a result of the Born-Markov approximation, typical solutions of Eq. (2.35) are of the form of an exponential, “Markovian” decay. For the example in Eq. (2.33) we find

$$\rho_{11}(t) = \frac{1}{2}e^{-\gamma t} \quad (2.36)$$

$$\rho_{00}(t) = \frac{1}{2}(1 - e^{-\gamma t}) \quad (2.37)$$

$$\rho_{01}(t) = \rho_{10}(t) = \frac{1}{2}e^{-\frac{\gamma}{2}t}. \quad (2.38)$$

As can be seen from these expressions, the master equation describes the de-coherent or dissipative evolution in continuous time. Several examples will be discussed in Sec. 3.4.

Steady states

The notion of a dark state in Sec. 2.2 can be generalized to the dissipative context. Here, a state is called a **steady state** if it fulfills the requirement

$$\dot{\rho} = \mathcal{L}(\rho) = 0. \quad (2.39)$$

The steady state is thus the fixed point of the time evolution of the system. While in principle several linear independent steady states are possible, we will deal with situations where the steady state is unique. The system then approaches the steady state asymptotically as a result of its time evolution described by the master equation.

Convergence to a steady state

The speed of convergence to a steady state can be approximated using the eigenvalue of the lowest-lying eigenstate of the Liouvillian of the system, \mathcal{L} , by the so-called **spectral gap**. Here, we refer to the absolute value of the real part of the eigenvalue, as the real part determines the decay of the state and is therefore typically negative. We will use the spectral gap to estimate the speed of convergence in Chapter 4, but subsequently develop more complete measures to describe the preparation time of a desired steady state.

2.4 Quantum information processing

As pointed out previously, quantum computing [6] bears the promise to outperform classical computing. Theoretically, the most pronounced improvement is found for the factorization of large numbers. While this turns out to be a problem that is believed to require exponential time on a classical computer, it only requires polynomial time when using quantum operations for the so-called Shor's algorithm [9]. An improvement is also found for a quantum search algorithm, the Grover algorithm [8].

While quantum computing has so far only been performed at a very small scale, quantum communication and quantum cryptography [10], also referred to as quantum key distribution (QKD), is already a commercialized technique. Here, due to the quantum-mechanical no-cloning theorem, eavesdropping a conversation is physically not possible without inferring errors, which offers a secure method for transmitting information.

A variety of systems has been considered as candidates for a potential quantum computer and other quantum devices. However, it is hard to predict which system will end up being the preferred one for which task. In Sec. 2.4.1, we briefly discuss a number of systems. This is done in view of our studies of dissipative state preparation in Chapter 4–7 which deal with several quantum optical and solid state systems.

As we previously mentioned, most quantum information tasks take advantage of superposition and entanglement, which allow for the simultaneous processing of several parts of a quantum state, due to quantum parallelism. The use of entanglement also renders quantum measurements more accurate than classical ones. The preparation of entanglement by unitary gates is thus among the most important tasks in quantum information. So far, such tasks have mostly been considered using unitary operations, so-called **quantum gates**. Several theoretical proposals for quantum gates, in particular the Cirac-Zoller gate [32], and the Mølmer-Sørensen gate [33] were realized experimentally [34–36]. As it turns out, the operation of unitary quantum gates is limited by certain effects, typically in connection with decoherence. In Sec. 2.4.2 we will discuss a quantum gate operation and address its limitations.

Finally, we give an overview over the newly emerged field of dissipative quantum computing and dissipative state engineering in Sec. 2.4.3.

2.4.1 Systems

In the following, we will briefly address a number of systems which are relevant for quantum information processing. Rather than presenting these systems in detail here, we refer to the individual sections for their graphical illustration and mathematical description.

In general, building a quantum computer to perform quantum information processing requires a register consisting of a number of sufficiently stable qubits. These are, e.g., two-level systems addressed by external fields, or multi-level systems, where additional states are used to mediate interactions. Systems of this kind will be discussed in detail in the following chapters. Such a register coupled to an external field is, however, not sufficient to perform quantum

information tasks, as these typically involve quantum-mechanical interactions between the qubits. Such interactions can be facilitated by another quantum system which is coupled to the qubits, e.g. an additional ‘ancilla’ qubit or a quantum-mechanical harmonic oscillator. By the aid of such a “bus”, the qubits can then be made interact quantum-mechanically.

Cavity QED

An example of a coupled system of qubits and a harmonic oscillator is given by atoms trapped in an optical cavity [37–42]. Here, two highly reflective mirrors comprise an optical “Fabry-Perot” resonator, in which many reflections of the light are possible so that photons can be effectively stored. Individual atoms are trapped in local extrema of a standing laser wave. Due to the high field strengths of the light in the resonator, strong quantum-mechanical coupling between atoms and light can be achieved. For a two-level atom, this coupling is described by the so-called Jaynes-Cummings Hamiltonian,

$$H_{JC} = g \left(a^\dagger |0\rangle\langle 1| + a |1\rangle\langle 0| \right). \quad (2.40)$$

Here, g is the coupling constant, $\{a^\dagger, a\}$ are the creation/annihilation operators for a photon in the cavity, and $H.c.$ denotes the Hermitian conjugate. Cavities are characterized by their cooperativity $C = \frac{g^2}{\gamma\kappa}$, where γ is the spontaneous emission rate and κ the rate for photon loss from the cavity. High cooperativities represent a strong coherent coupling between light and matter. In such systems, study of quantum-mechanical light-matter interaction down to the single-photon level becomes possible, which is also referred to as cavity QED. The coupling to the environment through the mirror renders cavity QED systems attractive for quantum communication tasks, since information encoded in photons can be transmitted and single photon sources can be built. Entangling two atoms in an optical cavity seems to be a promising route towards the production of entangled states of stationary atoms with photons as “flying qubits”, which is useful for quantum repeater schemes. The preparation of an entangled state of two atoms requires a quantum-mechanical interaction between them. In a cavity QED system this can be achieved by the common coupling to a mode of the Fabry-Perot resonator. The generation of entanglement in cavity QED was studied theoretically [43–49] and realized in microwave cavities [50, 51], but has not yet been achieved in optical cavities. In Sec. 2.4.2 we discuss an entangling protocol for two atoms in an optical cavity and its limitations.

Trapped ions

While the trapping of neutral atoms in dipole traps is a demanding task even with feedback techniques, atomic ions can, thanks to their electric charge, be trapped efficiently using electromagnetic traps. It is thus possible to keep chains or crystals consisting of tens of ions in a trap for long time. Also, the ions are so confined in the trap, that the quantized character of their motion becomes important. The electronic transitions of the ions can be addressed by external fields, by which cooling, storing and reading out of information can be facilitated. For quantum information purposes, long-lived qubit states are found

as meta-stable states which exhibit lifetimes up to about one second. When the ions are sufficiently cooled, quantum-mechanical sideband couplings can be used to let their quantized common motional degrees of freedom interact with their internal, electronic degrees of freedom. In this way, quantum information processing protocols can be realized [32, 33]. Beside preparation of an initial state, typically by optical pumping (discussed in Sec. 3.4.4), and detection of the state of the ions, entangling operations [33, 52–54] are crucial in quantum computation algorithms [13, 55–57]. Entanglement preparation is mostly achieved using unitary operations, so called quantum gates. Thanks to the long lifetime of the ion levels of about seconds, entangled states of up to six [53] and 14 [54] ions have been achieved. The fidelity of such states has, however, been found to decrease with the number of qubits.

Superconducting qubits

In addition to atomic systems such as optical cavities and trapped ions, there exist also solid state systems which are promising for quantum information processing, in particular superconducting systems [58]. A superconducting qubit consists of two superconducting “islands”, connected by a Josephson junction, across which electron pairs can tunnel. This so-called “Cooper pair box” [59] constitutes an anharmonic oscillator, where two or more levels can be accessed by coupling fields to the transitions. The particular type of the qubit is achieved by controlling the Coulomb energy on the one hand and the Josephson energy on the other hand by the voltage bias. These include “charge” qubits, “flux” qubits, and “phase” qubits. More recently, the so-called “transmon” qubit [59] has become popular due to its long coherence times. Another type, “fluxonium” is said to be very flexible and may therefore be closer to the configurations of atomic systems.

Typically, one or more superconducting qubits can be located inside a coplanar waveguide microwave resonator, which is analogue to the atoms in an optical Fabry-Perot resonator in cavity QED, but without the need for trapping. Due to the similarity to cavity QED systems, such superconducting resonator-qubit setups are referred to as **circuit QED**. Since inside the resonator very high field strengths are present, strong coupling can be achieved between the qubits and the microwave field. As one difference it remains that the actual qubit is still an anharmonic oscillator and thus exhibits a somewhat different coupling configuration between resonator and qubits, as well as ground-state decoherence. It is, however, possible to achieve very long coherence times of the order of $\sim 100 \mu\text{s}$ [60–65] which render superconducting qubits attractive for quantum information processing [14, 66, 67].

Emitters coupled to waveguides

Another solid state system are emitters coupled to lossy waveguides [68]. This system is similar to cavity QED, but works in a different parameter regime. Here, the radiation field of the emitter is extremely tightly confined by the waveguide. Also, while in a cavity the atoms couple to a single localized mode, here the emitters couple to a continuum, typically resulting in a very pronounced decay

of the emitters through the waveguide. Nevertheless, high cooperativity can be achieved so that the emitter system resembles a lossy cavity. Taking advantage of the strong coupling, such systems may be used for the switching and routing of quantum information stored in photons [69], thereby constituting building blocks in a potential photonic quantum computing architecture [70].

Other systems

Making use of nuclear-magnetic resonance (NMR) techniques for molecules, pioneering quantum information processing experiments were performed [12]. Other highly relevant systems for quantum information include all-optical setups [71] and Rydberg atoms [72].

2.4.2 Unitary preparation of entanglement and limitations

In the following, we discuss an example of a unitary protocol for the preparation of an entangled state between two atoms in a cavity as a task that is widely used in quantum information processing. In addition, we address the main limitation of the protocol.

Example: Entangling two atoms in a cavity

For cavity QED systems, various ways to prepare entanglement have been considered theoretically [43, 44, 47–49] typically for two three-level atoms with two stable ground states $|0\rangle$, $|1\rangle$, and a decaying excited state $|e\rangle$. The system is assumed to be initially prepared in a ground state of the atoms, $|01\rangle|0\rangle = |0\rangle_1|1\rangle_2|n\rangle$, where the last ket denotes the cavity mode. A coherent driving field

$$H = \frac{\Omega}{2} e^{-i\Delta t} (|e\rangle_1\langle 0| + |e\rangle_2\langle 0|) + H.c. \quad (2.41)$$

is used to couple the initial state to an excited state,

$$|01\rangle|0\rangle \rightarrow |e1\rangle|0\rangle. \quad (2.42)$$

The interaction between the atoms and the cavity mode,

$$H_{JC} = ga^\dagger e^{-i\delta t} (|1\rangle_1\langle e| + |1\rangle_2\langle e|) + H.c., \quad (2.43)$$

then takes the system to a cavity-excited state,

$$|e1\rangle|0\rangle \rightarrow |11\rangle|1\rangle \quad (2.44)$$

From this state, the system can couple back to $|e1\rangle|0\rangle$ or further to $|10\rangle|0\rangle$ by the above interactions. Letting the driving field act for a suitable time transfers the system from $|01\rangle|0\rangle$ into a superposition state

$$|\psi\rangle = \frac{1}{\sqrt{2}}(|01\rangle + |10\rangle)|0\rangle, \quad (2.45)$$

which is the maximally entangled triplet state of the atoms.

Limitation by the square-root error

The above protocol is limited by the two dissipative processes present in the cavity QED system, spontaneous emission and leakage of photons from the cavity. A derivation of the error of unitary entangling protocols for cavity QED has been given in Ref. [49]. As can easily be reproduced using the formalism we will present in Chapter 3, the effective coupling constant for the processes in Eqs. (2.41)–(2.43) is found to be $g_{\text{eff}} \sim \frac{\Omega g}{\Delta}$. Assuming a spontaneous emission rate $\gamma \ll \Delta$ for the excited level, the effective decay rate is given by $\gamma_{\text{eff}} \sim \frac{\gamma \Omega^2}{\Delta^2}$. When considering a cavity detuning δ and a cavity leakage rate $\kappa \ll \delta$ we obtain an effective coupling constant $\chi \sim \frac{g_{\text{eff}}^2}{\delta}$ between the atoms, together with an effective leakage rate $\kappa_{\text{eff}} \sim \frac{\kappa g_{\text{eff}}^2}{\delta^2}$. The error of the entangling protocol due to both sources of dissipation, spontaneous emission and cavity photon loss, is then approximated by

$$1 - F \sim \epsilon_{\gamma} + \epsilon_{\kappa} \sim \frac{\gamma \delta^2}{g^2} + \frac{\kappa}{\delta}, \quad (2.46)$$

where F denotes the fidelity of the triplet state. We optimize this expression by choosing $\delta = \sqrt{\frac{\kappa}{\gamma}} g$ and $\Delta = \sqrt{\frac{\gamma}{\kappa}} g$, which results in

$$1 - F \sim \sqrt{\frac{\kappa \gamma}{g^2}} = \frac{1}{\sqrt{C}}, \quad (2.47)$$

where $C = \frac{g^2}{\kappa \gamma}$ is the **cooperativity** of the cavity (cf. Sec. 2.4.1). The optimized error of the protocol thus scales with the square-root of the cooperativity.

2.4.3 Dissipative quantum computation and state engineering

In Sec. 2.3 we have seen that decoherence acts detrimentally on quantum-mechanical systems, deteriorating their coherences over time. In addition, as we addressed in Sec. 2.4, also unitary entangling operations can be limited by dissipation. Quantum information tasks require, however, high-fidelity state preparation, as is, e.g., discussed in Ref. [73]. The logical consequence has therefore been to seek full isolation of the system from the environment and to try to establish full control over the system parameters [17].

Since perfect isolation of a system is, however, hard to achieve and comes at the expenses of the accessibility of the system, other approaches need to be considered. In particular, it has been suggested to take the opposite approach to actively use interactions of the system with the environment, such as noise and dissipation, to perform quantum information tasks. In this way, detrimental processes are turned into driving forces of a protocol.

The early precursors of this idea are **optical pumping** [74] and **cooling** [75]. For optical pumping, which we consider in Sec. 3.4.4, coherent excitation is combined with dissipation to prepare a system in a certain state. While optical pumping often refers to spin systems with a number of states without giving a reference to the energy of the states, cooling typically means the evolution of a – usually bosonic – system towards its ground state. A generalization of these

principles is **reservoir engineering** [18, 76], where interactions with an environment drive the system towards a non-trivial state of interest. This approach is also referred to as **dissipative state preparation**. In particular, it has early on been shown that entangled states can be prepared using dissipation as a resource [45, 77–83]. These states need not, however, be steady states of the evolution. Since then, proposals for entangled steady states [84–96] or squeezed steady states [97–100] have become available. By now, a number of physical systems has been considered, in particular cavity QED [45, 77, 84–86, 90, 97, 101, 102], atomic ensembles [97–100], ion traps [78, 87, 91, 92, 103–105], plasmonic waveguides [88, 89, 93, 94], light fields [95], optical lattices [85, 96], Rydberg atoms [106–108], NV centers [109] and superconducting systems [110–115]. First experimental studies along these lines have been performed by Refs. [76, 91, 99, 105, 113, 116].

The concept of dissipative preparation of entangled steady states has been formalized in Ref. [19] and generalized to **dissipative quantum computation** and **dissipative state engineering** in Ref. [20]. The central idea of dissipative quantum computation is to tailor the dissipative dynamics such that the steady state of the time evolution contains the outcome of a universal computation [20]. In Refs. [19, 20], it was furthermore generally demonstrated that large classes of states, such as Matrix Product States (MPS) and Tensor Product States [117, 118], can in principle be prepared efficiently using dissipation. Other tasks that have been considered in this context are quantum memories [119], quantum communication [120] and the simulation of open quantum systems [91, 92, 121].

Two highly relevant questions that need to be addressed are whether the dissipative approach is viable in practice, and whether it possibly has an advantage over unitary protocols. Generally, it can be argued that converting the detrimental source of noise into a resource is likely to result in an improvement. In particular, as opposed to unitary methods, dissipative protocols can be used to prepare steady states. These states are inherently stable against the dissipation that was used to produce them. The continuous return towards the steady state upon a perturbation of the system can also be seen as **stabilization** mechanism against other kinds of decoherence. In addition, we will show that in certain settings it is possible to achieve an improved error scaling.

In the following chapters, we consider dissipative preparation of entanglement in concrete physical systems. We start out at a small scale, studying dissipative preparation of an entangled state of two qubits in Chapter 4–6 and then move on to many-body entangled states in Chapter 7. The experimental realization of our scheme for trapped ions is presented along with the theoretical scheme in Chapter 6.

Effective dynamics of open quantum systems

In the previous chapter, we have introduced the master equation which describes the dynamics of an open quantum system coupled to a Markovian reservoir. As an equation of motion for the density matrix ρ , it determines the temporal evolution of the system. Solving the master equation for the full density matrix is, however, in many situations cumbersome. To make the description of an open quantum system manageable as well as to gain physical insight into the evolution of the system, it is therefore desirable to develop effective theories which reduce the complexity of the system. In this chapter, we present an effective operator formalism for open quantum systems based on the master equation.

We begin with an introduction to effective theories for open quantum systems in Sec. 3.1, leading over to a brief presentation of our formalism in Sec. 3.2. In Sec. 3.3, we proceed to the derivation of the effective operators. Here, we provide several extensions which account for different physical situations. In Sec. 3.4, we give examples for the application of our formalism, deriving effective coherent and dissipative processes in typical quantum systems. Finally, we compare our method with other methods in Sec. 3.5, give an account on its realm in Sec. 3.6, and address the reduction to rate equations in Sec. 3.7.

3.1 Effective theories for open quantum systems

In an open system there are often quite different time scales associated with different effects, such that the Hilbert space can be divided into two parts, one for the rapidly decaying (excited) states, and one for the comparably stable (ground) states. For instance, for weakly driven atoms the evolution and decay of the excited states happen on a time scale which is fast compared to any other time scale in the system. In such situations it is desirable to eliminate the rapidly evolving excited states to get a simpler description of the slow evolution of the ground states. A standard method for doing this is adiabatic elimination [122], where the density matrix equations involving the excited states are solved by assuming a slow evolution of the ground states. This can then be used to describe

an effective evolution of the ground states. This procedure can, however, be rather involved, as there are many density matrix elements if the system is large.

For closed systems with purely unitary couplings effective theories have been used to derive effective Hamiltonians, in particular by James and co-workers [33, 123, 124]. If decoherence is added to the system, the joint unitary and dissipative dynamics can be captured by introducing non-Hermitian descriptions. The use of complex energies allows for the combination of the energy of a resonance with its width [125]. Correspondingly, non-Hermitian Hamiltonians are commonly used to describe the dynamics of open systems [126–130]. In quantum optics the use of non-Hermitian Hamiltonians is put in a more rigorous form by the so-called quantum jump formalism, or Monte Carlo wave function method [126], which is equivalent to the evolution by a Markovian master equation. In this method the non-Hermitian Hamiltonian describes the evolution in the absence of decay, whereas quantum jumps are introduced at random times to account for the resulting state after a decay.

The separation of the Hilbert space into rapidly and slowly evolving ground and excited states, similar to what we will consider here, has been studied also for non-Hermitian Hamiltonians. In particular for a coupling of the ground to the excited states much weaker than the evolution inside the subspaces, a formalism for effective processes is provided by the Feshbach projection-operator approach [131]. Similar formalisms for successive nuclear reactions have been studied by Weidenmüller and co-workers [132]. Methods based on the Feshbach projection operator method have been used in several fields [133]. However, these treatments are only concerned with the evolution from the effective non-Hermitian Hamiltonian and therefore ignore the quantum jumps describing the state after the decay.

In the following, we present a method to eliminate the excited states and to reduce the system dynamics to the ground states. The method we present is essentially equivalent to adiabatic elimination, but is much easier to apply in practice. By formalizing the procedures leading to adiabatic elimination we obtain simple expressions for the effective operators describing the ground-state evolution. With our expressions one avoids the often tedious steps leading to adiabatic elimination and can obtain the effective operators by evaluating simple formulas. In particular, we have found that these methods are very convenient for studying dissipative state preparation [19, 20, 101, 102, 121], where the goal is to engineer decay processes such that a system evolves into a desired state. Here, it is highly desirable to have a convenient tool to rapidly identify the effective dissipative dynamics of the system. The procedure we present here is an extension of the Feshbach projection-operator approach to also include these quantum jumps. As a result, our formalism can be used to describe the full evolution of the density matrix of the system after elimination of the excited states. This generalization is crucial for describing situations where we are also interested in the state of the system after a decay.

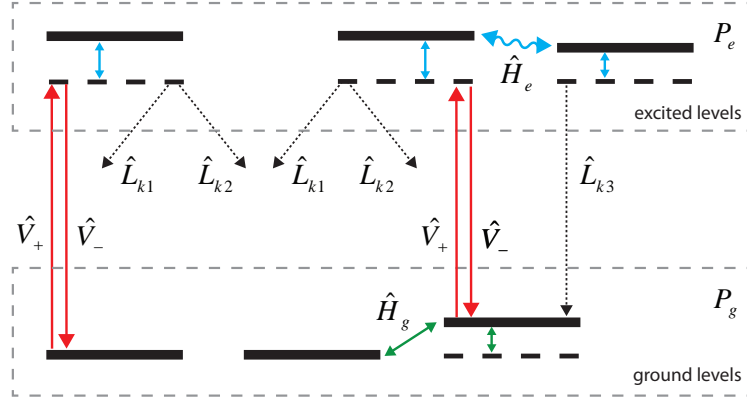


FIGURE 3.1: Ground and excited subspaces and couplings. The nondecaying ground states (corresponding to projector P_g) are coupled to the decaying excited states (projector P_e) by the perturbative (de-) excitations \hat{V}_+ (\hat{V}_-) [solid lines connecting the subspaces (red)]. The Lindblad operators \hat{L}_k represent various decay process (dotted lines). The couplings inside the ground and excited subspaces are given by \hat{H}_g [solid lines inside the lower subspace (green)] and \hat{H}_e [solid lines inside the upper subspace (blue)], respectively.

3.2 Effective operator formalism for open quantum systems

Before proceeding to its derivation, we first outline the effective operator formalism. As illustrated in Fig. 3.1, we assume the open system to consist of two distinct subspaces, one for the ground states and one for the decaying excited states. The couplings of these two subspaces are assumed to be perturbative. Furthermore, we assume that the dynamics of the system is Markovian such that the time evolution of the density operator ρ can be described by a master equation of Lindblad form, introduced in Sec. 2.3.2,

$$\dot{\rho} = -i [\hat{H}, \rho] + \sum_k \hat{L}_k \rho \hat{L}_k^\dagger - \frac{1}{2} \left(\hat{L}_k^\dagger \hat{L}_k \rho + \rho \hat{L}_k^\dagger \hat{L}_k \right), \quad (3.1)$$

where \hat{H} is the Hamiltonian of the system and each of the Lindblad operators \hat{L}_k represents a source of decay which we assume to take the system from the excited to the ground subspace. By combining perturbation theory of the density operator and adiabatic elimination of the excited states we reduce the dynamics to an effective master equation involving only the ground-state manifold

$$\dot{\rho} = -i [\hat{H}_{\text{eff}}, \rho] + \sum_k \hat{L}_{\text{eff}}^k \rho (\hat{L}_{\text{eff}}^k)^\dagger - \frac{1}{2} \left((\hat{L}_{\text{eff}}^k)^\dagger \hat{L}_{\text{eff}}^k \rho + \rho (\hat{L}_{\text{eff}}^k)^\dagger \hat{L}_{\text{eff}}^k \right) \quad (3.2)$$

with effective Hamilton and Lindblad operators

$$\hat{H}_{\text{eff}} = -\frac{1}{2} \hat{V}_- \left(\hat{H}_{\text{NH}}^{-1} + (\hat{H}_{\text{NH}}^{-1})^\dagger \right) \hat{V}_+ + \hat{H}_g \quad (3.3)$$

$$\hat{L}_{\text{eff}}^k = \hat{L}_k \hat{H}_{\text{NH}}^{-1} \hat{V}_+. \quad (3.4)$$

connecting only the ground states. Here, \hat{V}_+ (\hat{V}_-) are the perturbative (de-) excitations of the system and \hat{H}_g is the ground-state Hamiltonian. \hat{H}_{NH} is the non-Hermitian Hamiltonian of the quantum jump formalism

$$\hat{H}_{\text{NH}} = \hat{H}_e - \frac{i}{2} \sum_k \hat{L}_k^\dagger \hat{L}_k, \quad (3.5)$$

with \hat{H}_e being the Hamiltonian in the excited-state manifold. The effective master equation of Eq. (3.2) provides an approximation of the dynamics in Eq. (3.1) by the effective dynamics of its ground states. Thus, the effective operator formalism allows for a substantial reduction of the complexity of the dynamics of an open system. In essence, adiabatic elimination of the excited states in the presence of both coherent and dissipative processes is formalized in a compact form by the effective operators of Eqs. (3.3) and (3.4).

We derive the effective operators of Eqs. (3.3) and (3.4) in the following section, Sec. 3.3. An elementary application of our formalism to a driven dissipative two-level system is shown in Sec. 3.4.1. Another relevant example is given in Sec. 3.4.3, where we discuss the possibility to use our effective operator formalism to engineer decay processes in a four-level system. Optical pumping and dissipative state preparation are briefly addressed in Sec. 3.4.4. In Sec. 3.3.5 we present an extension of the formalism which includes non-perturbative ground-state couplings. This extended formalism will then be used for a detailed analysis of the effective processes in a three-level Raman system in Sec. 3.4.2. In Sec. 3.3.6 we introduce a second extension of the effective operator formalism that allows for several perturbations or fields. The most general formalism is presented in Sec. 3.3.7. A comparison to similar existing methods is provided in Sec. 3.5, the possibility to use the formalism beyond the perturbative limit and its reduction to rate equations are discussed in Sec. 3.6 and 3.7.

3.3 Derivation of the effective operator formalism

We now present the derivation of the effective equation of motion in Eqs. (3.2)–(3.4). The evolution of the density operator $\rho(t)$ in the Schrödinger picture is governed by the master equation of Lindblad form, given by Eq. (3.1). The Hamiltonian \hat{H} stands for unitary couplings of the system, such as coherent driving. Each Lindblad “jump” operator \hat{L}_k accounts for a dissipative process, such as spontaneous emission.

3.3.1 Projection-operator formalism

We use the projection-operator method of Feshbach [131] to structure the Hilbert space into two subspaces, one for the ground states and one for the excited states, represented by the projection operators P_g and P_e , with $P_g + P_e = \mathbb{1}$ and $P_g P_e = 0$. Accordingly, we divide the Hamiltonian into four parts:

$$\hat{H} = \hat{H}_g + \hat{H}_e + \hat{V}_+ + \hat{V}_-. \quad (3.6)$$

Here, the interactions inside the ground subspace are labeled by $\hat{H}_g \equiv P_g \hat{H} P_g$, and inside the excited subspace by $\hat{H}_e \equiv P_e \hat{H} P_e$. The perturbative excitations

$\hat{V}_+ \equiv P_e \hat{H} P_g$ and deexcitations $\hat{V}_- \equiv P_g \hat{H} P_e$ ($\hat{V}_+^\dagger = \hat{V}_-$ and $\hat{V} = \hat{V}_+ + \hat{V}_-$) connect the two subspaces.

We assume the ground states as stable and the excited states to be decaying to the ground states. The Lindblad operators can then always be written as $\hat{L}_k = P_g \hat{L}_k P_e$. The mentioned couplings inside and between the subspaces are illustrated in Fig. 3.1.

3.3.2 Non-Hermitian time evolution in the quantum jump picture

Combining unitary and dissipative dynamics within a single non-Hermitian Hamiltonian has widely been studied in various areas of physics, as mentioned in Chapter 1. In quantum optics the use of non-Hermitian Hamiltonians is formalized by the so-called quantum jump picture [126], in which an effective non-Hermitian Hamiltonian describes the evolution of the system in the absence of a quantum jump. In order to distinguish the non-Hermitian Hamiltonian of the excited states from the effective (Hermitian) Hamiltonian of Eq. (3.3) we have denoted it as \hat{H}_{NH} in Eq. (3.5). It incorporates the excited state Hamiltonian \hat{H}_e and the decay terms of the anticommutator part of the master equation (3.1). Introducing \hat{H}_{NH} to Eq. (3.1) we obtain a reduced master equation

$$\dot{\rho} = -i \left((\hat{H}_{\text{NH}} + \hat{H}_g + \hat{V}) \rho - \rho (\hat{H}_{\text{NH}}^\dagger + \hat{H}_g + \hat{V}) \right) + \sum_k \hat{L}_k \rho \hat{L}_k^\dagger. \quad (3.7)$$

Here, we have included the decay terms which describe the loss of population from the excited states to \hat{H}_{NH} in the commutator-like Hamiltonian part. The last “feeding term” describes the gain of the population of the ground states by decay from the excited states remains.

For ground-state interactions \hat{H}_g much weaker than those between the excited states \hat{H}_e , the dynamics of the decaying excited states are mainly governed by the non-Hermitian Hamiltonian \hat{H}_{NH} . As all excited states are decaying, all eigenvalues of \hat{H}_{NH} are nonzero so that its inverse \hat{H}_{NH}^{-1} exists within the excited-state subspace.

3.3.3 Perturbation theory in the interaction picture

In the following, we assume the couplings of the ground and excited subspaces \hat{V}_\pm to be sufficiently weak to be described as perturbations of the evolution governed by an unperturbed Hamiltonian $\hat{H}_0 \equiv \hat{H}_g + \hat{H}_{\text{NH}}$. Based on this assumption we perform perturbation theory [1] of the density operator. To this end, we change into the interaction picture by a transformation with the operator

$$\hat{O}(t) = e^{-i\hat{H}_0 t} = e^{-i(\hat{H}_{\text{NH}} + \hat{H}_g)t}. \quad (3.8)$$

Then the reduced master equation of Eq. (3.7) transforms into

$$\dot{\tilde{\rho}}(t) = -i \left(\tilde{V}(t) \tilde{\rho}(t) - \tilde{\rho}(t) \tilde{V}^\dagger(t) \right) + \sum_k \tilde{L}_k(t) \tilde{\rho}(t) \tilde{L}_k^\dagger(t) \quad (3.9)$$

with operators transformed accordingly

$$\tilde{\rho}(t) = \hat{O}^{-1}(t)\rho\hat{O}, \quad (3.10)$$

$$\tilde{V}(t) = \hat{O}^{-1}(t)(\hat{H}_0 + \hat{V})\hat{O}(t) + i\frac{d\hat{O}^{-1}}{dt}\hat{O}(t) = \hat{O}^{-1}(t)\hat{V}\hat{O}(t), \quad (3.11)$$

$$\tilde{L}_k(t) = \hat{O}^{-1}(t)\hat{L}_k\hat{O}(t). \quad (3.12)$$

To derive the effective operators we perform a perturbative expansion of the density operator in a small parameter ϵ

$$\tilde{\rho}(t) = \frac{1}{N}(\tilde{\rho}^{(0)}(t) + \epsilon\tilde{\rho}^{(1)}(t) + \epsilon^2\tilde{\rho}^{(2)}(t) + \dots) \quad (3.13)$$

and obtain a recursive formulation of the reduced master equation in powers of ϵ ,

$$\dot{\tilde{\rho}}^{(n)}(t) = -i(\tilde{V}(t)\tilde{\rho}^{(n-1)}(t) - \tilde{\rho}^{(n-1)}(t)\tilde{V}^\dagger(t)) + \sum_k \tilde{L}_k(t)\tilde{\rho}^{(n)}(t)\tilde{L}_k^\dagger(t), \quad (3.14)$$

where we have used that \hat{V} is a small parameter $\hat{V} \propto \epsilon$. The first three orders of the recursive reduced master equation read

$$\dot{\tilde{\rho}}^{(0)}(t) = \sum_k \tilde{L}_k(t)\tilde{\rho}^{(0)}(t)\tilde{L}_k^\dagger(t), \quad (3.15)$$

$$\dot{\tilde{\rho}}^{(1)}(t) = -i\left(\tilde{V}(t)\tilde{\rho}^{(0)}(t) - \tilde{\rho}^{(0)}(t)\tilde{V}^\dagger(t)\right) + \sum_k \tilde{L}_k(t)\tilde{\rho}^{(1)}(t)\tilde{L}_k^\dagger(t), \quad (3.16)$$

$$\dot{\tilde{\rho}}^{(2)}(t) = -i\left(\tilde{V}(t)\tilde{\rho}^{(1)}(t) - \tilde{\rho}^{(1)}(t)\tilde{V}^\dagger(t)\right) + \sum_k \tilde{L}_k(t)\tilde{\rho}^{(2)}(t)\tilde{L}_k^\dagger(t). \quad (3.17)$$

In the absence of initial excitations, decay processes can be neglected for orders $n \leq 1$ so that

$$\dot{\tilde{\rho}}^{(0)}(t) = 0, \quad (3.18)$$

$$\dot{\tilde{\rho}}^{(1)}(t) = -i\left(\tilde{V}(t)\tilde{\rho}^{(0)}(t) - \tilde{\rho}^{(0)}(t)\tilde{V}^\dagger(t)\right), \quad (3.19)$$

$$\dot{\tilde{\rho}}^{(2)}(t) = -i\left(\tilde{V}(t)\tilde{\rho}^{(1)}(t) - \tilde{\rho}^{(1)}(t)\tilde{V}^\dagger(t)\right) + \sum_k \tilde{L}_k(t)\tilde{\rho}^{(2)}(t)\tilde{L}_k^\dagger(t). \quad (3.20)$$

We use the projection operator approach for the density operator to separate the evolution of ground and excited states. In doing so we reduce the evolution of the ground states to

$$P_g\dot{\tilde{\rho}}^{(0)}(t)P_g = P_g\dot{\tilde{\rho}}^{(1)}(t)P_g = 0, \quad (3.21)$$

$$P_g\dot{\tilde{\rho}}^{(2)}(t)P_g = -iP_g\left(\tilde{V}(t)\tilde{\rho}^{(1)}(t) - \tilde{\rho}^{(1)}(t)\tilde{V}^\dagger(t)\right)P_g + \sum_k \tilde{L}_k(t)P_e\tilde{\rho}^{(2)}(t)P_e\tilde{L}_k^\dagger(t). \quad (3.22)$$

In the last line we have used that for each Lindblad operator we can write $\tilde{L}_k = P_g\tilde{L}_kP_e$, as decay only occurs from the excited to the ground states. Consequently, the ground states are connected by unitary and dissipative processes of second order. Also note that since the transformation in Eq. (3.8) is nonunitary, the

perturbation $\tilde{V}(t)$ is non-Hermitian. For the dynamics of the excited states we find

$$P_e \dot{\tilde{\rho}}^{(0)}(t) P_e = P_e \dot{\tilde{\rho}}^{(1)}(t) P_e = 0 \quad (3.23)$$

$$P_e \dot{\tilde{\rho}}^{(2)}(t) P_e = -i P_e \left(\tilde{V}(t) \tilde{\rho}^{(1)}(t) - \tilde{\rho}^{(1)}(t) \tilde{V}^\dagger(t) \right) P_e. \quad (3.24)$$

As we have assumed that the excited states do not gain population from decay, Eq. (3.24) does not exhibit any dissipative feeding terms. Hence, the evolution of the excited part of the density operator is solely driven by the interaction Hamiltonian $\tilde{V}(t)$. While the dynamics of the second-order processes connect the states either in the ground or in the excited subspace we note that interactions between the subspaces are given by the first-order terms $P_g \dot{\tilde{\rho}}^{(1)}(t) P_e$ and $P_e \dot{\tilde{\rho}}^{(1)}(t) P_g$.

3.3.4 Adiabatic elimination of the excited states

In principle, a solution to the remaining second-order master equations for the ground and the excited states in Eqs. (3.22) and (3.24) can be computed. This solution can, however, still be very complicated. In particular, if the decaying excited states are almost unpopulated, it is preferable to obtain a more comprehensible solution. In the following, we choose to reduce the complexity of the dynamics by restricting it to the ground states. To this end, we perform adiabatic elimination of the excited states:

$$P_e \dot{\tilde{\rho}}^{(2)}(t) P_e \approx 0. \quad (3.25)$$

Consequently, the dynamics of second order in Eq. (3.20) are approximated by the dynamics of the ground states given by Eq. (3.22). Below we follow the recursion of the perturbative expansion and carry out the perturbation integrals.

We obtain $P_e \tilde{\rho}^{(2)}(t) P_e$ by integrating Eq. (3.24), and $\tilde{\rho}^{(1)}(t)$ by integrating Eq. (3.19), and insert the resulting expressions into Eq. (3.22). Having excluded the dynamics of the excited states by adiabatic elimination, we find the open system to evolve according to

$$\begin{aligned} P_g \dot{\tilde{\rho}}^{(2)}(t) P_g &= -P_g \tilde{V}(t) \left(\int_0^t dt' \tilde{V}(t') \tilde{\rho}^{(0)}(t') \right) P_g \\ &\quad - P_g \left(\int_0^t dt' \tilde{\rho}^{(0)}(t') \tilde{V}^\dagger(t') \right) \tilde{V}^\dagger(t) P_g \\ &\quad + P_g \sum_k \tilde{L}_k(t) P_e \int_0^t dt' \int_0^{t'} dt'' \left(\tilde{V}(t') \tilde{\rho}^{(0)}(t'') \tilde{V}^\dagger(t'') \right) P_e \tilde{L}_k^\dagger(t) P_g \\ &\quad + P_g \sum_k \tilde{L}_k(t) P_e \int_0^t dt' \int_0^{t'} dt'' \left(\tilde{V}(t'') \tilde{\rho}^{(0)}(t'') \tilde{V}^\dagger(t') \right) P_e \tilde{L}_k^\dagger(t) P_g. \end{aligned} \quad (3.26)$$

Here, we have omitted terms where the density operator is sandwiched between perturbations $P_g \tilde{V}$ and $\tilde{V} P_g$. As $\tilde{\rho}^{(0)}$ lives in the ground-state subspace, these

terms do not contribute to the ground-state evolution and can therefore be neglected. The remaining expression in Eq. (3.26) contains two Hamiltonian-like and two Lindblad-like terms, for which we will carry out the integrals:

$$I_1 \equiv P_g \tilde{V}(t) \int_0^t dt' \tilde{V}(t') \tilde{\rho}^{(0)}(t') P_g \quad (3.27)$$

$$I_2 \equiv P_e \int_0^t dt' \int_0^{t'} dt'' \tilde{V}(t') \tilde{\rho}^{(0)}(t'') \tilde{V}^\dagger(t'') P_e. \quad (3.28)$$

In this section we assume the direct interactions within the ground-state subspace to be perturbative. Hence, the ground-state evolution is negligibly small compared to the one for the excited states so that we have $\hat{O}(t)P_g \simeq P_g$. Consequently, I_1 simplifies to

$$I_1 \approx \hat{V}_- \hat{O}(t) \left(\int_0^t dt' \hat{O}^{-1}(t') \right) \hat{V}_+ \tilde{\rho}^{(0)}(t) \quad (3.29)$$

Carrying out the integral we find

$$\begin{aligned} I_1 &\approx \hat{V}_- e^{-i\hat{H}_{\text{NH}}t} \left[(i\hat{H}_{\text{NH}})^{-1} e^{i\hat{H}_{\text{NH}}t'} \right]_0^t \hat{V}_+ \tilde{\rho}^{(0)}(t) \\ &\approx \hat{V}_- (i\hat{H}_{\text{NH}})^{-1} \hat{V}_+ \tilde{\rho}^{(0)}(t). \end{aligned} \quad (3.30)$$

In the last step we have used that the term emerging from the lower limit of the integral at $t' = 0$ maintains its time dependence of $e^{-i\hat{H}_{\text{NH}}t}$ and is therefore detuned with respect to the term originating from the integral limit at $t' = t$, i.e., by an approximation similar to the rotating wave approximation we keep the unity term in the expression $1 - \exp(-i\hat{H}_{\text{NH}}t)$. This condition is equivalent to the standard approximation of adiabatic elimination and is justified provided that the time evolution of the ground states is slow compared to the time scale set by \hat{H}_{NH}^{-1} . The second term of Eq. (3.26) is treated accordingly, yielding the Hermitian conjugate of the result in Eq. (3.30).

For the last two Lindblad-type terms in Eq. (3.26) we carry out the double integral I_2 . To this end, we approximate $\tilde{\rho}^{(0)}(t'')$ in Eq. (3.28) by $\tilde{\rho}^{(0)}(t)$. This can be argued the following way: Above we have assumed that the density matrix of the ground states $\tilde{\rho}^{(0)}(t)$ evolves slowly and to second-order in \hat{V} . Another dependence on $\tilde{V}(t')$ and $\tilde{V}(t'')$ would only involve features of fourth order in the evolution. We neglect these higher orders by dropping the dependence of $\tilde{\rho}^{(0)}(t')$ and $\tilde{\rho}^{(0)}(t'')$ on the time scales of $\tilde{V}(t')$ and $\tilde{V}(t'')$, which yields $\tilde{\rho}^{(0)}(t)$. Thus, we can separate the integral and write

$$\begin{aligned} I_2 &\approx \frac{1}{2} \left(\int_0^t dt' \tilde{O}^{-1}(t') \right) \hat{V}_+ \tilde{\rho}^{(0)}(t) \hat{V}_- \int_0^t dt' (\tilde{O}^{-1})^\dagger(t') \\ &\approx \frac{1}{2} (i\hat{H}_{\text{NH}})^{-1} \hat{V}_+ \tilde{\rho}^{(0)}(t) \hat{V}_- (-i\hat{H}_{\text{NH}}^\dagger)^{-1}. \end{aligned} \quad (3.31)$$

Again we have assumed that the ground states are slowly varying compared to the time scale of \hat{H}_{NH}^{-1} so that $\hat{O}(t)P_g \simeq P_g$ and discarded detuned terms. The remaining term of Eq. (3.26) yields the same result as Eq. (3.31).

We insert Eqs. (3.30) and (3.31) back into Eq. (3.26) and transform back into the Schrödinger picture. In doing so, we obtain the effective unitary and dissipative dynamics of the ground states,

$$P_g \dot{\rho}^{(2)} P_g = \left[-i \left(\hat{H}_{\text{eff}} - \frac{i}{2} \sum_k (\hat{L}_{\text{eff}}^k)^\dagger \hat{L}_{\text{eff}}^k \right) \rho^{(0)} + H.c. \right] + \sum_k \hat{L}_{\text{eff}}^k \rho^{(0)} (\hat{L}_{\text{eff}}^k)^\dagger. \quad (3.32)$$

with an effective Hamiltonian and effective Lindblad operators as defined in Eqs. (3.3) and (3.4). To reach this form we have used the equality

$$\begin{aligned} \sum_k (\hat{L}_{\text{eff}}^k)^\dagger \hat{L}_{\text{eff}}^k &= \hat{V}_- (\hat{H}_{\text{NH}}^{-1})^\dagger \left(\sum_k \hat{L}_k^\dagger \hat{L}_k \right) \hat{H}_{\text{NH}}^{-1} \hat{V}_+ \\ &= -i \hat{V}_- \left(\hat{H}_{\text{NH}}^{-1} - (\hat{H}_{\text{NH}}^{-1})^\dagger \right) \hat{V}_+. \end{aligned} \quad (3.33)$$

From here it can easily be seen that Eq. (3.32) is equivalent to Eq. (3.2). Thus, we have reduced the unitary and dissipative dynamics of the open quantum system described by Eq. (3.1) to the effective master equation of Lindblad form in Eq. (3.2), obtaining the effective Hamiltonian \hat{H}_{eff} and Lindblad operators \hat{L}_{eff}^k of Eqs. (3.3) and (3.4).

The effective Hamiltonian of Eq. (3.3) is the same as the original result of Feshbach [131]. In addition, we have found effective Lindblad operators for second-order decay processes. As can be seen from Eq. (3.4), each of them consists of weak coherent excitation \hat{V}_+ , evolution between the excited states by a “propagator” \hat{H}_{NH}^{-1} , and subsequent decay \hat{L}_k . Thus, adiabatic elimination of the excited states of an open quantum system is formalized in a compact manner by Eqs. (3.2)–(3.5).

3.3.5 Non-perturbative ground-state coupling

The formalism of Eqs. (3.2)–(3.4) was derived assuming that the ground-state couplings \hat{H}_g are much weaker than those of the excited states contained by \hat{H}_{NH} . Under this assumption of a perturbative ground-state coupling it was possible to neglect the effect of \hat{H}_g on the effective processes.

For strong interactions between the ground states, the action of \hat{H}_g can no longer be ignored in the effective processes so that the accuracy of the effective dynamics of Eqs. (3.3) and (3.4) will decrease when \hat{H}_g approaches \hat{H}_{NH} . We will now show how to overcome this drawback by diagonalizing the ground-state Hamiltonian \hat{H}_g and including its action in the effective operators.

We can build on the dynamics of the separate subspaces as given by Eqs. (3.24) and (3.26), derived without any assumption about the strength of \hat{H}_g . In contrast to the above derivation, we can no longer assume $\hat{O}(t)P_g \simeq 1P_g$. Since \hat{H}_g and \hat{H}_{NH} do not couple the ground and excited subspaces, we can separate the evolution operator into one part for each of the subspaces:

$$\begin{aligned} \hat{O}(t) &= P_g \hat{O}_g(t) P_g + P_e \hat{O}_e(t) P_e \\ &= e^{-i\hat{H}_g t} P_g + e^{-i\hat{H}_{\text{NH}} t} P_e. \end{aligned} \quad (3.34)$$

We assume that \hat{H}_g can be diagonalized

$$\hat{H}_g = \sum_l E_l P_l \quad (3.35)$$

with dressed state energies E_l and a projector $P_l \equiv |l\rangle\langle l|$ for each ground state l . Accordingly, we decompose the perturbative excitations \hat{V}_+ with respect to the ground states,

$$\hat{V}_+ = \sum_l \hat{V}_+^l, \quad (3.36)$$

where we have defined $\hat{V}_+^l \equiv \hat{V}_+ P_l$ as the excitation from ground state l . Given the different energies of the dressed ground states, the effective evolution is now no longer identical for ground states with different energy E_l . This additional complication in the integral is taken into account by introducing the sum in Eq. (3.36). For instance, for the first term of Eq. (3.26) we have

$$I_1 = P_g \tilde{V}(t) \sum_l \int_0^t dt' \tilde{V}_l(t) \tilde{\rho}_l^{(0)}(t') P_l \quad (3.37)$$

With Eqs. (3.34)–(3.36) this term becomes

$$\begin{aligned} I_1 &= P_g \hat{O}_g^{-1}(t) \hat{V}_- \hat{O}_e(t) \sum_l \int_0^t dt' e^{i(\hat{H}_{\text{NH}} - E_l)t'} \hat{V}_+^l \tilde{\rho}^{(0)}(t) \\ &\approx iP_g \hat{O}_g^{-1}(t) \hat{V}_- \sum_l (\hat{H}_{\text{NH}} - E_l)^{-1} \hat{V}_+^l \hat{O}_g(t) \tilde{\rho}^{(0)}(t). \end{aligned}$$

The integration is carried out similarly for the other terms in Eq. (3.26) (the “sandwich” terms can be neglected for the same reasons as above). Transforming back into the Schrödinger picture and arranging the terms as in Eqs. (3.3) and (3.4) we find for the effective operators, including non-perturbative ground-state evolution,

$$\hat{H}_{\text{eff}} = -\frac{1}{2} \left[\hat{V}_- \sum_l \left(\hat{H}_{\text{NH}}^{(l)} \right)^{-1} \hat{V}_+^l + H.c. \right] + \hat{H}_g, \quad (3.38)$$

$$\hat{L}_{\text{eff}}^k = \hat{L}_k \sum_l \left(\hat{H}_{\text{NH}}^{(l)} \right)^{-1} \hat{V}_+^l. \quad (3.39)$$

We see that in order to apply this formalism rather than Eqs. (3.3)–(3.4) we replace the general inverse non-Hermitian Hamiltonian \hat{H}_{NH} by initial-state dependent propagators

$$\left(\hat{H}_{\text{NH}}^{(l)} \right)^{-1} \equiv (\hat{H}_{\text{NH}} - E_l)^{-1} \quad (3.40)$$

for each ground state l . In doing so we obtain the accurate effective dynamics in the presence of non-perturbative ground-state coupling. In Chapter 4 we will use this technique to investigate rapid preparation of entanglement by engineered decay. In Sec. 3.4.2 we consider a simpler example of a three-level Raman system.

3.3.6 Several perturbations or fields

In the following, we present an extension of our effective operator formalism to several perturbations or fields \hat{V}_f , where f denotes the particular field and ω_f its frequency. Then we can write the perturbations as

$$\hat{V}(t) = \sum_f \hat{V}_+^f(t) + H.c. = \sum_f \hat{v}_+^f e^{-i\omega_f t} + H.c. \quad (3.41)$$

The formalism we develop can also be used to include non-perturbative ground-state coupling as in Sec. 3.3.5. Still, at the first glance the assumption of several fields seems problematic: so far we assumed a rotating frame of reference in which \hat{V} is time independent. However, our formalism can be derived without this claim, starting from Eqs. (3.24) and (3.26). As opposed to the previous case, where we chose to work in the interaction picture, we now keep the time dependence in the perturbations. For simplicity we choose a time-independent frame with respect to the interactions inside the subspaces ($\frac{\partial \hat{H}_e}{\partial t} = \frac{\partial \hat{H}_g}{\partial t} = 0$). Again, for perturbative ground-state coupling \hat{H}_g the ground-state evolution becomes negligible, $\hat{O}_g(t) \approx \mathbb{1}$. The perturbative evolution of the ground states turns into a sum for the different fields f :

$$\begin{aligned} I_1 &= P_g \tilde{V}(t) \int_0^t dt' \tilde{V}(t') \tilde{\rho}^{(0)}(t') P_g \\ &\approx P_g \hat{V}_-(t) \hat{O}_e(t) \sum_f \int_0^t dt' e^{i(\hat{H}_{\text{NH}} - \omega_f)t'} \hat{v}_+^f P_k \rho^{(0)}(t) \\ &\approx iP_g \hat{V}_-(t) \sum_f (\hat{H}_{\text{NH}} - \omega_f)^{-1} \hat{V}_+^f(t) P_g \rho^{(0)}(t). \end{aligned} \quad (3.42)$$

We then obtain the effective operators

$$\hat{H}_{\text{eff}} = -\frac{1}{2} \left[\hat{V}_-(t) \sum_f \left(\hat{H}_{\text{NH}}^{(f)} \right)^{-1} \hat{V}_+^f(t) + H.c. \right] + \hat{H}_g \quad (3.43)$$

$$\hat{L}_{\text{eff}}^k = \hat{L}_k \sum_f \left(\hat{H}_{\text{NH}}^{(f)} \right)^{-1} \hat{V}_+^f(t) \quad (3.44)$$

with one propagator $(\hat{H}_{\text{NH}}^{(f)})^{-1} \equiv (\hat{H}_{\text{NH}} - \omega_f)^{-1}$ for each field f . This extension will be used in Chapter 7, where we apply multi-tone fields.

3.3.7 General formalism

In Sec. 3.3.5 we derived an extension of the effective operators in Eqs. (3.3) and (3.4) for non-perturbative ground-state coupling and in Sec. 3.3.6 an extension for several fields. In a situation with both aspects present these two extensions can be directly combined. We find the effective operators

$$\hat{H}_{\text{eff}} = -\frac{1}{2} \left[\hat{V}_- \sum_{f,l} \left(\hat{H}_{\text{NH}}^{(f,l)} \right)^{-1} \hat{V}_+^{(f,l)}(t) + H.c. \right] + \hat{H}_g \quad (3.45)$$

$$\hat{L}_{\text{eff}}^k = \hat{L}_k \sum_{f,l} \left(\hat{H}_{\text{NH}}^{(f,l)} \right)^{-1} \hat{V}_+^{(f,l)}(t) \quad (3.46)$$

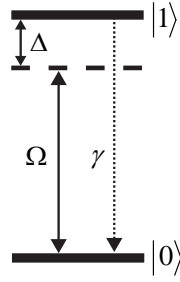


FIGURE 3.2: Two-level system. A ground state $|0\rangle$ is coherently coupled to an excited state $|1\rangle$ by a field with a Rabi frequency Ω . The excited state $|1\rangle$ is subject to spontaneous decay at a γ .

with field- and state-dependent propagators

$$\left(\hat{H}_{\text{NH}}^{(f,l)}\right)^{-1} \equiv (\hat{H}_{\text{NH}} - E_l - \omega_f). \quad (3.47)$$

This quantity contains both the information about the initial state and the exciting field; it is thus the most general propagator expression presented. It will be used in Chapter 5 to construct an effective two-photon drive across a dipole-forbidden transition.

3.4 Examples

In the following, we discuss a number of example systems to which we apply our formalism. We first consider two standard setups, a dissipative two-level system and a three-level Raman system. Here, we derive the effective interactions, and compare them to the results obtained using other methods. We then move on to a four-level system, where an effective decay process can be engineered, and discuss the available degrees of freedom and the effective quantities. Based on these examples we give a brief account on the general principles of dissipative state preparation which will be applied in Chapter 4–7.

3.4.1 The two-level system

The most elementary configuration our formalism can be applied to is a two-level system with a ground state $|0\rangle$ coherently coupled to a spontaneously decaying excited state $|1\rangle$ (Fig. 3.2). This example is rather straightforward also without the theory developed here; yet, we include it to demonstrate the general formalism. The Hamiltonian for this system reads

$$\hat{H} = \hat{H}_e + \hat{V} \quad (3.48)$$

$$\hat{H}_e = \Delta|1\rangle\langle 1|, \hat{H}_g = 0 \quad (3.49)$$

$$\hat{V} = \frac{\Omega}{2} (|0\rangle\langle 1| + |1\rangle\langle 0|). \quad (3.50)$$

The levels $|0\rangle$ and $|1\rangle$ are coupled with a Rabi frequency Ω and a detuning Δ . We write the (de-) excitation as $\hat{V}_+ = \frac{\Omega}{2}|1\rangle\langle 0|$ ($\hat{V}_- = \frac{\Omega}{2}|0\rangle\langle 1|$). Spontaneous

emission from the excited to the ground level at a rate γ is represented by the Lindblad operator,

$$\hat{L} = \sqrt{\gamma}|0\rangle\langle 1|. \quad (3.51)$$

Consequently, the non-Hermitian Hamiltonian is found to be

$$\hat{H}_{\text{NH}} = \left(\Delta - \frac{i\gamma}{2} \right) |1\rangle\langle 1| \equiv \tilde{\Delta}|1\rangle\langle 1|. \quad (3.52)$$

Here, we have assigned a complex energy $\tilde{\Delta} \equiv \Delta - \frac{i\gamma}{2}$ that combines the detuning Δ and the line width γ of the excited state $|1\rangle$ to a single complex quantity.

By applying the effective Hamiltonian formula of Eq. (3.3) we adiabatically eliminate the excited state $|1\rangle$ and obtain an effective Hamiltonian for the ground state $|0\rangle$:

$$\begin{aligned} \hat{H}_{\text{eff}} &= -\frac{1}{2} \left(\frac{\Omega}{2}|0\rangle\langle 1| \right) \left(\frac{|1\rangle\langle 1|}{\tilde{\Delta}} + H.c. \right) \left(\frac{\Omega}{2}|1\rangle\langle 0| \right) \\ &= -\frac{\Omega^2\Delta}{4\Delta^2 + \gamma^2} |0\rangle\langle 0| \equiv \Delta_{\text{eff}}|0\rangle\langle 0|. \end{aligned} \quad (3.53)$$

This effective Hamiltonian describes an effective AC Stark shift Δ_{eff} of level $|0\rangle$ caused by the coherent driving. By applying Eq. (3.4) together with \hat{V} , \hat{H}_{NH} , and \hat{L}_γ as specified above, we obtain a single effective Lindblad operator

$$\begin{aligned} \hat{L}_{\text{eff}}^\gamma &= (\sqrt{\gamma}|0\rangle\langle 1|) \left(\frac{1}{\tilde{\Delta}}|1\rangle\langle 1| \right) \left(\frac{\Omega}{2}|1\rangle\langle 0| \right) \\ &= \frac{\sqrt{\gamma}\Omega}{2\Delta - i\gamma} |0\rangle\langle 0|. \end{aligned} \quad (3.54)$$

The effective scattering rate is thus given by

$$\gamma_{\text{eff}} \equiv |\langle 0|\hat{L}_{\text{eff}}|0\rangle|^2 = \frac{\gamma\Omega^2}{4\Delta^2 + \gamma^2}. \quad (3.55)$$

The effective Lindblad operator \hat{L}_{eff} describes Rayleigh scattering, i.e., elastic scattering of incident laser photons by the transition $|0\rangle \leftrightarrow |1\rangle$. Seen from the atom this effect will contribute to the effective dynamics of state $|0\rangle$ not as a decay but as a dephasing of potential coherent couplings to other states.

Above we have given a rather simple example which could also be easily solved without these techniques. For more complicated situations the formalism developed here is highly useful. In particular, in the following we consider a three-level Raman scheme and a four-level scheme relevant for dissipative state preparation.

3.4.2 The three-level Raman system

A three-level system in Raman configuration is a widely used quantum system so that the understanding of its effective processes is highly relevant. In particular Ref. [124] deals with its effective dynamics in the absence of decoherence in

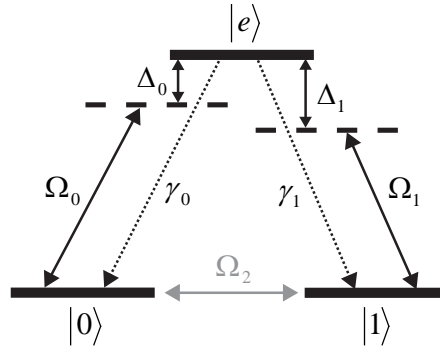


FIGURE 3.3: The three-level Raman system. Two ground states $|0\rangle$ and $|1\rangle$ are driven up to an excited state $|e\rangle$ with different detunings Δ_0, Δ_1 and Rabi frequencies Ω_0, Ω_1 . $|e\rangle$ decays to the ground states via spontaneous emission at rates γ_0 and γ_1 . Effects originating from non-perturbative interactions between the ground states (indicated by Ω_2) can also be taken into account by our extended formalism.

great detail. In the following, we give a description of the effective dynamics of a three-level Raman system that includes dissipation.

As illustrated in Fig. 3.3, the system consists of two ground states $|0\rangle$ and $|1\rangle$ and an excited state $|e\rangle$. Coherent driving of the transitions $|0\rangle \leftrightarrow |e\rangle$ and $|1\rangle \leftrightarrow |e\rangle$ is facilitated by two fields, generally with different detunings, Δ_0 and Δ_1 , and strengths, Ω_0 and Ω_1 . In a time-independent frame the system is described by

$$\hat{H}_g = -\Delta_0|0\rangle\langle 0| - \Delta_1|1\rangle\langle 1|, \quad \hat{H}_e = 0, \quad (3.56)$$

$$\hat{V} = \frac{\Omega_0}{2} (|0\rangle\langle e| + |e\rangle\langle 0|) + \frac{\Omega_1}{2} (|1\rangle\langle e| + |e\rangle\langle 1|), \quad (3.57)$$

assuming an arbitrarily strong non-perturbative \hat{H}_g . The time-independent formulation of Eq. (3.56) with detunings Δ_0 and Δ_1 assigned to the ground states allows us to use the formalism of Sec. 3.3.5. Alternatively, we could load the time dependence on the fields and use the formalism presented in Sec. 3.3.6. Decay from the excited level $|e\rangle$ into ground states $|0\rangle$ and $|1\rangle$ at rates γ_0 and γ_1 is described by the Lindblad operators

$$\hat{L}_{\gamma,0} = \sqrt{\gamma_0}|0\rangle\langle e|, \quad (3.58)$$

$$\hat{L}_{\gamma,1} = \sqrt{\gamma_1}|1\rangle\langle e|. \quad (3.59)$$

The non-Hermitian Hamiltonian can be divided into two parts, denoted by the initial state of the exciting field

$$\hat{H}_{\text{NH}}^{(0)} = \left(\Delta_0 - \frac{i\gamma}{2} \right) |e\rangle\langle e| \equiv \tilde{\Delta}_0 |e\rangle\langle e| \quad (3.60)$$

$$\hat{H}_{\text{NH}}^{(1)} = \left(\Delta_1 - \frac{i\gamma}{2} \right) |e\rangle\langle e| \equiv \tilde{\Delta}_1 |e\rangle\langle e|. \quad (3.61)$$

In the last step we have assigned complex energies that combine the real detuning and the imaginary decay of the levels.

Using the non-Hermitian Hamiltonians of Eqs. (3.60) and (3.61) together with Eqs. (3.38)-(3.57) we obtain the effective Hamiltonian

$$\begin{aligned} \hat{H}_{\text{eff}} = & \left(\Delta_0 - \frac{\Delta_0 \Omega_0^2}{4\Delta_0^2 + \gamma^2} \right) |0\rangle\langle 0| + \left(\Delta_1 - \frac{\Delta_1 \Omega_1^2}{4\Delta_1^2 + \gamma^2} \right) |1\rangle\langle 1| \\ & + \left(\frac{(\Delta_0 + \Delta_1)\Omega_0\Omega_1}{8(\Delta_0 - i\gamma/2)(\Delta_1 + i\gamma/2)} |0\rangle\langle 1| + H.c. \right), \end{aligned} \quad (3.62)$$

where we have defined an overall decay rate $\gamma = \gamma_0 + \gamma_1$. We note that despite the complex terms the effective Hamiltonian is Hermitian. Besides two shift terms similar to the one in Eq. (3.53), it contains an effective two-photon transition between the two ground states with an effective Rabi frequency

$$\tilde{\Omega}_{\text{eff}} \equiv \frac{(\Delta_0 + \Delta_1)\Omega_0\Omega_1}{8(\Delta_0 - i\gamma/2)(\Delta_1 + i\gamma/2)}. \quad (3.63)$$

In the absence of dissipative processes ($\gamma = 0$), this effective Hamiltonian equals the time-averaged ground-state Hamiltonian of Gamel and James [124], viz.,

$$\hat{H}_{\text{eff}} = - \left(\frac{\Omega_0\Omega_1}{4\Delta_0} + \frac{\Omega_0\Omega_1}{4\Delta_1} \right) (|0\rangle\langle 1| + |1\rangle\langle 0|) - \frac{\Omega_0^2}{4\Delta_0} |0\rangle\langle 0| - \frac{\Omega_1^2}{4\Delta_1} |1\rangle\langle 1| + \hat{H}_{\text{g}}. \quad (3.64)$$

We will encounter couplings of this kind when we consider an effective two-photon drive in Chapter 5. Furthermore, we derive the effective Lindblad operators

$$\hat{L}_{\text{eff}}^{\gamma,0} = \frac{\sqrt{\gamma_0}\Omega_0}{2(\Delta_0 - i\gamma/2)} |0\rangle\langle 0| + \frac{\sqrt{\gamma_0}\Omega_1}{2(\Delta_1 - i\gamma/2)} |0\rangle\langle 1|, \quad (3.65)$$

$$\hat{L}_{\text{eff}}^{\gamma,1} = \frac{\sqrt{\gamma_1}\Omega_0}{2(\Delta_0 - i\gamma/2)} |1\rangle\langle 0| + \frac{\sqrt{\gamma_1}\Omega_1}{2(\Delta_1 - i\gamma/2)} |1\rangle\langle 1|. \quad (3.66)$$

Besides one loop-term for each of the ground states in this setup, these operators contain effective decays from either ground state to the other, the strength of which is given by

$$\gamma_{\text{eff}}^{0 \rightarrow 1} \equiv |\langle 1 | \hat{L}_{\text{eff}}^{\gamma,1} | 0 \rangle|^2 = \frac{\gamma_1 \Omega_0^2}{4\Delta_0^2 + \gamma^2}, \quad (3.67)$$

$$\gamma_{\text{eff}}^{1 \rightarrow 0} \equiv |\langle 0 | \hat{L}_{\text{eff}}^{\gamma,0} | 1 \rangle|^2 = \frac{\gamma_0 \Omega_1^2}{4\Delta_1^2 + \gamma^2}. \quad (3.68)$$

We note that depending on the relative strength of the effective quantities Ω_{eff} and γ_{eff} , the resulting effective dynamics will either be governed by coherent or decoherent behavior.

This is visualized in Fig. 3.4 where we have plotted simulated curves of the full and effective dynamics obtained by numerical integration of the master equations (3.1)–(3.2). In Fig. 3.4 a) we show a purely unitary case, and in 3.4 b) a mixed case with both coherent and dissipative processes present.

In the purely unitary case ($\gamma = 0$) shown in Fig. 3.4 a) we see that the populations of the two ground levels exhibit Rabi oscillations at a high and a low frequency.

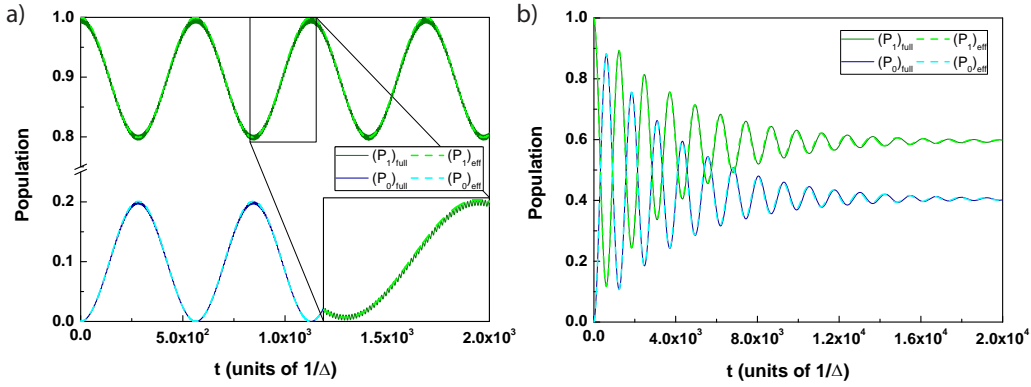


FIGURE 3.4: Comparison of effective and full evolution of a three-level Raman system. Curves obtained from numerical integration of the effective master equation (dashed) agree with results from the full master equation (solid) both (a) in the absence ($\gamma = 0$) and (b) in the presence of dissipation ($\gamma \neq 0$). The effective operators are found to model the slow dynamics of the two ground states $|0\rangle$ (blue, starting from 0) and $|1\rangle$ (green, starting from 1) very accurately, averaging out the fast oscillations (inset in a). For the simulations we used the parameters $\Omega_{0,1} = \Delta/10$ ($\Delta = \Delta_0 + \Delta_1$): (a) $\Delta_1 - \Delta_0 = \Delta/1000$, $\gamma_{0,1} = 0$, (b) $\Delta_1 - \Delta_0 = \Delta/100$, $\gamma_{0,1} = \Delta/10$.

The high-frequency oscillations correspond to the virtual excitation of the excited state $|e\rangle$. These oscillations are explicitly excluded from the formalism developed here and are therefore not present in the evolution with the effective operators, as can be seen from the inset in Fig. 3.4 a). Nevertheless, the formalism captures the slow dynamics of the ground states.

A case including dissipation ($\gamma \neq 0$) is shown in Fig. 3.4 b). Here, we see that even for Rabi oscillations sweeping almost the entire population between the ground states, the effective dynamics match the time evolution of the full master equation with very high precision. For large times t the oscillations are damped out and the evolution converges to a steady state.

Finally, we comment on the situation where the ground states are coupled by another field of strength Ω_2 , as illustrated in Fig. 3.3. In case this additional interaction is perturbative it can simply be included in \hat{H}_g , and hence, in \hat{H}_{eff} , without affecting the other terms. In the non-perturbative case the effect of Ω_2 on the effective processes is caught by changing into a frame in which the ground-state Hamiltonian \hat{H}_g is diagonal. From there the formalism of Sec. 3.3.5 can be applied.

3.4.3 Engineered decay

As we will see in Chapter 4–7, our formalism will allow us to engineer schemes that serve the purpose of dissipative state preparation. Here, the goal is to prepare a certain desired steady state as the outcome of the evolution of the open system. This is done by engineering its dissipative dynamics. To this end, we use the effective operators of Eqs. (3.3) and (3.4) to take nontrivial interactions between the excited states into account and to identify effective decay processes of the system. By an appropriate choice of the system parameters these processes

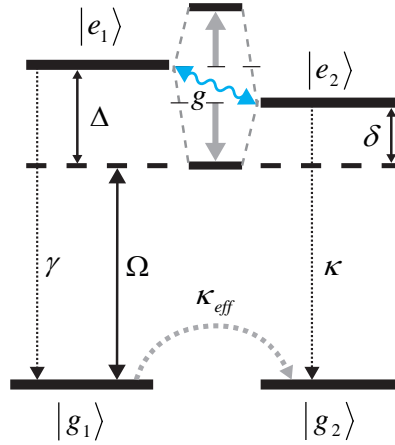


FIGURE 3.5: Dissipative state preparation in a four-level system. An effective decay process consisting of weak excitation from ground state $|g_1\rangle$ with a resonant Rabi frequency Ω , evolution between the excited levels $|e_1\rangle$ and $|e_2\rangle$, coupled with g , and subsequent decay κ prepares ground state $|g_2\rangle$. The effective decay rate κ_{eff} is engineered by the choice of the detunings of the excited states, Δ and δ ; κ_{eff} depends on how close the dressed states of $|e_1\rangle$ and $|e_2\rangle$ are shifted into resonance with the driving (Ω) by their coupling (g).

can be engineered. This is done by tailoring the “propagator” \hat{H}_{NH}^{-1} , as will be discussed below.

An example of this is depicted in Fig. 3.5, showing a four-level system consisting of two ground states $|g_1\rangle, |g_2\rangle$ and two excited states $|e_1\rangle, |e_2\rangle$. The excited-state Hamiltonian

$$\hat{H}_e = \Delta|e_1\rangle\langle e_1| + \delta|e_2\rangle\langle e_2| + g(|e_1\rangle\langle e_2| + |e_2\rangle\langle e_1|) \quad (3.69)$$

contains the detunings Δ for $|e_1\rangle$ and δ for $|e_2\rangle$, respectively, and a coupling with a strength g between $|e_1\rangle$ and $|e_2\rangle$. We assume that there are no processes between the ground states so that $\hat{H}_g = 0$. The weak classical driving described by

$$\hat{V} = \frac{\Omega}{2} (|g_1\rangle\langle e_1| + |e_1\rangle\langle g_1|) \quad (3.70)$$

drives the system between $|g_1\rangle$ and $|e_1\rangle$ with a Rabi frequency Ω . We assume $|e_1\rangle$ to decay to $|g_1\rangle$ at a rate γ and $|e_2\rangle$ to $|g_2\rangle$ at a rate κ , represented by the Lindblad operators

$$\hat{L}_\gamma = \sqrt{\gamma}|g_1\rangle\langle e_1|, \quad (3.71)$$

$$\hat{L}_\kappa = \sqrt{\kappa}|g_2\rangle\langle e_2|. \quad (3.72)$$

The non-Hermitian Hamiltonian is then given by

$$\hat{H}_{\text{NH}} = \tilde{\Delta}|e_1\rangle\langle e_1| + \tilde{\delta}|e_2\rangle\langle e_2| + g(|e_1\rangle\langle e_2| + H.c.), \quad (3.73)$$

with complex detunings $\tilde{\delta} \equiv \delta - \frac{i\kappa}{2}$ and $\tilde{\Delta} \equiv \Delta - \frac{i\gamma}{2}$. Using Eqs. (3.3) and (3.4) we obtain the effective Hamiltonian and Lindblad operators:

$$\hat{H}_{\text{eff}} = -\frac{\Omega^2}{4} \text{Re} \left(\frac{\tilde{\delta}}{\tilde{\delta}\tilde{\Delta} - g^2} \right) |g_1\rangle\langle g_1|, \quad (3.74)$$

$$\hat{L}_{\text{eff}}^\gamma = \frac{\sqrt{\gamma}\tilde{\delta}\Omega}{2(\tilde{\delta}\tilde{\Delta} - g^2)} |g_1\rangle\langle g_1|, \quad (3.75)$$

$$\hat{L}_{\text{eff}}^\kappa = \frac{\sqrt{\kappa}g\Omega}{2(g^2 - \tilde{\delta}\tilde{\Delta})} |g_2\rangle\langle g_1|. \quad (3.76)$$

We note that the effective Hamiltonian \hat{H}_{eff} only contains a shift of $|g_1\rangle$. The effective decay process $\hat{L}_{\text{eff}}^\kappa$ effectively prepares the ground state $|g_2\rangle$ from $|g_1\rangle$ at a rate of

$$\kappa_{\text{eff}} \equiv |\langle g_2 | \hat{L}_{\text{eff}}^\kappa | g_1 \rangle|^2 = \frac{\kappa g^2 \Omega^2}{4|g^2 - \tilde{\delta}\tilde{\Delta}|^2}. \quad (3.77)$$

The other process $\hat{L}_{\text{eff}}^\gamma$ is a dephasing of $|g_1\rangle$ with a rate

$$\gamma_{\text{eff}} \equiv |\langle g_1 | \hat{L}_{\text{eff}}^\gamma | g_1 \rangle|^2 = \frac{\gamma |\tilde{\delta}|^2 \Omega^2}{4|\tilde{\delta}\tilde{\Delta} - g^2|^2}. \quad (3.78)$$

The strength of the effective Lindblad operator concept is obvious: We immediately derive the effective pumping rates and dynamics of the ground states from the initial operators. If one desires to optimize the preparation of $|g_2\rangle$ from $|g_1\rangle$ which happens at a rate κ_{eff} , this can be realized by an appropriate choice of the system parameters, Δ , δ , and eventually, g .

Let us assume that γ , κ , and g are fixed, that the coupling g is strong, $g \gg \gamma, \kappa$, and that the detunings Δ and δ are adjustable. Then the optimum is reached by adjusting the detunings to $\delta_{\text{opt}} = g^2/\Delta$ and $\Delta_{\text{opt}} = g\sqrt{\gamma/\kappa}$, which leads to a maximized effective decay rate of

$$\kappa_{\text{eff}}^{\text{opt}} \approx \frac{\Omega^2}{8\gamma}. \quad (3.79)$$

To compare the effective with the full dynamics, we perform simulations of the evolution of the system by numerically integrating the master equations (3.1) and (3.2). The resulting curves are plotted in Fig. 3.6. Here, we show dissipative preparation of $|g_2\rangle$ from $|g_1\rangle$ for the optimal choice of Δ and δ as given above. We note that for weak driving Ω (solid lines, $\Omega = \gamma/10$), the curves of the effective and full dynamics exhibit excellent agreement. For stronger driving Ω (dash-dot, $\Omega = \gamma/2$; dot, $\Omega = \gamma$), the effective dynamics exhibit increasing deviations. These result from the breakdown of the assumption of weak driving used to derive the effective operators.

Interpretation and application of the inverse non-Hermitian Hamiltonian. In general, a good physical understanding of the effective decay mechanisms of an open quantum system is desirable. Even more so, it is essential for developing

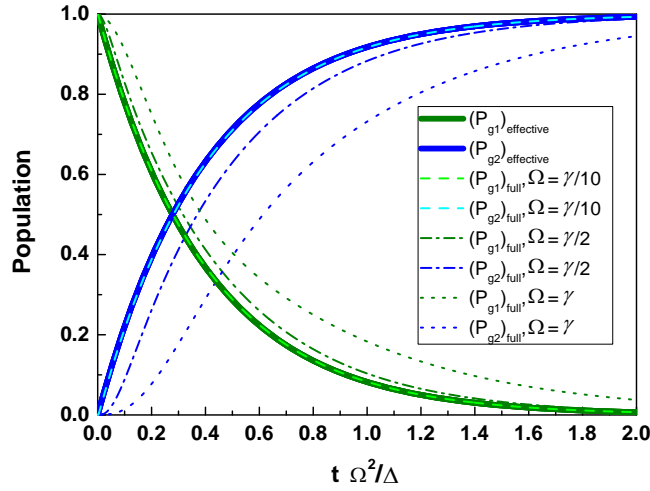


FIGURE 3.6: Effective and full time evolution of a system with engineered decay. The curves illustrate the preparation of the ground state $|g_2\rangle$ (blue lines, starting from 0) by decay of the ground state $|g_1\rangle$ (green lines, starting from 1). For weak driving $\Omega \leq \gamma/5$ the effective operators (thick solid) match the full evolution (dash, $\Omega = \gamma/10$) very accurately. With increasing driving Ω the assumption of perturbative excitation is no longer valid and the effective evolution deviates from the full dynamics (dash-dot, $\Omega = \gamma/2$; dot, $\Omega = \gamma$). For the simulations the system parameters $\gamma = \kappa = g/10$ and the optimized detunings $\delta = g^2/\Delta$ and $\Delta = g\sqrt{\gamma/\kappa}$ were used.

dissipative state preparation schemes such as the ones in Chapter 4–7. There, effective decay processes will be engineered to prepare a desired steady state. To a large extent this is done through the elements of the inverse non-Hermitian Hamiltonian. In the following, we discuss the physical meaning of these elements for the example at hand. We find that \hat{H}_{NH}^{-1} can be written as

$$\hat{H}_{\text{NH}}^{-1} = \tilde{\Delta}_{\text{eff}}^{-1} |e_1\rangle\langle e_1| + \tilde{\delta}_{\text{eff}}^{-1} |e_2\rangle\langle e_2| + \tilde{g}_{\text{eff}}^{-1} (|e_1\rangle\langle e_2| + |e_2\rangle\langle e_1|), \quad (3.80)$$

having defined the quantities

$$\tilde{\Delta}_{\text{eff}} \equiv 1/\langle e_1|\hat{H}_{\text{NH}}^{-1}|e_1\rangle = \tilde{\Delta} - g^2/\tilde{\delta} \quad (3.81)$$

$$\tilde{\delta}_{\text{eff}} \equiv 1/\langle e_2|\hat{H}_{\text{NH}}^{-1}|e_2\rangle = \tilde{\delta} - g^2/\tilde{\Delta} \quad (3.82)$$

$$\tilde{g}_{\text{eff}} \equiv 1/\langle e_1|\hat{H}_{\text{NH}}^{-1}|e_2\rangle = g - \tilde{\delta} \cdot \tilde{\Delta}/g. \quad (3.83)$$

Each of the latter quantities can be seen as an effective complex detuning ($\tilde{\Delta}_{\text{eff}}$, $\tilde{\delta}_{\text{eff}}$) or coupling (\tilde{g}_{eff}) of the excited states. \hat{H}_{NH}^{-1} contains their inverses which act as “propagators” for the effective operators of Eqs. (3.3) and (3.4) and therefore govern the strength of the effective processes. We can now express the effective decay rates of Eqs. (3.77) and (3.78) in terms of the effective complex energies and couplings of the excited states:

$$\kappa_{\text{eff}} = \frac{\kappa\Omega^2}{4|\tilde{g}_{\text{eff}}|^2}, \quad (3.84)$$

$$\gamma_{\text{eff}} = \frac{\gamma\Omega^2}{4|\tilde{\Delta}_{\text{eff}}|^2}. \quad (3.85)$$

We note that our above choice of $\delta = \delta_{\text{opt}}$ minimizes $|\tilde{\Delta}_{\text{eff}}|^2$, $|\tilde{\delta}_{\text{eff}}|^2$, and $|\tilde{g}_{\text{eff}}|^2$. Physically, this corresponds to the case where the driving \hat{V} is in resonance with the lower dressed state of the excited states $|e_1\rangle$ and $|e_2\rangle$ (or the upper dressed state for $\delta = -\frac{g^2}{\Delta}$, respectively), as can be seen from Fig. 3.5. Accordingly, the absolute values of the propagators of \hat{H}_{NH}^{-1} in Eq. (3.80) are maximized under this choice, resulting in an enhanced decay from $|g_1\rangle$ to $|g_2\rangle$. This can be used for dissipative state preparation as we discuss in the section below.

3.4.4 Dissipative state preparation

Based on the presented examples, we briefly address some basic principles of dissipative state preparation. We begin by discussing optical pumping and then move on to a more advanced engineered decay processes.

Optical pumping [74] constitutes a widely used technique for the preparation of pure – albeit not entangled – states by means of decay. The necessary ingredients for optical pumping are present in the Raman scheme in Fig. 3.3: A single field couples to one of two optical transitions of a three-level (Λ) system. The field, e.g. the one with Ω_0 in Eq. (3.57), thereby excites one of the two ground levels, $|0\rangle$ to the excited level, $|e\rangle$. The level $|e\rangle$ is, in turn, subject to decay, such as spontaneous emission, described by the Lindblad operators in Eqs. (3.58)–(3.59), with a total decay rate $\gamma = \gamma_0 + \gamma_1$. In the absence of a detuning Δ_0 and assuming for simplicity $\gamma_1 = \frac{\gamma}{2}$, the effective decay from $|0\rangle$ to $|1\rangle$ is described by the effective Lindblad operator

$$L_{\text{eff}}^{\gamma,0} = \frac{i\Omega}{\sqrt{2\gamma}} |1\rangle\langle 0|, \quad (3.86)$$

which yields an effective decay rate

$$\gamma_{\text{eff}}^{0 \rightarrow 1} = |\langle 1|L_{\text{eff}}^{\gamma,1}|0\rangle|^2 = \frac{\Omega^2}{2\gamma}. \quad (3.87)$$

As we can see from this expression, the population of level $|0\rangle$ can, in principle, be completely transferred to level $|1\rangle$, thus allowing for a theoretical fidelity 1 of state $|1\rangle$ in the steady state. From Eq. (3.87) it also appears that there is some degree of freedom to engineer the decay by adjusting the driving strength Ω , and possibly also the line width γ . One can now think of a situation where two such decay processes are concatenated. This can, e.g., be the case for two driven atoms, where we have the decay processes $|00\rangle \xrightarrow{|0e\rangle, |e0\rangle} \{|01\rangle, |10\rangle\} \xrightarrow{|1e\rangle, |e1\rangle} |11\rangle$. Here, the rate for each decay process is determined by the decay rate of a single excitation to $|e\rangle$. It is therefore not possible to favor, say, the first decay process over the second one. Such a requirement will, however, turn out to be essential for the preparation of an entangled state of two qubits in Chapter 4–6. In the following, we will sketch how dissipative state preparation can be achieved when using a four-level system with engineered decay.

Engineered decay has previously been discussed in Sec. 3.4.3 for a four-level system. Such a setting allows us to tailor effective decay processes: In engineer-

ing several such processes to be different in strength we lay the foundations for developing schemes for dissipative state preparation in the succeeding chapters. We consider two concatenated decay processes, each of the kind shown in Fig. 3.5. We assume them to lead from a state $|0\rangle$ to a state $|1\rangle$ and, by a similar process, to a state $|2\rangle$. Using the results of Sec. 3.4.3, we can describe these by

$$L_{\kappa,\text{eff}} = \sqrt{\kappa_{\text{eff},1}}|1\rangle\langle 0| + \sqrt{\kappa_{\text{eff},2}}|2\rangle\langle 1|, \quad (3.88)$$

$$\kappa_{\text{eff},n} = \frac{\kappa\Omega^2}{4|\tilde{g}_{\text{eff},n}|^2}, \quad (3.89)$$

$$\tilde{g}_{\text{eff},n} = \sqrt{n}g - \frac{\Delta\tilde{\delta}}{\sqrt{n}g}. \quad (3.90)$$

The physical meaning of the parameter n will become clear in Chapter 4, for now it is only important to state that $\tilde{g}_{\text{eff},n}$ can differ. We now engineer the first decay process to be strong and the second one to be weak. This is achieved by making the same parameter choice as in Sec. 3.4.3, $\Delta\delta = g^2$ and $\frac{\Delta}{\delta} = \frac{\gamma}{\kappa}$. For $g^2 \gg \gamma\kappa$ this results in

$$\tilde{g}_{\text{eff},1} \approx i\sqrt{\gamma\kappa}, \quad (3.91)$$

$$\tilde{g}_{\text{eff},2} \approx g. \quad (3.92)$$

Assuming $g^2 \gg \gamma\kappa$ we have thereby achieved that $|\tilde{g}_{\text{eff},1}| \ll |\tilde{g}_{\text{eff},2}|$, and hence that $|\kappa_{\text{eff},1}| \gg |\kappa_{\text{eff},2}|$. A similar effect is found when considering effective spontaneous emission (γ_{eff}). Two excited state situations with a difference in the couplings thus allow us to favor one decay process over the other: While $\kappa_{\text{eff},1}$ is suppressed by a detuning, $\kappa_{\text{eff},2}$ is only limited by the line width of the involved levels. The dissipative preparation of state $|1\rangle$ is then much faster than the losses to $|2\rangle$. This example will prove useful when we consider dissipative state preparation schemes in actual physical systems in Chapter 4–7.

3.5 Comparison to other methods

Covering both coherent Hamiltonian and dissipative Lindblad interactions, our effective operator formalism allows us to reduce the complexity of an open quantum system considerably by restricting its time evolution to an effective master equation describing ground-state to ground-state processes. It is thus useful for understanding the quantum dynamics of complex open systems by identifying their effective dissipative interactions and by reducing high-dimensional evolution to an effective master equation of the ground states. More specifically, our effective operators can be applied to identify and tailor effective decay processes involving coherent driving and naturally occurring sources of noise in open quantum systems. In particular, the presented operators allow for the development of physical schemes for dissipative quantum computing and dissipative state engineering, as will be seen in the succeeding chapters.

In the following, we compare the results obtained here with other methods from the literature. The formalism we have presented here is equivalent to the standard approach of adiabatic elimination in quantum optics (see, e.g., Ref. [122])

and is essentially a formalization of it. In most approaches adiabatic elimination is done at the level of equations of motion. This procedure can therefore be rather tedious, as it requires the derivation of the equations of motion followed by various manipulations of the equations, which are then often used to extract effective operators. For comparison, our formalism works directly at the operators and immediately gives the effective operators without reverting to the equations of motion.

The effective operators of Eqs. (3.3) and (3.4) are the most compact formalism presented in this work. For the assumption of perturbative ground-state coupling and a single perturbative exciting field these operators match the time evolution very precisely. The extended operators of Eqs. (3.38) and (3.39), (3.43) and (3.44), and (3.45) and (3.46) allow for the same precision, but also in the presence of non-perturbative ground-state interactions and several exciting fields.

As could be seen from the example of the three-level Raman scheme in Sec. 3.4.2, in the absence of decoherence the effective Hamiltonian method of James and co-workers [123, 124] can lead to similar results as our formalism. However, as opposed to Ref. [124], we do not find any additional decoherence terms emerging from averaging over the fast coherent evolution of the fields.

Also, the Feshbach projection-operator method of Refs. [131, 133] allows for descriptions of open system dynamics by means of an effective non-Hermitian Hamiltonian. We see that if we ignore the feeding term $\sum_k \hat{L}_{\text{eff}}^k \rho^{(0)} (\hat{L}_{\text{eff}})^{\dagger}$ in Eq. (3.32) the evolution is described by an effective non-Hermitian Hamiltonian

$$\hat{H}_{\text{eff,NH}} = \hat{H}_{\text{eff}} - \frac{i}{2} \sum_k (\hat{L}_{\text{eff}}^k)^{\dagger} \hat{L}_{\text{eff}}^k \quad (3.93)$$

$$= \hat{V}_- \hat{H}_{\text{NH}}^{-1} \hat{V}_+ + \hat{H}_g. \quad (3.94)$$

This Hamiltonian is equivalent to the one of Refs. [131, 133]. In the language of the Monte Carlo wave function method [126], $\hat{H}_{\text{eff,NH}}$ accounts for the “no-jump” evolution of the ground states. In contrast to this method, our effective formalism goes beyond including effects of non-Hermitian time evolution in the effective Hamiltonian, as we also include the feeding term. As a result we separate the non-Hermitian effective evolution into a Hermitian part with a (Hermitian) Hamiltonian \hat{H}_{eff} and a non-Hermitian part with effective Lindblad operators \hat{L}_{eff}^k .

3.6 Beyond perturbation theory

In several places we will encounter situations with strong driving. This contradicts the assumption of a perturbative drive made in the derivation of the effective operator formalism. In Sec. 4.4, the dominant effect is the dressing of the ground states. This mechanism can be included using the generalized formalism in Sec. 3.3.5. In Sec. 6.4.2, 7.4 and 7.6, the dominant effect is power broadening of the excited resonances which cannot be included using the extensions of the formalism presented so far. Still, it will be possible to add phenomenological terms from adiabatic elimination to the effective operators to make them account

for the effect of power broadening. The effective operators which are patched-up in this way describe the behavior of the strongly driven system quite accurately.

3.7 Reduction of the dynamics to rate equations

Using the effective operator formalism, we can achieve a reduction of the dynamics of the open system to an effective master equation of the ground states. This description is exact to second order perturbation theory. If, in addition, the effective Hamiltonian vanishes, $H_{\text{eff}} = 0$, the remaining dynamics is purely dissipative. We can then, in another step, reduce the complexity of the dynamics to rate equations of the populations. This is achieved by choosing subspaces of interest between which the interactions present in the system do not build up coherences. The subspaces are defined by projection operators, e.g. P_A and P_B . For negligible coherences between the subspaces A and B we can then trace over the Liouvillian evolution to obtain decay rates from subspace A to subspace B

$$\Gamma_{A \rightarrow B} \equiv \text{Tr}(P_B \mathcal{L}(P_A \rho_i P_A) P_B) = \sum_k \text{Tr}(P_B L_k P_A \rho_i P_A L_k^\dagger P_B) \quad (3.95)$$

$$= \sum_k \sum_f \langle \psi_f | P_B L_k P_A \rho_i P_A L_k^\dagger P_B | \psi_f \rangle \quad (3.96)$$

$$\equiv \sum_k \Gamma_{A \rightarrow B, k} \quad (3.97)$$

For the subspaces we will consider, the decay rate is the same for all states in the subspace. We can then calculate the decay rates using a single state $|\psi_i\rangle$,

$$\Gamma_{A \rightarrow B, k} = \sum_f |\langle \psi_f | P_B L_k P_A | \psi_i \rangle|^2 \quad (3.98)$$

We will use this rate equation approach to analyze the scaling of the preparation time of the protocols in Chapters 4–7.

Dissipative preparation of entanglement in cavity QED

As we pointed out in Chapter 2, the reliable and efficient preparation of entanglement is one of the main tasks in quantum information science. The effort has been driven on the one hand by the desire to understand these quintessentially non-classical states of matter, and on the other by their promise as building blocks for quantum information processing tasks. In particular entangled states are believed to be the main ingredient responsible for the additional information processing power of quantum machines over classical ones and are an important resource in quantum communication. Having access to a reliable source of entanglement thus cannot be overestimated.

Since the advent of quantum information science, noise has been considered a detrimental element in entanglement preparation schemes (cf. Sec. 2.4.2). A few years ago, however, it has been suggested that dissipative noise can be used as a resource for quantum information processing, supporting the preparation of entangled states. Since then many quantum information processing tasks have been reconsidered within the framework of dissipative state engineering and dissipative quantum computing, which are summarized in Sec. 2.4.3. Theoretical and experimental studies along these lines have shown these new ideas to be realistic and promising as a new path for harnessing the potential of quantum information.

In this chapter, we present schemes for the dissipative preparation of a maximally entangled steady state. As a concrete physical system we consider a cavity QED setup (cf. Sec. 2.4.1) with two atoms coupled to a high-finesse optical cavity [37–42]. Generating entanglement in this system by unitary evolution has been studied in great detail theoretically [43–49] and the limitations coming from dissipation are therefore well understood (see Sec. 2.4.2).

The setup is described in detail in Sec. 4.1. In Sec. 4.3–4.5 we demonstrate that a maximally entangled steady state (stationary state) of the two atoms in an optical cavity can be prepared dissipatively with a very high fidelity. This can be achieved by several qualitatively different state preparation mechanisms, depending on the strengths and limitations of the experiment at hand. In each of the schemes, the two atoms are rapidly driven into a singlet state, indepen-

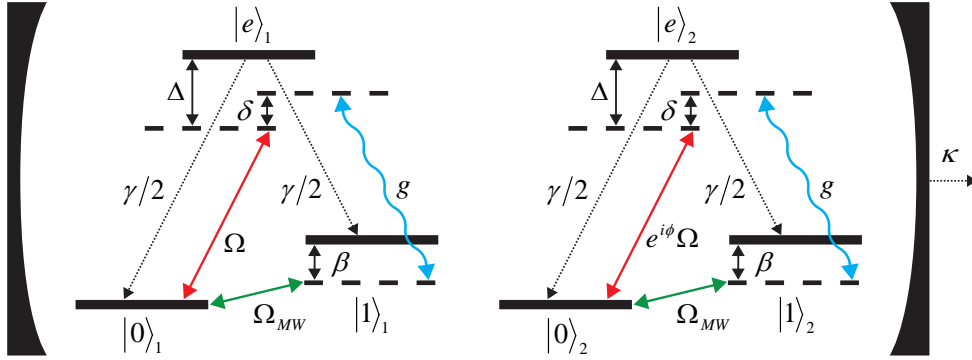


FIGURE 4.1: Cavity QED setup for dissipative preparation of an entangled state between two Λ -type atoms in an optical cavity. Coherent driving Ω is performed from ground state $|0\rangle$ to the excited state $|e\rangle$. Atom-cavity interaction g takes place between $|e\rangle$ and ground state $|1\rangle$; the ground states are coupled by a microwave or Raman field Ω_{MW} . Spontaneous emission and cavity photon loss are present as sources of decay.

dent of the initial state of the system, and without need for any unitary feedback control. Consequently, the lifetime of the state is dictated by the lifetime of the experiment.

In Sec. 4.3 we present a scheme that employs spontaneous emission mediated by a dark state of the atom-cavity interaction. This scheme leads to the highest fidelity of the entangled steady state among the presented schemes. In Sec. 4.5 we present schemes suitable for existing cavity QED experiments which do not have transversal confinement of the atoms, cf. Ref. [41]. For comparison we discuss an adaptation of a dissipative protocol presented in Ref. [86] to Λ atoms in optical cavities in App. A.

To identify and engineer the relevant interactions, we apply the effective operator formalism presented in Chapter 3 to the system in Sec. 4.1, resulting in the effective dynamics discussed in Sec. 4.2. This gives us an effective master equation for each scheme, from which all of the desired performance measures can be analytically derived. We analyze the scheme in Sec. 4.3 in full detail and derive benchmarks for error and speed of the protocol. In Sec. 4.3.6 we argue that our protocols for the dissipative preparation of entanglement exhibit an improved error scaling as compared to previous methods for entanglement generation. We analytically derive the optimal steady-state fidelity and preparation time of the scheme as a function of the system parameters in Sec. 4.4 and the robustness against a difference in the coupling of the atoms to the cavity in App. B. Our analytic results are verified by numerical simulations. We collect the results and compare the schemes in Sec. 4.6. A summary is given in Sec. 4.7.

4.1 Cavity QED setup

We consider a single-mode cavity QED system consisting of two distantly trapped Λ -type atoms with ground states $|0\rangle$ and $|1\rangle$ and an excited state $|e\rangle$. These levels are coupled by a laser, a microwave field or Raman transition, and a cavity mode. Within the dipole and rotating wave approximation the couplings of this

system are described by a Hamiltonian

$$\hat{H} = \hat{H}_0 + \hat{H}_{\text{ac}} + \hat{H}_{\text{laser}} + \hat{H}_{\text{MW}}. \quad (4.1)$$

We assume that the level splittings are the same for the two atoms, and do not fluctuate in time. This can for instance be achieved by cooling the atoms to the ground states of identical trapping potentials or by using ‘magic wavelength traps’. Then the Hamiltonian for the atoms and the cavity mode is given by

$$\hat{H}_0 = \omega_c \hat{a}^\dagger \hat{a} + \sum_{j=1,2} (\omega_0 |0\rangle_j \langle 0| + \omega_1 |1\rangle_j \langle 1| + \omega_e |e\rangle_j \langle e|). \quad (4.2)$$

The couplings of the levels are expressed by the interaction Hamiltonians

$$\hat{H}_{\text{laser}} = \frac{\Omega}{2} e^{-i\omega_{\text{laser}} t} \left(|e\rangle_1 \langle 0| + e^{i\phi} |e\rangle_2 \langle 0| \right) + H.c., \quad (4.3)$$

$$\hat{H}_{\text{MW}} = \frac{\Omega_{\text{MW}}}{2} \sum_{j=1,2} e^{-i\omega_{\text{MW}} t} |1\rangle_j \langle 0| + H.c., \quad (4.4)$$

$$\hat{H}_{\text{ac}} = g \sum_{j=1,2} \hat{a} |e\rangle_j \langle 1| + H.c. \quad (4.5)$$

The coherent laser field \hat{H}_{laser} drives the transition between the ground state $|0\rangle$ and the excited state $|e\rangle$ with resonant Rabi frequency Ω . The angle ϕ determines the phase difference of the driving field for the two atoms with respect to the atom-cavity coupling; for convenience we assume it on the driving of the second atom. The two ground states $|0\rangle$ and $|1\rangle$ are coupled by means of a coherent microwave field or Raman transition \hat{H}_{MW} of Rabi frequency Ω_{MW} . The atom-cavity interaction \hat{H}_{ac} describes that the cavity field $\{\hat{a}, \hat{a}^\dagger\}$ couples the $|1\rangle$ and $|e\rangle$ states with a strength of g and identical phase for both atoms. Assuming that the ground and excited subspace are coupled perturbatively, the system Hamiltonian can be structured according to

$$\hat{H} = \hat{H}_g + \hat{H}_e + \hat{V}_+ + \hat{V}_-, \quad (4.6)$$

with \hat{H}_g (\hat{H}_e) as the Hamiltonian of the ground (excited) subspace and $\hat{V} = \hat{V}_+ + \hat{V}_-$ ($\hat{V}_- = \hat{V}_+^\dagger$) as the perturbative (de-)excitation term between the ground and excited subspaces. We change into a frame rotating at the frequency of the level $|0\rangle$, ω_0 , and the frequencies of the laser and the microwave, ω_{laser} and ω_{MW} , to obtain the time-independent couplings illustrated in Fig. 4.1,

$$\hat{H}_g = \frac{\Omega_{\text{MW}}}{2} \sum_{j=1,2} (|1\rangle_j \langle 0| + H.c.) + \beta \sum_{j=1,2} |1\rangle_j \langle 1|, \quad (4.7)$$

$$\hat{H}_e = \Delta \sum_{j=1,2} |e\rangle_j \langle e| + \delta \hat{a}^\dagger \hat{a} + g \sum_{j=1,2} \left(\hat{a}^\dagger |1\rangle_j \langle e| + H.c. \right), \quad (4.8)$$

$$\hat{V}_+ = \frac{\Omega}{2} \left(|e\rangle_1 \langle 0| + e^{i\phi} |e\rangle_2 \langle 0| \right), \quad \hat{V}_- = \hat{V}_+^\dagger. \quad (4.9)$$

Here, $\Delta \equiv \omega_e - \omega_0 - \omega_{\text{laser}}$ and $\beta \equiv \omega_1 - \omega_0 - \omega_{\text{MW}}$ are the detunings of the laser and of the microwave field, respectively; a cavity excitation has an energy of $\delta \equiv \omega_c - \omega_{\text{laser}} + \omega_{\text{MW}}$.

The noise processes resulting from interactions between the system and the environment are assumed Markovian so that the time evolution of the system can be described by a master equation $\dot{\rho} = \mathcal{L}(\rho)$ with a Liouvillian in Lindblad form

$$\dot{\rho} = \mathcal{L}(\rho) = -i [\hat{H}, \rho] + \sum_k \hat{L}_k \rho \hat{L}_k^\dagger - \frac{1}{2} \left(\hat{L}_k^\dagger \hat{L}_k \rho + \rho \hat{L}_k^\dagger \hat{L}_k \right). \quad (4.10)$$

The Lindblad operators \hat{L}_k are associated with the following naturally occurring noise processes: (i) loss of a cavity excitation, $\hat{L}_\kappa = \sqrt{\kappa} \hat{a}$, with a photon decay rate κ , and (ii) decay by spontaneous emission from the excited atomic state $|e\rangle_j$ into ground states $|0\rangle_j$ and $|1\rangle_j$, with Lindblad operators $\hat{L}_{\gamma,0,j} = \sqrt{\gamma/2} |0\rangle_j \langle e|$ and $\hat{L}_{\gamma,1,j} = \sqrt{\gamma/2} |1\rangle_j \langle e|$, respectively. Given that the separation of the atoms will typically be more than one wavelength for typical experimental conditions we neglect collective components of the spontaneous emission. Furthermore, we see from the arguments below that the bandwidth of the laser plays a minor role, as long as it is kept within the linewidth of the transition we want to drive, e.g. ~ 6 MHz for the parameters of Ref. [41]. Note that for simplicity we assume equal rates $\gamma/2$ into the two ground states; an asymmetric decay of $|e\rangle$ does not modify the results significantly and can even be used to improve the protocols. We ignore the influence from sources of noise other than spontaneous emission and cavity decay, such as dephasing due to stray fields or blackbody radiation. This is justified if the coherence time of the hyperfine transition exceeds the preparation time. As we shall see later, the preparation time is on the order of μs justifying this approximation for most experiments.

As a measure for the quality of the cavity we introduce the *cooperativity* parameter, $C = \frac{g^2}{\gamma\kappa}$. As we will find below, the cooperativity is the main parameter quantifying how well the entanglement protocols work. We note here, that we define γ as the decay of population of the excited state and κ as the photon loss rate of the cavity, which differ from polarization and field decay rates which are also commonly referred to as (γ, κ) [41] by a factor of two each; hence, for the parameters of Ref. [41] we get $C \approx 17$. In this work, we will always assume strong coupling $C \gg 1$, but we distinguish between the regimes of weak driving $(\Omega, \Omega_{\text{MW}}, \beta) \ll (g, \kappa, \gamma)$ and increased driving $(\Omega, \Omega_{\text{MW}}, \beta) \lesssim (\kappa, \gamma)$.

In the following, it will be convenient to work in the triplet-singlet basis of the ground states: $\{|00\rangle, |11\rangle, |T\rangle, |S\rangle\}$, where $|00\rangle = |0\rangle_1 |0\rangle_2$, $|11\rangle = |1\rangle_1 |1\rangle_2$, $|T\rangle = \frac{1}{\sqrt{2}} (|0\rangle_1 |1\rangle_2 + |1\rangle_1 |0\rangle_2)$, and $|S\rangle = \frac{1}{\sqrt{2}} (|0\rangle_1 |1\rangle_2 - |1\rangle_1 |0\rangle_2)$; the latter is the desired maximally entangled singlet state for all the protocols that we investigate. We further define the following excited states which will appear throughout the chapter: $|T_0\rangle = \frac{1}{\sqrt{2}} (|0\rangle_1 |e\rangle_2 + |e\rangle_1 |0\rangle_2)$, $|S_0\rangle = \frac{1}{\sqrt{2}} (|0\rangle_1 |e\rangle_2 - |e\rangle_1 |0\rangle_2)$, $|T_1\rangle = \frac{1}{\sqrt{2}} (|1\rangle_1 |e\rangle_2 + |e\rangle_1 |1\rangle_2)$ and $|S_1\rangle = \frac{1}{\sqrt{2}} (|1\rangle_1 |e\rangle_2 - |e\rangle_1 |1\rangle_2)$. The excited states of the cavity read $|00\rangle|1\rangle$, $|11\rangle|1\rangle$, $|T\rangle|1\rangle$, $|S\rangle|1\rangle$. We will truncate the Hilbert space by excluding states with two or more excitations (of the cavity or of the atoms), as we always work in the perturbative regime with weak driving in our analytical calculations. The states and their couplings (for $\phi = 0$) are shown in Fig. 4.2.

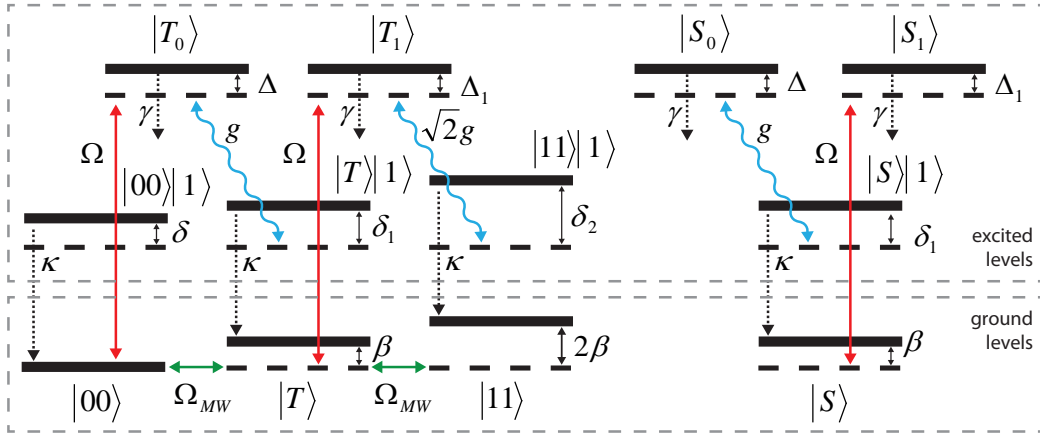


FIGURE 4.2: Coherent and dissipative interactions between ground and excited states. Ground states are coherently excited by an optical field (Ω) to excited atomic states (straight red arrow). Exchange of excitation via the atom-cavity interaction (g) couples these to cavity-excited states (wiggled blue arrow). Ground states are coupled by a microwave or Raman transition Ω_{MW} . Atomic excitations decay by spontaneous emission at a rate γ and cavity loss occurs at a rate κ (both indicated with dotted arrows). The ground to excited subspace interactions are drawn for $\phi = 0$ where excitation happens inside the triplet/singlet subspaces, whereas $\phi = \pi$ leads to crossings between the triplet and singlet sectors. The detunings are defined in the text.

4.2 Effective dynamics of the system

The key to establishing an entangled ground state by dissipative state preparation is to identify and engineer decay processes present in the physical system in a systematic and reliable way. In the following section we present the model of the physical system at hand. We use the effective operator formalism presented in Chapter 3 (see also Ref. [134]) to reduce the unitary and dissipative dynamics of the open quantum system to the non-decaying ground states and to tailor the effective decay processes to achieve a desired steady state.

4.2.1 Complex energies and non-Hermitian time evolution of the excited states

In Fig. 4.2 we have visualized the coherent and dissipative interactions of the ground and excited states present in the system. It is evident that the dynamics of the excited states, which are subject to decay, is governed by both, unitary and dissipative couplings. For the excited levels we can combine the real detunings of the levels with imaginary terms, that correspond to broadening by decay, to yield complex energy terms. The resulting non-Hermitian time evolution of the excited states is expressed compactly in terms of a non-Hermitian Hamiltonian

$$\hat{H}_{NH} \equiv \hat{H}_e - \frac{i}{2} \sum_k \hat{L}_k^\dagger \hat{L}_k. \quad (4.11)$$

Also referred to as the no-jump Hamiltonian in the language of the quantum jump formalism [126], \hat{H}_{NH} combines the Hamiltonian of the decaying excited

subspace \hat{H}_e with the jump terms of the master equation (4.10). For the system at hand we find

$$\begin{aligned} \hat{H}_{\text{NH}} = & \tilde{\Delta}_0 (|T_0\rangle\langle T_0| + |S_0\rangle\langle S_0|) + \tilde{\Delta}_1 (|T_1\rangle\langle T_1| + |S_1\rangle\langle S_1|) + \\ & + \tilde{\delta}_0 |00\rangle\langle 1| \langle 1| \langle 00| + \tilde{\delta}_1 |T\rangle\langle 1| \langle 1| \langle T| + \\ & + \tilde{\delta}_2 |11\rangle\langle 1| \langle 1| \langle 11| + \tilde{\delta}_1 |S\rangle\langle 1| \langle 1| \langle S| + \\ & + g (|T_0\rangle\langle 1| \langle T| + |S_0\rangle\langle 1| \langle S| + |T_1\rangle\langle 1| \langle 11| + H.c.). \end{aligned} \quad (4.12)$$

Here, we have defined complex ‘energies’ $\tilde{\Delta}_n \equiv \Delta_n - \frac{i\gamma}{2}$, $\tilde{\delta}_n \equiv \delta_n - \frac{ik}{2}$, $\Delta_n \equiv \Delta + m \cdot \beta$, and $\delta_n \equiv \delta + m \cdot \beta$, with m being the number of atoms in state $|1\rangle$ ($\Delta_0 = \Delta$, $\delta_0 = \delta$). As will become clear further below, it is useful to set $\Delta_{-1} \equiv \Delta_1$. In doing so, the detunings of the excited states are conveniently combined with their decay widths to complex detunings, where both their real and imaginary parts govern the strengths of the transitions involving the excited states.

4.2.2 Effective Hamiltonian and Lindblad operators

As can be recognized from Fig. 4.2, the coherent and dissipative couplings of the excited states can be concatenated to effective second-order processes between the ground states. An example for such an effective unitary process is given by the transition $|00\rangle \xrightarrow{\Omega} |T_0\rangle \xrightarrow{\Omega} |00\rangle$, facilitated by the coherent driving \hat{V} of strength Ω , resulting in an effective shift of ground level $|00\rangle$. In case the coherent de-excitation is replaced by a decay an effective dissipative process is formed. Here, $|00\rangle \xrightarrow{\Omega} |T_0\rangle \xrightarrow{\gamma} |S\rangle$ is an example for an effective decay from state $|00\rangle$ to $|S\rangle$, involving spontaneous emission of an atomic excitation at a rate γ . In this manner, all available combinations of weak optical excitation, non-Hermitian coupling between the excited states and either subsequent weak optical de-excitation or decay bundle together to effective second-order processes between the ground states. We assume the optical excitation \hat{V} to be a perturbation of the non-Hermitian evolution of the excited levels given by \hat{H}_{NH} . Consequently, their population will always be much lower than the population of the ground levels. On these grounds, we can perform adiabatic elimination of the excited levels and restrict the dynamics to the ground states.

In Chapter 3 we have presented an effective operator formalism based on second-order perturbation theory and adiabatic elimination to reduce the evolution of an open system to effective unitary and dissipative processes between its ground states. Applying this method simplifies the complexity of the Liouvillian dynamics of Eq. (4.10) considerably, resulting in an effective master equation in Lindblad form

$$\dot{\rho} = i [\rho, \hat{H}_{\text{eff}}] + \sum_k \hat{L}_{\text{eff}}^k \rho (\hat{L}_{\text{eff}}^k)^\dagger - \frac{1}{2} \left((\hat{L}_{\text{eff}}^k)^\dagger \hat{L}_{\text{eff}}^k \rho + \rho (\hat{L}_{\text{eff}}^k)^\dagger \hat{L}_{\text{eff}}^k \right), \quad (4.13)$$

represented by an effective Liouvillian $\mathcal{L}_{\text{eff}}(\rho) = \dot{\rho}$. It contains an effective Hamiltonian \hat{H}_{eff} and effective Lindblad operators \hat{L}_{eff}^k

$$\hat{H}_{\text{eff}} \equiv -\frac{1}{2} \hat{V}_- \left(\hat{H}_{\text{NH}}^{-1} + (\hat{H}_{\text{NH}}^{-1})^\dagger \right) \hat{V}_+ + \hat{H}_g, \quad (4.14)$$

$$\hat{L}_{\text{eff}}^k \equiv \hat{L}_k \hat{H}_{\text{NH}}^{-1} \hat{V}_+, \quad (4.15)$$

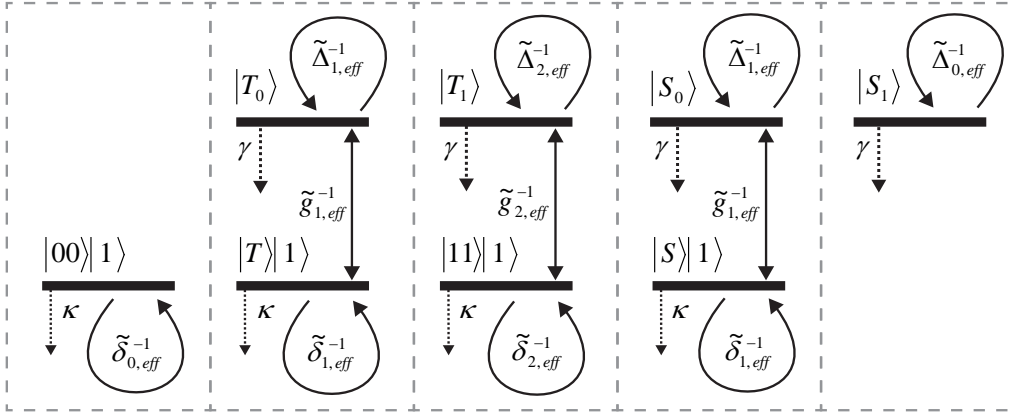


FIGURE 4.3: Propagators in the excited-state subspace. The loop-like elements $\tilde{\Delta}_{n,\text{eff}}^{-1}$, $\tilde{\delta}_{n,\text{eff}}^{-1}$ and transition-like elements $\tilde{\gamma}_{n,\text{eff}}^{-1}$ contained in \hat{H}_{NH}^{-1} govern the non-Hermitian evolution of the excited states. Grouped according to the three interacting and two non-interacting excited subspaces these propagators determine the strength of effective processes involving the excited states, depending on the state reached by initial excitation and the one left by either coherent de-excitation or decay.

incorporating the inverse of the non-Hermitian Hamiltonian \hat{H}_{NH} of Eq. (4.11) and the unperturbed ground-state Hamiltonian \hat{H}_{g} .

As expected, these effective processes consist of an initial weak optical excitation \hat{V}_+ and a final de-excitation \hat{V}_- or decay \hat{L}_k depending on their unitary or dissipative character. In-between, the inverse non-Hermitian Hamiltonian \hat{H}_{NH}^{-1} acts as a ‘propagator’, representing the non-Hermitian evolution of the excited subspace which determines the strength of the effective processes depending on which excited states take part in it. Its properties will be addressed in more detail in the following section.

4.2.3 Effective propagators of the excited states

In the excited-state basis defined earlier, \hat{H}_{NH} can be broken up into 5 block diagonal elements which evolve independently. \hat{H}_{NH}^{-1} is then also in block diagonal form, and can be written out explicitly as

$$\hat{H}_{\text{NH}}^{-1} = \hat{H}_{\text{NH},|T_0\rangle}^{-1} + \hat{H}_{\text{NH},|S_0\rangle}^{-1} + \hat{H}_{\text{NH},|T_1\rangle}^{-1} + \hat{H}_{\text{NH},|S_1\rangle}^{-1} + \hat{H}_{\text{NH},|00\rangle|1\rangle}^{-1}, \quad (4.16)$$

with three blocks for the interacting excited subspaces

$$\hat{H}_{\text{NH},|T_0\rangle}^{-1} = \tilde{\Delta}_{1,\text{eff}}^{-1}|T_0\rangle\langle T_0| + \tilde{\delta}_{1,\text{eff}}^{-1}|T\rangle|1\rangle\langle 1| \langle T| + \tilde{\gamma}_{1,\text{eff}}^{-1}(|T\rangle|1\rangle\langle T_0| + H.c.), \quad (4.17)$$

$$\hat{H}_{\text{NH},|S_0\rangle}^{-1} = \tilde{\Delta}_{1,\text{eff}}^{-1}|S_0\rangle\langle S_0| + \tilde{\delta}_{1,\text{eff}}^{-1}|S\rangle|1\rangle\langle 1| \langle S| + \tilde{\gamma}_{1,\text{eff}}^{-1}(|S\rangle|1\rangle\langle S_0| + H.c.), \quad (4.18)$$

$$\hat{H}_{\text{NH},|T_1\rangle}^{-1} = \tilde{\Delta}_{2,\text{eff}}^{-1}|T_1\rangle\langle T_1| + \tilde{\delta}_{2,\text{eff}}^{-1}|11\rangle|1\rangle\langle 1| \langle 11| + \tilde{\gamma}_{2,\text{eff}}^{-1}(|11\rangle|1\rangle\langle T_1| + H.c.), \quad (4.19)$$

and two blocks for the non-interacting excited states

$$\hat{H}_{\text{NH},|S_1\rangle}^{-1} = \tilde{\Delta}_{0,\text{eff}}^{-1}|S_1\rangle\langle S_1|, \quad (4.20)$$

$$\hat{H}_{\text{NH},|00\rangle|1\rangle}^{-1} = \tilde{\delta}_{0,\text{eff}}^{-1}|00\rangle|1\rangle\langle 1| \langle 00|. \quad (4.21)$$

In order to keep the notation compact we have defined here

$$\tilde{\Delta}_{n,\text{eff}} \equiv \tilde{\Delta}_{n-1} - \frac{ng^2}{\tilde{\delta}_n}, \quad (4.22)$$

$$\tilde{\delta}_{n,\text{eff}} \equiv \tilde{\delta}_n - \frac{ng^2}{\tilde{\Delta}_{n-1}}, \quad (4.23)$$

$$\tilde{g}_{n,\text{eff}} \equiv \sqrt{ng} - \frac{\tilde{\delta}_n \cdot \tilde{\Delta}_{n-1}}{\sqrt{ng}}. \quad (4.24)$$

The entries of \hat{H}_{NH}^{-1} , shown in Fig. 4.3, are generally complex and their magnitudes have dimension of inverse energy. As has been discussed in Sec. 3.4.3, they play the role of propagators or complex magnitudes in the effective ground state to ground state processes of Eqs. (4.14)–(4.15). Each effective process that is formed from perturbative optical excitation \hat{V}_+ and subsequent de-excitation \hat{V}_- or decay includes a propagator depending on which excited states are involved. As can be seen in Fig. 4.3, \hat{H}_{NH}^{-1} contains both loop-like and transition-like propagators, grouped according to the five separable subspaces. Their index n reflects the coupling strength between the atomic and cavity excited state of the interacting subspace, the latter of which has n atoms in state $|1\rangle$. The states $|S_1\rangle$ and $|00\rangle|1\rangle$ are dark-states of the atom-cavity interaction and are uncoupled ($n = 0$). By our definitions of Eqs. (4.22)–(4.23) we have associated the loop-like propagators $\tilde{\Delta}_{n,\text{eff}}^{-1}$ and $\tilde{\delta}_{n,\text{eff}}^{-1}$ with the complex detunings of the excited states such that for a vanishing coupling g the shifts in $\tilde{\Delta}_{n,\text{eff}}$ and $\tilde{\delta}_{n,\text{eff}}$ would disappear, and we would find $\tilde{\Delta}_{n,\text{eff}} = \tilde{\Delta}_{n-1}$ and $\tilde{\delta}_{n,\text{eff}} = \tilde{\delta}_n$. Similarly, in case of negligible complex detunings $\tilde{\Delta}_{n-1}$ and $\tilde{\delta}_n$ the transition-like propagators $\tilde{g}_{n,\text{eff}}^{-1}$ in Eqs. (4.17)–(4.19) would simplify to the inverse of a real coupling $\tilde{g}_{n,\text{eff}} = \sqrt{ng}$, the well-known dressed state energy for n atoms resonant with a cavity.

All propagators of \hat{H}_{NH} and Fig. 4.3 can be written in terms of a denominator $\tilde{D}_n \equiv ng^2 - \tilde{\delta}_n \cdot \tilde{\Delta}_{n-1}$ which equals the reduced determinant of the Hamiltonian of the according subspace and is highly dependent on the system parameters. As we will show, an appropriate choice of the parameters Δ , δ and β engineers certain propagators of the excited states, and hence, effective decay processes mediated by them, to be very strong, while others are effectively suppressed. Physically this can be understood as shifting one of the dressed states into resonance to enhance the coupling. In the following discussion we present various schemes that build upon this principle of engineered decay. Here, each of the schemes is denoted by the atomic excited state that mediates the engineered decay into the desired maximally entangled singlet state $|S\rangle$.

Applying the discussed methods we will be able to analytically derive the optimal parameters and benchmarks for each of the presented schemes, the most important of which are the steady-state fidelity with the desired entangled state and the convergence time, estimated by the inverse of the spectral gap. We back up all of our analytic results by numerical integration of the master equations (4.10) and (4.13).

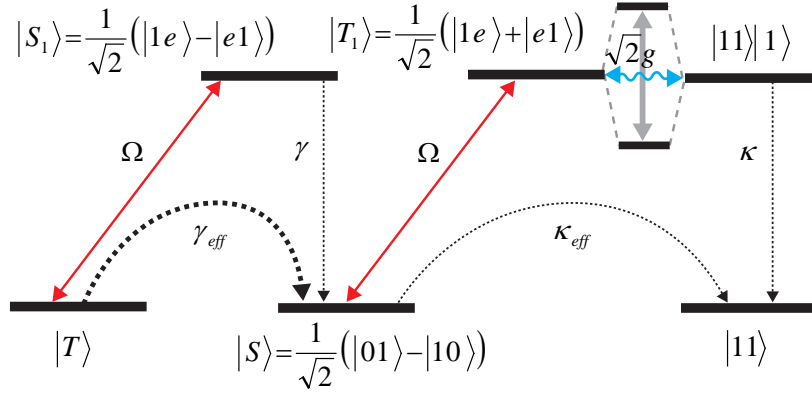


FIGURE 4.4: Effective decay processes of the $|S_1\rangle$ scheme. The optical excitation Ω drives population from $|T\rangle$ to $|S_1\rangle$. From there it decays spontaneously into the desired steady state $|S\rangle$ with a certain probability. Since $|S_1\rangle$ is the dark state of the atom-cavity interaction \hat{H}_{ac} the initial excitation is not shifted and is close to resonance so that the effective decay γ_{eff} from $|T\rangle$ prepares $|S\rangle$ very rapidly. Due to the strong coupling \hat{H}_{ac} of $|T_1\rangle$ and $|11\rangle|1\rangle$ with a strength $\sqrt{2}g$ these states form dressed states that are shifted out of resonance. Effective spontaneous emission γ_{eff} and cavity loss κ_{eff} from $|S\rangle$ into $|11\rangle$, mediated by $|T_1\rangle$, are hence effectively suppressed. A microwave/Raman transition (not shown) couples $|00\rangle$ and $|11\rangle$ to $|T\rangle$.

4.3 An entangling scheme using engineered spontaneous emission

In the following, we present a scheme for the preparation of an entangled steady state by an engineered spontaneous emission process mediated by the dark state of the atom-cavity interaction, $|S_1\rangle$. From the considered schemes it exhibits the lowest error in the preparation of the entangled state.

As for all schemes discussed in this chapter, we begin by outlining the physical mechanisms that underlie the dissipative state preparation, and proceed with a discussion of the effective operators. Depending on the driving regime we analytically derive the benchmarks for each scheme, in particular steady-state fidelity and speed of convergence, from the effective dynamics.

For the scheme at hand, we choose to engineer the effective decay by spontaneous emission into the maximally entangled singlet state to be as strong as possible. To this end, we set both the optical driving and the cavity transition to be resonant ($\Delta = 0$, $\delta = -\beta$) and the microwave or Raman transition to be slightly detuned ($\beta \neq 0$). Furthermore, we set $\phi = \pi$ so that the optical driving crosses the singlet/triplet subspace, i.e. $|T\rangle \xleftrightarrow{\Omega} |S_1\rangle$ and $|S\rangle \xleftrightarrow{\Omega} |T_1\rangle$.

4.3.1 Mechanism of the state preparation

The mechanism is illustrated in Fig. 4.4. Population from $|T\rangle$ is excited up to $|S_1\rangle = \frac{1}{\sqrt{2}}(|1e\rangle - |e1\rangle)$. The atomic excited state $|S_1\rangle$ is the dark state of the atom-cavity interaction, \hat{H}_{ac} , and is therefore resonant with the optical driving ($\Delta = 0$). Consequently, $|T\rangle$ decays very rapidly over $|S_1\rangle$ into $|S\rangle$. On the other hand, population from $|S\rangle$ is excited to $|T_1\rangle$ which is coupled to $|T\rangle|1\rangle$ with a

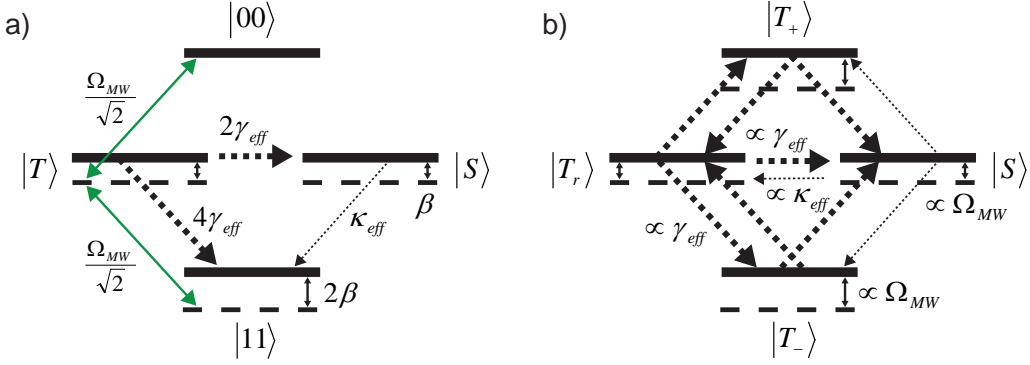


FIGURE 4.5: Effective ground-state processes of the $|S_1\rangle$ scheme. (a) Detuning and interactions in the shuffling picture, where $|00\rangle$, $|T\rangle$ and $|11\rangle$ are coupled by Ω_{MW} to avoid population in $|00\rangle$ and $|11\rangle$. Engineered spontaneous emission prepares the maximally entangled singlet state $|S\rangle$ at a rate of $2\gamma_{eff}$. Effective cavity decay out of $|S\rangle$ happens at a rate κ_{eff} . (b) Dressed state picture. Strong spontaneous emission $\propto \gamma_{eff}$ reshuffles the dressed triplet states (not shown between $|T_{\pm}\rangle$). Population in $|S\rangle$ is gained from ($\propto \gamma_{eff}$) and lost to ($\propto \kappa_{eff}$) each of the dressed triplet states.

strength of $\sqrt{2}g$. This strong coupling shifts their dressed states out of resonance by $\pm\sqrt{2}g$ which is much more than the natural linewidth. Decay out of $|S\rangle$ is thus strongly suppressed, while $|T\rangle$ is rapidly pumped into $|S\rangle$. Accumulation of population in $|00\rangle$ or $|11\rangle$ is prevented by the microwave/Raman field that couples the three triplet states $|00\rangle$, $|T\rangle$ and $|11\rangle$ and reshuffles population to $|T\rangle$ from which engineered decay prepares $|S\rangle$ again. The detuning β of the microwave is needed to prevent $\frac{1}{\sqrt{2}}(|00\rangle - |11\rangle)$ from being a dark state of the microwave which would not be reshuffled to $|T\rangle$. The effective processes resulting from the coupling are illustrated in Fig. 4.5 a). We note that even though the state $|T_1\rangle$ is far out of resonance the desired steady state $|S\rangle$ is still weakly coupled to $|T_1\rangle$ by the laser driving; $|S\rangle$ is hence not an ideal dark state. The fidelity of the steady state with $|S\rangle$ and the error rate of the protocol depend on the ratio of the rate of the dissipative preparation of $|S\rangle$ and the rate of decay from $|S\rangle$. In the following sections we will model these processes quantitatively by considering the effective operators to derive the optimal parameters and the error of the protocol analytically.

4.3.2 Effective processes

We begin our discussion of the effective processes, shown in Fig. 4.5 a), by deriving the general effective operators for optical driving with $\phi = \pi$. Given \hat{V} and \hat{L}_k the terms for the effective processes can be read off directly from the map of propagators in Fig. 4.3. These operators are equally valid for the $|S_0\rangle$ scheme in Sec. 4.5.2 that also uses $\phi = \pi$. For the effective decay of an atomic excitation $|e\rangle$ into ground state $|0\rangle$ by spontaneous emission we obtain

the effective Lindblad operators

$$\begin{aligned} \hat{L}_{\text{eff}}^{\gamma,0,\{1,2\}} = & \pm \frac{\sqrt{\gamma/2}\Omega}{2\tilde{\Delta}_{1,\text{eff}}} |00\rangle\langle 00| + \frac{\sqrt{\gamma/2}\Omega}{4\tilde{\Delta}_{0,\text{eff}}} (\pm|T\rangle\langle T||S\rangle\langle T|) + \\ & + \frac{\sqrt{\gamma/2}\Omega}{4\tilde{\Delta}_{2,\text{eff}}} (|T\rangle\langle S| \pm |S\rangle\langle S|). \end{aligned} \quad (4.25)$$

The superscript γ on the Lindblad operators stands for spontaneous emission, 0 for the decay into ground state $|0\rangle$, and the index $\{1,2\}$ for the atom at which the decay occurs refers to the upper (lower) set of signs of the terms. Similarly, the effective decay by spontaneous emission into ground state $|1\rangle$ is given by

$$\begin{aligned} \hat{L}_{\text{eff}}^{\gamma,1,\{1,2\}} = & + \frac{\sqrt{\gamma}\Omega}{4\tilde{\Delta}_{1,\text{eff}}} (\pm|T\rangle\langle 00| - |S\rangle\langle 00|) \pm \frac{\sqrt{\gamma}\Omega}{4\tilde{\Delta}_{0,\text{eff}}} |11\rangle\langle T| \\ & + \frac{\sqrt{\gamma}\Omega}{4\tilde{\Delta}_{2,\text{eff}}} |11\rangle\langle S|. \end{aligned} \quad (4.26)$$

The effective decay of a cavity excitation is found to be

$$\hat{L}_{\text{eff}}^{\kappa} = \frac{\sqrt{\kappa}\Omega}{2\tilde{g}_{2,\text{eff}}} |11\rangle\langle S| - \frac{\sqrt{\kappa/2}\Omega}{\tilde{g}_{1,\text{eff}}} |S\rangle\langle 00|. \quad (4.27)$$

Finally, the effective unitary processes are given by

$$\begin{aligned} \hat{H}_{\text{eff}} = & -\text{Re} \left[\frac{\Omega^2}{2\tilde{\Delta}_{1,\text{eff}}} \right] |00\rangle\langle 00| - \text{Re} \left[\frac{\Omega^2}{4\tilde{\Delta}_{0,\text{eff}}} \right] |T\rangle\langle T| \\ & - \text{Re} \left[\frac{\Omega^2}{4\tilde{\Delta}_{2,\text{eff}}} \right] |S\rangle\langle S| + \hat{H}_g, \end{aligned} \quad (4.28)$$

where $\text{Re}[\]$ denotes the real part of the argument. While the above effective operators hold whenever $\phi = \pi$, we can simplify them for the particular scheme at hand by discussing the propagators for the parameter choices made in the previous section. In the absence of an atomic detuning, $\Delta = 0$, the complex energy of $|S_1\rangle$, as the dark-state of the cavity interaction, is given by $\tilde{\Delta}_1 = \beta - \frac{i\gamma}{2}$. As we will discuss below it is desirable to have $\beta \propto \Omega$ so that for the assumption of weak driving ($\Omega \ll \gamma$) we can write $\tilde{\Delta}_1 \approx -\frac{i\gamma}{2}$. The propagator of the effective $|S_1\rangle$ -mediated decay processes then simplifies to

$$\langle S_1 | \hat{H}_{\text{NH}}^{-1} | S_1 \rangle = \tilde{\Delta}_{0,\text{eff}}^{-1} \approx -\frac{2}{i\gamma}. \quad (4.29)$$

Hence, the effective decay processes mediated by $|S_1\rangle$ that incorporate this propagator are tailored to be very strong compared to the decay out of the singlet state which involves the subspace consisting of the states $|T_1\rangle$ and $|11\rangle|1\rangle$, and the transition-like propagator

$$\langle 1 | \langle T | \hat{H}_{\text{NH}}^{-1} | T_1 \rangle = \tilde{g}_{2,\text{eff}}^{-1} \approx \frac{1}{\sqrt{2}g}. \quad (4.30)$$

The last denominator reflects the strong shift of the dressed states of $|T_1\rangle$ and $|11\rangle|1\rangle$ out of resonance, slowing down the effective decay out of $|S\rangle$. Consequently, we have reached $|\tilde{\Delta}_{0,\text{eff}}^{-1}| \gg |\tilde{g}_{n,\text{eff}}^{-1}|$ so that effective processes mediated by the dark state $|S_1\rangle$ are engineered to be much stronger than those involving other states, in particular $|T_1\rangle$. We have thus found that the triplet ground state $|T\rangle$ undergoes rapid effective spontaneous emission at a rate $\propto 1/\gamma$, while cavity decay from $|S\rangle \propto \kappa/g^2$ is suppressed in the strong coupling regime where $C \gg 1$. For finding the steady state we can drop the suppressed terms unless they affect the singlet state. In addition, spontaneous emission from $|S\rangle \propto \gamma\kappa^2/g^4$ is negligible and will be ignored. The effective decay processes then simplify to

$$\hat{L}_{\text{eff}}^{\gamma,0,\{1,2\}} = \pm i\sqrt{\gamma_{\text{eff}}}|T\rangle\langle T| + i\sqrt{\gamma_{\text{eff}}}|S\rangle\langle T|, \quad (4.31)$$

$$\hat{L}_{\text{eff}}^{\gamma,1,\{1,2\}} = \pm i\sqrt{2\gamma_{\text{eff}}}|11\rangle\langle T|, \quad (4.32)$$

$$\hat{L}_{\text{eff}}^{\kappa} = \sqrt{\kappa_{\text{eff}}}|11\rangle\langle S|. \quad (4.33)$$

Here, we have set $\kappa_{\text{eff}} = |\langle 11|\hat{L}_{\text{eff}}^{\kappa}|S\rangle|^2 = \frac{\kappa\Omega^2}{8g^2}$ and $\gamma_{\text{eff}} = |\langle S|\hat{L}_{\text{eff}}^{\gamma,0,\{1,2\}}|T\rangle|^2 = \frac{\Omega^2}{8\gamma}$. Furthermore, for the scheme at hand the effective Hamiltonian \hat{H}_{eff} of Eq. (4.28) is well approximated by the unperturbed ground-state Hamiltonian \hat{H}_g ,

$$\hat{H}_g = \frac{\Omega_{\text{MW}}}{2} (|00\rangle\langle T| + |T\rangle\langle 11| + H.c.) + \beta (2|11\rangle\langle 11| + |T\rangle\langle T| + |S\rangle\langle S|),$$

if we have neglect the minor effective shifts $\mathcal{O}(\Omega^2)$. The resulting effective decay processes of this scheme are illustrated in Fig. 4.5 a) together with the microwave/Raman reshuffling. The singlet state $|S\rangle$ is efficiently prepared from $|T\rangle$ by spontaneous emission at a rate of $2\gamma_{\text{eff}}$. The singlet $|S\rangle$ decays by effective cavity loss κ_{eff} into $|11\rangle$. The mechanism that allows us to engineer a strong effective spontaneous emission from $|T\rangle$ into $|S\rangle$ at the same time causes strong decay at a rate of $4\gamma_{\text{eff}}$ from $|T\rangle$ into $|11\rangle$. Hence, accumulation in $|11\rangle$ needs to be inhibited by the microwave/Raman shuffling Ω_{MW} . The fidelity of the steady state with the desired entangled state will be derived analytically in the following sections after changing into a dressed state picture with respect to Ω_{MW} .

4.3.3 Parameter analysis at weak driving

We first analyze the dynamics of this $|S_1\rangle$ scheme for weak optical driving Ω . After a basis transform into a dressed ground-state picture, this assumption will allow us to reduce the dynamics to rate equations for the ground-state populations. From these, we derive the important benchmarks for a comparison of the presented schemes; the steady-state fidelity with the desired entangled state, and the spectral gap as a measure for the rate of convergence.

The basis used so far, involving the triplet states $|00\rangle$, $|T\rangle$ and $|11\rangle$ coupled by Ω_{MW} , will be referred to as ‘shuffling picture’ in the remainder of the chapter. We now simplify the analysis by identifying a basis in which non-diagonal elements of the density matrix of the reduced system are suppressed, as a consequence of the weak driving. It is then possible to express the dynamics as a set of linear rate equations, cf. Sec. 3.7. The basis of the new ‘dressed state picture’

contains the original singlet state $|S\rangle$, and the three dressed triplet states

$$|T_{\pm}\rangle = -1/2(B \mp 1)|00\rangle + 1/2(B \pm 1)|11\rangle + A/\sqrt{2}|T\rangle, \quad (4.34)$$

$$|T_r\rangle = A/\sqrt{2}|00\rangle - A/\sqrt{2}|11\rangle + B|T\rangle, \quad (4.35)$$

where we have defined $A = \Omega_{\text{MW}}/\sqrt{\Omega_{\text{MW}}^2 + \beta^2}$ and $B = \beta/\sqrt{\Omega_{\text{MW}}^2 + \beta^2}$. In this basis the effective Hamiltonian is diagonal

$$\hat{H}_{\text{eff}} = \sum_{+/-} (\beta \pm (B\beta + A\Omega_{\text{MW}})) |T_{\pm}\rangle\langle T_{\pm}| + \beta (|T_r\rangle\langle T_r| + |S\rangle\langle S|). \quad (4.36)$$

The parameters A and B , and hence the ratio of β to Ω_{MW} , determine the contribution of $|T\rangle$ to each of the dressed states. We find the optimal parameter choice to be given by $A = \sqrt{\frac{2}{3}}$, $B = \sqrt{\frac{1}{3}}$, and $\beta = \Omega_{\text{MW}}/\sqrt{2}$. Here, each of the dressed states contains an equal share of the triplet state $|T\rangle$ from which $|S\rangle$ is prepared. In the weak driving regime ($\Omega \ll \gamma$), the rephasing of the dressed states is much faster than the effective decay $\gamma_{\text{eff}} \propto \frac{\Omega^2}{\gamma}$. Consequently, in the new basis the evolution of the coherences can be dropped from the master equation. The dissipative time evolution is then well approximated by a set of coupled linear differential rate equations. The rate equation for the population of the singlet state P_S is

$$\dot{P}_S = \frac{\Omega^2}{12\gamma} (P_{T_+} + P_{T_-} + P_{T_r}) - \frac{\kappa\Omega^2}{8g^2} P_S. \quad (4.37)$$

Here, we have used that for weak driving the decay from the three dressed triplet states into the singlet are of the same strength due to the equal weight of $|T\rangle$ in the dressed states and equals one third of the total rate $\Omega/4\gamma$.

4.3.4 Derivation of the spectral gap for weak driving

The quality of a dissipative state preparation protocol is determined by two main benchmarks: (i) fidelity of the stationary state, and (ii) speed of the protocol. We first consider the latter and turn to the fidelity in the sections below. Estimating the speed of a dissipative state preparation protocol is in general a difficult task, but, for small systems, the spectral gap of the Liouvillian is a very good estimate of the rate of convergence. As mentioned in Sec. 2.3.2 the spectral gap of a Liouvillian \mathcal{L} is defined as the magnitude of the smallest (in absolute value) non-zero real part of the eigenvalues of \mathcal{L} , where the Liouvillian is written as a linear operator in the matrix units basis (see Ref. [135] for further details). The spectral gap can thus be seen as the decay rate of the slowest-decaying quasi-stationary eigenstate. If the gap is small, then the quasi-stationary eigenstate remains populated for a long period of time, whereas if the gap is large, then all eigenstates except the stationary one get depopulated rapidly.

In the setting at hand, the gap can in fact be read off from the expressions for the effective decay process $\hat{L}_{\text{eff}}^{\gamma,0,\{1,2\}}$, which have a rate $\gamma_{\text{eff}} = \frac{\Omega^2}{8\gamma}$. As stated above, the dressed states each contain an equal share of $\frac{1}{\sqrt{3}}|T\rangle$. Hence, the singlet is

prepared equally fast by decay of the three dressed states at an individual rate of $2 \cdot \frac{1}{3} \cdot \gamma_{\text{eff}}$ which results in the spectral gap

$$\lambda = \frac{\Omega^2}{12\gamma}. \quad (4.38)$$

Furthermore, $P_{\mathcal{T}} \equiv \frac{1}{3} (P_{T_+} + P_{T_-} + P_{T_r})$ is recognized as the according lowest-lying eigenvector of the Liouvillian, as can be seen from Eq. (4.37) above.

4.3.5 Derivation of the static error

From the rate equation (4.37) we can derive the fidelity of the steady state with respect to the maximally entangled singlet state as $F_S = \lim_{t \rightarrow \infty} P_S$. Equivalently, the error of the protocol is found as the stationary population of the undesired triplet states $(1 - F_S)$. Inserting $1 - P_S = P_{T_+} + P_{T_-} + P_{T_r}$ into Eq. (4.37), we use $\dot{P}_S = 0$ and obtain for the static error of the protocol

$$(1 - F_S)_{\text{stat}} = \frac{3\gamma\kappa}{2g^2} \equiv \frac{3}{2C}, \quad (4.39)$$

with the cooperativity C as defined in Sec. 4.1. Note that Eq. (4.39) indicates that in the strong coupling regime ($C \gg 1$) the only non-negligible error term scales linear in C^{-1} . This linear scaling of the error in the cooperativity comprises an improvement to unitary protocols for entanglement preparation. We discuss this point in Sec. 4.3.6 below.

4.3.6 Improved error scaling as compared to unitary protocols

In Sec. 4.3.5 we have derived the error of the protocol for weak driving. This has lead to an error scaling

$$(1 - F_S)_{\text{stat}} \propto C^{-1}, \quad (4.40)$$

where $C = \frac{g^2}{\kappa\gamma}$ is the cooperativity of the cavity. Our protocol thus, quite remarkably, exhibits a linear scaling of the fidelity with one over the cooperativity. This is in contrast to schemes based on controlled unitary dynamics, where the purely detrimental sources of noise typically result in a weaker square root scaling of the fidelity. Here, as we discussed in Sec. 2.4.2, the fidelity will suffer errors coming from spontaneous emission on the one hand, and from cavity decay on the other. Decreasing one of the error sources will typically increase the other in such a way that the optimal value of the fidelity is $1 - F \propto 1/\sqrt{C}$ [49]. Indeed, to the best of our knowledge, all entangled state preparation protocols based solely on controlled unitary dynamics scale at best as $1/\sqrt{C}$ [43, 44, 47, 48]. This means that the linear scaling of the fidelity from Eq. (4.40) is a quadratic improvement as compared to any known closed system entanglement preparation protocol. The reason for the improvement stems from the fact that the available decay processes are engineered to be a resource in our dissipative scheme, so that the only purely detrimental source of noise are the decay rates which are engineered to be weak. We note, however, that it is also possible to beat the square-root scaling if one exploits measurement and feedback [45, 46, 49].

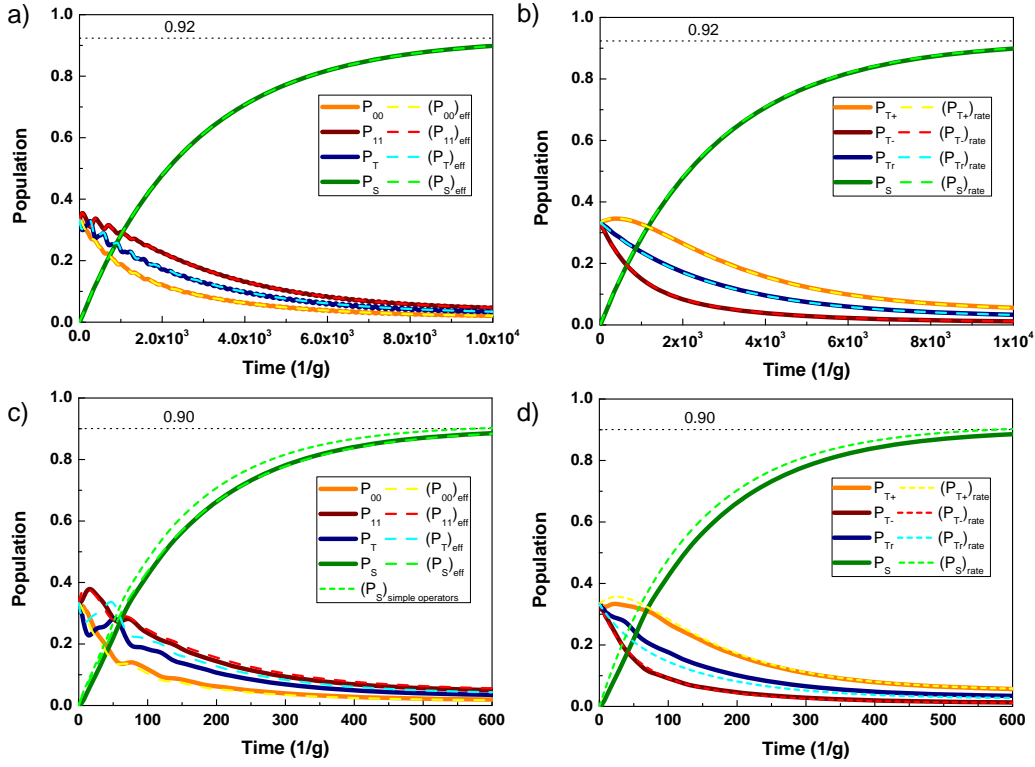


FIGURE 4.6: Evolution of the system towards the entangled steady state for $(\gamma, \kappa) = \left(\frac{3g}{8}, \frac{5g}{32}\right)$ similar to Ref. [41], corresponding to $C \approx 17$. The evolution due to the full master equation (solid lines) is compared with the effective evolution in the shuffling picture (a, c) and rate equations in the dressed state picture (b, d) for weak-driving (a, b) and increased driving (c, d). Starting from a completely mixed triplet state (see legend for details) the system evolves towards the maximally entangled singlet state ($|S\rangle$ – green) approaching the steady-state fidelity (dotted line, indicated). For a weak driving of $\Omega = \frac{\gamma}{10}$ (a-b) the dynamics is completely described by rate equations of the populations, shown in (b). At increased driving $\Omega = \frac{\gamma}{2}$ (c, d) the dressed effective operators (long dash in (c)) are almost indistinguishable from the full dynamics, while simple effective operators and rate equations (short green dash in (c), d) resp.) exhibit increasing inaccuracies. For all curves the optimized parameters $\Omega = 2^{5/4}\Omega_{\text{MW}} = 2^{7/4}\beta$ (see also Sec. 4.4) were used.

As can be seen from Eq. (4.39) one gets a proportionality factor of $\frac{3}{2}$ for the scaling of the scheme at hand which is also essentially independent of the ratio κ/γ . In Sec. 4.5 we will compare the analytical results obtained for this scheme with those from the other schemes in Sec. 4.6 and give numerical examples.

In addition to the asymptotic fidelity, one needs to pay particular attention to the time it takes to reach equilibrium. In the following sections we address the evolution of the system towards steady state both for weak driving and beyond the weak driving regime.

4.3.7 Time evolution for weak driving

To confirm the predictions about the fidelity and the convergence rate of our scheme from the last two sections we perform numerical simulation of the dynamics of the system. Fig. 4.6 (a-b) summarizes the results obtained by numerical integration of the master equation of the full system in Eq. (4.10), consisting of ground states and singly excited states. These curves are plotted together either with those from the effective master equation in Eq. (4.13) in (a), or from the rate equations (such as Eq. (4.37) for the singlet) in (b): For a weak driving ($\Omega = \frac{\gamma}{10}$) we compare the numerically obtained curves of the population dynamics of the full master equation (solid lines) with (a) the effective master equation in the shuffling picture and (b) the rate equations in the dressed state picture (both dashed). We see that in this regime the full and the effective dynamics of the system are in excellent agreement. In addition, the analytical quantities derived from the rate equations are found to describe the fidelity of the steady state with the maximally entangled singlet state and the convergence time very accurately.

Throughout this section we have worked with the assumption of weak driving, using the spectral gap as an indicative measure for the convergence. Below, in Sec. 4.4, we will study the performance of the protocol in the strong driving regime and introduce the preparation time as a more complete measure. Minimizing the time to achieve a desired fidelity by the available parameters we will achieve optimal dissipative state preparation.

4.4 How fast can two atoms be entangled by dissipation?

The fidelity of the prepared state with respect to the desired state gives us a measure of the quality of our scheme once the system has reached equilibrium. The second figure of merit of a dissipative state preparation protocol is the time required to reach convergence. In this section, we analyze how fast the scheme presented above can be performed. We emphasize in particular the trade-off between the speed of the protocol and its fidelity.

Speeding up the state preparation can be done by increasing the optical driving. Indeed, as can be seen from Fig. 4.6 (c, d), using an increased optical driving Ω improves the convergence time by several orders of magnitude at the expense of only a few per cent additional error. The main reason for the decrease in fidelity is that the strong driving requires a strong microwave shuffling of the population of the triplet ground states. The microwave field, in turn, shifts the ground states out of resonance with the optical drive. This results in a decrease of the fidelity at increased optical driving which we will investigate in detail below.

In order to model the effective dynamics of our scheme accurately even for increased optical driving, we begin this section by applying the extended effective operator formalism of Sec. 3.3.5 to account for the coherent coupling of the ground states which has so far been ignored when adiabatically eliminating the excited states. We then proceed to analytically derive the scaling of the two main performance measures, error and convergence rate (spectral gap), as a function of the strength of the coherent driving, and perform a study of the optimal preparation time of an entangled state of a given fidelity.

4.4.1 Effective processes in the presence of ground-state dressing

In the following section we will apply the extended effective operator formalism for non-perturbative ground-state coupling, presented in Sec. 3.3.5. It allows us to include the effects of increased driving and dressing of the ground states and to derive the dynamic benchmarks of the scheme at hand.

So far, we have worked within the weak driving limit ($\Omega \ll \gamma, \kappa$), where simple perturbation theory holds very reliably. We now want to consider how our scheme behaves as we approach the increased driving regime. From the curves of Fig. 4.6 a) and b) we notice an excellent agreement between the dynamics simulated with the full and effective master equation, and the rate equations for a weak optical driving as low as $\Omega = \frac{\gamma}{10}$. On the other hand, for Fig. 4.6 c) and d), we have used $\Omega = \frac{\gamma}{2}$ which is clearly beyond the weak driving limit. Here, the previously employed simple effective operators and rate equations become increasingly inaccurate. This is due to the fact that in our derivation of Eqs. (4.14)–(4.15) we have neglected the influence of the ground-state Hamiltonian \hat{H}_g on the effective processes. As we derive below, Ω_{MW} has to be proportional to Ω so that an increased Ω also leads to a higher Ω_{MW} . For the case at hand, this influence induces a shift of the ground states by the microwave driving ('dressing'). In a frame where \hat{H}_g is diagonal we can include these effects by using the effective operators of Eqs. (3.38)–(3.39),

$$\hat{H}_{\text{eff}} = -\frac{1}{2} \left[\hat{V}_- \sum_l (\hat{H}_{\text{NH}} - E_l)^{-1} \hat{V}_+^l + H.c. \right] + \hat{H}_g, \quad (4.41)$$

$$\hat{L}_{\text{eff}}^k = \hat{L}_k \sum_l (\hat{H}_{\text{NH}} - E_l)^{-1} \hat{V}_+^l, \quad (4.42)$$

where E_l is the energy of the initial ground state l and \hat{V}_+^l the excitation from it. For non-negligible ground-state energies E_l , the elements of \hat{H}_{NH}^{-1} are generally replaced by $\hat{H}_{\text{NH}}^{-1} \rightarrow (\hat{H}_{\text{NH}} - E_l)^{-1}$. Yet, we note that in order to capture the effects of the dressed ground states it will not be necessary to keep the dressed state energies E_l in all propagators, but only those engineered to be strong. In fact, numerical curves obtained from these extended operators match the evolution of the full master equation very accurately, as can be seen from Fig. 4.6 c).

Once ground-state dressing is taken into account, the decay rates from the dressed triplet states $|T_{\pm}\rangle$ and $|T_r\rangle$ into $|S\rangle$ are no longer identical. Effective spontaneous emission from the dressed triplet states into the singlet mediated by $|S_1\rangle$ has the non-degenerate propagators

$$\langle S_1 | (\hat{H}_{\text{NH}} - E_{T_{\pm}})^{-1} | S_1 \rangle = (\tilde{\Delta}_{0,\text{eff}} - E_{T_{\pm}})^{-1} = \left(-\frac{i\gamma}{2} \mp \sqrt{\frac{3}{2}} \Omega_{\text{MW}} \right)^{-1}, \quad (4.43)$$

$$\langle S_1 | (\hat{H}_{\text{NH}} - E_{T_r})^{-1} | S_1 \rangle = (\tilde{\Delta}_{0,\text{eff}} - E_{T_r})^{-1} = \left(-\frac{i\gamma}{2} \right)^{-1}, \quad (4.44)$$

resulting in detuned decay rates $\gamma_{\text{eff}}^{(T_{\pm})} = \gamma_{\text{eff}} \cdot \gamma^2 / (\gamma^2 + \Omega_{\text{MW}}^2)$, while $\gamma_{\text{eff}}^{(T_r)} = \gamma_{\text{eff}}$ and $\kappa_{\text{eff}}^{(S)} \approx \kappa_{\text{eff}}$ are effectively unchanged. Taking these into account we can set up the rate equations in the same manner as in the weak driving case in Sec. 4.3.5.

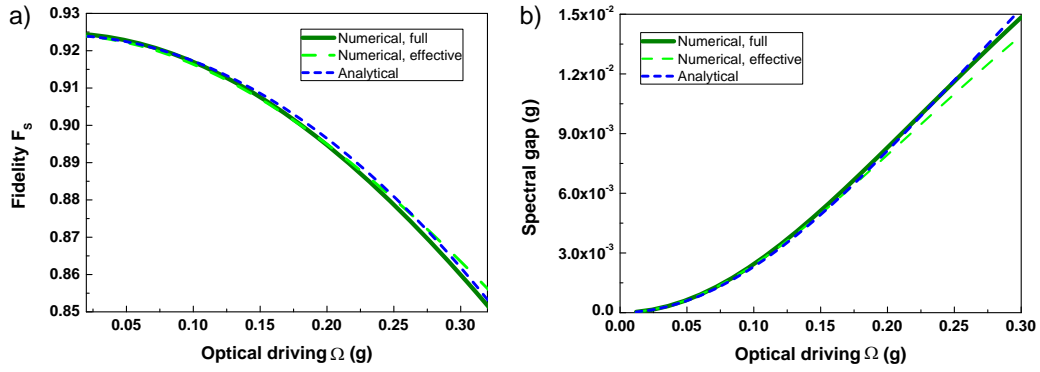


FIGURE 4.7: Fidelity and spectral gap as a function of driving strength. (a) Fidelity of the steady state with the singlet state and (b) spectral gap as a measure of the speed of convergence with respect to the optical driving strength Ω . Analytical results (blue, short dash) are in very good agreement with numerical curves obtained from the full (dark green) and effective (green dash) Liouvillian even at $\Omega \approx \gamma/2 \approx g/5$. For all curves the cavity parameters $(\gamma, \kappa) = (\frac{3g}{8}, \frac{5g}{32})$ [41], corresponding to $C \approx 17$, and the optimized driving parameters $\Omega = 2^{5/4}\Omega_{\text{MW}} = 2^{7/4}\beta$ were used. Note that the analytical curve in a) contains terms that are not included in Eq. (4.47) (see discussion of Eq. (4.58)).

4.4.2 Derivation of the error and of the spectral gap in the presence of ground-state dressing

Employing the state-dependent decay rates $\gamma_{\text{eff}}^{(T_i)}$ the additional error originating from the dressing of the triplet states is derived the following way:

Despite the different decay rates into the singlet, the population of the dressed triplet states is kept close to an equilibrium by strong dissipative shuffling $\propto 1/\gamma$ in-between them (see Fig. 4.5 b). Consequently, an equal mixture of the triplet states $P_{\mathcal{T}} \equiv \frac{1}{3}(P_{T_+} + P_{T_-} + P_{T_r})$ is the slowest decaying eigenvector of the Liouvillian. Using this definition we set up the rate equation for the population of the singlet state

$$\dot{P}_S = \frac{\Omega^2}{12\gamma} \frac{\gamma^2 + 2\Omega_{\text{MW}}^2}{\gamma^2 + 6\Omega_{\text{MW}}^2} P_{\mathcal{T}} - \frac{\kappa\Omega^2}{8g^2} P_S. \quad (4.45)$$

While the loss of population from the singlet by cavity decay κ_{eff} is unaffected by the dressing, the decay rate of the triplet population through spontaneous emission has now become dependent on Ω_{MW} : Introducing $P_{\mathcal{T}}$ results in an effective decay rate $\gamma_{\text{eff}}^{(\mathcal{T})} \equiv \frac{3}{2} \cdot \eta \cdot \gamma_{\text{eff}}$ with a factor $\eta \equiv \frac{\gamma^2 + 2\Omega_{\text{MW}}^2}{\gamma^2 + 6\Omega_{\text{MW}}^2}$ originating from averaging the decay rates $\gamma_{\text{eff}}^{(T_i)}$. For the steady state ($\dot{P}_S = 0$, $P_S \approx 1$) we derive the error

$$(1 - F_S) = \frac{3}{2C} \cdot \frac{\gamma^2 + 6\Omega_{\text{MW}}^2}{\gamma^2 + 2\Omega_{\text{MW}}^2} \approx \frac{3}{2C} \left(1 + \frac{4\Omega_{\text{MW}}^2}{\gamma^2} \right) \quad (4.46)$$

$$\equiv (1 - F_S)_{\text{stat}} + (1 - F_S)_{\text{dres}}. \quad (4.47)$$

As can be seen from the second step where we have expanded for $\Omega_{\text{MW}} \ll \gamma$, the errors decouple into the static error, derived in Sec. 4.3.5, and another, dynamic error $(1 - F_S)_{\text{dres}}$. The latter emerges from the dressing of the ground states by

Ω_{MW} . Just as the static error, it decreases linearly with one over the cooperativity C^{-1} .

In the same manner, the spectral gap in the presence of ground-state dressing is found from Eq. (4.45), determined by the decay rate of the lowest-lying eigenvector $P_{\mathcal{T}}$,

$$\lambda = \frac{\Omega^2}{12\gamma} \cdot \frac{\gamma^2 + 2\Omega_{\text{MW}}^2}{\gamma^2 + 6\Omega_{\text{MW}}^2}. \quad (4.48)$$

This result can also be derived more rigorously if we set up the full rate equations and extract the spectral gap as their smallest non-zero eigenvalue. We find

$$\lambda = \frac{\Omega^2 \left(5\gamma^2 + 18\Omega_{\text{MW}}^2 - \sqrt{9\gamma^4 + 84\gamma^2\Omega_{\text{MW}}^2 + 324\Omega_{\text{MW}}^4} \right)}{24\gamma(\gamma^2 + 6\Omega_{\text{MW}}^2)} \quad (4.49)$$

$$\approx \frac{\Omega^2}{12\gamma} \cdot \frac{\gamma^2 + 2\Omega_{\text{MW}}^2}{\gamma^2 + 6\Omega_{\text{MW}}^2}. \quad (4.50)$$

In the last line we have used $\gamma \gg \Omega_{\text{MW}}$ and expanded up to second order in Ω_{MW} which reproduces the result of Eq. (4.48). For $\Omega_{\text{MW}} \rightarrow 0$ the derived expressions reduce to the weak driving case as expected. In Fig. 4.7 b) we have plotted the analytic result for the spectral gap (from Eq. (4.49)) with respect to the optical driving Ω , together with the numerically obtained spectral gap of the full and effective Liouvillians of Eqs. (4.10) and (4.13). We see that also for increased driving the curves are in good agreement.

4.4.3 Beyond rate equations

So far, we have carried out our analytic study using rate equations formulated in a dressed state picture, where \hat{H}_{g} is diagonal. In the same picture, we have included the dressed ground-state energies into the effective operators. However, in order to fully describe the system, in particular the effects at low microwave driving, we change back into the original ‘shuffling picture’ with triplet states $|00\rangle$, $|11\rangle$ and $|T\rangle$ coupled by $\Omega_{\text{MW}}/\sqrt{2}$. Introducing new decay rates we can write the dressed effective operators as

$$\hat{L}_{\text{eff}}^{\gamma,0,\{1,2\}} = \pm i\sqrt{\gamma_d}|T\rangle\langle T| + i\sqrt{\gamma_d}|S\rangle\langle T| \mp \quad (4.51)$$

$$\mp \tilde{\chi}_a|T\rangle\langle 00| - \tilde{\chi}_a|S\rangle\langle 00| \mp \tilde{\chi}_a^*|T\rangle\langle 11| - \tilde{\chi}_a^*|S\rangle\langle 11|, \quad (4.52)$$

$$\hat{L}_{\text{eff}}^{\gamma,1,\{1,2\}} = \mp \sqrt{2}\tilde{\chi}_a|11\rangle\langle 00| \mp \sqrt{2}\tilde{\chi}_a^*|11\rangle\langle 11| \pm i\sqrt{2\gamma_d}|11\rangle\langle T|, \quad (4.53)$$

$$\hat{L}_{\text{eff}}^{\kappa} = + \sqrt{\kappa_{\text{eff}}}|11\rangle\langle S| - 2\sqrt{\kappa_{\text{eff}}}|S\rangle\langle 00|, \quad (4.54)$$

with the previous but shifted effective spontaneous emission rate

$$\gamma_d = \frac{\Omega^2}{8\gamma} \frac{\gamma^2 + 2\Omega_{\text{MW}}^2}{\gamma^2 + 6\Omega_{\text{MW}}^2} = \gamma_{\text{eff}} \cdot \eta, \quad (4.55)$$

and an additional spontaneous emission process activated by Ω_{MW} , with an amplitude $\tilde{\chi}_a = \frac{\Omega\Omega_{\text{MW}}}{2\sqrt{\gamma}} \frac{\gamma - i\sqrt{2}\Omega_{\text{MW}}}{\gamma^2 + 6\Omega_{\text{MW}}^2}$. Here, $\tilde{\chi}_a$ carries a phase; the according effective

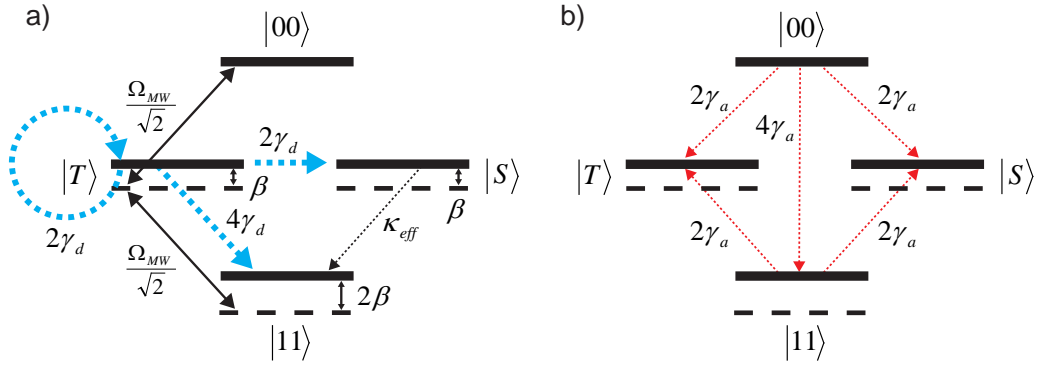


FIGURE 4.8: Effective processes at increased driving. (a) Unaffected (black) and reduced (blue) processes. A detuning $\beta = \Omega_{MW}/\sqrt{2}$ and dephasing $2\gamma_d$ of state $|T\rangle$ retard the “recycling” of population $|11\rangle \rightarrow |T\rangle \rightarrow |S\rangle$. (b) Effective decay processes activated by dressing of the ground states by Ω_{MW} (red).

decay rate is defined by $\gamma_a = |\tilde{\chi}_a|^2$, with $\gamma_a \ll \gamma_d$. The effective cavity decay $\kappa_{eff} = \frac{\kappa\Omega^2}{8g^2}$ as the main loss process remains unaffected by the dressing since $\Omega_{MW} \ll g$. The shifts of the effective Hamiltonian are again negligible so that $\hat{H}_{eff} \approx \hat{H}_g$.

The effects of increased driving are illustrated in Fig. 4.8. The dressing of the triplet ground states $|T_{\pm}\rangle$ by Ω_{MW} causes a reduction of the advantageous decay processes to γ_d from γ_{eff} , while the amplitude of the detrimental process κ_{eff} remains unchanged. The scaling of γ_d with η is the result of averaging over the decay rates of the dressed triplet states $\gamma_{eff}^{(T)}$ through back-transform. In addition, new decay channels at rates γ_a are activated for high Ω_{MW} and increase the error of the protocol by accumulation of population in state $|11\rangle$.

4.4.4 Derivation of the recycling error and optimal reshuffling

Above we have derived the static error and the driving-dependent error originating from the shift of the ground states. An additional error emerges from the dynamics of the coherences which is not caught by rate equations of the populations:

From Fig. 4.6 a), c) we can see that accumulation of population in $|11\rangle$ is the bottleneck of the scheme. Coherent reshuffling Ω_{MW} from $|11\rangle$ to $|T\rangle$ is used to “recycle” the population of $|11\rangle$. Hence, the additional error of accumulation of $|11\rangle$ is more pronounced the weaker Ω_{MW} is compared to Ω , regardless of the driving regime. The effective dephasing of $|T\rangle$ at a rate γ_d and a detuning $\beta = \Omega_{MW}/\sqrt{2}$, however, tend to slow down the recycling process. Still, justified by its rapid decay of $6\gamma_d$ altogether, the state $|T\rangle$ can be considered transient and can hence be adiabatically eliminated. In addition, we can ignore the evolution of $|00\rangle$ and the much weaker effective decay processes activated by Ω_{MW} which have rates γ_a . After adiabatic elimination of the rapidly dephasing coherences ($\dot{\rho}_{11,T}, \dot{\rho}_{T,11} \approx 0$) and the population of $|T\rangle$ ($\rho_{T,T} \ll \rho_{11,11}$) we can write the dynamics in terms of two rates affecting the population of the desired singlet

state

$$\dot{P}_S \approx -\kappa_{\text{eff}} P_S + \frac{8\gamma_d \Omega_{\text{MW}}^2}{96\gamma_d^2} P_{11}. \quad (4.56)$$

Thus, for the steady state ($\dot{P}_S = 0$, $P_S \approx 1$) we derive the error

$$(1 - F_S)_{\text{recy}} \approx \frac{12\kappa_{\text{eff}}\gamma_d}{\Omega_{\text{MW}}^2}. \quad (4.57)$$

In order to make sure that the errors of Eqs. (4.46) and (4.57) are actually sufficient to describe the fidelity of the protocol at increased driving we also derive the steady state from the Liouvillian dynamics. To this end, we solve the master equation represented by the effective Liouvillian \mathcal{L}_{eff} for $\dot{\rho}_{j,k} = 0$ for all j, k .

The extended decay rates γ_d and γ_a also hold for stronger driving. Since the shuffling Ω_{MW} is still much lower than the spontaneous emission γ , we also neglect dephasing originating from the Ω_{MW} -activated processes (γ_a), as well as dephasing at a rate κ_{eff} , in the presence of dephasing at rates γ_d ($\gamma_a, \kappa_{\text{eff}} \ll \gamma_d$). Normalizing the obtained expression for the steady state and expanding it up to the second order in Ω and Ω_{MW} , we extract the complete driving-dependent error as

$$(1 - F_S)_{\text{comb}} \approx \frac{3\gamma\kappa}{2g^2} + \frac{6\kappa\Omega_{\text{MW}}^2}{g^2\gamma} + \frac{3\kappa\Omega^4}{16g^2\gamma\Omega_{\text{MW}}^2} \quad (4.58)$$

$$\equiv (1 - F_S)_{\text{stat}} + (1 - F_S)_{\text{dres}} + (1 - F_S)_{\text{recy}}. \quad (4.59)$$

This is exactly the sum of the driving-dependent errors of Eqs. (4.46) and (4.57), expanded for small Ω_{MW} . We see that in fact the errors decouple. As one of these terms scales as Ω_{MW}^{+2} and the other as Ω_{MW}^{-2} , the optimum for Ω_{MW} is a trade-off between fast recycling requiring large Ω_{MW} and the need not to shift states out of resonance favoring small Ω_{MW} . We use the result of Eq. (4.58) to derive an optimal reshuffling of

$$\Omega_{\text{MW,opt}} = \frac{\Omega}{2^{5/4}}. \quad (4.60)$$

Inserting $\Omega_{\text{MW,opt}}$ into Eq. (4.58) we obtain the combined error

$$(1 - F_S)_{\text{comb}} = \frac{3}{2C} \left(1 + \sqrt{2} \left(\frac{\Omega}{\gamma} \right)^2 \right). \quad (4.61)$$

We will use this result below to discuss the scaling of the error with the speed of convergence and with the preparation time.

In Fig. 4.7 a) we plot the analytical result for $(1 - F_S)_{\text{comb}}$ together with numerical curves obtained by extracting the steady state from the full and the effective Liouvillian for different optical driving Ω , using the parameters of Ref. [41], $(\gamma, \kappa) = (\frac{3g}{8}, \frac{5g}{32})$, corresponding to a cooperativity of $C \approx 17$. Note that for the analytical curve in Fig. 4.7 a) we have not discarded terms of higher order in C^{-1} , as in Eq. (4.58), but have kept terms up to second order in C^{-1} after solving for the steady state of the Liouvillian. For higher cooperativities, the higher orders

become negligible and the expression for $(1 - F_S)_{\text{comb}}$ reduces to Eq. (4.58). Fig. 4.7 b) contains the analytical and numerical results for the spectral gap, as a measure for the convergence rate. We find that for our initial assumption of weak driving ($\Omega \ll \gamma$) the analytic results for the scaling of both important performance measures, error and spectral gap, with the driving strength are very accurate. In addition, we find very good agreement with numerical results obtained from both the full and the effective master equation even up to an increased driving of $\Omega \approx \gamma/2 \approx g/5$. Despite the increased driving, the population of the excited states, in particular the close-to-resonant $|S_1\rangle$, does not exceed $\sim 5\%$ for $\Omega = \gamma/2$ (cavity parameters of Ref. [41]) so that both the initial truncation of the Hilbert space to at most singly excited states as well as the concept of the effective dynamics of the ground states are well-justified even in the regime of increased driving.

4.4.5 Performance of the scheme at increased driving

We evaluate the performance of the scheme, this time at increased driving, by estimating the trade-off between fidelity and convergence time. To this end, we use the results for the driving-dependent spectral gap λ and error of Eqs. (4.49) and (4.61) from which we eliminate the driving Ω . In doing so we find

$$(1 - F_S)_{\text{per}} \approx \frac{3}{2C} \frac{2\sqrt{2}\gamma + 21\lambda}{2\sqrt{2}\gamma - 27\lambda} \stackrel{\lambda \ll \gamma}{\approx} \frac{3}{2C} + \frac{18\sqrt{2}\kappa\lambda}{g^2}. \quad (4.62)$$

For strong coupling $g \gg (\gamma, \kappa)$, or sufficiently high cooperativities $C \gg 10$, the static and the dynamic error decouple when the expression is expanded in λ . Thereby we obtain the slope of the tangent of F_S for a small λ . The analytic result shown in Fig. 4.9 agrees very well with the numerical results obtained from the full and dressed effective master equation as long as the assumption of perturbative optical driving is justified. For very rapid state preparation, the analytic expressions reproduce the decreasing trend of the numerical curves correctly. In Sec. 4.6 we compare these benchmarks for the scheme at hand with the ones for the schemes presented in Sec. 4.5.1, Sec. 4.5.2, Sec. 4.5.4, and App. A.

4.4.6 Scaling of the dynamic error with the preparation time

In the discussed setting, the scaling of the error and spectral gap provides an estimate of how fast the population decays into a desired steady state and to which extent the fidelity is lowered by an increased driving. For preparation within a fixed time one will thus have to make a compromise between the convergence rate and the detrimental effects of increased driving. These two effects can be used to derive the optimal driving for a desired preparation time. To this end, the error of the protocol with respect to the preparation time t , consisting of a static and a dynamic part, can be written as

$$(1 - F_S)(\Omega, t) = \frac{3}{2C} + f\Omega^2 + \frac{3}{4}e^{-\Omega^2 t/r}. \quad (4.63)$$

with f and r specified below. Here, we have assumed that the evolution begins in a complete statistical mixture of the four states. We minimize the error for

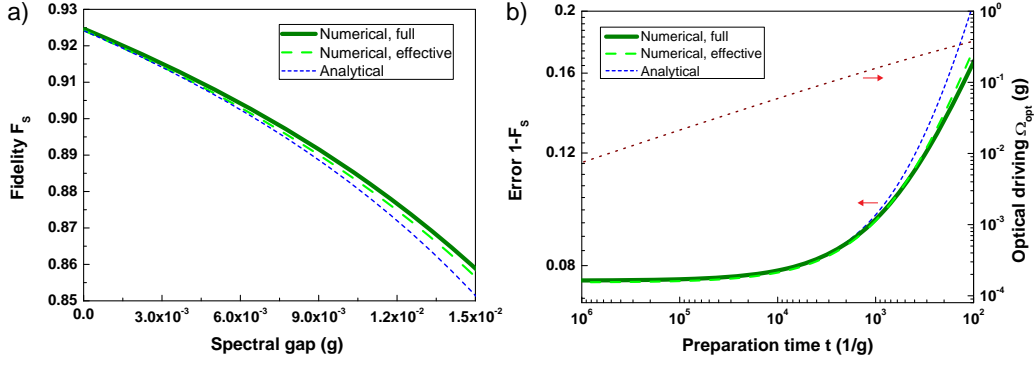


FIGURE 4.9: Performance of the dissipative state preparation at increased driving. a) The fidelity of the steady state is lowered by the increase of the dynamic error when the spectral gap increases. (b) Error of the protocol (left axis) and optimal driving strength (right axis) vs. desired preparation time. Analytic results (blue, short dash) are in good agreement with numerical curves obtained from the full (dark green) and effective Liouvillian (green dash). The cavity parameters $(\gamma, \kappa) = (\frac{3g}{8}, \frac{5g}{32})$ [41] ($C \approx 17$) and the optimized driving parameters $\Omega = 2^{5/4}\Omega_{\text{MW}} = 2^{7/4}\beta$ were used; in (b) we also use and plot the optimized optical driving Ω_{opt} (red dot) of Eq. (4.64).

a given state preparation time t by taking its derivative with respect to Ω^2 and obtain for the optimal driving strength

$$\Omega_{\text{opt}}^2 = -\frac{r}{t} \log \frac{4fr}{3t}. \quad (4.64)$$

Above we have derived the combined static and dynamic error and the spectral gap (Eqs. (4.61) and (4.49)) which we now associate with the quantities f and r . With $f = \frac{3\kappa}{\sqrt{2}g^2\gamma}$ and $r = 12\gamma$ we get $fr = \frac{36\kappa}{\sqrt{2}g^2}$. We thus obtain for the optimized error of the protocol

$$\begin{aligned} (1 - F_S)_{\text{opt}}(t) &= \frac{3}{2C} + \frac{36\kappa}{\sqrt{2}g^2t} \left(1 + \log \frac{\sqrt{2}g^2t}{48\kappa} \right) \\ &= \frac{3}{2C} + \frac{36}{\sqrt{2}} \sqrt{\frac{\kappa}{\gamma}} \sqrt{\frac{1}{C}} \frac{1}{gt} \left(1 + \log \left(\frac{\sqrt{2}}{48} \sqrt{\frac{\gamma}{\kappa}} \sqrt{C} gt \right) \right). \end{aligned} \quad (4.65)$$

In the second line we have expressed the optimized error in terms of the cooperativity and the ratio of the decay rates γ and κ . We find that – apart from the linear static error ($\frac{3}{2C}$) – the above expression for the optimized error also exhibits a favorable scaling of the dynamic error part with the square-root of the cooperativity. We plot this analytical result in Fig. 4.9 b), together with curves obtained numerically from the full/effective Liouvillian, using the cavity parameters $(\gamma, \kappa) = (\frac{3g}{8}, \frac{5g}{32})$ [41] ($C \approx 17$) and the optimized driving parameters $\Omega = 2^{5/4}\Omega_{\text{MW}} = 2^{7/4}\beta$, as well as the optimized optical driving Ω_{opt} of Eq. (4.64). We find good agreement even for reasonably short preparation times $\approx 10^3 g^{-1}$ where we get fidelities above 90%.

4.5 Schemes for various experimental situations

The scheme for effective spontaneous emission mediated by a dark state, discussed in the preceding sections, assumes a phase difference of $\phi = \pi$ between the optical driving of the two atoms. While in present-day cavity experiments the position of the atoms along the cavity axis with respect to the cavity standing wave is well-controllable within the Lamb-Dicke regime, their transversal position is not necessarily confined. If the atoms are driven by laser fields oriented transverse to the cavity axis this results in a random phase factor $e^{ik \cdot r(t)}$ (with wave vector k and relative position of the atoms $r(t)$). Hence, the assumption of a relative and stable phase relation ϕ rules out common transversal driving of the atoms in the absence of transversal trapping.

This section deals with better suited alternatives for today's cavity experiments: Here, we present schemes that can be implemented with a driving with $\phi = 0$, or even with a randomly fluctuating driving phase $\phi(t)$.

The phase relation $\phi = 0$ can be obtained by driving the cavity with a strong laser which is strongly detuned from a cavity mode but near resonance with the atomic transition $|0\rangle \leftrightarrow |e\rangle$. The detuned drive creates a coupling mediated by the off-resonant cavity mode and the phase relation will then be set by the phase of the cavity mode. If the cavity driving mode and the mode used to create the entanglement are commensurate, this will ensure that we have the phase relation $\phi = 0$. Schemes that are well-suited for this situation will be presented in Sec. 4.5.1 and 4.5.4.

We also discuss the possibility to use common addressing by a transverse laser with an arbitrary relative phase $\phi(t)$. In the following two sections, Sec. 4.5.1 and 4.5.2, we present two schemes, one of which is operated with $\phi = 0$, and one with $\phi = \pi$. The combination of these schemes allows for a phase-insensitive scheme, as will be carried out in Sec. 4.5.3.

4.5.1 A scheme for an identical driving phase of the atoms

We consider a drive with an identical phase for both atoms, $\phi = 0$. In addition, we choose to work in the subspace containing the atomic excited state $|T_0\rangle$ and the cavity-excited state $|T\rangle|1\rangle$, in order to realize strong spontaneous emission from $|00\rangle$ into $|S\rangle$, mediated by $|T_0\rangle$. For this “ $|T_0\rangle$ ” scheme we use non-vanishing laser (Δ) and cavity (δ) detuning, but a vanishing detuning $\beta = 0$ of the microwave/Raman field. This means that $\tilde{\Delta} = \tilde{\Delta}_n$ and $\tilde{\delta} = \tilde{\delta}_n$ for all n .

Mechanism of the state preparation. The working principle is illustrated in Fig. 4.10. Population from state $|00\rangle$ is excited to $|T_0\rangle$ by a weak optical field of strength Ω . The atomic excited state $|T_0\rangle$ is coupled to the cavity excited state $|T\rangle|1\rangle$ by the atom-cavity interaction \hat{H}_{ac} . Due to the strong coupling (g), the states $|T_0\rangle$ and $|T\rangle|1\rangle$, initially detuned by $\tilde{\Delta}$ and $\tilde{\delta}$, form dressed states. Treating the detunings of the excited states as complex, as discussed in Sec. 4.2, the detunings of these dressed states can be written as

$$\tilde{\Delta}_{\pm} = \frac{\tilde{\Delta} + \tilde{\delta}}{2} \pm \frac{1}{2} \sqrt{(\tilde{\Delta} + \tilde{\delta})^2 - 4(\tilde{\Delta}\tilde{\delta} - g^2)}, \quad (4.66)$$

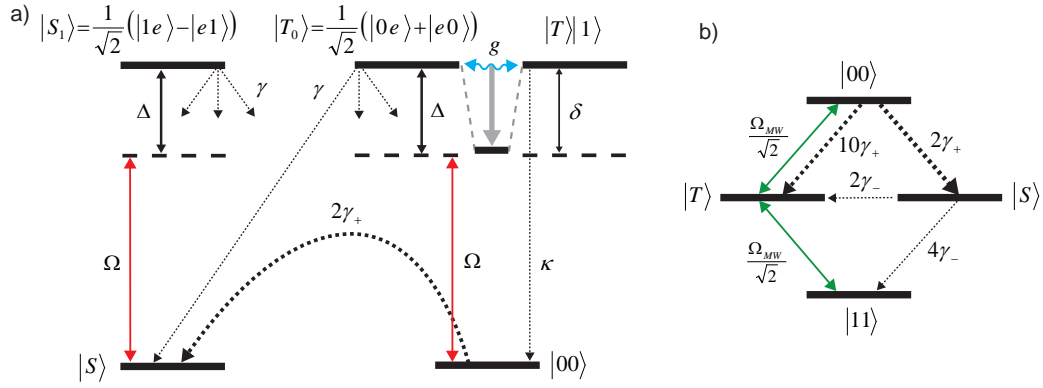


FIGURE 4.10: Mechanism and effective processes of the $|T_0\rangle$ scheme. (a) Dissipative preparation of the maximally entangled singlet state $|S\rangle$. For an appropriate choice of atomic and cavity detuning Δ and δ the cavity interaction of strength $\sqrt{2}g$ enhances the effective spontaneous emission γ_{eff} from state $|00\rangle$ by shifting the lower dressed state of $|T_0\rangle$ and $|T\rangle|1\rangle$ into resonance with the optical driving Ω . States $|T\rangle$ and $|11\rangle$ are coupled to $|00\rangle$ by a microwave field or Raman transition Ω_{MW} (not shown). Effective decay from $|S\rangle$ is suppressed as it involves the atom-cavity interaction dark state $|S_1\rangle$, the detuning Δ of which is not compensated. (b) Effective level scheme and ground state to ground-state processes for the presented scheme.

where $\tilde{\Delta} = \Delta - \frac{i\gamma}{2}$ and $\tilde{\delta} = \delta - \frac{i\kappa}{2}$. We engineer an efficient spontaneous emission process that prepares the singlet state $|S\rangle$ by setting the cavity detuning equal to the cavity line shift $\delta = g^2/\Delta$. With this choice the lower dressed state of $|T_0\rangle$ and $|T\rangle|1\rangle$ is shifted close to resonance, $\text{Re}(\tilde{E}_-) \approx 0$. Consequently, population from $|00\rangle$ – which is coupled to $|T_0\rangle$ – is rapidly transferred to $|S\rangle$ by spontaneous emission via the lower dressed state of $|T_0\rangle$ and $|T\rangle|1\rangle$. On the other hand, decay out of $|S\rangle$ involves excitation of $|S_1\rangle$. Since $|S_1\rangle$ is the only dark state of the atom-cavity interaction, its detuning Δ means that it is not in resonance. Hence, the decay into the singlet state $|S\rangle$ is engineered to be much stronger than the decay out of $|S\rangle$ so that the maximally entangled state $|S\rangle$ is efficiently prepared. The atomic detuning provides a trade-off between virtual character of the excited dressed states on the one hand, and spontaneous and cavity decay on the other hand; by setting $\Delta = g\sqrt{\frac{\gamma}{\kappa}}$ we minimize the line width of the dressed states, $\tilde{\Delta}_- \approx \text{Im}(\tilde{\Delta}_-) \approx \frac{i}{2}(\Delta\kappa + \delta\gamma)$. Furthermore, coherent coupling of the triplet states $|00\rangle$, $|11\rangle$, and $|T\rangle$ by the microwave/Raman field Ω_{MW} guarantees that all triplet states decay rapidly towards the singlet state $|S\rangle$.

Effective processes. For the discussed scheme we have assumed the relative phase of the optical driving between the atoms to be zero ($\phi = 0$). Using this, the effective processes can be read off from Figs. 4.2 and 4.3. Given our choice of the parameters δ , Δ and β the terms of the effective detunings can be simplified to obtain the scaling of the effective decay processes. Using $\tilde{g}_{1,\text{eff}} \approx i\sqrt{\gamma\kappa}$, $\tilde{g}_{2,\text{eff}} \approx$

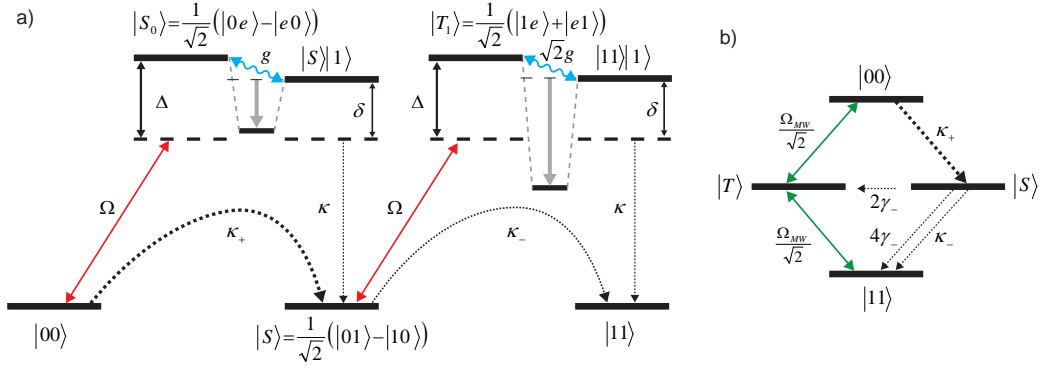


FIGURE 4.11: Mechanism and effective processes of the $|S_0\rangle$ scheme. (a) Setting $\delta = \frac{g^2}{\Delta}$ shifts the lower dressed state of $|S_0\rangle$ and $|S\rangle|1\rangle$ into resonance with the optical driving Ω , while the dressed states of $|T_1\rangle$ and $|11\rangle|1\rangle$ are detuned due to a different coupling strength of $\sqrt{2}g$. Hence, effective cavity decay κ_+ from $|00\rangle$ into $|S\rangle$ is enhanced while cavity loss κ_- from $|S\rangle$ into $|11\rangle$ is suppressed. The populations of the triplet states are shuffled by a microwave or Raman transition Ω_{MW} , shown together with the effective decay processes in (b).

$g/\sqrt{2}$, $\tilde{\Delta}_{0,\text{eff}} \approx \Delta$, $\tilde{\Delta}_{1,\text{eff}} \approx -i\gamma$ and $\tilde{\Delta}_{2,\text{eff}} \approx -\Delta$ the effective operators simplify to

$$\hat{L}_{\text{eff}}^{\gamma,0,\{1,2\}} = i\sqrt{2\gamma_+}|00\rangle\langle 00| \pm \sqrt{\gamma_-}|T\rangle\langle S|, \quad (4.67)$$

$$\hat{L}_{\text{eff}}^{\gamma,1,\{1,2\}} = i\sqrt{\gamma_+}(|T\rangle\langle 00| \mp |S\rangle\langle 00|) \pm \sqrt{2\gamma_-}|11\rangle\langle S|, \quad (4.68)$$

$$\hat{L}_{\text{eff}}^{\kappa} = -i\sqrt{\kappa_{\text{eff}}}|T\rangle\langle 00|. \quad (4.69)$$

Here, the spontaneous emission processes $\hat{L}_{\text{eff}}^{\gamma,0,\{1,2\}}$ transfer population from $|00\rangle$ into the desired state $|S\rangle$ at a strongly enhanced rate of $2\gamma_+ = \frac{\Omega^2}{16\gamma}$. Loss from the singlet state also occurs by spontaneous emission at a much weaker rate $\gamma_- = \frac{\kappa\Omega^2}{32g^2}$. As opposed to the $|S_0\rangle$ and $|S_1\rangle$ schemes, the effective cavity decay, here with a rate $\kappa_{\text{eff}} = \frac{\Omega^2}{4\gamma}$, does not directly affect the singlet state. The effective processes are illustrated in Fig. 4.10 b).

Parameter and performance analysis Setting up the rate equations in the same manner as for the previous scheme is straightforward. We obtain for the error and the spectral gap

$$(1 - F_S)_{|T_0\rangle} = \frac{11}{2C} \quad (4.70)$$

$$\lambda_{|T_0\rangle} = \frac{2 - \sqrt{3}}{8} \frac{\Omega^2}{\gamma}. \quad (4.71)$$

Both the error and the spectral gap are found to have the same scaling with the parameters of the system as the $|S_1\rangle$ scheme, but exhibit different proportionality factors. The performance of the schemes presented in this section is optimal for an Ω_{MW} in the interval of $\Omega_{\text{MW}} = \frac{\Omega}{2}$ to $\Omega_{\text{MW}} = \frac{\Omega}{3}$; the latter value is used for the simulations below.

4.5.2 A scheme using engineered cavity decay

We now turn to a scheme with $\phi = \pi$ which uses engineered cavity decay for the dissipative preparation of the singlet state $|S\rangle$. Since for this scheme we assume that the atoms are driven with opposite phase $\phi = \pi$ we can conduct our discussion based on the effective operators of Eqs. (4.31)–(4.33) used for the scheme presented in Sec. 4.3 and 4.4.

In brief, the mechanism, as visualized in Fig. 4.11, is the following: Population from state $|00\rangle$ is driven up to the excited state $|S_0\rangle = \frac{1}{2}(|0e\rangle - |e0\rangle)$, at a laser detuning Δ with $\beta = 0$. The state $|S_0\rangle$ is in turn coupled by the atom-cavity interaction to $|S\rangle|1\rangle$ with a strength of g . $|S\rangle|1\rangle$ decays into $|S\rangle$ via cavity decay at a rate κ . As only one atom is in $|e\rangle$ or $|1\rangle$, the coupling $|S_0\rangle|0\rangle \leftrightarrow |S\rangle|1\rangle$ causes an AC stark shift of g^2/Δ to $|S_0\rangle|0\rangle$ and $|S\rangle|1\rangle$, whereas the coupling $|T_1\rangle|0\rangle \leftrightarrow |11\rangle|1\rangle$ with two atoms in $|1\rangle$ or $|e\rangle$ causes an AC stark shift of $2g^2/\Delta$ of the states $|T_1\rangle|0\rangle$ and $|11\rangle|1\rangle$. Thus, setting the cavity detuning to $\delta = \frac{g^2}{\Delta}$ greatly enhances the effective cavity decay $|00\rangle \xrightarrow{\Omega} |S_0\rangle \xrightarrow{g} |S\rangle|1\rangle \xrightarrow{\kappa} |S\rangle$. As in the $|T_{0,1}\rangle$ schemes, this is due to the fact that the lower dressed state of $|S_0\rangle$ and $|S\rangle|1\rangle$ is shifted into resonance. Loss of population from the singlet via $|T_1\rangle$ is effectively suppressed, since $|T_1\rangle$ and $|11\rangle|1\rangle$ are coupled with a larger strength $\sqrt{2}g$, shifting the dressed states out of resonance. The triplet states are shuffled by a microwave or Raman field with optimal strength $\Omega_{\text{MW}} \approx \Omega/3$.

We find that the optimal atomic detuning is $\Delta = g\sqrt{\frac{\gamma}{\kappa}}$. At this detuning we obtain the effective operators

$$\hat{L}_{\text{eff}}^\kappa = \sqrt{\kappa_-}|11\rangle\langle S| + i\sqrt{\kappa_+}|S\rangle\langle 00| \quad (4.72)$$

$$\hat{L}_{\text{eff}}^{\gamma,0,\{1,2\}} = \pm i\sqrt{2\gamma_+}|00\rangle\langle 00| - \sqrt{\gamma_-}(|T\rangle\langle S| \pm |S\rangle\langle S|) \quad (4.73)$$

$$\hat{L}_{\text{eff}}^{\gamma,1,\{1,2\}} = -\sqrt{2\gamma_-}|11\rangle\langle S| + i\sqrt{\gamma_+}(\pm|T\rangle\langle 00| - |S\rangle\langle 00|), \quad (4.74)$$

where we have assigned $\kappa_+ = \frac{\Omega^2}{2\gamma} = 8\gamma_+$, $\kappa_- = \frac{\kappa\Omega^2}{2g^2} = 16\gamma_-$. Indeed, the most pronounced process is the strongly enhanced effective cavity decay from $|00\rangle$ into $|S\rangle$. The static error and the spectral gap are found to be

$$(1 - F_S)_{|S_0\rangle} = \frac{7}{2C} \quad (4.75)$$

$$\lambda_{|S_0\rangle} = \frac{5 - \sqrt{5}}{16} \frac{\Omega^2}{\gamma}. \quad (4.76)$$

A comparative numerical study of the performance of this scheme is given in Sec. 4.6.

4.5.3 A scheme with robustness to the driving phase

One can think of experimental situations for which neither transversal confinement of the atoms (and hence a stable phase relation $\dot{\phi} = 0$), nor cavity driving ($\phi = 0$) are available. In the following, we argue that using laser addressing of the two atoms at random relative phase $\phi(t)$ can be suitable for the preparation of an entangled steady state of high fidelity.

We set out by noting that, apart from the driving phase ϕ , the conditions for the

operation of the above $|T_0\rangle$ scheme in Sec. 4.5.1 using $\phi = 0$ and the $|S_0\rangle$ scheme in Sec. 4.5.2 using $\phi = \pi$ are identical; in particular we use $\delta = g^2/\Delta$. In the experiment, transversal drift of the atoms can result in a random $\phi(t)$ with fluctuations much slower than the couplings of the system. Depending on the actual value of ϕ the driving either crosses the singlet/triplet subspace, $|00\rangle \xrightarrow{\Omega} |S_0\rangle$, as illustrated in Fig. 4.11 or stays within the subspace, $|00\rangle \xrightarrow{\Omega} |T_0\rangle$, similar to Fig. 4.10. Therefore, effective decay channels are instantaneously weighted with ϕ , as $\gamma_{\text{eff}}(t) = (\gamma_{\text{eff}})_{|T_0\rangle} \cdot \cos^2 \phi(t) + (\gamma_{\text{eff}})_{|S_0\rangle} \cdot \sin^2 \phi(t)$. Thus, the system mechanisms are a combination of the two individual schemes. Averaging the decay rates results in a combined error and spectral gap

$$(1 - F_S)_{|T_0\rangle/|S_0\rangle} = \frac{9}{2C} \quad (4.77)$$

$$\lambda_{|T_0\rangle/|S_0\rangle} = \frac{(9 - 2\sqrt{3} - \sqrt{5})\Omega^2}{32\gamma} \approx \frac{\Omega^2}{10\gamma}. \quad (4.78)$$

We conclude that a setup with arbitrary driving phase is also suitable for an experimental realization of a high-fidelity entangled state of two atoms in an optical cavity.

4.5.4 A scheme for cavity driving

We briefly discuss a possible “ $|T_1\rangle$ ” scheme that combines elements of the “ $|T_0\rangle$ ” scheme in Sec. 4.5.1 and of the “ $|S_1\rangle$ ” scheme presented in Sec. 4.5.1. It exhibits an improved error and spectral gap as compared to the $|T_0\rangle$ scheme (which is also suitable for cavity driving).

Setting $\delta = \frac{2g^2}{\Delta}$ and accordingly, $\Delta = g\sqrt{\frac{2\gamma}{\kappa}}$, shifts one of the dressed states of $|T_1\rangle$ and $|11\rangle|1\rangle$ into resonance. Then, $|S\rangle$ is effectively prepared through $|T_1\rangle$ by spontaneous emission. Similar to the $|S_1\rangle$ -scheme, a choice of $\beta = \frac{\Omega_{\text{MW}}}{\sqrt{2}}$ guarantees an equal share of $|T\rangle$ in the dressed triplet states so that these states decay equally rapidly into $|S\rangle$.

As compared to the $|T_0\rangle$ scheme the contrast between the unwanted $|S_1\rangle$ -mediated terms and the desired $|T_1\rangle$ -mediated terms is more pronounced than previously for the decay through $|S_1\rangle$ and $|T_0\rangle$. The error and spectral gap are therefore improved compared to the $|T_0\rangle$ scheme:

$$(1 - F_S)_{|T_1\rangle} = \frac{9}{2C} \quad (4.79)$$

$$\lambda_{|T_1\rangle} = \frac{\Omega^2}{48\gamma} \quad (4.80)$$

The performance of this $|T_1\rangle$ scheme at increased optical driving will also be addressed numerically in the section below.

4.6 Comparison of the presented schemes

In the following, we provide an overview of the presented schemes and compare their error in the preparation of the maximally-entangled singlet state and their

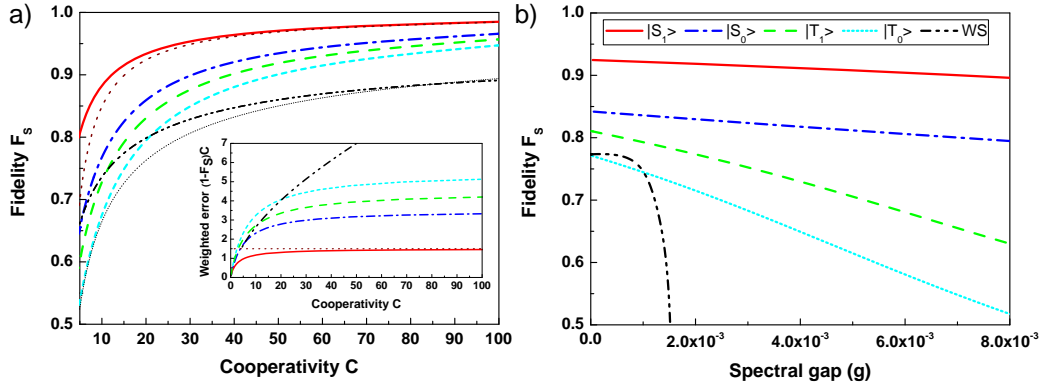


FIGURE 4.12: Comparison of static and dynamic error for the presented schemes, obtained numerically from the full Liouvillian of Eq. (4.10). (a) Scaling of the fidelity with the cooperativity (inset: error weighted with the cooperativity). The lowest error is found for the $|S_1\rangle$ scheme ($\frac{3}{2C}$, red solid), followed by the $|S_0\rangle$ scheme ($\frac{7}{2C}$, blue dash-dot) and the schemes suitable for cavity driving, $|T_1\rangle$ ($\frac{9}{2C}$, green dash) and $|T_0\rangle$ ($\frac{11}{2C}$, sky-blue short dash). Noticeable is the qualitative difference between linear scaling of these schemes and the square-root scaling law for the WS scheme ($\frac{3}{2\sqrt{2C}}$, black dash-dot-dot). Analytical results for the asymptotic scaling are shown for the $|S_1\rangle$ and WS scheme (red and black dots) (b) Fidelity vs. speed of convergence (spectral gap). A compromise between fidelity and speed limits the performance of the WS scheme, while close-to-linear scaling of both the $|S_{1/0}\rangle$ and $|T_{1/0}\rangle$ schemes allows rapid state preparation. For b) the cavity parameters $(\gamma, \kappa) = (\frac{3g}{8}, \frac{5g}{32})$ [41], with $C \approx 17$ were used, in a) C was varied keeping the ratio $\gamma/\kappa = 12/5$ constant. The optimized parameters used for each of the presented schemes are specified in the corresponding section. The same line format is used to denote the schemes in (a) and (b).

spectral gap as a measure for the rate of convergence. We separately discuss the scaling of the static error due to the imperfections of the cavity (as discussed in Sec. 4.3.5), and the dynamic error originating from increased optical driving by dressing of the levels (as in Sec. 4.4.4). An overview of all the schemes and in which section they can be found is shown in Table 4.1 along with a few key results on the performance of each scheme.

4.6.1 Static error scaling with the cavity parameters

In Fig. 4.12 a) we have plotted the fidelity of the steady state with the maximally-entangled singlet state, as a function of the cooperativity $C = \frac{g^2}{\gamma\kappa}$ for all schemes presented in this work. The curves were obtained numerically by extracting the steady state from the full Liouvillian of Eq. (4.10), using the optimized parameters specified in the corresponding section. For the error scaling of the $|S_1\rangle$ scheme and the WS scheme discussed in App. A, we plot the analytical curves along with the numerical ones. The linear scaling of the static error with C is more clearly seen in the inset, where we plot the weighted error $(1 - F_s)C$. In agreement with our analytic results, we find this quantity to be independent of C for $C \gg 10$ for the $|T_0\rangle$, $|T_1\rangle$, $|S_0\rangle$ and $|S_1\rangle$ schemes, while the adapted Wang-Schirmer (WS) scheme exhibits an error scaling $\propto \sqrt{C}$ as is the case for coherent unitary protocols. The best error scaling of $\frac{3}{2C}$ is provided by the $|S_1\rangle$

TABLE 4.1: Comparison of the discussed schemes: Analytic scaling of the error and rate of convergence (spectral gap) with respect to the cavity parameters for $C \gg 10$; comparative numbers for a cavity QED system as in Ref. [41], $(g, \gamma, \kappa)/2\pi = (16, 6, 2.5)$ MHz, $C \approx 17$. Characteristic dynamic measures are given for a driving that causes a dynamic error of 2%.

Scheme	Static error max. fidelity	Spectral gap at 2% error	Convergence time at 2% error	Transversal confinement required?
$ S_1\rangle$ (Sec. 4.3)	$3/2 C^{-1}$ 92.5%	$\Omega^2/12\gamma$ $6 \cdot 10^{-3}g$	$10 \mu s$	yes
$ S_0\rangle$ (Sec. 4.5.2)	$7/2 C^{-1}$ 84.2%	$(5 - \sqrt{5})\Omega^2/16\gamma$ $3 \cdot 10^{-3}g$	$20 \mu s$	yes
$ T_1\rangle$ (Sec. 4.5.4)	$9/2 C^{-1}$ 81.1%	$\Omega^2/48\gamma$ $1 \cdot 10^{-3}g$	$60 \mu s$	no
$ T_0\rangle$ (Sec. 4.5.1)	$11/2 C^{-1}$ 77.2%	$(2 - \sqrt{3})\Omega^2/8\gamma$ $8 \cdot 10^{-4}g$	$80 \mu s$	no
$ T_0\rangle/ S_0\rangle$ (Sec. 4.5.3)	$9/2 C^{-1}$ 79.7%	$\Omega^2/10\gamma$ $1 \cdot 10^{-3}g$	$60 \mu s$	no
WS (Sec. A)	$3/2 \sqrt{2C}^{-1}$ 77.3%	$2g^2\Omega^2/3\Delta^2\kappa$ $9 \cdot 10^{-4}g$	$70 \mu s$	no

scheme; an increase of the error to $\frac{7}{2C}$ is found for the $|S_0\rangle$ scheme. The schemes that are suitable for cavity driving in the absence of transversal confinement, $|T_1\rangle$ and $|T_0\rangle$ also exhibit linear scaling with the cooperativity with further increasing proportionality factors $\frac{9}{2C}$ and $\frac{11}{2C}$. Above cooperativities of $C \approx 10$ the square-root scaling error of the WS scheme $\frac{3}{2\sqrt{2C}}$ is outperformed by the $|T_1\rangle$ scheme which uses similar conditions. An overview and numerical examples are given in Table 4.1.

4.6.2 Dynamic error scaling with the speed of convergence

In addition to the static error scaling of Fig. 4.12 a) we present the dynamic error scaling with the spectral gap in Fig. 4.12 b). These curves were obtained by numerically extracting the spectral gap from the full Liouvillian of Eq. (4.10). Again, the best performance is shown by the $|S_1\rangle$ scheme, followed by the other three schemes which all exhibit an almost linear scaling; the schemes suitable for cavity driving, $|T_1\rangle$ and $|T_0\rangle$, have a steeper slope. On the other hand, the performance of the adapted WS scheme is governed by a compromise between fidelity and speed, that also affects the preparation time. Here, the fidelity with the entangled state drops considerably at increased speed, so that the state preparation of the WS scheme is found to be slow (cf. Ref. [86]). Numerical examples of the performance are also given in Table 4.1.

We conclude that all relevant benchmarks, both static and dynamic are best for the $|S_1\rangle$ scheme that was discussed in detail in Sec. 4.3 and 4.4. Theoretically, this scheme allows for the generation of a maximally-entangled state with fidelities of more than 90% and convergence times of about $10 \mu s$ for present-day cavity experiments.

Yet, for a possible experimental realization of steady-state entanglement in optical cavities in the absence of transversal confinement of the atoms, the cavity-driven schemes $|T_1\rangle$ and $|T_0\rangle$ and the randomly laser-driven $|T_0\rangle/|S_0\rangle$ scheme are more suitable. Despite the lower proportionality factors, these schemes provide preparation of an entangled state with convergence times of a few tens of microseconds at fidelities $\approx 80\%$ with present day optical cavities.

4.7 Summary and realization perspectives

We have performed a detailed study of the dissipative preparation of a highly entangled steady state of two Λ -atoms in a single-mode optical cavity by engineering the naturally occurring sources of noise, spontaneous emission and cavity loss. We have employed the effective operator formalism developed in Chapter 3 to identify and understand the effective decay processes. The schemes we have proposed and analyzed use various engineered effective decay processes of either spontaneous emission or cavity decay to rapidly reach a maximally entangled singlet state as the steady state of the dissipative time evolution at high fidelity. Our schemes are suitable for various experimental situations and require coherent driving by only a single laser field and another microwave or Raman field; in particular we have proposed schemes which work in the absence of trapping of the atoms in the cavity in the transversal direction, some of which are tailored for cavity driving.

In showing that all our schemes provide a favorable scaling of the static error that is linear with the cooperativity of the cavity, we have demonstrated that it is not only possible to produce entanglement dissipatively between two atoms in an optical cavity, but also that the error scaling is improved as compared to unitary protocols for entanglement preparation. These results indicate that the approach of turning detrimental noise sources into resources in a dissipative state preparation scheme has an advantage over other techniques. Studying the speed of the protocol, we have investigated the scaling of the dynamic error and resolved the underlying mechanisms. Building upon these results we have derived the optimal conditions for the rapid preparation of an entangled steady state for a given preparation time.

It should be noted that the mechanisms for dissipative state preparation presented in this chapter can also be applied to systems of emitters coupled to lossy waveguides, which have been briefly described in Sec. 2.4.1. Here, a similar improvement of the error scaling with the system parameters can be achieved. Details can be found in [136].

We consider our study relevant for the demonstration of an entangled steady state by means of dissipation in today's cavity QED experiments. A thorough theoretical understanding of the mechanisms allowing for dissipative state preparation of two atoms in an optical cavity has proven to be important for studies considering other physical systems such as circuit QED in Chapter 5 and trapped ions in Chapter 6, and as a stepping stone for more complicated schemes involving many particles, such as the ones in Chapter 7.

Steady-state entanglement of two superconducting qubits

In the previous chapter we have considered the dissipative preparation of entanglement in cavity QED which is a standard quantum optical system. We now turn to superconducting systems which are solid state systems.

Superconducting systems (cf. Sec. 2.4.1) have proven to be good candidates for the realization of quantum algorithms involving many gate operations [14, 66, 67]. Still, despite impressive reductions of the decoherence [60–65], today’s quantum computation and simulation are still limited to elementary protocols on small scales. Taking the approach of dissipative state preparation (Sec. 2.4.3) is therefore worth considering. The realization of effects similar to the ones in Chapter 4 for superconducting systems raises, however, a number of additional challenges. These are (1) a different energy level diagram, (2) additional, undesired transitions between qubit levels since these are not, as in atomic systems, suppressed by selection rules, and (3) additional decoherence mechanisms acting on the qubit. In addition, the dissipative entangling operation shall be independent of the initial state and reach a highly entangled steady state within reasonable time, also in the presence of imperfections in the setup.

In this chapter we present a scheme for the dissipative preparation of entanglement of two superconducting qubits which fulfills the requirements of a circuit QED system, surmounting the above challenges. Several different state preparation tasks involving dissipation have previously been considered for superconducting systems [110–113]. So far, generation of a maximally entangled steady state of two superconducting qubits coupled through a common resonator has not been demonstrated. The scheme we present in the following is directed towards the high-fidelity generation of such a state.

As detailed in Sec. 5.1, our scheme is specifically designed to exploit (1) the level structure of typical transmon qubits [59], which constitute weakly anharmonic oscillators. The scheme is, however, not particularly restricted to transmons, but can also be applied to phase qubits [137] coupled to a resonator. Utilizing a coherent two-photon drive of a dipole-forbidden transition with a two-tone microwave field similar to Refs. [63, 138], we engineer an effective resonator loss process which deterministically prepares the maximally entangled singlet state

$|S\rangle$, as is described in Sec. 5.2. Here, we also show that (2) the coupling of the resonator to several transitions of the transmon is in fact an advantage, as it provides a transfer from the undesired states to the one from which the target state $|S\rangle$ is prepared. Given that $|S\rangle$ is produced by a time-independent loss process and continuous wave fields, it is a steady state of the dissipative evolution.

In Sec. 5.3 we investigate the performance of our scheme, both analytically, to derive benchmarks for the protocol, and numerically, to verify the mechanisms that underlie the presented dissipative state preparation scheme. Our results show that a maximally entangled state of two superconducting qubits can be prepared rapidly and with a high fidelity, even in the presence of (3) realistic qubit decoherence rates and imperfections. High fidelities are obtained both for state-of-the-art three-dimensional (3D), as well as for the more common two-dimensional (2D) transmons. By fulfilling the above requirements our proposal thus opens a route for the dissipative preparation of maximally entangled states of superconducting systems using existing technology.

5.1 Setup: coherent and dissipative interactions of two coupled transmons

For our study we consider two superconducting transmons [59] coupled to a common resonator in a circuit QED setup. The coherent dynamics of the system is described by a Hamiltonian $H = H_{\text{free}} + H_{\text{cav}} + H_{\text{d}}$. The energy levels are illustrated in Fig. 5.1 a) and described by the free Hamiltonian

$$H_{\text{free}} = \omega_c a^\dagger a + \sum_{j=1,2} (2\omega - 2A) |2\rangle_j \langle 2| + \omega |1\rangle_j \langle 1|, \quad (5.1)$$

with levels $|k\rangle$ of transmon j and the resonator mode a . Here, ω denotes the level spacing of the two lower levels and A the anharmonicity, with $\hbar = 1$. In our analytical discussion we will focus on the first three levels of the transmons, $|0\rangle$, $|1\rangle$ and $|2\rangle$. Our numerical assessment will also include the fourth level, $|3\rangle$. The transitions of the transmons, $|0\rangle \leftrightarrow |1\rangle$ and $|1\rangle \leftrightarrow |2\rangle$, are coupled by the coherent interactions shown in Fig. 5.1 b). They are described by a Hamiltonian $H_{\text{cav}} + H_{\text{d}}$. Here, H_{cav} represents the coupling of the resonator to the transitions of the transmons,

$$H_{\text{cav}} = \sum_{j=1,2} g a^\dagger \left(|0\rangle_j \langle 1| + \sqrt{2} |1\rangle_j \langle 2| \right) + H.c., \quad (5.2)$$

with a coupling constant g , and a factor of $\sqrt{2}$ for the matrix element of the upper transition. The coherent drive

$$H_{\text{d}} = \sum_{j=1,2} \left(\frac{\Omega_1}{2} e^{-i\omega_1 t} + (-1)^j \frac{\Omega_2}{2} e^{-i\omega_2 t} \right) \left(|1\rangle_j \langle 0| + \sqrt{2} |2\rangle_j \langle 1| \right) + H.c.$$

contains several microwave fields which couple the transitions $|0\rangle \leftrightarrow |1\rangle$ and $|1\rangle \leftrightarrow |2\rangle$. We assume that the drive with Ω_1 exhibits an identical phase, whereas the phase of Ω_2 is opposite for the two transmons. This can be achieved by driving the qubits with the field Ω_1 through a common wire and with the field

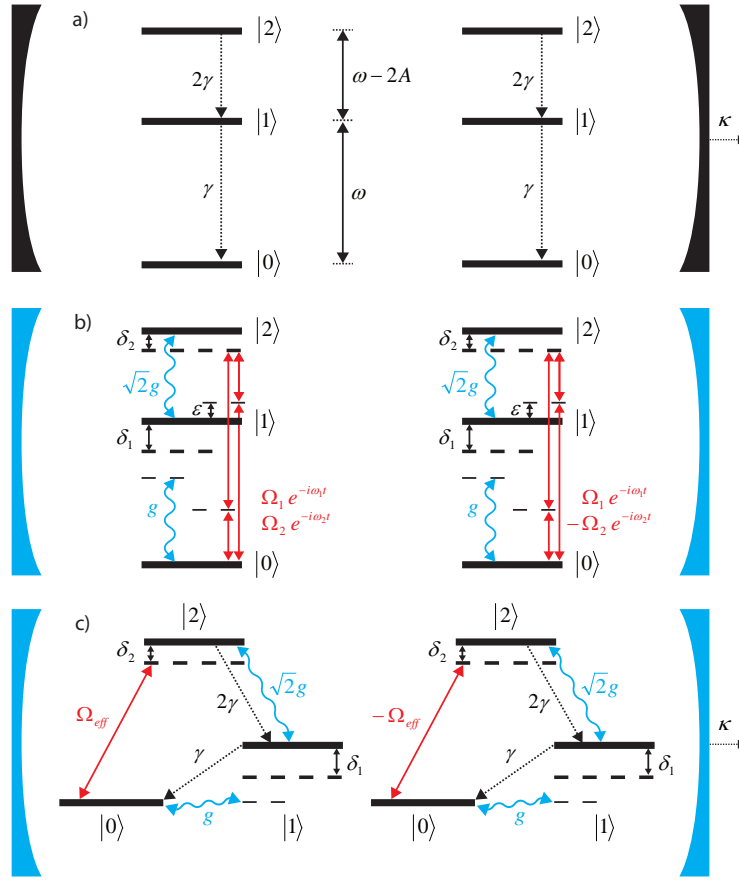


FIGURE 5.1: Setup. The internal levels of two transmons (a) are coupled by coherent interactions (b) to mimic the Λ system in (c). Two microwave fields $\Omega_{1/2}$ provide virtual couplings of the transitions $|0\rangle \leftrightarrow |1\rangle$ and $|1\rangle \leftrightarrow |2\rangle$ (b) which combine to an effective two-photon drive Ω_{eff} of the transition $|0\rangle \leftrightarrow |2\rangle$. The transmon-resonator coupling (g) is resonant with the upper transition and detuned by $\delta_1 - \delta_c$ from the lower transition. Spontaneous emission (γ) and resonator photon loss (κ) are present as decoherence processes. The detunings are defined in the text.

Ω_2 through additional individual wires, similar to Refs. [139–141]. As we will see, this choice of phases allows us to break the symmetry of the system and thereby drive certain transitions which play an important role in our proposal. We choose the frequencies of the two fields in such a way that they combine to an effective two-photon drive of the transition $|0\rangle \leftrightarrow |2\rangle$ with a coupling constant Ω_{eff} that will be derived in Sec. 5.2.1. In doing so, we render the couplings of the system resembling the Λ system shown in Fig. 5.1 c), with (meta-) stable lower levels $|0\rangle$ and $|1\rangle$ and an “excited” level $|2\rangle$ for each of the transmons. “Excitation” from $|0\rangle$ to $|2\rangle$ is then accomplished by the two-photon drive with Ω_{eff} . For most of this chapter, we will assume that the resonator coupling is resonant with the transition $|1\rangle \leftrightarrow |2\rangle$, while being somewhat detuned from the lower transition $|0\rangle \leftrightarrow |1\rangle$.

In the following, we will avoid the fast dynamics in the drive by changing into a

frame rotating with a Hamiltonian

$$H_{\text{rot}} = \bar{\omega} \left(a^\dagger a + \sum_k \sum_{j=1,2} k |k\rangle_j \langle k| \right), \quad (5.3)$$

where $\bar{\omega} \equiv \frac{1}{2}(\omega_1 + \omega_2)$ is the mean frequency of the classical driving fields. Applying a unitary $\mathcal{U} = \exp[iH_{\text{rot}}t]$ we obtain a transformed Hamiltonian $H' = \mathcal{U}H\mathcal{U}^\dagger + i\dot{\mathcal{U}}\mathcal{U}^\dagger = H'_{\text{free}} + H'_{\text{cav}} + H'_d$ in a frame rotating with H_{rot} . The transformed free Hamiltonian can be expressed as

$$H'_{\text{free}} = \delta_c a^\dagger a + \sum_{j=1,2} \delta_1 |1\rangle_j \langle 1| + \delta_2 |2\rangle_j \langle 2|, \quad (5.4)$$

where $\delta_1 = \omega - \bar{\omega}$, $\delta_2 = 2(\omega - \bar{\omega}) - 2A$, and $\delta_c \equiv \omega_c - \bar{\omega}$ denote the energies of the transmons and the resonator in the rotating frame. Furthermore, we obtain the interaction Hamiltonians $H'_{\text{cav}} = H_{\text{cav}}$ for the transmon-resonator coupling and

$$H'_d = \sum_{j=1,2} \left(\frac{\Omega_1}{2} e^{i\Delta_1 t} + (-1)^j \frac{\Omega_2}{2} e^{i\Delta_2 t} \right) (|1\rangle_j \langle 0| + \sqrt{2}|2\rangle_j \langle 1|) + H.c. \quad (5.5)$$

for the drive. With this choice of the reference frame rotating with the mean frequency, we find the detunings of the microwave fields $\Delta_{1/2} \equiv \bar{\omega} - \omega_{1/2} = \pm \frac{1}{2}(\omega_2 - \omega_1)$.

In addition to the coherent dynamics discussed so far, the system also exhibits dissipative couplings, which is essential for the dissipative state preparation mechanisms we would like to engineer. The dissipative dynamics of the open system is determined by its coupling to the bath and the properties of the bath. Assuming the bath to be Markovian, the system dynamics is governed by a master equation of Lindblad form,

$$\dot{\rho} = i[\rho, H] + \sum_k L_k \rho L_k^\dagger - \frac{1}{2} \left(L_k^\dagger L_k \rho + \rho L_k^\dagger L_k \right), \quad (5.6)$$

with one Lindblad operator L_k for each physical decay process present in the system. As illustrated in Fig. 5.1 a), we assume that transmon j undergoes spontaneous decay which in the transmon regime can be described by

$$L_{\gamma 1, j} = \sqrt{\gamma} |0\rangle_j \langle 1|, \quad (5.7)$$

$$L_{\gamma 2, j} = \sqrt{2\gamma} |1\rangle_j \langle 2|. \quad (5.8)$$

For simplicity we restrict ourselves to only considering decay and neglect dephasing in our calculations unless explicitly mentioned. As we will argue and numerically verify below, the exact nature of the decoherence only plays a minor role for our proposal. The photon loss out of the resonator is described by

$$L_\kappa = \sqrt{\kappa} a, \quad (5.9)$$

where κ is the photon loss rate.

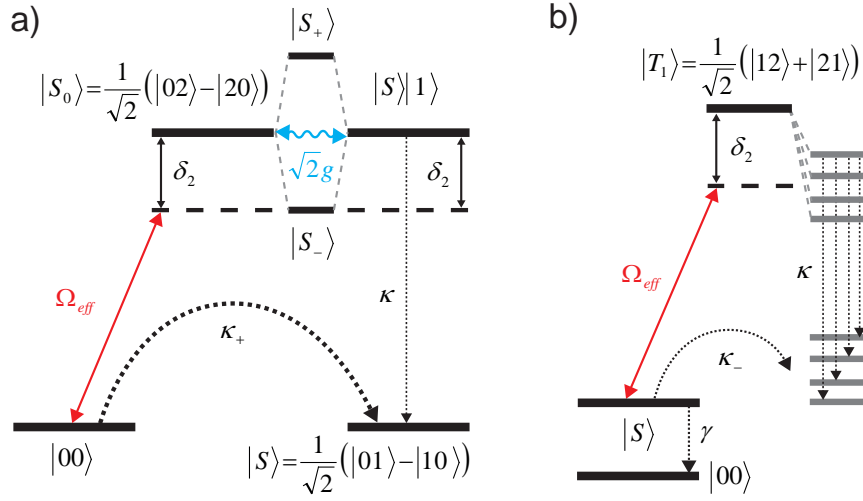


FIGURE 5.2: Dissipative state preparation mechanism and loss mechanism. (a) Effective resonator decay from $|00\rangle$ into $|S\rangle$ involves coherent coupling to $|S_0\rangle$. $|S_0\rangle$ and $|S\rangle|1\rangle$ are strongly coupled ($\sqrt{2}g$) so that these states hybridize and form dressed states $|S_{\pm}\rangle$ (shown here for a choice of $\delta_c = \delta_2 - \delta_1$, by which the resonator is resonant with the upper transition). By setting $\delta_2 = \sqrt{2}g$ the driving from $|00\rangle$ is resonant with the lower dressed state $|S_-\rangle$. Population from $|00\rangle$ is thus rapidly excited and decays into $|S\rangle$ via the effective engineered resonator decay κ_+ . (b) The two-photon drive also causes an undesired coupling of the otherwise dark target state $|S\rangle$ to an excited state $|T_1\rangle$. $|T_1\rangle$, in turn, couples to a number of (resonator-) excited states which form dressed states at different energies (indicated) and eventually decay to other states. These can generally be made off-resonant with the drive from $|S\rangle$ by an appropriate choice of the resonator and microwave detunings so that the effective resonator decay κ_- from $|S\rangle$ is suppressed. In addition, since $|S\rangle$ is a dark state of the cavity interaction, the only direct decay mechanism is through the weak qubit decay γ to $|00\rangle$.

Due to our choice of the couplings similar to a Λ configuration, most of the dynamics will happen in the two lower levels. To describe them we choose a two-atom basis with triplet states $|00\rangle = |0\rangle_1|0\rangle_2$, $|11\rangle$, $|T\rangle = \frac{1}{\sqrt{2}}(|01\rangle + |10\rangle)$, and the singlet state $|S\rangle = \frac{1}{\sqrt{2}}(|01\rangle - |10\rangle)$ as the desired entangled steady state. For the detailed discussion of the engineered decay processes, we also introduce the excited atomic states $|T_0\rangle = \frac{1}{\sqrt{2}}(|02\rangle + |20\rangle)$, $|S_0\rangle = \frac{1}{\sqrt{2}}(|02\rangle - |20\rangle)$, $|T_1\rangle = \frac{1}{\sqrt{2}}(|12\rangle + |21\rangle)$ and $|S_1\rangle = \frac{1}{\sqrt{2}}(|12\rangle - |21\rangle)$. The presence of resonator excitations is indicated by a second ket vector, e.g. $|00\rangle|1\rangle$. For simplicity we omit this ket vector when the resonator is in the vacuum state. We use this notation to explain the mechanisms of our scheme in Sec. 5.2 below.

5.2 Mechanisms for dissipative preparation of the maximally entangled singlet state

In this section we will show how to engineer effective decay processes which prepare a steady state close to the maximally entangled singlet state $|S\rangle$. For now, we will focus our discussion on the physical mechanisms behind the effec-

tive decay processes, while Sec. 5.2.1 and 5.2.2 will deal with the derivation of quantitative expressions for the effective operators and rates.

The mechanism of our scheme is illustrated in Fig. 5.2 a). The working principle is as follows: Since the singlet state $|S\rangle$ is a dark state of the resonator interaction, it can only gain or lose population by effective decay mechanisms mediated by the weak coherent drives or through the slow decay by the weak qubit decoherence. A strong asymmetry between the rapid decay into $|S\rangle$ and the slow loss processes out of it results in the dissipative preparation of $|S\rangle$ with high fidelity. In the following, we will discuss the physical mechanism for the preparation of $|S\rangle$.

In the previous section we have introduced a coherent driving H_d . The purpose of it is to drive a two-photon transition $|0\rangle \leftrightarrow |2\rangle$. For now, we will assume that we have a coherent drive of $|0\rangle \leftrightarrow |2\rangle$ with a coupling constant Ω_{eff} and defer the derivation to later. Due to the opposite phase of Ω_2 on the two transmons, this drive then couples $|00\rangle$ to an excited state $|S_0\rangle$ with a detuning δ_2 , as can be seen from Fig. 5.2 a). $|S_0\rangle$ is in turn coupled to $|S\rangle|1\rangle$ by the resonator coupling H_{cav} . From here, $|S\rangle|1\rangle$ decays into $|S\rangle$ via resonator decay at a rate κ . These processes combine to an effective resonator decay process from $|00\rangle$ into $|S\rangle$ with a rate κ_+ .

In order to engineer this process to be as strong as possible we have to fulfill two requirements: First, we need to make sure that the coupling of the transmon-excited state $|S_0\rangle$ to the resonator-excited state $|S\rangle|1\rangle$ is close to resonance, given that only the latter can decay to $|S\rangle$ through resonator photon loss. To this end, we set the resonator into or close to resonance with the upper transition of the transmons, $|2\rangle \leftrightarrow |1\rangle|1\rangle$. This is reached by choosing $\omega_c = \omega - 2A$ ($\delta_c = \delta_2 - \delta_1$), and results in an equal energy of $|S_0\rangle$ and $|S\rangle|1\rangle$, as shown in Fig. 5.2 a). The two states hybridize and form dressed states

$$|S_{\pm}\rangle = \frac{1}{\sqrt{2}} (|S_0\rangle \pm |S\rangle|1\rangle), \quad (5.10)$$

located at frequencies of $2\omega - 2A \pm \sqrt{2}g$ (or $\delta_2 \pm \sqrt{2}g$).

The second requirement is that the two-photon drive from $|00\rangle$ is resonant with one of the dressed states in Eq. (5.10). Choosing a detuning $\delta_2 = \sqrt{2}g$, we tune the drive into resonance with the transition from $|00\rangle$ to $|S_-\rangle$. Population from $|00\rangle$ is then rapidly excited to $|S_-\rangle$, which, through its contribution from $|S\rangle|1\rangle$, decays into $|S\rangle$. For a strong resonant drive, the resulting effective decay process is only limited by the line width $\frac{\kappa}{2}$ of $|S_-\rangle$, the state which mediates it. Thus, the dissipative preparation mechanism of the singlet and its rate κ_+ can be engineered to be rather large.

Loss from the singlet can occur through the couplings of $|S\rangle$ to any excited state other than $|S_0\rangle$ by the available microwave fields, e.g. to $|T_1\rangle$ by Ω_{eff} . As indicated in Fig. 5.2 b), these excited states are coupled to a number of other, in particular resonator-excited states. For instance $|T_1\rangle$ couples to $|11\rangle|1\rangle$, $|T_0\rangle|1\rangle$, $|T\rangle|2\rangle$, and $|00\rangle|3\rangle$. Consequently, this establishes a loss channel from $|S\rangle$ through effective resonator decay, e.g. into $|11\rangle$, which causes losses at a rate κ_- from the desired steady state $|S\rangle$. Fortunately, the photon-number dependent

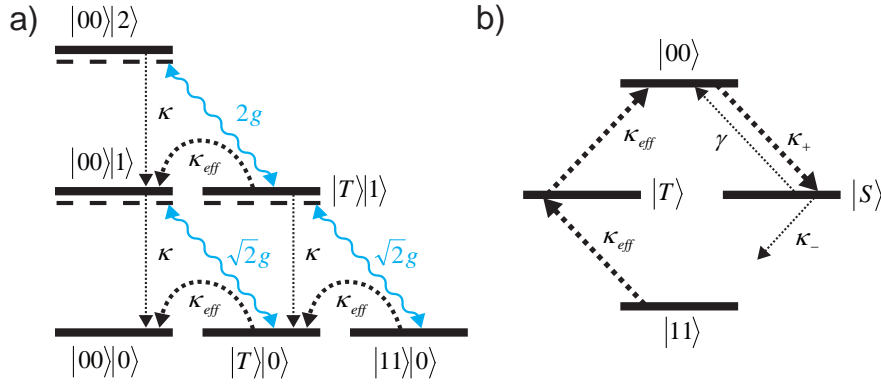


FIGURE 5.3: (a) Shuffling mechanism and (b) effective lower-level decay processes. (b) The population of the bright states $|11\rangle$ and $|T\rangle$ is shuffled to $|00\rangle|0\rangle$ by the resonator coupling g and successive resonator decay at an effective rate κ_{eff} . The effective decay processes of the lower levels shown in (a) and in Fig. 5.2 are summarized in (d).

coupling strength between transmons and resonator provides us with a non-equidistant spectrum which consequently makes it possible to have the two-photon drive resonant with the transition from $|00\rangle$ to $|S_{-}\rangle$ while keeping it off-resonant with the transitions from $|S\rangle$ to other hybridized excited states. In this way, loss processes from the singlet are suppressed by their detunings.

In order to reach $|S\rangle$ independently from the initial state and to maintain it as the steady state, an additional mechanism is required to transfer population from lower states other than $|00\rangle$, i.e. from $|T\rangle$ and $|11\rangle$, to $|S\rangle$. So far, we have assumed that the resonator is resonant with the upper transition. This means that due to the anharmonicity, the resonator is off-resonant with the lower transition. For reasonable anharmonicities the off-resonant coupling is, however, still sufficient to allow a reshuffling of population from the bright states $|11\rangle$ and $|T\rangle$ to $|00\rangle$, while $|S\rangle$ as the dark state of the resonator coupling remains unaffected. As shown in Fig. 5.3 a), this reshuffling process involves the resonator coupling of the lower transition ($\sqrt{2}g$), e.g. $|T\rangle \leftrightarrow |00\rangle|1\rangle$, and decay of a resonator excitation at a rate κ . It can be seen as an effective decay process with a decay rate $\kappa_{\text{eff}} = 2\kappa g^2 / [2g^2 + (\delta_c - \delta_1)^2/2 + \kappa^2/4]$. This expression contains both limiting cases, where one can either eliminate the resonator-excited states, or where the ground states can be seen as dressed states with resonator-excited states, for instance the triplet states

$$|T_{\pm}\rangle = \frac{1}{\sqrt{2}} (|T\rangle \pm |00\rangle|1\rangle), \quad (5.11)$$

which decay towards $|00\rangle$ at rates $\propto \kappa$. Ideally, the reshuffling mechanism rapidly transfers the population of the triplet states to $|00\rangle$, from where they decay into $|S\rangle$ by the dissipative preparation mechanism discussed above. The fastest reshuffling is reached by tuning the resonator into resonance with the lower transition, i.e. $\delta_c = \delta_1$. This choice is, however, different from the above choice of $\delta_c = \delta_2 - \delta_1$ which optimizes the dissipative state preparation process. With this choice of the resonator frequency we get $\kappa_{\text{eff}} = 2\kappa g^2 / [2g^2 + 2A^2 + \kappa^2/4]$, from

which we see that the reshuffling works best for small anharmonicity A . For larger A the process becomes less effective. Having both processes, state preparation and reshuffling, simultaneously active might therefore seem problematic for large anharmonicities. However, as we shall see below, the scheme can still be effective for large A if we allow for longer time for the reshuffling. Furthermore, as is also addressed below, the two requirements for δ_c above are far less critical than the resonant set-up of the two-photon drive. Consequently, both processes, the dissipative state preparation and the reshuffling, can be effective at the same time over a wide parameter range, as we will numerically demonstrate in Sec. 5.3.

In addition to effective resonator decay, qubit decoherence present in the system can cause loss from the singlet independent of the drives. Most notably, it can cause a loss from $|S\rangle$ into $|00\rangle$, as shown in Fig. 5.2 b). The presented mechanisms are summarized in Fig. 5.3 b): On the left hand side we see the reshuffling mechanisms enabled by the resonator coupling to the lower transition, represented by κ_{eff} , and on the right hand side the state preparation (κ_+) and loss (κ_-) mechanisms affecting the singlet state, as well as the decay from $|S\rangle$ by qubit decoherence at a rate γ .

To sum up this section, we have identified suitable mechanisms for the dissipative preparation of the singlet state and discussed the physical effects behind them. In the following two sections we will analytically derive the couplings and the rates for the effective coherent and dissipative processes in our scheme. Based on these, we derive benchmarks for the performance of the scheme in Sec. 5.3.

5.2.1 Effective coherent driving of the dipole-forbidden transition $|0\rangle \leftrightarrow |2\rangle$ by a two-photon process

The implementation of the dissipative state preparation scheme discussed above requires a coherent coupling of the transition $|0\rangle \leftrightarrow |2\rangle$. Since this transition is dipole-forbidden, such a coupling cannot be accomplished in a single step. One way to overcome this is to use a two-photon process, achieved by the combination of two individual fields. In \hat{H}_d we have chosen two such fields, Ω_1 and Ω_2 . As we will derive in the following, these provide complementary virtual single-photon excitations which form the desired coupling.

In the following, we will apply the effective operator formalism presented in Chapter 3 to obtain a simple effective Hamiltonian for a single transmon with a two-photon drive. Here, we separate the Hamiltonian into a perturbative part $V(t) = H_d$, which contains the fields, and a perturbed part $H_0 = H'_{\text{free}} - \delta_c a^\dagger a$. (Note that the derivation below is for a single transmon only. With this in mind, the reuse of Hamiltonian definitions should not cause any confusion.) While in Chapter 3 only effective processes with an initial excitation are considered, here we also allow for an initial deexcitation. We therefore set up the effective

Hamiltonian as $H_{\text{eff}} = H_{\text{eff}}^{(+)} + H_{\text{eff}}^{(-)}$ with

$$H_{\text{eff}}^{(\pm)} = -\frac{1}{2}V(t) \sum_{f=1}^2 \sum_{k=0}^2 \left(H_0^{(k,f,\pm)} \right)^{-1} V_{\pm}^{(k,f)}(t) + H.c., \quad (5.12)$$

Here, we have applied the most general form of the operator formalism presented in Sec. 3.3.7, where we specify the initial state k and the field f of the perturbation $V_{\pm}^{(k,f)}$ and the unperturbed Hamiltonian $H_0^{(k,f,\pm)}$. The latter is defined as $H'_{\text{free}} \pm \Delta_f - \omega_k$ and contains ω_k as the frequency of level $k \in \{0,1,2\}$ and Δ_f as the detuning of field $f \in \{1,2\}$. We use a projector $P_k = |k\rangle\langle k|$ on the levels k to identify coherent drive terms $V_{\pm}^{(k,f)} = V^{(f)}P_k$ starting from an initial state k . The superscript $f \in \{1,2\}$ is used to split $V(t)$ into $V_{\pm}^{(k,1)}$ for those terms which depend on Ω_1 and $V_{\pm}^{(k,2)}$ for the ones with Ω_2 ; a sign (\pm) denotes whether the initial process is an excitation $(+)$, i.e. a term containing a factor $e^{-i\omega_f t}$, or a de-excitation $(-)$, with a factor $e^{+i\omega_f t}$.

Using this formalism we find a considerable number of terms, time-independent and -dependent ones, some closer to resonance and others stronger detuned. Neglecting the time-varying terms rotating at twice a detuning $\Delta_{1/2}$ we obtain the effective two-photon Hamiltonian

$$\begin{aligned} H_{\text{eff}} \approx & \sum_{j=1}^2 \sum_{f=1}^2 \frac{\Omega_1^2}{4(\delta_1 + \Delta_f)} (|1\rangle_j\langle 1| - |0\rangle_j\langle 0|) - \frac{(-1)^j \Omega_1 \Omega_2}{4\sqrt{2}(\delta_1 + \Delta_f)} (|2\rangle_j\langle 0| + |0\rangle_j\langle 2|) \\ & + \frac{\Omega_f^2}{2(\delta_1 - \delta_2 - \Delta_f)} (|1\rangle_j\langle 1| - |2\rangle_j\langle 2|) - \frac{(-1)^j \Omega_1 \Omega_2}{4\sqrt{2}(\delta_1 - \delta_2 - \Delta_f)} (|2\rangle_j\langle 0| + |0\rangle_j\langle 2|) \end{aligned} \quad (5.13)$$

Setting the detunings of the fields to $\Delta_{1/2} = \mp(\delta_1 + \epsilon)$ we have that $\Delta_1 + \Delta_2 = 0$ and keep a certain virtual character of the single fields by a detuning $\pm\epsilon$, as shown in Fig. 5.1 b). In this configuration, there exists an effective two-photon drive where the first field (with Ω_1) drives the lower transition $|0\rangle \leftrightarrow |1\rangle$ and the second field (with Ω_2) drives the upper transition. Expressing the resulting effective Hamiltonian in terms of the anharmonicity (using $\delta_1 = \frac{\delta_2}{2} - A$) we obtain

$$\begin{aligned} H_{\text{eff}} \approx & \sum_{j=1,2} \left(\frac{\Omega_1^2}{4\epsilon} - \frac{\Omega_2^2}{4(2A + \delta_2 + \epsilon)} \right) (|0\rangle_j\langle 0| - |1\rangle_j\langle 1|) \\ & + \left(-\frac{\Omega_2^2}{2(\delta_2 + \epsilon)} + \frac{\Omega_1^2}{2(2A + \epsilon)} \right) (|1\rangle_j\langle 1| - |2\rangle_j\langle 2|) \\ & + \frac{\Omega_{\text{eff}}}{2} (-1)^j (|2\rangle_j\langle 0| + |0\rangle_j\langle 2|) \end{aligned} \quad (5.14)$$

with an effective two-photon Rabi frequency

$$\begin{aligned} \Omega_{\text{eff}} &= \frac{\Omega_1 \Omega_2}{2\sqrt{2}} \left(\frac{1}{\epsilon} + \frac{1}{\delta_2 + \epsilon} - \frac{1}{2A + \epsilon} - \frac{1}{2A + \delta_2 + \epsilon} \right) \\ &= \frac{\Omega_1 \Omega_2}{2\sqrt{2}} \frac{2A\delta_2[2(A - \epsilon) + \delta_2]}{\epsilon(\delta_2 + \epsilon)(2A + \epsilon)(2A + \delta_2 + \epsilon)}. \end{aligned} \quad (5.15)$$

From here we see that for the case of zero anharmonicity $A = 0$, i.e. for harmonic transmons, no effective two photon drive is possible. For $A \neq 0$, however, there exists a possibility of driving the transition $|0\rangle \leftrightarrow |2\rangle$. Note that the remaining diagonal terms in Eq. (5.14) represent shifts which can be compensated by suitable (minor) detunings of the fields. Their effect on Eq. (5.14) can be considered very small so that H_{eff} is approximately given by a single coherent coupling of the transition $|0\rangle \leftrightarrow |2\rangle$,

$$H_{\text{d,eff}} = \sum_{j=1,2} \frac{\Omega_{\text{eff}}}{2} (-1)^j |2\rangle_j \langle 0| + H.c. \quad (5.16)$$

We have thus obtained the coupling constant Ω_{eff} of the effective two-photon coupling we introduced in Sec. 5.1. With this result we can turn to the derivation of the effective Lindblad operators for the engineered decay mechanisms used for the preparation of the singlet state.

5.2.2 Engineered decay processes and their effective Lindblad operators

To model the effective, dissipative evolution we use the effective formalism of Chapter 3 to derive the effective Lindblad operators

$$L_{\text{eff}}^m = L_m \sum_k \sum_f \left(H_{\text{NH}}^{(k,f)} \right)^{-1} V^{(k,f)}(t), \quad (5.17)$$

with the perturbative coherent excitation $V^{(k,f)}(t)$ from an initial state k by a field f . In addition, we derive a non-Hermitian Hamiltonian

$$H_{\text{NH}}^{(k,f)} = H_0^{(k,f)} - \frac{i}{2} \sum_n L_n^\dagger L_n, \quad (5.18)$$

with the perturbed Hamiltonian $H_0^{(k,f)}$ defined previously. We focus on the effective resonator decay process activated by the two-photon drive H_{eff} and followed by decay of a resonator excitation L_κ . With $H_0 = H'_{\text{free}} + H'_{\text{cav}}$, $V(t) = H_{\text{eff}}$ ($\Omega \ll \delta_2$), and $L_m = L_\kappa$ we arrive at an effective Lindblad operator

$$L_{\text{eff}}^\kappa \approx \sqrt{\kappa_+} |S\rangle \langle 00| + \sum_j \sqrt{\kappa_j^-} |\phi_j\rangle \langle S|, \quad (5.19)$$

with effective decay rates κ_+ and κ_j^- . This operator represents the dissipative mechanism we engineer to rapidly prepare the singlet state $|S\rangle$ from $|00\rangle$. In addition, it includes the loss processes at rates κ_j^- from $|S\rangle$ into other states $|\phi_j\rangle \in \{|11\rangle, |T_0\rangle, |T, 1\rangle, |00, 2\rangle\}$. Note that here we have ignored some less important terms as their effect on the population of the singlet is small.

We calculate κ_+ of Eq. (5.19), using the driving from $|00\rangle$ to $|S_0\rangle$ as given by Eq. (5.16), with a matrix element of $\frac{\Omega_{\text{eff}}}{\sqrt{2}}$. The dynamics of the excited state $|S_0\rangle$ is described by the non-Hermitian Hamiltonian in Eq. (5.18) which couples $|S_0\rangle$ to $|S\rangle|1\rangle$ through the resonator interaction H'_{cav} , forming a coupled subspace. For the non-Hermitian Hamiltonian $H_{\text{NH}}^{(00), \Omega_{\text{eff}}}$ of this subspace which contains $|S_0\rangle$

and is reached by excitation from $|S\rangle$ with the two-photon drive H_{eff} , we define $H_{S_0} \equiv H_{\text{NH}}^{(|00\rangle, \Omega_{\text{eff}})}$ with

$$H_{S_0} = \tilde{\delta}_2 |S_0\rangle\langle S_0| + (\tilde{\delta}_1 + \tilde{\delta}_c) |S\rangle\langle 1| \langle 1| \langle S| + \sqrt{2}g (|S\rangle\langle 1| \langle S_0| + H.c.). \quad (5.20)$$

In order to keep the notation compact, we have written the Hamiltonian in terms of the complex detunings $\tilde{\delta}_j = \delta_j - \frac{ij\gamma}{2}$ and $\tilde{\delta}_c = \delta_c - \frac{i\kappa}{2}$ combining the energy with the imaginary line width of the levels. For the inverted operator we find

$$H_{S_0}^{-1} = \tilde{\delta}_{2,\text{eff}}^{-1} |S_0\rangle\langle S_0| + \tilde{\delta}_{1c,\text{eff}}^{-1} |S\rangle\langle 1| \langle 1| \langle S| + \tilde{g}_{\text{eff}}^{-1} (|S\rangle\langle 1| \langle S_0| + H.c.). \quad (5.21)$$

Here, we have introduced effective detunings $\delta_{2,\text{eff}} = \tilde{\delta}_2 - \frac{2g^2}{\tilde{\delta}_2}$ and $\delta_{1c,\text{eff}} = (\tilde{\delta}_1 + \tilde{\delta}_c) - \frac{2g^2}{\tilde{\delta}_1 + \tilde{\delta}_c}$, and an effective coupling constant $\tilde{g}_{\text{eff}} = \sqrt{2}g - \frac{\tilde{\delta}_2(\tilde{\delta}_1 + \tilde{\delta}_c)}{\sqrt{2}g}$. Since the rate for resonator decay from $|S\rangle\langle 1|$ into $|S\rangle$ is given by κ , we generally find an effective decay of $\kappa_+ = \frac{\kappa\Omega_{\text{eff}}^2}{2|\tilde{g}_{\text{eff}}|^2}$ from $|00\rangle$ to $|S\rangle$, concluding that the effective coupling rate \tilde{g}_{eff} governs the strength of the engineered decay process.

The decay rate κ_+ is maximized by a parameter choice of $\delta_2 = \sqrt{2}g$ and $\delta_c = \delta_2 - \delta_1$, which corresponds to the two-photon drive from $|00\rangle$ being in resonance with $|S_0\rangle$ and the resonator being resonant with the upper transition. We then obtain $\tilde{g}_{\text{eff}} \approx \frac{i\kappa}{2}$, and thus $\kappa_+ \approx \frac{\Omega_{\text{eff}}^2}{\kappa}$. In Sec. 5.3 we will make use of this result to derive the error and the speed of the protocol.

We now turn to the effective loss processes κ_j^- as they appear in Eq. (5.19). Given that $|S\rangle$ is a dark state of the resonator coupling, these rates can be calculated using the same procedure we applied for the derivation of κ_+ above: As $|S\rangle$ is coupled to $|T_1\rangle$ by the two-photon drive we need to consider the non-Hermitian Hamiltonian $H_{T_1} \equiv H_{\text{NH}}^{(|S\rangle, \Omega_{\text{eff}})}$ which describes the subspace consisting of $|T_1\rangle$ and the states coupled to it by H'_{cav} . For low anharmonicities $A \lesssim \delta_2$, H_{NH,T_1} needs to reflect the full complexity of the coupled subspace containing $|T_1\rangle$, $|11\rangle|1\rangle$, $|T_0\rangle|1\rangle$, $|T\rangle|2\rangle$ and $|00\rangle|3\rangle$. For anharmonicities of $A \gtrsim \delta_2$, however, the subspace of $|T_1\rangle$ and $|11\rangle|1\rangle$ begins to decouple from the other states so that the dynamics of the excited states can be approximated using only $|T_1\rangle$ and $|11\rangle|1\rangle$. The Lindblad operator of Eq. (5.19) for the effective resonator decay then reduces to

$$L_{\text{eff}}^\kappa \approx \sqrt{\kappa_+} |S\rangle\langle 00| + \sqrt{\kappa_-} |11\rangle\langle S|, \quad (5.22)$$

containing a single loss rate $\kappa_- = \kappa_{|11\rangle}^-$ from $|S\rangle$ into $|11\rangle$.

To derive κ_- , we approximate H_{NH,T_1} by the non-Hermitian Hamiltonian of the excited subspace consisting of $|T_1\rangle$ and $|11\rangle|1\rangle$,

$$H_{T_1} \approx \tilde{\delta}_2 |T_1\rangle\langle T_1| + (\tilde{\delta}_1 + \tilde{\delta}_c) |11\rangle\langle 1| \langle 1| \langle 11| + 2g (|11\rangle\langle 1| \langle T_1| + H.c.), \quad (5.23)$$

using the complex detunings defined above. The inverted operator is then given by

$$H_{T_1}^{-1} \approx \tilde{\delta}_{2,\text{eff}}^{-1} |T_1\rangle\langle T_1| + \tilde{\delta}_{1c,\text{eff}}^{-1} |11\rangle\langle 1| \langle 1| \langle T| + \tilde{g}_{2,\text{eff}}^{-1} (|11\rangle\langle 1| \langle T_1| + H.c.). \quad (5.24)$$

Here, we have found effective detunings $\delta_{2,\text{eff},T_1} = \tilde{\delta}_2 - \frac{4g^2}{\delta_2}$ and $\delta_{1c,\text{eff},T_1} = (\tilde{\delta}_1 + \tilde{\delta}_c) - \frac{4g^2}{\tilde{\delta}_1 + \tilde{\delta}_c}$, and an effective coupling constant $\tilde{g}_{\text{eff},T_1} = 2g - \frac{\tilde{\delta}_2(\tilde{\delta}_1 + \tilde{\delta}_c)}{2g}$, which are different from the ones in the previous case of $|S_0\rangle$. With a decay rate κ from $|11\rangle|1\rangle$ into $|11\rangle$, we obtain an effective decay rate $\kappa_- \approx \frac{\kappa\Omega_{\text{eff}}^2}{|\tilde{g}_{\text{eff},T_1}|^2}$ for the losses from $|S\rangle$. For the above choice of δ_2 and δ_c , the effective coupling constant becomes $\tilde{g}_{\text{eff},T_1} \approx g$ which results in $\kappa_- \approx \frac{\kappa\Omega_{\text{eff}}^2}{4g^2}$. From here we conclude that for $\kappa^2 \ll g^2$ the effective loss rate κ_- from the singlet is engineered to be much smaller than its preparation rate $\kappa_+ \approx \frac{\Omega_{\text{eff}}^2}{2\kappa}$. These results confirm the explanations in Sec. 5.2.

Note that, on the one hand, the above treatment of the coupled excited subspace where we restrict the excited state subspace to $|T_1\rangle$ and $|11\rangle|1\rangle$ is quite simplistic, given that it reduces the number of resonances from five to only two. In particular, one needs to ensure that one does not hit an accidental resonance with one of the dressed states of the system. On the other hand, the parameter space consisting of δ_c , δ_2 and ϵ is sufficiently big to avoid an excitation of the remaining undesired resonances as there are sufficiently many suitable points in different regions of parameter space for which all of these resonances are off-resonant with the two-photon drive. In Fig. 5.4, we draw the dressed states of the coupled resonator-transmon system. Here, the single-photon fields are tuned to resonantly excite the transition $|00\rangle \leftrightarrow |S_- \rangle$ by a two-photon transition, mediated by the triplet state $|T\rangle$. The same two-photon drive also couples $|S\rangle$ to a number of dressed states with contributions from $|T_1\rangle$. These transitions, however, generally have different frequencies than the desired one from $|00\rangle$ to $|S_- \rangle$ so that excitation of $|S\rangle$ by the drive Ω_{eff} is off-resonant and suppressed by its detuning from the dressed states. This can be seen from Fig. 5.4, where we draw the dressed states together with the two-photon drive for the choice of $\delta_c = \delta_2 - \delta_1$. In the figure, we show an example near $A = \frac{3g}{2}$ where the driving is off-resonant with the excited states which contain contributions from $|T_1\rangle$. We also draw an example at $A \approx 2g$ where this is not the case and where a resonance is hit accidentally. Here, it is necessary to choose a different detuning δ_c . Below, we will verify by numerical simulation for a broad parameter range that it is always possible to avoid such resonances.

In addition to losses caused by the two-photon drive, also the individual fields Ω_1 and Ω_2 couple $|S\rangle$ to other states. The coupling of the even-phase single-photon drive Ω_1 from $|S\rangle$ to $|S_0\rangle$ does not cause any significant loss from $|S\rangle$, since population in $|S_0\rangle$ is recycled via $|S\rangle|1\rangle$ back into $|S\rangle$. The odd-phase single-photon drive Ω_2 , on the other hand, couples $|S\rangle$ to $|00\rangle$ and to a superposition state $\frac{1}{\sqrt{2}}(|11\rangle - |T_0\rangle)$. Both these states are dark states of the resonator coupling. Thus, no exchange excitation to a resonator-excited state can shift them into resonance with the off-resonant drive Ω_2 from $|S\rangle$ and no effective resonator decay process from $|S\rangle$ is established involving them. Accumulation in these states does not occur, either, given that $\frac{1}{\sqrt{2}}(|11\rangle - |T_0\rangle)$ decays through qubit decoherence and $|00\rangle$ decays into $|S\rangle$ as discussed earlier. As a consequence, neither of the two drives causes significant loss from the singlet.

Another source of errors emerges for small anharmonicities $A \lesssim \delta_2$ from the

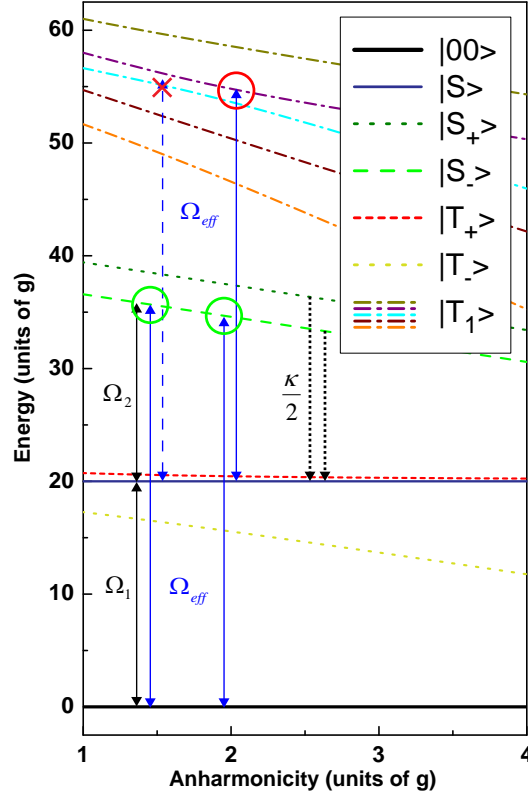


FIGURE 5.4: Dressed state energy vs. anharmonicity. An effective two-photon drive Ω_{eff} from $|00\rangle$ (solid black line) to $|S_{-}\rangle$ (green dashed) is implemented as two consecutive single-photon excitations by two microwave fields, Ω_1 and Ω_2 . The individual drives are mediated by $|T_{+}\rangle$ (short-dashed red), which is a dressed state of $|T\rangle$, and made virtual through a detuning ϵ (not shown). The two virtual excitations combine to an effective drive Ω_{eff} resonant with the transition $|00\rangle \leftrightarrow |S_{-}\rangle$; $|S_{-}\rangle$ then decays into $|S\rangle$ (indicated). The same field couples to the transition from $|S\rangle$ to the dressed states of $|T_1\rangle$ (dashed-dotted). By an appropriate choice of the oscillator detuning δ_c (here plotted for $\delta_c = \delta_2 - \delta_1$ with $\omega = 20g$), this coupling to $|T_1\rangle$ is made off-resonant (left set of arrows). In case that $|T_1\rangle$ is hit by the drive (right set of arrows), δ_c needs to be chosen differently to make the coupling off-resonant.

coherent coupling of $|S\rangle$ to other states like $|00\rangle$ by the single-photon drives Ω_1 and Ω_2 . However, for $A \gtrsim \delta_2$, these couplings are sufficiently detuned to be ignored. Also, beside effective resonator decay processes, qubit decoherence occurs according to Eqs. (5.7)-(5.8). Provided that the decay rate γ is much weaker than all other physical couplings present in the system, i.e. $\gamma \ll \kappa, g$, effective processes combining qubit decoherence with coherent excitation can be safely neglected.

We conclude that the sources of error originating from effective resonator decay which can cause losses from the singlet state are suppressed for the right parameter choice. These processes are, together with the engineered dissipative state preparation process, contained in the effective resonator decay operator in Eq. (5.22).

5.3 Parameter and performance analysis, imperfections and realization aspects

In the previous section we have identified the effective coherent and dissipative processes which are relevant for our dissipative state preparation scheme and investigated the corresponding Lindblad operators and rates. In this section, we will use these results to derive approximate expressions for the error and speed of the presented protocol as the main benchmarks for our scheme. Later, we will examine the temporal evolution of the system numerically.

5.3.1 Error and speed of the protocol

In the previous section we have derived the effective resonator decay operator L_{eff}^κ , given in Eq. (5.22), which describes both the preparation of the singlet state $|S\rangle$ and the inherent losses of our scheme. The derivation of Eq. (5.22) was carried out in the limit of weak driving. As we will find numerically below, the dissipative preparation of the singlet at a rate $\kappa_+ \approx \frac{\Omega_{\text{eff}}^2}{2\kappa}$ works well for a driving strength up to $\Omega_{\text{eff}} \approx \frac{\kappa}{8}$, which yields a preparation rate $\kappa_+ \approx \frac{\kappa}{128}$ for the singlet state $|S\rangle$ and a loss rate $\kappa_- \approx \frac{\kappa^3}{256g^2}$ from it. In addition, $|S\rangle$ decays at a rate γ , as described by the operators in Eq. (5.7)-(5.8).

Based on these rates we can approximate the temporal dynamics for weak driving using rate equations of the populations $P_i \equiv \langle \psi_i | \rho | \psi_i \rangle$. We assume that the reshuffling mechanism rapidly transfers all population from the triplet states to the state $|00\rangle$, which is correct for small anharmonicity A . The evolution of the population of the singlet P_S can then be described by a single rate equation,

$$\dot{P}_S = \kappa_+ P_{00} - (\kappa_- + \gamma) P_S, \quad (5.25)$$

formulated in terms of the decay rates specified above. Note that in this limit it is only the total decay rate out of the singlet state which matters, since any population lost from it is rapidly reshuffled to the $|00\rangle$ state regardless of the nature of the loss. Hence additional decoherence mechanisms, e.g. dephasing causing decay from $|S\rangle$ to $|T\rangle$, can easily be incorporated by replacing γ by an appropriate total loss rate from the singlet. By simply comparing the gain and loss of the singlet in the steady state, i.e. $\dot{P}_S = 0$, we can estimate the steady-state fidelity $F_S = \lim_{t \rightarrow \infty} P_S$ of the singlet and, consequently, the error of the protocol $(1 - F_S)$. Assuming a near unit fidelity we obtain

$$(1 - F_S) \approx \frac{\gamma + \kappa_-}{\kappa_+} = \frac{128\gamma}{\kappa} + \frac{\kappa^2}{2g^2}. \quad (5.26)$$

From this expression we can readily see that the error of the protocol has a promising scaling with the physical parameters. Specifically, the error depends on the ratios of coupling and noise, g/κ and κ/γ so that it will be small for strong coupling, $g^2 \gg \kappa^2$, and modest qubit decoherence, $\gamma \ll \kappa$. Under the assumption that we can vary the resonator decay rate κ we can minimize the error in Eq. (5.26) by a suitable choice of κ . Considering $\frac{\partial}{\partial \kappa}(1 - F_S) = 0$, we derive the optimal resonator decay rate $\kappa_{\text{opt}} = 4\sqrt[3]{2\gamma g^2}$. Inserting this yields the

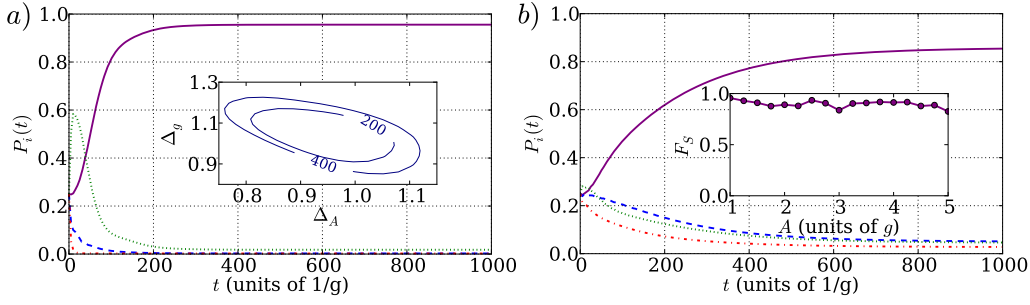


FIGURE 5.5: Evolution of the system towards an entangled steady state. Initially prepared in an equal mixture of the lower states ($|00\rangle$ – green, dotted line, $|11\rangle$ – red, dashed-dotted line, $|T\rangle$ – blue, dashed line, $|S\rangle$ – purple, solid line) the system evolves towards its steady state which is close to the maximally entangled singlet state of the two transmons. Part a) and b) show the result for an anharmonicity of $A = g$ and $A = 4.75g$ respectively. The remaining parameter values are $\Omega_{1/2} = g/3$, $\kappa = 3g/10$ and $\gamma = g/5400$ for all plots. The values of $\bar{\omega}$, $\Delta_{1/2}$ and δ_c are obtained through numerical optimization. The inset in a) shows the region in the $\Delta_A - \Delta_g$ plane where the singlet fidelity is high, $F_S > 90\%$, for $A = g$. The number on each contour line indicates the preparation time in units of $1/g$. The inset in b) shows the singlet state fidelity at $t = 1000/g$ as a function of anharmonicity.

optimized error of the protocol,

$$(1 - F_S)_{\text{opt}} \approx 24 \left(\frac{2\gamma}{g} \right)^{2/3}. \quad (5.27)$$

From here we conclude that for $\gamma \lll g$ the inherent error of the protocol can be limited to very small values. We will later confirm this finding numerically.

In addition, the convergence time, i.e. the decay time of the undesired states, can be approximated using Eq. (5.25), assuming rapid reshuffling of the undesired states to $|00\rangle$. Given that here the preparation of the singlet at a rate κ_+ is the dominant process, the convergence time τ for weak driving is given by

$$\tau \approx \kappa_+^{-1} \approx \frac{32}{\sqrt[3]{2\gamma g^2}}, \quad (5.28)$$

where we have used $\Omega_{\text{eff}} \approx \frac{\kappa_{\text{opt}}}{g}$ and κ_{opt} from above.

Note that the above expressions for the error and the convergence time are approximate and are derived using results obtained for the assumption of weak driving in Sec. 5.2.2. In our numerical simulations below we will optimize a number of parameters including the driving strength to achieve highly entangled states within a preparation time as short as possible. In doing so, we arrive at particular choices of the available parameters which allow us to achieve high fidelities in short time. These optimal parameters are in a regime beyond the weak driving regime where the effective Lindblad operators no longer accurately describe the dynamics (cf. Sec. 3.6). The findings of Eqs. (5.26)-(5.28) therefore deviate from the simulation results below.

5.3.2 Numerical results

To verify the findings above as well as to investigate the limitations of the approximation we now depart from the analytical treatment in the previous sections and assess the performance of the scheme numerically [142, 143]. To this end, we integrate the master equation in Eq. (5.6) including the three lowest levels of each transmon, $|0\rangle$, $|1\rangle$ and $|2\rangle$, considered in the analytics, as well as the fourth level of each transmon, $|3\rangle$, and up to three photons in the resonator. While level $|3\rangle$ already has a minor effect, the effect of higher excitations is expected to be negligible. Due to the Stark shifts induced by the driving, we have numerically optimized the sum- and difference frequencies $\bar{\omega}$ and $\Delta_{1/2}$ of the drives, as well as the resonator frequency δ_c . In Fig. 5.5 we plot the populations

$$P_i(t) = \text{Tr}(|\psi_i\rangle\langle\psi_i| \otimes 1_{\text{cav}} \rho(t)) \quad (5.29)$$

between the time evolved density matrix $\rho(t)$ and the four lower states $|\psi_i\rangle = |00\rangle, |11\rangle, |S\rangle, |T\rangle$ introduced in Sec. 5.1. The results of our simulation are shown in Fig. 5.5 a)-b), where we plot the populations, starting with an initially equal mixture of all four lower states. In Fig. 5.5 a), we consider a rather low anharmonicity $A = g$, which is also what is typically used in experiments [62, 64, 65]. Here, the populations of the states $|11\rangle$ and $|T\rangle$ show a fast drop due to the reshuffling to $|00\rangle$. At the same time, albeit on a slightly longer timescale, the dissipative preparation of the singlet is performed, reaching a fidelity of 90% within a time of about $\tau \approx 200/g$, and a steady state fidelity of $\sim 96\%$. For a transmon experiment with $g/(2\pi) = 300$ MHz this would allow preparation times of about $\tau \approx 80$ ns. For the results in Fig. 5.5 we have chosen $\gamma/(2\pi) \approx 60$ kHz $\approx g/(2\pi 5400)$ corresponding to a relaxation time of $T_1 \approx 3 \mu\text{s}$ [60] for the above parameter choice. This is much shorter than current state-of-the-art 3D transmon qubits where decoherence times of up to $T_2 \sim 95 \mu\text{s}$ and $T_1 \sim 70 \mu\text{s}$ [61, 62] have been measured. To accurately simulate this situation we include decay and dephasing rates corresponding to the decoherence times and find that with the numbers for 3D transmons it is possible to reach a steady state fidelity of $\sim 97\%$ for $A = g$. Our analytical results (excluding the negligible effect of pure dephasing) suggest that fidelities of $\gtrsim 99\%$ can be achieved for $T_1 \gtrsim 150 \mu\text{s}$ (or, in the presence of dephasing, for a corresponding T_2 time). The numbers for the transmon decoherence may, however, be somewhat lower than $70 \mu\text{s}$ in the described circuit QED setup, where two qubits need to be tuned into resonance. In the numerical assessment of our scheme we therefore chose to work with a shorter coherence time of $3 \mu\text{s}$ for the transmon relaxation time, comparable to the coherence time obtained for 2D transmons. In doing so we show the robustness of our scheme against such imperfections as well as the possibility to demonstrate a maximally entangled steady state not only in state-of-the-art 3D, but also in the more commonly used 2D transmon systems.

5.3.3 Anharmonicity of the transmon

As discussed in the previous sections, the coupling of the resonator to the $|0\rangle \leftrightarrow |1\rangle$ transition for each transmon contributes to the scheme by reshuffling the unwanted populations to $|00\rangle$. This coupling, however, gets increasingly

detuned for higher anharmonicities A . In Fig. 5.5 b) we show the effect of an increasing A on the preparation scheme. Here, for a rather high anharmonicity of $A = 4.75g$, the reshuffling of the states $|11\rangle$ and $|T\rangle$ to $|00\rangle$ is slowed down as compared to the result for $A = g$ in Fig. 5.5 a). This can be seen from the drop in the population of $|T\rangle$ and $|11\rangle$ which is much less pronounced in b) than in a). In addition, we observe an increase in the steady state populations of these states. It is therefore advantageous to work with a rather low anharmonicity, where the coupling to the lower transition is still effective. Such anharmonicities are typical for state-of-the-art experiments [62, 64, 65].

In the following, we will assess the possibility to operate our scheme for a broader range of anharmonicities, despite the breakdown of the reshuffling. To this end, we allow for a rather long preparation time $t = 1000/g$. In the inset in Fig. 5.5 b) we show results achieved using a numerical optimization routine to optimize the fidelity by fine-tuning the frequencies of the microwave fields and the resonator. These degrees of freedom in the parameter choice are used by the optimization routine to avoid undesired resonances by a slight departure from the resonance conditions of the previous sections. The range of our protocol is then limited by the breakdown of the reshuffling to $A \lesssim 4g$, as well as to $A \gtrsim g$. For lower A the effective two-photon drive becomes ineffective and couplings to higher levels of the transmons add shifts to the resonances required for the state preparation mechanism. To reach a high fidelity $F_S > 90\%$ of the steady state one should therefore work with anharmonicities between $A \approx g$ and $A \approx 4g$.

Finally, we briefly comment on the possibility for dissipative state preparation with even more anharmonic systems: In this case we choose to have the resonator in (or close to) resonance with the upper transition. Consequently, the lower transition is largely detuned and its effect negligible. We thereby achieve a situation which is very similar to optical cavity QED with atomic Λ schemes – a system where various schemes for dissipative preparation of entanglement are available, see Chapter 4. These schemes can then be mapped to the highly anharmonic circuit QED setup. In those schemes the role of the far-detuned resonator coupling on the lower transition is accomplished by an additional microwave field which takes over the reshuffling of the triplet states. In this way, preparation of a steady state close to the maximally entangled singlet state can be achieved for any anharmonicity. For low anharmonicity, however, the coupling of the resonator to the lower transition allows us to avoid this field and thus to simplify the experimental implementation.

5.3.4 Experimental imperfections

From the previous discussion it is clear that our scheme relies on the fact that the two transition frequencies of the transmons are identical. Moreover, we have so far only considered the case when the coupling, g , is identical for both transmons. In this section, we depart from these assumptions and consider the effect of experimental imperfections. The transmons are characterized by their spectrum which is set by the effective Josephson energy, E_J and the charging energy $E_C = 2A$ [59]. Here, we assume that both $\omega = \sqrt{8E_J E_C} - E_C$ and the anharmonicity differ between the transmons. We also consider the possibility of

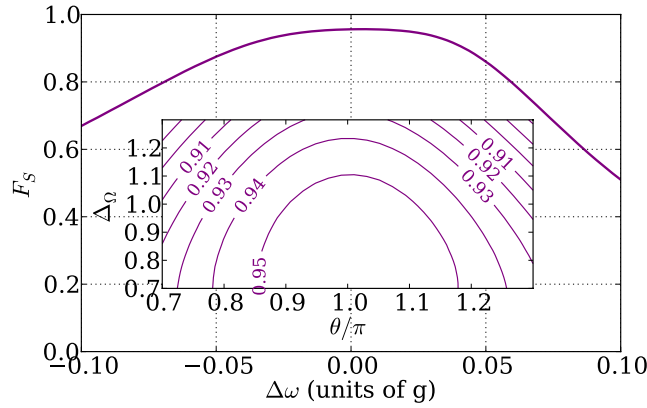


FIGURE 5.6: The fidelity as a function of the difference in resonance frequency $\Delta\omega$ between the two transmons. The parameters are as in Fig. 5.5 with $t = 400/g$ and $A = g$. The inset shows the fidelity when varying the amplitude and phase of the microwave signals.

having different couplings to the resonator. In Fig. 5.5 a), we focus our analysis on the charging energy (anharmonicity) and the couplings by considering $A_2 = \Delta_A A_1$ and $g_2 = \Delta_g g_1$ where the subscript denotes transmon number. In the inset of Fig. 5.5 a), we plot the region in the $\Delta_A - \Delta_g$ plane where $F > 90\%$ for $A_1 = g$. The different contours correspond to the indicated preparation time and we see that there is roughly a 10 – 20% error tolerance built into the system with respect to these parameters. The reproducibility of E_C and g is set by the precision of the e-beam lithography process and these tolerances are well within the limits of current technology.

In Fig. 5.6, we consider the effect of different resonance frequencies, $\omega_2 = \omega_1 + \Delta\omega$, where subscripts denote transmon number. The error tolerance with respect to this parameter is substantially smaller than that for differences in anharmonicity and coupling. We believe that this larger sensitivity is due to the fact that for $\omega_1 \neq \omega_2$ there is no longer an exact dark state of the transmon-resonator system, and the singlet state begins to suffer from the Purcell enhanced decay, which far exceeds the intrinsic decay rates of the qubits. It is not, however, necessary to have ω the same for the two transmons and the tolerance is well within reach of transmon experiments of today.

Apart from differences in circuit parameters, experimental imperfections can also originate from errors in the amplitudes and phases of the continuous microwave tones used to realize the engineered environment. To estimate the robustness of the scheme against such imperfections we consider the drive Hamiltonian

$$H'_d = \left(\frac{\Omega_1}{2} e^{i\Delta_1 t} + e^{-i\theta} \frac{\Omega_2}{2} e^{i\Delta_2 t} \right) \left(|1\rangle_1 \langle 0| + \sqrt{2} |2\rangle_1 \langle 1| \right) + \left(\frac{\Omega_1}{2} e^{i\Delta_1 t} + \Delta_\Omega \frac{\Omega_2}{2} e^{i\Delta_2 t} \right) \left(|1\rangle_2 \langle 0| + \sqrt{2} |2\rangle_2 \langle 1| \right). \quad (5.30)$$

In the inset of Fig. 5.6, we plot the fidelity as a function of Δ_Ω and the phase θ . It is clear that there is a substantial robustness in the scheme against imperfections

in the microwaves so that no involved tuning scheme is required. We note that the maximum fidelity is not obtained for $\Delta_\Omega = 1$, which indicates that it is in principle possible to optimize all parameters including Δ_Ω to achieve even higher values of F_S .

A different requirement needs to be imposed on the average number of residual thermal photons in the resonator \bar{n} . In the absence of residual photons, the target state $|S\rangle$ is a dark state. The preparation of $|S\rangle$ from $|00\rangle$, however, involves a coherent coupling of $|S_0\rangle$ and $|S\rangle|1\rangle$. The singlet is therefore not a dark state in the presence of photons in the resonator which causes a decrease of fidelity for nonzero occupancy numbers, $\bar{n} > 0$. Still, as our numerical simulations show, fidelities of above 90% are achieved for $\bar{n} \leq 0.02$, a value which is experimentally feasible as demonstrated in Ref. [65].

5.4 Summary

In this chapter we have presented a scheme for the preparation of an entangled steady state of two superconducting transmons by means of dissipation. We have engineered effective decay mechanisms for the dissipative preparation of the desired maximally entangled singlet state and verified them analytically and numerically. We have demonstrated that high fidelity with the singlet state can be reached within favorable time for realistic experimental parameters, both with 2D and 3D transmons. In addition, our scheme has proven to be robust against experimental imperfections such as non-degeneracy of the transmon levels and couplings.

We consider our proposal for the generation of a small scale entangled state to be a first step towards more advanced protocols in the framework of dissipative state engineering and dissipative quantum computation implemented in superconducting systems. We hope that our scheme will find application in the generation of high-fidelity steady state entanglement in circuit QED setups and that this will stimulate further investigations aiming to harness dissipation for large scale quantum information processing.

Entangling two trapped ions by engineered dissipation

The two preceding chapters have dealt with theoretical schemes for the dissipative preparation of entanglement in cavity QED and superconducting setups. In this chapter we present a protocol for two cold trapped ions, along with its experimental realization¹.

Systems of trapped ions (see 2.4.1) are one of the leading experimental platforms for quantum information processing. To date, controlled unitary interactions applied to a quantum system, so-called “quantum gates” (cf. Sec. 2.4), have been the most widely used method to deterministically create entangled states of trapped ions [7, 33, 52–54]. Using quantum gates, advanced protocols have been demonstrated, see for example Refs. [13, 55–57]. However, quantum information protocols require minimizing the decoherence that inevitably arises from coupling between the system and the environment and imperfect control of the system parameters. One approach to overcome this relies on active feedback [144–150]. Such feedback techniques may be extended to quantum error correction, which can stabilize entangled states or realize fault-tolerant quantum computations. This will, however, require high-fidelity quantum gates and large qubit overheads that are beyond the reach of current experiments [7].

Our scheme combines unitary processes with engineered dissipation to deterministically produce and stabilize an approximate Bell state of two trapped-ion qubits independent of their initial state. We thereby follow the approach to create entangled states or perform quantum computing by engineering the continuous interaction of the system with its environment, discussed in Sec. 2.4.3.

In our experiment, we take a step towards harnessing dissipation for quantum information processing by producing an entangled state that is inherently stabilized against decoherence by the applied interactions in a setting fully compatible with quantum computation. While previous works along this line involved the application of sequences of multiple time-dependent gates [91] or generated entanglement of atomic ensembles dissipatively, but relied on a measurement

¹The experiments were performed at the National Institute of Standards and Technology (NIST) at Boulder, Colorado, USA, by Y. Lin, J. P. Gaebler, T. R. Tan, R. Bowler, D. Leibfried, and D. J. Wineland.

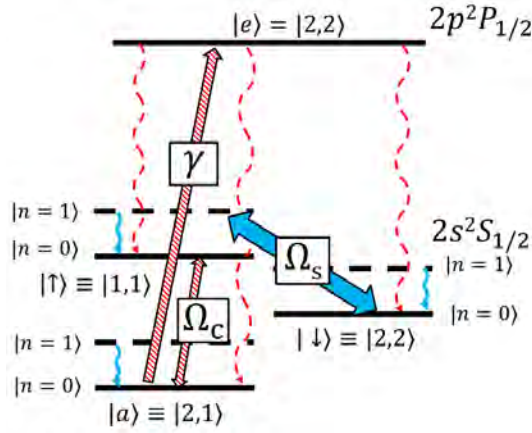


FIGURE 6.1: **Energy Levels** The internal energy levels (not to scale) of ${}^9\text{Be}^+$ are shown as solid black lines for the ground motional state and dashed lines for the first excited motional state. The couplings needed to produce steady state entanglement are shown with blue arrows for the strong sideband coupling and sympathetic cooling and the patterned and dashed red arrows for the weak microwave coupling, repumper, and spontaneous emission from the $|e\rangle$ state. Wavy arrows depict the dissipative processes.

record for steady-state entanglement [99], we implement the process in a continuous time-independent fashion, analogous to optical pumping of atomic states. By continuously driving the system towards steady-state, the entanglement is stabilized even in the presence of experimental noise and decoherence. With this technique, we realize maximally entangled steady states with a fidelity of $F = 0.75(3)$ by simultaneously applying a combination of time-independent fields. We also demonstrate that a stepwise application of these fields can speed up the dynamics of the scheme and achieve a fidelity of $F = 0.89(2)$ after approximately 30 repetitions. In both cases, the errors can be attributed to known experimental imperfections.

We begin with a discussion of the general system in Sec. 6.1 and the entangling scheme in Sec. 6.2. The experimental realization is presented in Sec. 6.3. In Sec. 6.4 we present a thorough theoretical analysis of the experiment. A summary of the chapter is given in Sec. 6.5.

6.1 System

Our scheme utilizes an ion chain with two qubit ions and at least one “coolant” ion for sympathetic cooling [151] of the qubit ions’ motion. We consider a normal motional mode of this ion chain having frequency ν and mean motional quanta \bar{n} . The motional mode is cooled to $\bar{n} \approx 0$ by laser cooling the coolant ion (or ions) and thus the vibration effectively coupled to a zero-temperature bath with the phonon-loss rate denoted by κ . As depicted in Fig. 6.1, we consider four energy levels of each qubit ion (${}^9\text{Be}^+$), where $|\uparrow\rangle$ and $|\downarrow\rangle$ are the qubit “spin” states, $|a\rangle$ is an auxiliary state, and $|e\rangle$ is a fast-decaying excited electronic state. The coherent interactions in the system are described by a Hamiltonian $H_{\text{int}} = H_s + H_c$, where H_s is the sideband excitation and H_c is a carrier drive. The

sideband excitation, with Hamiltonian

$$H_s \equiv \Omega_s(|\uparrow\rangle_1\langle\downarrow| + |\uparrow\rangle_2\langle\downarrow|)b^+ + H.c. \quad (6.1)$$

in the atomic and motional rotating frame, couples the two ions' spins via the motion, where Ω_s denotes the Rabi frequency, b^+ is the motional-mode Fock-state creation operator, the number subscripts denote the qubit ion number, and $H.c.$ is the Hermitian conjugate. A carrier interaction with Hamiltonian

$$H_c \equiv \Omega_c(|a\rangle_1\langle\uparrow| + |a\rangle_2\langle\uparrow|) + H.c. \quad (6.2)$$

drives the $|\uparrow\rangle \leftrightarrow |a\rangle$ transition on each ion with Rabi frequency Ω_c , and a repump laser incoherently drives $|a\rangle \mapsto |\downarrow\rangle, |\uparrow\rangle$ by coupling to the intermediate state $|e\rangle$ with a rate γ . All the above transitions are homogeneously driven on both qubit ions, such that individual addressing is not needed for this scheme. As we will see below, these couplings ensure that the maximally entangled singlet state $|S\rangle \equiv \frac{1}{\sqrt{2}}(|\uparrow\downarrow\rangle - |\downarrow\uparrow\rangle)$ is the only steady state of the effective dynamics (cf. Chapter 3) in the regime $\gamma, \kappa, \Omega_c \ll \Omega_s$.

The scheme is described in terms of a two-atomic basis with triplet ground states $|\downarrow\downarrow\rangle, |\uparrow\uparrow\rangle$ and $|T\rangle = \frac{1}{\sqrt{2}}(|\uparrow\downarrow\rangle + |\downarrow\uparrow\rangle)$ and the singlet state $|S\rangle = \frac{1}{\sqrt{2}}(|\uparrow\downarrow\rangle - |\downarrow\uparrow\rangle)$ as the desired entangled steady state. For the discussion of the engineered decay processes, we also introduce the excited atomic states $|T_a\rangle = \frac{1}{\sqrt{2}}(|\uparrow a\rangle + |a \uparrow\rangle)$ and $|S_a\rangle = \frac{1}{\sqrt{2}}(|\downarrow a\rangle \pm |a \downarrow\rangle)$. The presence of motional excitations is indicated by a second ket vector, e.g. $|\uparrow\uparrow\rangle|1\rangle$.

6.2 Entangling scheme

The working principle of the presented state preparation scheme is shown in Fig. 6.2 a). The scheme is based on a strong asymmetry between the dissipative preparation of the singlet state $|S\rangle$ with an enhanced rate γ_+ on the one hand, and the suppressed decay out of the singlet state at a rate γ_- on the other hand. For an intuitive understanding of the scheme, we first consider only the sideband excitation and the sympathetic cooling (blue lines in Fig. 6.1), which, when applied together, have two dark states that are not affected by the interactions, $|\uparrow\uparrow\rangle|0\rangle$ and $|S\rangle|0\rangle$. The remaining basis states of the qubits, $|\downarrow\downarrow\rangle$ and $|T\rangle \equiv \frac{1}{\sqrt{2}}(|\uparrow\downarrow\rangle + |\downarrow\uparrow\rangle)$, are driven by H_s and eventually pumped to $|\uparrow\uparrow\rangle|0\rangle$ by the combination of the sideband drive and the sympathetic cooling (see Fig. 6.2 b). The effect of adding the carrier drive H_c is to couple the $|\uparrow\uparrow\rangle$ state to the $|T_a\rangle$ and $|aa\rangle$ states and the $|S\rangle$ state to the $|S_a\rangle \equiv \frac{1}{\sqrt{2}}(|a \downarrow\rangle - |\downarrow a\rangle)$ state. However, assuming the ions are in the ground state of motion, the dressed states of the sideband Hamiltonian H_s containing $|S_a\rangle$ have eigenenergies $\pm\Omega_s$, while $|S\rangle, |\uparrow\uparrow\rangle$, and $|T_a\rangle$ are dark states of H_s with zero eigenenergy. Thus, the transition from $|S\rangle|0\rangle$ to $|S_a\rangle|0\rangle$ is shifted out of resonance with the carrier drive and therefore suppressed for $\Omega_c \ll \Omega_s$. On the other hand, the transition from the $|\uparrow\uparrow\rangle|0\rangle$ state to the $|T_a\rangle$ state is not energy shifted and remains resonant. The repumper incoherently transfers the state $|a\rangle$ back to the $|\uparrow\rangle$ and $|\downarrow\rangle$ qubit manifold. Thus, the combination of H_c and the repumper creates a process to pump $|\uparrow\uparrow\rangle$ to $|S\rangle$

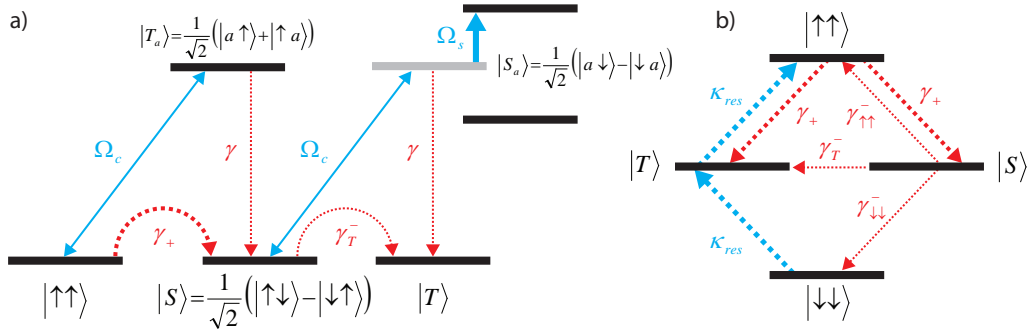


FIGURE 6.2: **Entanglement Preparation Scheme** Mechanisms (a) and effective ground-state processes (b) of the presented scheme. (a) Effective decay from $|\uparrow\uparrow\rangle$ involves coherent coupling to $|T_a\rangle$. Both these states are dark states of the sideband coupling H_s so that their coupling (Ω_s) is on resonance. Population from $|\uparrow\uparrow\rangle$ is therefore rapidly excited up to $|T_a\rangle$ from where it decays into $|S\rangle$ via spontaneous emission (denoted as γ_+). $|S_a\rangle$, on the other hand, is shifted out of resonance by the sideband coupling so that effective decay out of $|S\rangle$ (γ_-) is effectively suppressed. The effective decay processes connecting the ground states are summarized in (b): Transfer of the population of the triplet states to $|\uparrow\uparrow\rangle|0\rangle$ is accomplished by the sideband and sympathetic cooling (shown as blue dashed arrows), denoted as κ_{res} . Processes that occur by coupling the $|\uparrow\rangle$ state to the auxiliary $|a\rangle$ state followed by excitation with the repumper and decay by spontaneous emission are shown as dashed red arrows. Processes shown as thin lines are shifted out of resonance due to the strong sideband coupling, leading to accumulation of population in the maximally entangled state $|S\rangle$ in steady state. Further details on the rates for each process are given in Sec. 6.4.2.

as well as a depumping process from $|S\rangle$ to $|\downarrow\downarrow\rangle$, $|T\rangle$, and $|\uparrow\uparrow\rangle$, although the latter is significantly slower, as can be seen from Fig. 6.2 a). In the limit where the rate to pump other states into $|S\rangle$ is much greater than the depumping rate from $|S\rangle$, the steady state will approach $|S\rangle$. The ratio of these rates, summarized in Fig. 6.2 b), can be made arbitrarily high by reducing the values of γ, κ and Ω_c compared to Ω_s and in steady state the fidelity of the maximally entangled state $|S\rangle$ can approach unity. We will turn the details of the rates when discussing the theoretical model of the experiment in Sec. 6.4.2. In the sections below, we present the experimental implementation of the scheme.

6.3 Experimental realization

In the following, we discuss the experimental setup (Sec. 6.3.1) and present the results from the experimental realization of the continuous (Sec. 6.3.2) and the stepwise implementation of our scheme (Sec. 6.3.3). The measurement technique is detailed in App. C.

6.3.1 Experimental Setup

For our experimental implementation we confine a ${}^9\text{Be}^+ \cdot {}^{24}\text{Mg}^+ \cdot {}^{24}\text{Mg}^+ \cdot {}^9\text{Be}^+$ four-ion chain in a linear radio-frequency Paul trap described in [56, 152]. The two ${}^9\text{Be}^+$ ions serve as qubit ions while the two ${}^{24}\text{Mg}^+$ ions are used for sympathetic cooling. The ion chain lies along the axis of the trap, the axis of weakest

confinement, and has an extent of approximately $11 \mu\text{m}$. We label the four-ion axial modes $\{1, 2, 3, 4\}$, which have mode frequencies $\nu_{1-4} \simeq \{2.0, 4.1, 5.5, 5.8\}$ MHz, respectively. An internal-state quantization magnetic field $B \simeq 11.964$ mT is applied along a direction 45° to the trap axis, which breaks the degeneracy of the magnetic sub-levels of ${}^9\text{Be}^+$ and ${}^{24}\text{Mg}^+$. As depicted in Fig. 6.1 a), we utilize the ${}^9\text{Be}^+$ internal states $|F = 1, m_F = 1\rangle \equiv |\uparrow\rangle$, $|2, 2\rangle \equiv |\downarrow\rangle$, and $|2, 1\rangle \equiv |a\rangle$. To create the sideband coupling term H_s we apply two 313 nm laser beams in a Raman configuration tuned approximately 270 GHz below the $2s \ ^2S_{1/2}$ to $2p \ ^2P_{1/2}$ transition with a frequency difference equal to $f_0 + \nu_3$ where $f_0 \simeq 1.018$ GHz is the resonant transition frequency between the $|\downarrow\rangle$ and $|\uparrow\rangle$ states. The two beams are derived from the same laser and frequency-shifted using acousto-optic modulators [153]. The difference wave vector of the two beams is parallel to the trap axis. Microwaves are used to drive resonant transitions between the $|\uparrow\rangle$ state and the $|a\rangle$ state ($f \simeq 1.121$ GHz) to create H_c . We also apply a repump laser beam to drive the $|a\rangle$ state to the $2p \ ^2P_{1/2}|2, 2\rangle$ state, which subsequently spontaneously emits a photon and decays to $|\uparrow\rangle$, $|\downarrow\rangle$ or $|a\rangle$ with a branching ratio of approximately 5:4:3. Phonon excitations due to the photon recoil are removed by the sympathetic cooling. To cool the ${}^{24}\text{Mg}^+$ ions, a Doppler cooling beam, two Raman-sideband beams, and a repump beam co-propagate with the ${}^9\text{Be}^+$ Raman beams. These beams ($\lambda \simeq 280$ nm) interact negligibly with the internal states of the ${}^9\text{Be}^+$ ions. We initialize each experiment by first applying Doppler cooling to ${}^9\text{Be}^+$ and ${}^{24}\text{Mg}^+$, followed by ${}^{24}\text{Mg}^+$ sideband cooling of all the axial modes to near the ground state of motion [152]. An optical pumping pulse initializes the ${}^9\text{Be}^+$ ions to the $|\downarrow\downarrow\rangle$ state. We then apply the dissipative entanglement preparation operations, as detailed below. Finally, we perform spin-state analysis to measure the populations of the $|S\rangle$, $|T\rangle$, $|\uparrow\uparrow\rangle$, and $|\downarrow\downarrow\rangle$ spin states, as described in App. C.

6.3.2 Continuous implementation

We implement the entanglement scheme in Sec. 6.2 using mode 3, where the ${}^9\text{Be}^+$ ions oscillate in phase with each other but out of phase with the ${}^{24}\text{Mg}^+$ ions (which oscillate in phase). In a first, continuous implementation of the experiment, we apply the laser-induced sideband excitation, microwave-induced carrier excitation, repumper, and sympathetic cooling simultaneously for a duration t and obtain a steady-state singlet state fidelity of 0.75(3), as shown in Fig. 6.3. This result agrees with our theoretical models presented in Sec. 6.4.

For the continuous implementation we used a sideband Rabi rate $\Omega_s = 2\pi \times 7.8(1)$ kHz and a microwave Rabi rate $\Omega_c = 2\pi \times 0.543(6)$ kHz. The $1/e$ time for the repump beam to deplete the $|a\rangle$ state was $88 \mu\text{s}$. The $1/e$ time for continuous sympathetic sideband cooling of mode three was $203 \mu\text{s}$, determined from an exponential fit of the average Fock-state occupation number \bar{n} vs. sympathetic cooling time from the initial Doppler-cooled value of $\bar{n} \approx 2.5$ to a steady-state value with cooling on of $\bar{n} = 0.11(1)$. The continuous sympathetic cooling was achieved by applying the laser-induced Raman sideband for the ${}^{24}\text{Mg}^+$ ions that couples the electronic ground states $|F = \frac{1}{2}, m_F = -\frac{1}{2}\rangle|n\rangle \leftrightarrow |\frac{1}{2}, \frac{1}{2}\rangle|n-1\rangle$ simultaneously with a repump beam that transfers $|\frac{1}{2}, \frac{1}{2}\rangle|n\rangle \rightarrow |\frac{1}{2}, -\frac{1}{2}\rangle|n\rangle$. The continuous sympathetic cooling off-resonantly cooled the other axial modes 1, 2,

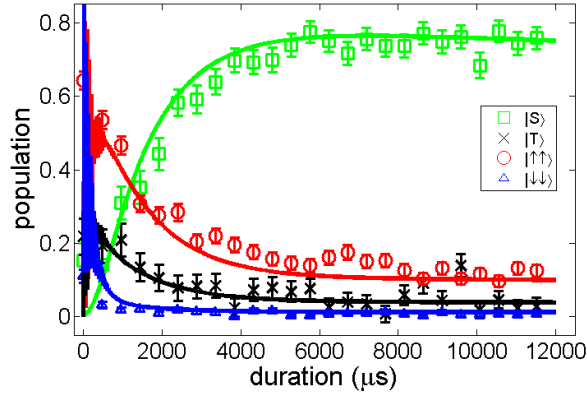


FIGURE 6.3: **Steady State Entanglement** The measured populations of the singlet, triplet, $|\uparrow\uparrow\rangle$ and $|\downarrow\downarrow\rangle$ states are shown as squares, crosses, circles, and triangles, respectively, as a function of the duration that all the elements of the dissipative entanglement scheme are applied simultaneously. The system reaches a steady state with a $0.75(3)$ population in the target singlet state after a few ms. The solid lines are the result of a simulation based on the experimental parameters (see Sec. 6.4.1). The slow decrease in the singlet state fidelity at long times is due to a leak of the qubits to spin states outside the $|\uparrow\rangle$, $|\downarrow\rangle$, $|a\rangle$ manifold caused by spontaneous emission from the lasers that generate the sideband coupling (see App. C and Sec. 6.4). Error bars represent standard deviations of each point.

and 4 with $1/e$ times of approximately $1300 \mu\text{s}$, $294 \mu\text{s}$, and $181 \mu\text{s}$ to thermal states with average Fock state occupation numbers of approximately 2.9, 0.95, and 0.12, respectively. The Rabi rate for the $^{24}\text{Mg}^+$ sideband transition on mode three was $\approx 2\pi \times 11.9 \text{ kHz}$ and the repumper rate was $\approx 2\pi \times 625 \text{ kHz}$ (corresponding to a $1/e$ repump time of $1.6 \mu\text{s}$). The repumper rate was made significantly stronger than the sideband rate to eliminate any coherent dynamics between the $^{24}\text{Mg}^+$ spins and ion-crystal motion.

In both cases, continuous and stepwise (discussed in Sec. 6.3.3 below), the ion spacing was set by adjusting the strength of the harmonic confinement, such that $\Delta_k z = 2\pi m$ where $\Delta_k \approx \frac{2\pi\sqrt{2}}{313 \times 10^{-9}} \text{ m}^{-1}$ is the wavevector difference of the $^9\text{Be}^+$ Raman sideband lasers, z is the distance between the $^9\text{Be}^+$ ions, and m is an integer, such that the phase of the sideband excitation was equal on both ions. For our confinement strength, $z \simeq 11 \mu\text{m}$ such that the value of m was near 300. For modes where the qubit ions move in phase, the integer value of m ensures H_s is as defined in the main text. However, in the general case $H_s \equiv \Omega_s(|\uparrow\rangle_1\langle\downarrow| + e^{i\phi}|\uparrow\rangle_2\langle\downarrow|)b^+ + H.c.$, where ϕ is the phase difference between the two $^9\text{Be}^+$ ions of the sideband coupling, and the steady state of the system (including the cooling, repumper, and microwave carrier) is $|D_\phi\rangle \equiv \frac{|\uparrow\downarrow\rangle - e^{i\phi}|\downarrow\uparrow\rangle}{\sqrt{2}}$.

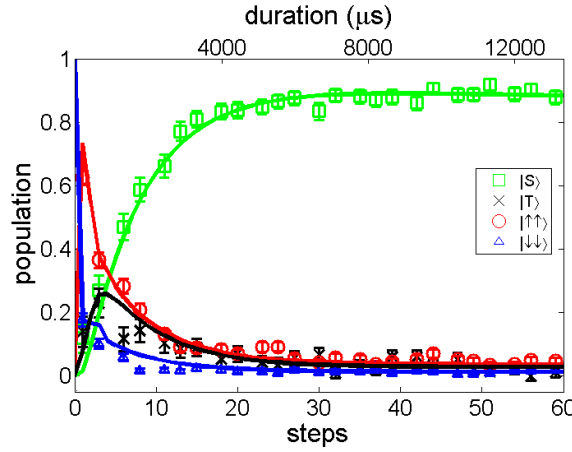


FIGURE 6.4: **Entanglement With Stepwise Scheme** The measured populations of the singlet, triplet, $|\uparrow\uparrow\rangle$ and $|\downarrow\downarrow\rangle$ states are shown as squares, crosses, circles, and triangles, respectively, as a function of the number of applied steps. Each step has a duration of approximately $220 \mu\text{s}$. The solid lines are the result of a model as explained in Sec. 6.4. Error bars represent standard deviations of each point.

6.3.3 Stepwise implementation

We also implement the scheme in a stepwise manner. In this case we can take advantage of coherences to speed up the entanglement creation process and thereby reduce the effect of the spontaneous emission induced by the ${}^9\text{Be}^+$ sideband laser beams. Specifically, we apply a sequence of steps with each step consisting of a coherent pulse with $H_{\text{coh}} = H_s + H_c$ followed by the dissipative processes of repumping and sympathetic cooling, applied sequentially (the order does not matter). In the steady-state entanglement procedure outlined above we required $\Omega_c, \gamma, \kappa \ll \Omega_s$ to suppress transitions from $|S\rangle$ to $|S_a\rangle$. However, when H_{coh} is applied without any dissipation, ions initially in the $|S\rangle$ state will oscillate between $|S\rangle$ and a superposition of $|S\rangle$ and $|S_a\rangle$, which is dressed by H_s , with an effective Rabi rate $\Omega_{\text{eff}} = \sqrt{\Omega_s^2 + \Omega_c^2}/2$ and an amplitude of $1 - A_{\text{eff}}$ where $A_{\text{eff}} = \frac{\Omega_c^2}{\Omega_{\text{eff}}^2}$, assuming the ions are in the motional ground state. Thus, by applying H_{coh} for a full oscillation period π/Ω_{eff} the interaction will be an identity operation for the $|S\rangle$ state while all other states will be partially transferred to the auxiliary level $|a\rangle$, which can then be repumped to create $|S\rangle$. However, if $n \neq 0$ some population will be transferred out of the $|S\rangle$ state since the oscillation period is dependent on n . By taking advantage of the coherent evolution, we relax the requirement $\Omega_c, \gamma, \kappa \ll \Omega_s$ and the entanglement preparation time scale can be shortened, which reduces the error due to spontaneous emission induced by the sideband laser beams. During the coherent process the entangled state $|S\rangle$ is no longer strictly a steady state; however, if the ratio Ω_c/Ω_s is small, the evolution of the state away from $|S\rangle$ will be correspondingly small and $|S\rangle$ remains an approximate steady state.

We implemented the stepwise scheme in the following way: in each step we first sympathetically cooled each of the modes of the ${}^9\text{Be}^+ - {}^{24}\text{Mg}^+ - {}^{24}\text{Mg}^+ - {}^9\text{Be}^+$ chain with ${}^{24}\text{Mg}^+$ Raman sideband cooling [34], followed by application of H_{coh}

for a duration $t_{2\pi}$, and at the end of each step we applied the repumper. The populations of the qubit state were measured at the end of each step and plotted in Fig. 6.4. The ${}^9\text{Be}^+$ sideband Rabi rate was $\Omega_s = 2\pi \times 8.4(1)$ kHz and the microwave Rabi rate was $\Omega_c = 2\pi \times 1.24(6)$ kHz. The repumper had a $1/e$ time of approximately $3 \mu\text{s}$ and was turned on for $6 \mu\text{s}$ in each step. In each step, two sympathetic cooling cycles were applied to mode 1, which has the largest heating rate, and one pulse was applied to each of the remaining modes, with mode 3 being the last. A sympathetic cooling cycle consists of a single motion subtracting sideband pulse applied to the ${}^{24}\text{Mg}^+$ ions followed by a repump pulse. The duration to apply all the cooling pulses was approximately $100 \mu\text{s}$ in each step.

The results of the stepwise experiment are shown in Fig. 6.4. We obtain the singlet state with fidelity $0.89(2)$. We use the same model as for the continuous case (see Sec. 6.4 below) to predict the outcome of the stepwise scheme, and find good agreement with the data (solid lines in Fig. 6.4) with the largest sources of error coming from heating processes, unequal sideband Rabi rates, spontaneous emission caused by the ${}^9\text{Be}^+$ sideband lasers, and off-resonant coupling of the sideband to mode 4.

6.4 Theoretical analysis

The entanglement creation scheme presented here can in principle produce maximally entangled states with arbitrarily low error. Because of experimental limitations, the observed fidelities for the steady states created were, however, $0.75(3)$ for the continuous implementation of the scheme and $0.89(2)$ for the stepwise implementation. Here, we examine the sources of error for the experiments and discuss the prospects for reducing these errors to achieve high-fidelity entangled states without the use of quantum gates. To this end, we utilize both a simplified rate model to approximate the dynamics of the system, presented in Sec. 6.4.2, and a direct numerical integration of the master equation, described in Sec. 6.4.1.

6.4.1 Numerical model

For our numerical model we use a master equation with a coherent component describing the ${}^9\text{Be}^+$ sideband and microwave carrier drives and Lindblad operators describing the sympathetic cooling, repumper, and spontaneous emission due to the ${}^9\text{Be}^+$ sideband lasers. The coherent Hamiltonian is

$$H_{\text{coh}} \equiv \Omega_s \left[\left(1 - \frac{r}{2}\right) |\uparrow\rangle_1 \langle \downarrow| + \left(1 + \frac{r}{2}\right) |\uparrow\rangle_2 \langle \downarrow| \right] b^\dagger + \Omega_c (|a\rangle_1 \langle \uparrow| + |a\rangle_2 \langle \uparrow|) + H.c.,$$

where r describes the Rabi-rate imbalance of the sideband on the two ions. The Lindblad operator describing sympathetic cooling is given by $L_\kappa = \sqrt{\kappa} b$, and the repumper is given by $L_{\gamma_{j,a}}$, where j is either the $|\uparrow\rangle$ or $|\downarrow\rangle$ state and $L_{\gamma_{j,a}} = \sqrt{\gamma_{j,a}} |j\rangle \langle a|$. Heating processes that limit the sympathetic cooling are modeled with a Lindblad operator $L_{\kappa_h} = \sqrt{\kappa_h} b^\dagger$, where κ_h is determined experimentally by measuring \bar{n} for mode three after sympathetic cooling (no other interactions are turned on). The heating rate is given by $\kappa_h = \frac{\kappa \bar{n}}{1 + \bar{n}}$. For the continuous cooling used for the data in Fig. 6.3 we found $\bar{n} = 0.11(1)$ and for

the stepwise case of Fig. 6.4 we found $\bar{n} = 0.08(1)$. We take into account spontaneous emission that incoherently changes population from the state i to the state j ($i \neq j$) caused by the ${}^9\text{Be}^+$ sideband laser beams with Lindblad operators of the form $L_{j,i} = \sqrt{\Gamma_{j,i}}|j\rangle\langle i|$, where $\Gamma_{j,i}$ can be calculated using the Kramers-Heisenberg formula [154]. The error caused by Rayleigh scattering ($i = j$) is negligible [155]. Off-resonant coupling to mode four is taken into account with an additional Hamiltonian term $H_4 = \Omega_s \frac{\eta_4}{\eta_3} (|\uparrow\rangle_1 \langle\downarrow| - |\uparrow\rangle_2 \langle\downarrow|) c^+ e^{-i\delta t} + H.c.$, where c^+ is the raising operator for the fourth mode, $\delta \approx 2\pi \times 250$ kHz is the splitting between modes three and four, and $\eta_3 = 0.180$ and $\eta_4 = 0.155$ are the Lamb-Dicke parameters of modes three and four, respectively.

The continuous implementation of the scheme is modeled by numerically solving a master equation that includes all terms for a variable duration and a given value of r . We then obtain the theoretical prediction shown in Fig. 6.3 by averaging simulations with different values of r using a Gaussian distribution with an r.m.s. value of 0.014. This r.m.s. value was determined from fits to qubit Rabi flopping curves for a single ${}^9\text{Be}^+$ ion and for the ${}^9\text{Be}^+ \text{-} {}^{24}\text{Mg}^+ \text{-} {}^{24}\text{Mg}^+ \text{-} {}^9\text{Be}^+$ ion chain. Percent-level fluctuations of Ω_s cause negligible changes to the predicted fidelity. The result of the calculation at the end of each step is plotted in Fig. 6.4. In both cases, the initial state of the ${}^9\text{Be}^+$ ions was taken to be $|\downarrow\downarrow\rangle|n=0\rangle$. The particular initial state chosen affects the dynamics only at short times and does not affect the steady state. All numerical models were implemented by use of the quantum optics toolbox [156].

We find that the numerical model is in close agreement with the data and suggests that the dominant errors come from the spontaneous emission induced by the sideband laser beams and unequal sideband Rabi rates. In Sec. 6.4.2 below, we explain these errors and discuss how they can be reduced.

6.4.2 Analytical model

Rate equation framework

In our simplified rate model, we restrict the dynamics of the master equation to the ground states $|\uparrow\uparrow\rangle$, $|\downarrow\downarrow\rangle$, $|T\rangle$ and $|S\rangle$, due to the fast repumping of the auxiliary level. We achieve this using our effective operator formalism in Chapter 3 to eliminate the decaying states. Thereby we obtain effective decay processes such as the preparation rate of the singlet and loss processes from the singlet. Our model involves a rate γ_+ for the preparation of the singlet from $|\uparrow\uparrow\rangle$. The same process also induces a decay at the same rate γ_+ from $|\uparrow\uparrow\rangle$ to $|T\rangle$ since the repumper incoherently pumps each ion independently. Furthermore, the reshuffling process that transfers $|\downarrow\downarrow\rangle$ to $|T\rangle$, and $|T\rangle$ to $|\uparrow\uparrow\rangle$ is described by a rate κ_{res} . The losses from the singlet are modeled by three loss rates γ_i^- , $i \in \{\uparrow\uparrow, \downarrow\downarrow, T\}$ (overall loss rate $\gamma_- = \gamma_{\uparrow\uparrow}^- + \gamma_T^- + \gamma_{\downarrow\downarrow}^-$), which can account for various loss processes present in the experiment. These interactions are illustrated in Fig. 6.2 b). As no coherences between the ground states are established by these processes, the dynamics of the coherences can be dropped from the master equation. The time evolution of the ground states is then described by rate equations of their populations (cf. Sec. 3.7). With the rates introduced above

these equations read

$$\dot{P}_S = +\gamma_+ P_{\uparrow\uparrow} - (\gamma_{\uparrow\uparrow}^- + \gamma_T^- + \gamma_{\downarrow\downarrow}^-) P_S, \quad (6.3)$$

$$\dot{P}_{\uparrow\uparrow} = -2\gamma_+ P_{\uparrow\uparrow} + \kappa_{\text{res}} P_T + \gamma_{\uparrow\uparrow}^- P_S, \quad (6.4)$$

$$\dot{P}_T = +\gamma_+ P_{\uparrow\uparrow} - \kappa_{\text{res}} P_T + \kappa_{\text{res}} P_{\downarrow\downarrow} + \gamma_T^- P_S, \quad (6.5)$$

$$\dot{P}_{\downarrow\downarrow} = -\kappa_{\text{res}} P_{\downarrow\downarrow} + \gamma_{\downarrow\downarrow}^- P_S. \quad (6.6)$$

The effect of other decay processes acting on the triplet states (suppressed by Ω_c^2/Ω_s^2) is negligible compared with the fast reshuffling of these states and is therefore not considered. Setting $\dot{P}_i = 0$ for all states i the steady state can then be read off from the system of coupled equations. The fidelity of the steady state with the maximally entangled singlet is given by

$$F = \frac{1}{1 + \mathcal{E}} \simeq 1 - \mathcal{E}, \quad (6.7)$$

with

$$\mathcal{E} = \frac{\gamma_-}{\gamma_+} + \frac{\gamma_{\uparrow\uparrow}^- + 2\gamma_T^- + 3\gamma_{\downarrow\downarrow}^-}{\kappa_{\text{res}}}. \quad (6.8)$$

The error of the protocol, i.e., the infidelity of the steady state with the singlet state, $\mathcal{E} \simeq 1 - F$, is thus determined by the ratios of the depumping rates out of the singlet and the pumping rates of other triplet states into the singlet, which result in a steady-state population of the three triplet states. Therefore, processes that affect either of these rates can cause error. Eq. (6.8) contains two types of errors: The first term accounts for the ratio between preparation of and loss from the singlet state and equals the error for the case of perfect reshuffling ($\kappa_{\text{res}} \rightarrow \infty$) of the triplet states. The second term reflects the need to reshuffle population lost from the singlet state to $|\downarrow\downarrow\rangle$ and $|T\rangle$ to $|\uparrow\uparrow\rangle$ in order to transfer it to the singlet again. In the following, we use this model as a framework to include the rates of the desired, engineered decay processes, as well as the experimental sources of loss. We thereby obtain a simple quantitative model for the dynamics observed in the experiment.

Entanglement Preparation

We start out with the entanglement preparation process: The rate for pumping other states to the singlet state is dependent on the process that takes $|\uparrow\uparrow\rangle|n=0\rangle$ to $|S\rangle|0\rangle$, which is achieved by weak excitation from $|\uparrow\uparrow\rangle$ to $|T_a\rangle = \frac{1}{\sqrt{2}}(|a\uparrow\rangle + |\uparrow a\rangle)$ and subsequent decay into $|S\rangle$. For weak microwave driving this results in an effective decay by spontaneous emission from $|\uparrow\uparrow\rangle$ to $|S\rangle$ with a rate

$$\gamma_+ = \frac{4\gamma_{\downarrow a}\Omega_c^2}{\gamma^2}, \quad (6.9)$$

where Ω_c denotes the microwave carrier Rabi rate, the repumper rates are $\gamma_{\downarrow a}$ (for repumping from $|a\rangle$ to $|\downarrow\rangle$) and $\gamma_{\uparrow a}$ (for repumping from $|a\rangle$ to $|\uparrow\rangle$). Here, all decay rates are written as γ_{ij} , leading to a state i from a state j . The line

width of level $|a\rangle$ is given by $\gamma = \gamma_{\downarrow a} + \gamma_{\uparrow a} + \gamma_{aa}$. The same process transfers population from $|\uparrow\uparrow\rangle$ to $|T\rangle$ at the same rate γ_+ .

Once the drive Ω_c from $|\uparrow\uparrow\rangle$ to $|T_a\rangle$ approaches the line width of $|T_a\rangle$ (γ) the excitation is no longer overdamped, the dynamics become more coherent and the above expression becomes inaccurate. The accuracy can be restored by including power broadening and the steady population of the excited level. This results in an adjusted preparation rate

$$\gamma_+ = \frac{4\gamma_{\downarrow a}\Omega_c^2}{\gamma^2 + 16\Omega_c^2}. \quad (6.10)$$

In the simulated curves below we plot the sum of the populations of the coupled states $|\uparrow\uparrow\rangle$ and $|T_a\rangle$ since these are mixed by the relatively strong drive Ω_c .

The preparation process from $|\uparrow\uparrow\rangle$ to $|S\rangle$ requires the ions to be in the motional ground state. This is because the transitions from the $|\uparrow\uparrow\rangle$ state to states containing $|a\rangle$ are shifted out of resonance with the carrier drive by the sideband coupling for $|n \neq 0\rangle$. Thus, imperfect cooling slows down the preparation rate for $|S\rangle$, which lowers the fidelity. For a nonzero population of the higher motional states, the preparation rate therefore has to be multiplied by the probability to be in the motional ground state, $P_0 = \frac{1}{1+\bar{n}}$. We then obtain the preparation rate

$$\gamma_+ = \gamma_+(\bar{n} = 0)P_0 = \frac{\gamma_{\downarrow a}\Omega_c^2}{\gamma^2(1 + \bar{n})} \quad (6.11)$$

for weak driving, or

$$\gamma_+ = \frac{\gamma_{\downarrow a}\Omega_c^2}{(\gamma^2 + 4\Omega_c^2)(1 + \bar{n})}, \quad (6.12)$$

including the strong driving effects from above. In the continuous experiment the motional mode is cooled to about $\bar{n} = 0.1$, which leads to a decrease in the preparation rate and an error for the singlet state of approximately 0.02 according to both the numerical simulation and the rate model.

In order to transfer population from all states to $|S\rangle|0\rangle$ via $|\uparrow\uparrow\rangle|0\rangle$, the population from $|\downarrow\downarrow\rangle|0\rangle$ is reshuffled to $|T\rangle|0\rangle$ by excitation to $|T\rangle|1\rangle$ through the sideband coupling and subsequent decay to $|T\rangle|0\rangle$ at a rate κ . Similarly, the population of $|T\rangle|0\rangle$ is transferred to $|\uparrow\uparrow\rangle|0\rangle$ through $|\uparrow\uparrow\rangle|1\rangle$. Given that $\Omega_s \gg \kappa$, the population oscillates back and forth several times between the coupled states before a decay happens. We can therefore assume the population spends half of the time in the phonon-excited state (and the other half in the respective ground state). The decay rate of the reshuffling process can then be approximated as

$$\kappa_{\text{res}} \approx \frac{\kappa}{2}, \quad (6.13)$$

regardless of the actual value of the sideband coupling Ω_s .

Inherent Depumping

We now turn to the loss processes: The only depumping rate inherent to the scheme is due to the off-resonant coupling of the $|S\rangle$ state to the state $|S_a\rangle = \frac{1}{\sqrt{2}}(|a \downarrow\rangle - |\downarrow a\rangle)$ and the decay from there into various states. This process is inhibited by the energy splitting Ω_s induced by the strong sideband driving such that the inherent depumping rate from the singlet amounts to

$$\gamma_{\text{inh}}^- = \frac{(\gamma + \kappa)\Omega_c^2}{4\Omega_s^2}, \quad (6.14)$$

where a fraction $\gamma_{\downarrow a}/(\gamma_{\uparrow a} + \gamma_{\downarrow a})$ decays to $|\downarrow\downarrow\rangle$, a fraction $\frac{1}{2}\gamma_{\uparrow a}/(\gamma_{\uparrow a} + \gamma_{\downarrow a})$ decays to $|T\rangle$ and the same amount returns to $|S\rangle$. We use the rate equation model to quantify this source of error. For the parameters of the experiment we find that for the continuous operation an error of about 0.11 originates from the inherent loss processes. These loss processes are not present in the stepwise scheme since (1) the repumper is applied separately from the coherent drives and (2) we adjust the duration of the coherent pulse such that all population has returned to the singlet state at its end.

The inherent loss rate γ_{inh}^- derived above can be decreased by increasing the sideband coupling Ω_s , and there is thus no fundamental limitation to the achievable fidelity of the scheme, which can ideally approach unity. In practice, there is always a limitation to the available sideband coupling strength and the parameters of the experiments thus have to be optimized given the available sideband coupling strength. The inherent loss rate (6.14) can also be decreased by decreasing the drive Ω_c . In the experiment we are, however, limited by the γ_-/γ_+ term in Eq. (6.8), and since the desirable process γ_+ also decreases with decreasing Ω_c , this will only increase the necessary waiting time to reach the steady state and will not improve the fidelity. Furthermore a small Ω_c will also increase the effect of other experimental imperfections that cause depumping from the entangled state due to the lower preparation rate of the state. In the experiment we therefore set $\Omega_c \approx \gamma/4$, which is the point where the desirable rate γ_+ begins to become limited by the saturation effect included in Eq. (6.10). The remaining parameters γ and κ of our experiment are then determined by the tradeoff between the reduction of γ_{inh}^- (favoring low γ and κ) and minimization of other loss processes (favoring fast preparation through large γ and κ).

The remaining sources of error are not inherent to the scheme, but arise from the particular setup used for the implementation. These are (1) spontaneous emission caused by the ${}^9\text{Be}^+$ Raman sideband lasers, (2) fluctuations of laser and microwave powers and spatial alignments, (3) heating of the motional mode, (4) off-resonant coupling of the ${}^9\text{Be}^+$ Raman sideband lasers to the carrier and other motional modes and (5) magnetic field gradients and fluctuations.

Raman Sideband Coupling Induced Spontaneous Emission

Because we implement the sideband coupling with a Raman laser configuration, the ions have a small amplitude in the electronically excited state from which they can spontaneously emit photons, reducing an entangled spin state to a

mixed state. This results in a decay from $|S\rangle$ to $|\uparrow\uparrow\rangle$ at a rate

$$\Gamma_{\uparrow\uparrow}^- = \Gamma_{\uparrow\downarrow} + \frac{\Gamma_{\uparrow a}\Gamma_{a\downarrow}}{\Gamma_{\uparrow a} + \Gamma_{\downarrow a}} + \frac{\Gamma_{\uparrow a}\Gamma_{a\uparrow}}{2(\Gamma_{\uparrow a} + \Gamma_{\downarrow a})} \left(1 + \frac{\kappa/2}{\Gamma_{\uparrow a} + \Gamma_{\downarrow a} + \kappa/2}\right), \quad (6.15)$$

from $|S\rangle$ to $|T\rangle$ (as well as from $|S\rangle$ to $|S\rangle$) at a rate

$$\Gamma_T^- = \frac{\Gamma_{\downarrow a}\Gamma_{a\downarrow}}{2(\Gamma_{\uparrow a} + \Gamma_{\downarrow a})} + \frac{(\Gamma_{\uparrow a} + \Gamma_{\downarrow a})\Gamma_{a\uparrow}}{4(\Gamma_{\uparrow a} + \Gamma_{\downarrow a} + \kappa/2)} + \frac{\Gamma_{\downarrow a}\Gamma_{a\uparrow}}{2(\Gamma_{\uparrow a} + \Gamma_{\downarrow a})} \frac{\kappa/2}{\Gamma_{\uparrow a} + \Gamma_{\downarrow a} + \kappa/2}, \quad (6.16)$$

and from $|S\rangle$ to $|\downarrow\downarrow\rangle$ at a rate

$$\Gamma_{\downarrow\downarrow}^- = \Gamma_{\downarrow\uparrow} + \frac{\Gamma_{\downarrow a}\Gamma_{a\uparrow}}{2(\Gamma_{\uparrow a} + \Gamma_{\downarrow a} + \kappa/2)}. \quad (6.17)$$

The effect of the dephasing from Rayleigh scattering $|\uparrow\rangle \leftrightarrow |\uparrow\rangle$ and $|\downarrow\rangle \leftrightarrow |\downarrow\rangle$ is negligible [154, 155]. The spontaneous emission rates can be calculated with the Kramers-Heisenberg formula [154, 155] and are proportional to the Rabi rate of the Raman sideband coupling. However, the ratio of the spontaneous emission rates to the Rabi rate can be reduced by increasing the Raman detuning from the excited state. The Raman detuning used here was 270 GHz below the $2s \ ^2S_{1/2}$ to $2p \ ^2P_{1/2}$ transition and the spontaneous emission rates are on the order of $10^{-4} \times \Omega_s$.

In addition, spontaneous emission causes loss from the state $|\uparrow\rangle = |1, 1\rangle$ to the $|2, 0\rangle$ and $|1, 0\rangle$ states, which are not repumped. As also addressed in App. C, this error can result in a decrease in fidelity. The additional losses to these states can be modeled by adding

$$\dot{P}_{\uparrow\uparrow} = \dots - 2\Gamma_{\uparrow}P_{\uparrow\uparrow}, \quad (6.18)$$

$$\dot{P}_T = \dots - \Gamma_{\uparrow}P_T, \quad (6.19)$$

$$\dot{P}_S = \dots - \Gamma_{\uparrow}P_S, \quad (6.20)$$

where Γ_{\uparrow} denotes the spontaneous emission rate from $|\uparrow\rangle$ to states other than $|\uparrow\rangle$, $|\downarrow\rangle$ and $|a\rangle$, and the dots represent the terms in Eqs. (6.3)-(6.6). From the simulations we find that the population of states containing at least one ion in either the $|2, 0\rangle$ or $|1, 0\rangle$ states is approximately 0.05 for the continuous case (averaging between 6 and 12 ms) and 0.03 for the stepwise case (averaging from 35 to 59 steps). These populations will continue to increase for increasing duration of the applied fields. According to our simulation, the singlet state fidelity for the continuous case would drop to 50% at approximately 84 ms. In the future, this loss could be avoided by repumping the $|1, 0\rangle$ and $|2, 0\rangle$ states back to the qubit states.

We have performed a numerical simulation with identical parameters to the experiment, but eliminated all spontaneous emission errors (while still including all other sources of error) and find that the fidelities increase by approximately 0.07 for the continuous and 0.04 for the stepwise implementations of the scheme. Similar results are obtained for the rate equation mode in the continuous case. Spontaneous emission errors could be reduced by increasing the Raman sideband detuning and correspondingly increasing the laser intensity to keep the sideband Rabi rate constant. Another potential future option would be to create the sideband coupling with microwaves, which would eliminate all spontaneous emission errors from the sideband excitation [157, 158].

Experimental Apparatus Noise

Due to fluctuations in the intensity of the laser beams and microwave fields (typically on the order of a percent), the values of Ω_s , Ω_c , γ , and κ will vary. However, for the continuous implementation of the scheme, insensitivity to fluctuations in the parameters is inherent to the method since the pumping effect relies only on that ratios between certain parameters be small, a major asset of dissipative state preparation. For the stepwise implementation of the scheme, however, there is a greater dependence of the fidelity on the sideband Rabi rate that arises from the coherent portion of each step. Nevertheless, in the limit $\Omega_c \ll \Omega_s$, the decrease in fidelity due to Rabi rate fluctuations can still be small. In our experiment we estimate $\frac{\delta\Omega_s}{\Omega_s} = 0.008$, where $\delta\Omega_s$ is the r.m.s. fluctuation in Ω_s , and this reduces the fidelity of the entangled state by less than 0.01 according to our numerical simulations.

A more significant problem for the scheme is fluctuations in the position of the ${}^9\text{Be}^+$ Raman sideband laser beams at the site of the ions. Because the lasers are each aligned at 45° to the crystal axis, fluctuations in the beam positions cause unequal Rabi rates on the two ${}^9\text{Be}^+$ ions. As above, this effect can be modeled with a modified sideband Hamiltonian $H_s \equiv \Omega_s[(1 - \frac{r}{2})|\uparrow\rangle_1\langle\downarrow| + (1 + \frac{r}{2})|\uparrow\rangle_2\langle\downarrow|]b^\dagger + H.c.$, where r characterizes the imbalance. In our experiment we estimate that the value of r fluctuates about zero from experiment to experiment with an r.m.s. deviation of approximately 0.014. A minor source of error caused by $r \neq 0$ is that the dark state of the system is no longer the singlet state but rather $|S_r\rangle = \frac{1}{\sqrt{2+r^2}}[(1 - \frac{r}{2})|\uparrow\downarrow\rangle - (1 + \frac{r}{2})|\downarrow\uparrow\rangle]$. The error from the difference between $|S\rangle$ and $|S_r\rangle$ is proportional to r^2 , which is negligible in our case. However, when the ions are not cooled to the ground state the above Hamiltonian creates an additional depumping process for the $|S_r\rangle$ state. Specifically, the state $|S_r\rangle|1\rangle$ is coupled by the sideband coupling to $|D\rangle \equiv \frac{1}{\sqrt{3}}(|\uparrow\uparrow\rangle|2\rangle - \sqrt{2}|\downarrow\downarrow\rangle|0\rangle)$ with a Rabi rate $\frac{2}{\sqrt{3}}r\Omega_s$. With sympathetic cooling $|D\rangle$ decays towards $|\uparrow\uparrow\rangle|0\rangle$ with a rate given by $\frac{2\kappa}{3}$. Taking into account the fraction of phonon-excited population $P_{>0} = \frac{\bar{n}}{\bar{n}+1} \approx \bar{n}$, we find an effective decay from $|S_r\rangle$ to $|\uparrow\uparrow\rangle$ at a rate

$$\kappa_r^- \approx \frac{16(r\Omega_s)^2\bar{n}}{5\kappa}. \quad (6.21)$$

In the ideal case, with no heating processes, the steady state will be $|S_r\rangle \approx |S\rangle$ and this depumping process can be avoided. However, as discussed below, the ions are cooled only to a steady state with $\bar{n} \approx 0.1$, and this depumping process causes errors in both the continuous and stepwise experiments. We perform a numerical simulation with identical parameters to the experiment but set $r = 0$ (while still including all other sources of error) and find the fidelity increases by 0.02 for the continuous (obtained from both the simulation and the rate equation model) and 0.01 for the stepwise implementation of the scheme. This source of error could be reduced or eliminated in several ways. For example, stabilizing the alignment of the beams will reduce fluctuations. A better approach would be to align the Raman beams to counter-propagate along the ion crystal axis. In this case alignment fluctuations would cause only fluctuations in Ω_s but not r . Potentially another approach would be to create the sideband coupling using

near-field microwaves (which would also eliminate the spontaneous emission errors) [157, 158].

The singlet state is insensitive to fluctuations in the magnetic field; however, gradients of the magnetic field lead to each qubit ion experiencing a different magnetic field, which breaks the degeneracy of the $|\uparrow\downarrow\rangle$ and $|\downarrow\uparrow\rangle$ states and therefore couples the singlet and triplet states. In our experiment we measured the singlet-to-triplet exchange period to be greater than 10 ms, which causes a negligible error in the scheme since the sideband coupling breaks the degeneracy of the singlet and triplet states. Fluctuations in the magnetic field also cause frequency offsets for the sideband and carrier drives by shifting the Zeeman splittings of the ${}^9\text{Be}^+$ energy levels. The typical frequency offset for the sideband drive is small compared to Ω_s and therefore negligible. The typical frequency offset for the carrier drive compared to Ω_s is more significant and leads to a decrease in the preparation since the $|\uparrow\rangle$ to $|a\rangle$ transition will not be resonant. However, for our estimated magnetic-field fluctuations of approximately 10^{-7} T, we find an error for the singlet state of less than one percent for both the continuous and stepwise implementations using the numerical simulations.

Heating Processes

Heating processes compete with the sympathetic cooling and lead to a steady state with a thermal distribution. The largest heating process is caused by spontaneous emission from the ${}^{24}\text{Mg}^+$ ions during the application of the ${}^{24}\text{Mg}^+$ sideband Raman beams and repump light. Other smaller sources of heating are photon recoil due to spontaneous emission from the repumper and electric-field noise at the ions' positions (including the so-called anomalous heating [159]). These heating processes limit the lowest achievable \bar{n} with sympathetic cooling for mode three to approximately 0.1 for both the continuous and stepwise cases. One error caused by these heating processes is the decrease in the singlet preparation rate as can be seen from Eq. (6.12), which leads to an error of 0.02 for the continuous case. However, if the only source of depumping from the singlet state is the inherent depumping (Eq. 6.14), the fidelity for the continuous case can still be made to approach unity in the presence of heating by further increasing the sideband Rabi rate relative to other rates and leaving the interactions on for a longer duration. Another source of error associated with the heating is due to the depumping process that results from unequal sideband Rabi rates on the ${}^9\text{Be}^+$ ions when the ions are not in the motional ground state, which leads to an error of 0.02 for the continuous case as discussed in the previous section.

For the stepwise implementation, there is an additional error associated with the heating that is due to the n dependence of Ω_{eff} , discussed in Sec. 6.3.3, that leads to depumping from the $|S\rangle$ state for $n \neq 0$. If we eliminate the heating processes in the numerical simulation of the stepwise implementation such that the ions are cooled to motional ground state the fidelity increases by approximately 0.04. This error combines the effects of the decrease in preparation rate, the depumping due to sideband Rabi rate imbalance, and the additional depumping effect due to the n dependence of Ω_{eff} .

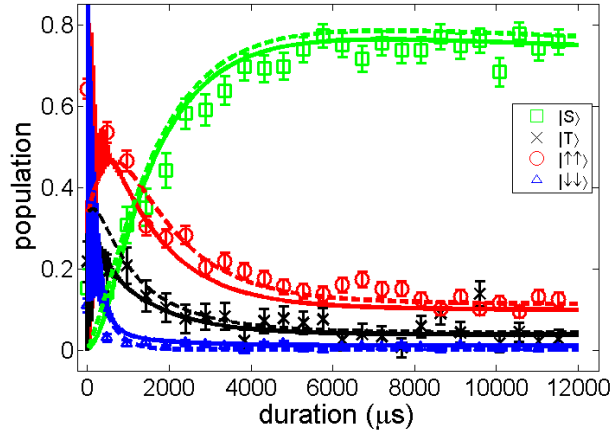


FIGURE 6.5: **Steady State Entanglement Data and Theory** We plot the dynamics of the ground-state populations obtained by solving the rate equations (dashed lines) and the master equation (solid lines) together with the experimental data (symbols). While the rate equations do not capture the fast oscillations in the beginning, they agree well with the dynamics of the master equation and the experimental data for longer durations.

Off-Resonant Coupling

Another potential source of error is off-resonant coupling of the ${}^9\text{Be}^+$ sideband beams to the qubit carrier transition or other motional mode sideband transitions. For our experimental parameters, the only significant coupling is that of the laser sideband to mode 4, which is detuned by approximately $\Delta\nu \approx 2\pi \times 250$ kHz from the sideband laser drive. The Hamiltonian term for this coupling is $H_4 = \Omega_s \frac{\eta_4}{\eta_3} (|\uparrow\rangle_1 \langle\downarrow| - |\uparrow\rangle_2 \langle\downarrow|) c^+ e^{-i\delta t} + H.c.$, where the minus sign occurs because the two ${}^9\text{Be}^+$ ions oscillate out of phase for mode 4. This couples $|S\rangle \leftrightarrow |\uparrow\uparrow\rangle|1\rangle_4$, where the motional excitation is in the fourth mode. Cooling of this mode with a rate $\kappa_4 \approx 0.8$ kHz leads to an effective loss process from $|S\rangle$ to $|\uparrow\uparrow\rangle$ at a rate

$$\kappa_4^- \approx \frac{2\kappa_4 (\Omega_s \frac{\eta_4}{\eta_3})^2}{\Delta\nu^2}. \quad (6.22)$$

The error due to this off-resonant coupling is estimated from the simulations to be 0.008 for the continuous (0.007 when using Eq. (6.7)) and 0.023 for the step-wise experiments. The strength of the off-resonant coupling could be reduced by using a better isolated motional mode frequency.

6.4.3 Results

In summary, we have derived the preparation rate γ_+ given in Eq. (6.12), the reshuffling rate κ_{res} in Eq. (6.13) and the loss rates

$$\gamma_{\uparrow\uparrow}^- = \frac{\gamma_{\text{inh}}^- \gamma_{\uparrow a}}{\gamma_{\uparrow a} + \gamma_{\downarrow a}} + \Gamma_{\uparrow\uparrow}^- + \kappa_r^- + \kappa_4^-, \quad (6.23)$$

$$\gamma_T^- = \frac{\gamma_{\text{inh}}^- \gamma_{\downarrow a}}{2(\gamma_{\downarrow a} + \gamma_{\uparrow a})} + \Gamma_T^-, \quad (6.24)$$

$$\gamma_{\downarrow\downarrow}^- = \Gamma_{\downarrow\downarrow}^-. \quad (6.25)$$

Using these rates we can model the experimental results by solving the coupled rate equations given by Eqs. (6.3)-(6.6). In Fig. 6.5 we plot the evolution of the ground states that is obtained using the experimental parameters to calculate the rates derived in this section. In total, we find for the continuous implementation an error of about 0.23 from the rate equation model, i.e., either from the steady-state fidelity in Eq. (6.7) or from the simulation of Eqs. (6.3)-(6.6). This is in good agreement with the value 0.24 obtained from the simulation of the master equation and the experimental results.

Reaching higher-fidelity maximally entangled states with this scheme should be possible if spontaneous emission rates and imbalances of the sideband coupling on the qubits can be reduced. As an example, if the Raman detuning is increased to 1.5 THz, which reduces the spontaneous emission error by approximately a factor of 23 compared to the experiments presented here, and the sideband coupling imbalance is eliminated, the maximum achievable fidelity would be approximately 0.97 using the continuous implementation. Here, we have kept the same heating rate, but assumed that errors due to off-resonant coupling have also been eliminated. To achieve the same sideband Rabi rate at this detuning, the laser intensity would need to be increased by a factor of 20. Implementing the sideband coupling with microwaves would eliminate both spontaneous emission and unequal sideband Rabi rates and may therefore be a possible future approach to achieve high-fidelity entangled states with this dissipative scheme if other issues with this approach, such as high anomalous background heating, can be addressed [160].

6.5 Summary

In conclusion, we have presented a theoretical scheme for deterministic steady state pumping of two trapped ions into a maximally entangled state, together with its experimental realization. By continuously driving the system towards steady state, the entangled state is prepared from an initial mixed state and then stabilized against decoherence. Our theoretical analysis of the experiment shows that the achieved fidelities are limited by known experimental imperfections.

Our demonstration that a maximally entangled steady state of two qubits can be prepared by engineered dissipation shows that dissipative state preparation is experimentally feasible. It represents a step towards the long term goals of dissipative state engineering, dissipative quantum computation, and dissipative

phase transitions [19, 20, 121]. Engineered coupling to the environment may be applied to a broad range of experimental systems to achieve desired quantum dynamics or steady states.

Dissipative preparation of many-body entanglement

In the preceding chapters we have presented schemes for the preparation of two-particle entanglement in several quantum optical and solid state systems. As we initially discussed in Chapter 2, such small entangled states can be useful to demonstrate non-locality of nature and for quantum communication tasks, whereas more advanced protocols require multi-particle entanglement. The two most widely discussed quantum states which exhibit entanglement of a large number of qubits are the Greenberger-Horne-Zeilinger (GHZ) and W states,

$$|\text{GHZ}\rangle = \frac{1}{\sqrt{2}} (|00\dots 00\rangle + |11\dots 11\rangle), \quad (7.1)$$

$$|\text{W}\rangle = \frac{1}{\sqrt{N}} (|0\dots 01\rangle + |0\dots 010\rangle + \dots + |10\dots 0\rangle), \quad (7.2)$$

previously introduced in Sec. 2.1.3. Beside quantum communication and cryptography, such states are of great interest for quantum error correction schemes [6], and quantum measurements [11].

Preparation of many-body entangled states has so far been performed using time-dependent unitary gates [33, 52], yielding impressive progress towards entangling larger numbers of qubits [53, 54, 57]. These operations, however, suffer from decoherence and dissipation and the generation of high-fidelity multi-particle entangled states remains an outstanding challenge. To resolve this obstacle, the idea of dissipative state preparation described in Sec. 2.4.3 has also been considered for the generation of multi-particle entanglement [87, 94, 96, 161, 162]. So far, however, no approach has been developed for the preparation of high-fidelity many-body entangled steady states.

In this chapter, we extend our techniques for dissipative preparation from two-particle entanglement to multi-particle entanglement. We show that by adding sources of dissipation to a generic system we can engineer complex many-body dissipation. Using this technique, we demonstrate that many-body Greenberger-Horne-Zeilinger (GHZ) and W states can be prepared and stabilized as the steady states of the dissipative time evolution. Our protocols exhibit a favorable scaling of the preparation time with the number of qubits. In addition to

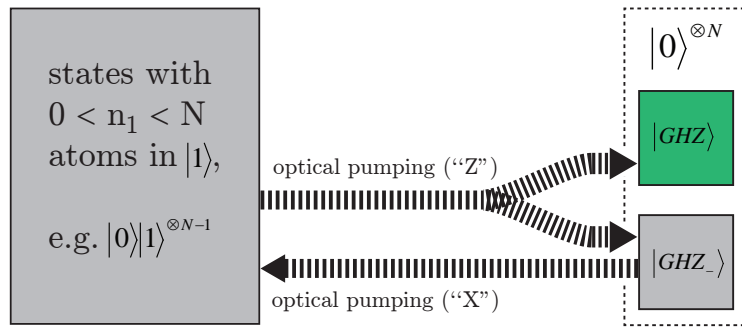


FIGURE 7.1: Protocol for the dissipative preparation of a GHZ state of N qubits. Preparation of a GHZ state can be realized by two operations: (i) Pumping of states with $0 < n_1 < N$ atoms in state $|1\rangle$ into $|0\rangle^{\otimes N}$, which is a superposition of $|GHZ\rangle$ and $|GHZ_-\rangle$, and (ii) removal of $|GHZ_-\rangle$.

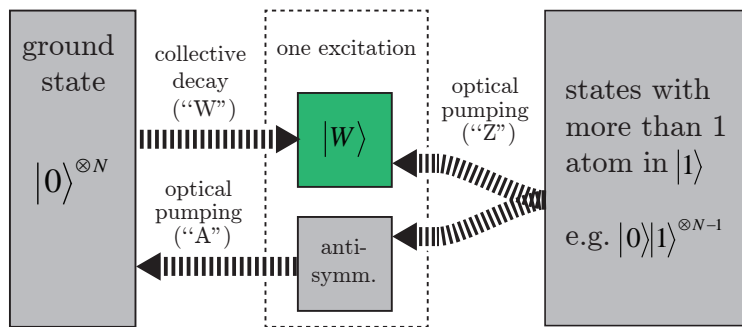


FIGURE 7.2: Protocols for the dissipative preparation of a W state of N qubits. W state preparation can be accomplished by pumping all states with $n_1 > 1$ atoms in $|1\rangle$ into those with $n_1 \leq 1$ and pumping the asymmetric states with $n_1 = 1$ into $|0\rangle^{\otimes N}$. Collective decay from $|0\rangle^{\otimes N}$ is used to prepare $|W\rangle$ from $|0\rangle^{\otimes N}$.

our a priori system-independent protocols, we consider an ion trap setup for the implementation of our schemes. Our study paves the way for the dissipative preparation of entangled steady states of a higher number of qubits.

We start by presenting the protocols for the dissipative preparation of GHZ and W states in Sec. 7.1. In Sec. 7.2 we discuss the generic system of atoms coupled to a harmonic oscillator to which we add tunable sources of dissipation. We show how to engineer effective decay processes to prepare steady GHZ states in Sec. 7.3 and W states in Sec. 7.5. This is done deterministically by continuous optical driving from any initial state towards the target state and is achieved using weak classical fields without the need to apply pulses or to measure the state of the system. The performance of the schemes for GHZ and W state preparation and their scaling¹ are examined in Sec. 7.4 and Sec. 7.6, and in App. E and App. F. The preparation times of our protocols are found to have a favorable polynomial scaling with the number of qubits. An implementation based on a system of trapped ions is presented in Sec. 7.7. We conclude the chapter with a summary in Sec. 7.8.

¹The analysis of the scaling of the presented schemes has been performed in collaboration with D. Reeb.

7.1 Protocols for the dissipative preparation of GHZ and W states

The challenge for any dissipative many-body protocol is to pump an exponential number of states efficiently, i.e. in polynomial time. In the following, we demonstrate that this is possible using only a small number of elementary operations: Preparation of a GHZ state starting from any initial state can, regardless of the number of qubits N , be divided into the two operations shown in Fig. 7.1: (i) Pumping all states with neither none nor all qubits in state $|1\rangle$ to the state $|0\rangle^{\otimes N}$ and (ii) removal of the GHZ state with the wrong phase, $|\text{GHZ}_-\rangle = \frac{1}{\sqrt{2}}(|0\rangle^{\otimes N} - |1\rangle^{\otimes N})$. These mechanisms are nontrivial as they require N -body dissipative interactions. Below we present a way to accomplish both (i) and (ii) in a realistic physical system.

Preparation of the W state can in principle be performed by a single collective jump from $|0\rangle^{\otimes N}$ to $|W\rangle$, as can be seen from Fig. 7.2. However, in order to guarantee $|W\rangle$ to be the steady state for any initial state, it is necessary to also remove states with more atoms in $|1\rangle$ and all superpositions that do not exhibit permutation symmetry like the W state.

7.2 System

For the realization of the protocols we assume a general system of N particles (“atoms”), shown in Fig. 7.3. Each atom consists of two stable ground states $|0\rangle$ and $|1\rangle$ and two excited states, $|e\rangle$ and $|f\rangle$. The atoms collectively couple to two harmonic oscillator modes, a , and b , such as two cavity modes in cavity QED or two phononic modes in an ion trap setup. We consider two dissipative processes: Spontaneous emission from the excited states to the ground states acts incoherently on all atoms. In addition, we assume loss of excitations from the oscillator modes, such as photon loss in cavity QED or phonon loss due to sympathetic cooling in a chain of ions. For our schemes we use classical fields which couple identically to all atoms. While the setup with two excited states and two oscillator modes is completely steady, it is also possible to implement our schemes in a stroboscopic manner. Here, a single excited level and a single oscillator mode are used in two interchanging coupling situations, resulting in a quasi-steady state (see also Sec. 7.7).

7.2.1 Dynamical model

The dynamics of the system is modeled by a master equation of Lindblad form

$$\dot{\rho} = \mathcal{L}(\rho) = -i[H, \rho] + \sum_k L_k \rho L_k^\dagger - \frac{1}{2} \left(L_k^\dagger L_k \rho + \rho L_k^\dagger L_k \right). \quad (7.3)$$

The Hamiltonian H is generally given by

$$H = H_{\text{free}} + H_{\text{int}} + H_{\text{drive}}. \quad (7.4)$$

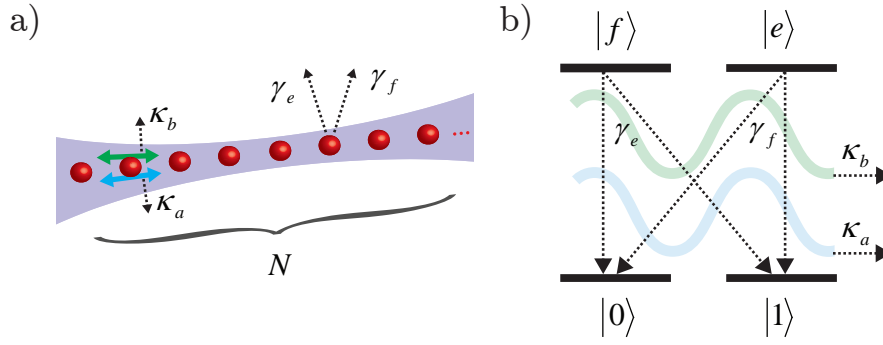


FIGURE 7.3: System. (a) We consider a chain of N sub-systems (“atoms”). (b) Each atom has four levels and is coupled to two harmonic oscillators. The decay processes present in the system are decay by incoherent spontaneous emission γ and decay of the common oscillator modes $\kappa_{a/b}$. Depending on the scheme, we apply classical fields and couplings of the atoms to the oscillator modes.

We consider a free Hamiltonian H_{free} which contains the energies of the levels of the N atoms and the harmonic oscillator modes,

$$H_{\text{free}} = \omega_e J_{ee} + \omega_f J_{ff} + \omega_a a^\dagger a + \omega_b b^\dagger b. \quad (7.5)$$

Here, we have introduced $J_{ij} = \sum_{a=1}^N \sigma_a^{ij} = \sum_{a=1}^N |i\rangle_a \langle j|$ and made the simplifications $\omega_0 = \omega_1 = 0$ and $\hbar = 1$. An interaction Hamiltonian H_{int} describes the atom-oscillator coupling, and a drive Hamiltonian H_{drive} contains the fields used to perform coherent excitations of the system. The particular coupling configurations, i.e. the interaction and drive terms required for either GHZ or W preparation, are detailed in the sections 7.3.1 and 7.5.1.

As pointed out above, the excited degrees of freedom in the system are subject to dissipation which we will later on consider to be adjustable (see Sec. 7.7). Here, the excited states $|e\rangle$ and $|f\rangle$ of each atom undergo spontaneous emission to each of the ground states $|0\rangle$ and $|1\rangle$, described by the jump operators

$$L_{\gamma_{0e},a} = \sqrt{\gamma_{0e}} |0\rangle_a \langle e|, \quad (7.6)$$

$$L_{\gamma_{1e},a} = \sqrt{\gamma_{1e}} |1\rangle_a \langle e|, \quad (7.7)$$

$$L_{\gamma_{0f},a} = \sqrt{\gamma_{0f}} |0\rangle_a \langle f|, \quad (7.8)$$

$$L_{\gamma_{1f},a} = \sqrt{\gamma_{1f}} |1\rangle_a \langle f|, \quad (7.9)$$

where the subscript a denotes the atom number. The total decay rates of the excited levels are given by $\gamma_e = \gamma_{0e} + \gamma_{1e}$ and $\gamma_f = \gamma_{0f} + \gamma_{1f}$. For simplicity we will assume equal decay rates for both excited states in the W scheme, which is, however, not crucial for the protocol. The decay of excitations of the two oscillator modes, a and b , is represented by

$$L_{\kappa_a} = \sqrt{\kappa_a} a, \quad (7.10)$$

$$L_{\kappa_b} = \sqrt{\kappa_b} b. \quad (7.11)$$

The GHZ scheme does not require oscillator decay at all ($\kappa_a = \kappa_b = 0$). It may, however, still be useful to avoid heating. For W preparation, on the other hand, we assume dissipation of one of the modes ($\kappa_a > 0$).

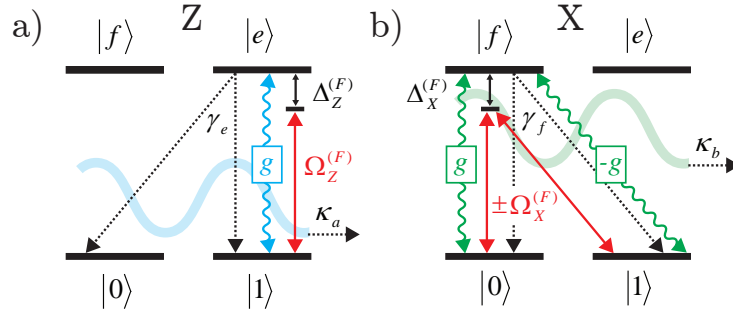


FIGURE 7.4: Setup for GHZ preparation. For the dissipative preparation of GHZ states in the system presented in Sec. 7.2 we combine two coupling configurations, ‘Z’ and ‘X’, each consisting of an atom-oscillator coupling and a weak coherent drive. (a) The ‘Z configuration’ consists of a coupling of the transition from $|e\rangle$ to $|1\rangle$ to the harmonic oscillator a with a coupling constant g . A multi-tone drive with individual Rabi frequencies $\Omega_Z^{(F)}$ and detunings $\Delta_Z^{(F)}$ for the tones F acts on the same transition. (b) In the ‘X configuration’ the harmonic oscillator b couples to both the transitions from $|f\rangle$ to $|0\rangle$ and from $|f\rangle$ to $|1\rangle$. Using opposite phases on both transitions thus creates an atom-oscillator coupling on the transition from $|f\rangle$ to $|-\rangle = \frac{1}{\sqrt{2}}(|0\rangle - |1\rangle)$. The corresponding multi-tone drive with $\Omega_X^{(F)}$ and $\Delta_X^{(F)}$ acts on the same transition.

7.3 Realization of the GHZ protocol

In the following, we demonstrate how the protocol for GHZ preparation proposed in Sec. 7.1 can be realized in the physical system described in Sec. 7.2. To this end, we present a suitable setup in Sec. 7.3.1. In Sec. 7.3.2 and 7.3.3 we engineer effective decay processes that allow for the preparation of a GHZ state. The performance of the scheme is discussed in Sec. 7.4.

7.3.1 Setup

For the preparation of GHZ states we consider two coupling configurations, ‘Z’ and ‘X’ (named after $\sigma_z = |1\rangle\langle 1| - |0\rangle\langle 0|$ and $\sigma_x = |1\rangle\langle 0| + |0\rangle\langle 1|$, as will become clear further below), shown in Fig. 7.4 a) and b). These consist of atom-oscillator couplings and classical drives. The atom-oscillator couplings are described by an interaction Hamiltonian $H_{\text{int}} = H_{\text{int,Z}} + H_{\text{int,X}}$ with

$$H_{\text{int,Z}} = g \left(a^\dagger J_{1e} + a J_{1e}^\dagger \right), \quad (7.12)$$

$$H_{\text{int,X}} = g \left(b^\dagger J_{-f} + b J_{-f}^\dagger \right). \quad (7.13)$$

Here, ‘Z’ and ‘X’ denote the coupling configurations, and g is the coupling constant of the atom-oscillator coupling. By $H_{\text{int,Z}}$, an atomic excitation in $|e\rangle$ is exchanged with the oscillator a , leaving the atom in $|1\rangle$. $H_{\text{int,X}}$ couples the excited level $|f\rangle$ to $|-\rangle = \frac{1}{\sqrt{2}}(|0\rangle - |1\rangle)$ while exchanging the atomic excitation with the oscillator b . In addition, we assume coherent excitation of the atoms by classical driving fields along the same transitions as the atom-oscillator couplings,

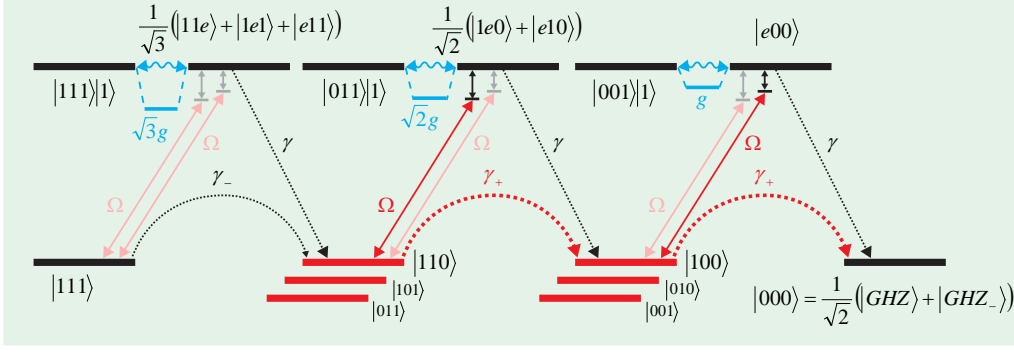


FIGURE 7.5: First dissipative mechanism for GHZ preparation, shown for $N = 3$ qubits. Pumping towards $|0\rangle^{\otimes N} = \frac{1}{\sqrt{2}}(|\text{GHZ}\rangle + |\text{GHZ}_-\rangle)$, “Z pumping”, is achieved using the coupling configuration shown in Fig. 7.4 a). Ground states are coupled to atom-excited states by weak driving. Dependent on the number n_1 of atoms in $|1\rangle$, the excited states form dressed states with oscillator-excited states at energies $\pm\sqrt{n_1}g$. By applying fields with detunings $\Delta_Z^{(F)} = \sqrt{F}g$ for $1 \leq F \leq N$, all states except $|\text{GHZ}\rangle$ and $|\text{GHZ}_-\rangle$ are pumped towards $|0\rangle^{\otimes N} = \frac{1}{\sqrt{2}}(|\text{GHZ}\rangle + |\text{GHZ}_-\rangle)$.

described by a Hamiltonian $H_{\text{drive}} = H_{\text{drive,Z}} + H_{\text{drive,X}}$ with

$$H_{\text{drive,Z}} = \frac{1}{2} \sum_F \Omega_Z^{(F)} e^{-i\omega_Z^{(F)} t} J_{e1} + H.c., \quad (7.14)$$

$$H_{\text{drive,X}} = \frac{1}{2} \sum_F \Omega_X^{(F)} e^{-i\omega_X^{(F)} t} J_{f-} + H.c. \quad (7.15)$$

Here, we generally allow for several field tones with Rabi frequencies $\Omega_{Z/X}^{(F)}$ and frequencies $\omega_{Z/X}^{(F)}$. We define detunings for each drive tone F ,

$$\Delta_Z^{(F)} = \omega_e - \omega_Z^{(F)}, \quad \delta_Z^{(F)} = \omega_a - \omega_Z^{(F)}, \quad (7.16)$$

$$\Delta_X^{(F)} = \omega_f - \omega_X^{(F)}, \quad \delta_X^{(F)} = \omega_b - \omega_X^{(F)}. \quad (7.17)$$

Below we will choose these detunings of the available fields in such a way as to the engineer effective decay processes in the system to be either enhanced or suppressed.

7.3.2 Preparing $|\text{GHZ}\rangle$: the Z pumping

We implement the first dissipative mechanism for the preparation of an N -particle GHZ state. In the following, we refer to this process as “Z pumping”, as it is best understood in the eigenbasis of $\sigma_z = |1\rangle\langle 1| - |0\rangle\langle 0|$, given by the states $|0\rangle$ and $|1\rangle$. According to requirement (i) in Sec. 7.1 this process shall transfer all states with $0 < n_1 < N$ atoms in $|1\rangle$, i.e., all states other than $|0\rangle^{\otimes N}$ and $|1\rangle^{\otimes N}$, to $|0\rangle^{\otimes N} = \frac{1}{\sqrt{2}}(|\text{GHZ}\rangle + |\text{GHZ}_-\rangle)$. This is achieved by making states with $1 \leq n_1 \leq N - 1$ decay into those with $n_1 - 1$. At the same time, we need to insure that the residual decay out of $|1\rangle^{\otimes N}$ by the same process is weak, in order to not cause losses from $|\text{GHZ}\rangle$.

We engineer this process using the coupling configuration in Fig. 7.4 a). Here, the oscillator coupling g of the transition $|e\rangle \leftrightarrow |1\rangle$ and a weak drive on the same transition are used to effectively “count” the number of atoms in state $|1\rangle$: As illustrated in Fig. 7.5 for the example of $N = 3$ qubits, the weak drive Ω couples any ground state with n_1 atoms in $|1\rangle$ to an atom-excited state. This state is coupled to an oscillator-excited state with n_1 atoms in $|1\rangle$ by an atom-oscillator coupling with a strength of $\sqrt{n_1}g$. Hence, the atom- and the oscillator-excited state form dressed states at energies $\pm\sqrt{n_1}g$. We pump all ground states with $1 \leq n_1 \leq N - 1$ towards those with $n_1 - 1$ by exciting them with weak driving tones $\Omega_Z^{(F)}$ detuned by $\Delta_Z^{(F)} = \sqrt{F}g$, where $1 \leq F \leq N - 1$. The excited states with n_1 then decay towards ground states with $n_1 - 1$ by spontaneous emission from $|e\rangle$ to $|0\rangle$. This operation continuously pumps population from all states with $1 \leq n_1 \leq N - 1$ to $|0\rangle^{\otimes N}$, resulting in the production of $|\text{GHZ}\rangle$ and $|\text{GHZ}_-\rangle$. As it will turn out further down, it is favorable to apply two sets of drives with red ($\Delta_{Z+}^{(F)} = +\sqrt{F}g$) and blue detunings ($\Delta_{Z-}^{(F)} = -\sqrt{F}g$). A second process, which is discussed in Sec. 7.3.3, is used to empty the state $|\text{GHZ}_-\rangle$. In the sections below we analyze the engineering of the Z pumping process quantitatively.

Effective operators for the Z configuration

In the following, we provide a detailed analysis of the dynamics of the system under the action of the Z pumping mechanism. Given that the dissipation affects the excited levels $|e\rangle$ and $|f\rangle$ and the oscillator modes a and b and assuming the drives to be sufficiently weak, we can adiabatically eliminate these decaying degrees of freedom from the master equation. This is done using the effective operator formalism presented in Chapter 3. In this way, the dynamics of the master equation (7.3) are reduced to effective couplings between the ground states of the system, described by an effective master equation

$$\dot{\rho} = -i[H_{\text{eff}}, \rho] + \sum_k L_{k,\text{eff}}\rho(L_{k,\text{eff}})^\dagger - \frac{1}{2} \left((L_{k,\text{eff}})^\dagger L_{k,\text{eff}}\rho + \rho(L_{k,\text{eff}})^\dagger L_{k,\text{eff}} \right), \quad (7.18)$$

where the F 's denote the driving field tones that give rise to the effective couplings. Instead of presenting the steps of the derivation of the effective operators H_{eff} and $L_{k,\text{eff}}$ for the GHZ scheme here, we refer the reader to App. D, where the calculations are given. Here, we focus on the discussion of the terms. In App. D, we find for the effective Lindblad operators for the Z configuration

$$L_{\kappa_a, Z}^{(F)} = \sum_{n_1=0}^N \frac{\sqrt{\kappa_a}\Omega_Z^{(F)}}{2\tilde{g}_{Z, n_1}^{(F)}} P_{n_1}, \quad (7.19)$$

$$L_{\gamma_{0e}, a, Z}^{(F)} = \sum_{n_1=0}^N \frac{\sqrt{\gamma_{0e}}\Omega_Z^{(F)}}{2\tilde{\Delta}_{Z, n_1}^{(F)}} |0\rangle_a \langle 1| P_{n_1}, \quad (7.20)$$

$$L_{\gamma_{1e}, a, Z}^{(F)} = \sum_{n_1=0}^N \frac{\sqrt{\gamma_{1e}}\Omega_Z^{(F)}}{2\tilde{\Delta}_{Z, n_1}^{(F)}} |1\rangle_a \langle 1| P_{n_1}. \quad (7.21)$$

These operators are formulated in terms of multiple tones of a driving field, denoted by F . Each tone acts on all states with the same number of atoms n_1

in state $|1\rangle$, represented by the projection operator P_{n_1} . The magnitude of the effective processes is determined by the effective detunings

$$\tilde{\Delta}_{Z,n_1}^{(F)} = \tilde{\Delta}_Z^{(F)} - \frac{n_1 g^2}{\tilde{\delta}_Z^{(F)}}, \quad (7.22)$$

$$\tilde{\delta}_{Z,n_1}^{(F)} = g - \frac{\tilde{\Delta}_Z^{(F)} \tilde{\delta}_Z^{(F)}}{n_1 g}. \quad (7.23)$$

Here, we have generalized the detunings in Eq. (7.16) to complex energies

$$\tilde{\Delta}_Z^{(F)} = \omega_e - \omega_Z^{(F)} - \frac{i\gamma_e}{2} = \Delta_Z^{(F)} - \frac{i\gamma_e}{2}, \quad (7.24)$$

$$\tilde{\delta}_Z^{(F)} = \omega_a - \omega_Z^{(F)} - \frac{i\kappa_a}{2} = \delta_Z^{(F)} - \frac{i\kappa_a}{2}, \quad (7.25)$$

which also account for the line widths of the excited states, given by their decay rates. We define effective decay rates for the operators in Eqs. (7.19)–(7.21),

$$\kappa_{a,Z,n_1}^{(F)} = \frac{\kappa_a (\Omega_Z^{(F)})^2}{4 |\tilde{\delta}_{Z,n_1}^{(F)}|^2}, \quad (7.26)$$

$$\gamma_{0,Z,n_1}^{(F)} = \frac{\gamma_{0e} (\Omega_Z^{(F)})^2}{4 |\tilde{\Delta}_{Z,n_1}^{(F)}|^2}, \quad (7.27)$$

$$\gamma_{1,Z,n_1}^{(F)} = \frac{\gamma_{1e} (\Omega_Z^{(F)})^2}{4 |\tilde{\Delta}_{Z,n_1}^{(F)}|^2}. \quad (7.28)$$

As can be seen from the expressions in Eqs. (7.22)–(7.23), the effective detunings $\tilde{\Delta}_{Z,n_1}^{(F)}$ and hence the rates $\gamma_{0,Z,n_1}^{(F)}$ and $\gamma_{1,Z,n_1}^{(F)}$ of the effective decay processes can be engineered very small by a suitable choice of the frequencies ω_F of the fields F .

The effective Hamiltonian is generally given by

$$H_Z \approx - \sum_{n_1=0}^N \sum_F \operatorname{Re} \left(\frac{n_1 (\Omega_Z^{(F)})^2}{4 \tilde{\Delta}_{Z,n_1}^{(F)}} \right) P_{n_1} \equiv \sum_{n_1=0}^N \sum_F s_{Z,n_1}^{(F)} P_{n_1}, \quad (7.29)$$

It contains, as effective Hamiltonian processes, AC Stark shifts with a magnitude

$$s_{Z,n_1}^{(F)} = -\operatorname{Re} \left(\frac{n_1 (\Omega_Z^{(F)})^2}{4 \tilde{\Delta}_{Z,n_1}^{(F)}} \right) \quad (7.30)$$

As we will see below, our choice of the field tones will make these Hamiltonian terms compensate each other.

Engineered operators for the Z configuration

In the following, we consider the engineering of the effective operators under the particular choice of parameters.

To transfer the population of all states except $|0\rangle^{\otimes N}$ and $|1\rangle^{\otimes N}$ to $|0\rangle^{\otimes N}$ without

affecting the GHZ state we have chosen to apply drives $\Omega_{Z\pm}^{(F)} = \Omega_Z^{(F)}$ in the Z configuration with detunings $\Delta_{Z\pm}^{(F)} = \delta_{Z\pm}^{(F)} = \pm\sqrt{F}g$, where $1 \leq F \leq N-1$. If the field index F coincides with the number n_1 of atoms in $|1\rangle$ for a certain initial state and driving field, the field is on resonance and the effective detunings in Eqs. (7.22)–(7.23) become

$$\tilde{\Delta}_{Z\pm, n_1}^{(F=n_1)} = \tilde{\Delta}_{Z\pm}^{(F)} - \frac{n_1 g^2}{\tilde{\delta}_{Z\pm}^{(F)}} \approx -\frac{i}{2}(\gamma_e + \kappa_a) \quad (7.31)$$

$$\tilde{g}_{Z\pm, n_1}^{(F=n_1)} = g - \frac{\tilde{\Delta}_{Z\pm}^{(F)} \tilde{\delta}_{Z\pm}^{(F)}}{n_1 g} \approx \frac{i}{2} \frac{\gamma_e + \kappa_a}{\sqrt{n_1}}. \quad (7.32)$$

Here, the subscript $Z+$ denotes the fields with positive detunings and $Z-$ those with negative detunings. Since we generally work in the strong coupling limit $\gamma, \kappa \ll g$, the above effective detunings are small compared to those for off-resonant driving fields with $n_1 \neq F$,

$$\tilde{\Delta}_{Z\pm, n_1}^{(F \neq n_1)} \approx \pm \frac{F - n_1}{\sqrt{F}} g, \quad (7.33)$$

$$\tilde{g}_{Z\pm, n_1}^{(F \neq n_1)} \approx \frac{n_1 - F}{n_1} g. \quad (7.34)$$

With the effective detunings we can then compute the effective decay rates in Eq. (7.26)–(7.28) for the resonant processes with $F = n_1$ and for the off-resonant ones with $F \neq n_1$,

$$\kappa_{Z\pm, n_1}^{(F=n_1)} = \frac{n_1 \kappa_a (\Omega_Z^{(F)})^2}{(\gamma_e + \kappa_a)^2}, \quad \kappa_{Z\pm, n_1}^{(F \neq n_1)} = \frac{n_1^2 \kappa_a (\Omega_Z^{(F)})^2}{4(n_1 - F)^2 g^2}. \quad (7.35)$$

$$\gamma_{0, Z\pm, n_1}^{(F=n_1)} = \frac{\gamma_{0e} (\Omega_Z^{(F)})^2}{(\gamma_e + \kappa_a)^2}, \quad \gamma_{0, Z\pm, n_1}^{(F \neq n_1)} = \frac{F \gamma_{0e} (\Omega_Z^{(F)})^2}{4(F - n_1)^2 g^2}, \quad (7.36)$$

$$\gamma_{1, Z\pm, n_1}^{(F=n_1)} = \frac{\gamma_{1e} (\Omega_Z^{(F)})^2}{(\gamma_e + \kappa_a)^2}, \quad \gamma_{1, Z\pm, n_1}^{(F \neq n_1)} = \frac{F \gamma_{1e} (\Omega_Z^{(F)})^2}{4(F - n_1)^2 g^2}, \quad (7.37)$$

We can clearly notice that the first group of rates is engineered to be strong, while the second group of rates is engineered to be suppressed. Using the entities above we obtain for the Lindblad operators in Eqs. (7.19)–(7.21).

$$L_{\kappa, Z\pm}^{(F)} \approx \sum_{n_1=1}^{N-1} \left[\sqrt{\kappa_{Z\pm, n_1}^{(F=n_1)}} + \mathcal{O}\left(\frac{1}{g^2}\right) \right] P_{n_1} \quad (7.38)$$

$$+ \sqrt{\kappa_{Z\pm, n_1}^{(F \neq N)}} P_N, \quad (1 \leq F \leq N-1), \quad (7.39)$$

$$L_{\gamma_{0,a}, Z\pm}^{(F)} \approx \sum_{n_1=1}^{N-1} \left[\sqrt{\gamma_{0, Z\pm, n_1}^{(F=n_1)}} |0\rangle_a \langle 1| + \mathcal{O}\left(\frac{1}{g^2}\right) \right] P_{n_1} + \quad (7.40)$$

$$+ \sqrt{\gamma_{0, Z\pm, n_1}^{(F \neq N)}} |0\rangle_a \langle 1| P_N, \quad (1 \leq F \leq N-1), \quad (7.41)$$

$$L_{\gamma_{1,a}, Z\pm}^{(F)} \approx \sum_{n_1=1}^{N-1} \left[\sqrt{\gamma_{1, Z\pm, n_1}^{(F=n_1)}} |1\rangle_a \langle 1| + \mathcal{O}\left(\frac{1}{g^2}\right) \right] P_{n_1} + \quad (7.42)$$

$$+ \sqrt{\gamma_{1, Z\pm, n_1}^{(F \neq N)}} |1\rangle_a \langle 1| P_N, \quad (1 \leq F \leq N-1). \quad (7.43)$$

From the above expression we see that for $1 \leq n_1 \leq N - 1$ there are always find terms with $n_1 = F$ to zeroth order in g^{-1} which are much larger rates than the ones with $n_1 \neq F$ which are to second order in g^{-1} . We can therefore drop the latter for $1 \leq n_1 \leq N - 1$. The terms with $n_1 = N$ which in particular affect the GHZ state need, however, to be kept. Since the effective detunings are engineered to depend on n_1 , photons scattered by resonances with different n_1 can be distinguished. Formally this is justified by the exponential factors $e^{-i\omega t}$ washing out interferences between terms (see App. D. We can therefore separate the terms with different n_1 into individual Lindblad operators, each acting on a set of states with n_1 atoms in $|1\rangle$. The enhanced processes are then given by

$$L_{\kappa, Z_{\pm}}^{(F=n_1)} \approx \sqrt{\kappa_{Z_{\pm}, n_1}^{(F=n_1)}} P_{n_1=F}, \quad (1 \leq F \leq N - 1), \quad (7.44)$$

$$L_{\gamma_{0,a}, Z_{\pm}}^{(F=n_1)} \approx \sqrt{\gamma_{0, Z_{\pm}, n_1}^{(F=n_1)}} |0\rangle_a \langle 1| P_{n_1=F}, \quad (1 \leq F \leq N - 1), \quad (7.45)$$

$$L_{\gamma_{1,a}, Z_{\pm}}^{(F=n_1)} \approx \sqrt{\gamma_{1, Z_{\pm}, n_1}^{(F=n_1)}} |1\rangle_a \langle 1| P_{n_1=F}, \quad (1 \leq F \leq N - 1). \quad (7.46)$$

The weak decay processes affecting $|1\rangle^{\otimes N}$, and thus, $|\text{GHZ}\rangle$ are found to be

$$L_{\kappa, Z_{\pm}}^{(F \neq n_1)} |\text{GHZ}\rangle \approx \sqrt{\kappa_{Z_{\pm}, n_1}^{(F \neq n_1)}} P_{n_1=N} |\text{GHZ}\rangle, \quad (1 \leq F \leq N - 1), \quad (7.47)$$

$$\approx \frac{1}{2} \sqrt{\kappa_{Z_{\pm}, n_1}^{(F \neq n_1)}} (|\text{GHZ}\rangle + |\text{GHZ}_-\rangle), \quad (1 \leq F \leq N - 1), \quad (7.48)$$

$$L_{\gamma_{0,a}, Z_{\pm}}^{(F \neq n_1)} |\text{GHZ}\rangle \approx \sqrt{\gamma_{0, Z_{\pm}, n_1}^{(F \neq n_1)}} |0\rangle_a \langle 1| P_{n_1=N} P_{\text{GHZ}}, \quad (1 \leq F \leq N - 1), \quad (7.49)$$

$$\approx \frac{1}{2} \sqrt{\gamma_{0, Z_{\pm}, n_1}^{(F \neq n_1)}} |0\rangle_a \langle 1| (|\text{GHZ}\rangle + |\text{GHZ}_-\rangle), \quad (1 \leq F \leq N - 1), \quad (7.50)$$

$$L_{\gamma_{1,a}, Z_{\pm}}^{(F \neq n_1)} |\text{GHZ}\rangle \approx \sqrt{\gamma_{1, Z_{\pm}, n_1}^{(F \neq n_1)}} |1\rangle_a \langle 1| P_{n_1=N} P_{\text{GHZ}}, \quad (1 \leq F \leq N - 1), \quad (7.51)$$

$$\approx \frac{1}{2} \sqrt{\gamma_{1, Z_{\pm}, n_1}^{(F \neq n_1)}} |1\rangle_a \langle 1| (|\text{GHZ}\rangle + |\text{GHZ}_-\rangle), \quad (1 \leq F \leq N - 1). \quad (7.52)$$

The result of the engineering of the effective processes for the Z configuration is thus the Z pumping by which all population from states with $1 \leq n_1 \leq N - 1$ is transferred to $|\text{GHZ}\rangle$ and $|\text{GHZ}_-\rangle$.

Beside effective decay processes, we also derive an effective Hamiltonian from by Eq. (7.29), which we write as $H_Z = H_{Z+} + H_{Z-}$ with

$$H_{Z_{\pm}} \approx \mp \sum_{n_1=0}^N \frac{n_1}{4g} \sum_{F \neq n_1} \frac{\sqrt{F} (\Omega_Z^{(F)})^2}{F - n_1} P_{n_1} \equiv \sum_{n_1=0}^N \sum_F s_{Z_{\pm}, n_1}^{(F)} P_{n_1}. \quad (7.53)$$

These terms are AC Stark shifts whose magnitude is obtained from Eq. (7.30),

$$s_{Z_{\pm}, n_1}^{(F)} \approx \mp \frac{n_1 \sqrt{F} (\Omega_Z^{(F)})^2}{4(F - n_1)g} \quad (7.54)$$

By our combination of red-detuned drives ($\Omega_{Z+}^{(F)}, \Delta_{Z+}^{(F)}$) and blue-detuned drives ($\Omega_{Z-}^{(F)}, \Delta_{Z-}^{(F)}$) with $\Omega_{Z+}^{(F)} = \Omega_{Z-}^{(F)}$ and $\Delta_{Z+}^{(F)} = -\Delta_{Z-}^{(F)}$ we achieve that the shifts compensate each other,

$$H_Z \approx H_{Z+} + H_{Z-} \approx 0. \quad (7.55)$$

Given that there are no Hamiltonian terms, we turn to a description of the dynamics in terms by rate equations below.

Engineered decay rates for Z pumping

In Sec. 3.7, we have described the possibility to reduce the effective dynamics further to rate equations. To perform such a step, we identify subspaces inside which all states have the same decay rate and in-between which no significant correlations are built up. It is therefore important that the effective Hamiltonian is zero. We define the subspaces by the projectors $P_{\text{GHZ}} = |\text{GHZ}\rangle\langle\text{GHZ}|$, $P_{\text{GHZ}_-} = |\text{GHZ}_-\rangle\langle\text{GHZ}_-|$, and P_{n_1} , which contain the states with a certain number of atoms in $|1\rangle$. The decay rates can then be calculated using Eq. (3.98). For resonant Z pumping ($F = n_1$) from a subspace with n_1 atoms in $|1\rangle$ to one with $n_1 - 1$ due to spontaneous emission to $|0\rangle$ we obtain the rate

$$\Gamma_{n_1 \rightarrow n_1-1, \gamma_0, Z\pm}^{(F=n_1)} \approx \sum_a \sum_k |\langle \psi_k | P_{n_1-1} L_{\gamma_0, a, Z\pm}^{(F=n_1)} P_{n_1} | \psi_j \rangle|^2 \approx \frac{n_1 \gamma_{0e} (\Omega_Z^{(F=n_1)})^2}{(\gamma_e + \kappa_a)^2}. \quad (7.56)$$

The subscripts in the above and the following decay rates specify the initial subspace, the final subspace, the physical process, i.e. oscillator decay (κ), spontaneous emission to $|0\rangle$ (γ_0) or $|1\rangle$ (γ_1), and the pumping process (here: Z). As opposed to the resonant rate ($F = n_1$) above, the decay rates due to off-resonant fields can be written as

$$\Gamma_{n_1 \rightarrow n_1-1, \gamma_0, Z\pm}^{(F \neq n_1)} = \sum_F \sum_a \sum_{k \neq j} |\langle \psi_k | P_{n_1-1} L_{\gamma_0, a, Z\pm}^{(F \neq n_1)} P_{n_1} | \psi_j \rangle|^2 \approx \frac{n_1 \gamma_{0e}}{4g^2} \sum_F F \left(\frac{\Omega_Z^{(F)}}{F - n_1} \right)^2, \quad (7.57)$$

$$\Gamma_{n_1 \rightarrow n_1, \gamma_1, Z\pm}^{(F \neq n_1)} = \sum_F \sum_a \sum_{k \neq j} |\langle \psi_k | P_{n_1} L_{\gamma_1, a, Z\pm}^{(F \neq n_1)} P_{n_1} | \psi_j \rangle|^2 \approx \frac{n_1 \gamma_{1e}}{4g^2} \sum_F F \left(\frac{\Omega_Z^{(F)}}{F - n_1} \right)^2. \quad (7.58)$$

From these expressions follow the loss rates from $|\text{GHZ}\rangle$ due to Z pumping:

$$\Gamma_{\text{GHZ} \rightarrow \text{GHZ}_-, \kappa, Z\pm}^{(F \neq n_1)} = \sum_F |\langle \text{GHZ}_- | L_{\kappa, Z\pm}^{(F \neq n_1)} | \text{GHZ} \rangle|^2 \approx \frac{N^2 \kappa_a}{16g^2} \sum_{F=1}^{N-1} \left(\frac{\Omega_Z^{(F)}}{N - F} \right)^2, \quad (7.59)$$

$$\Gamma_{\text{GHZ} \rightarrow N-1, \gamma_0, Z\pm}^{(F \neq n_1)} = \sum_F \sum_{a=1}^N \sum_{k \neq j} |\langle \psi_k | L_{\gamma_0, a, Z\pm}^{(F \neq n_1)} | \text{GHZ} \rangle|^2 \approx \frac{N \gamma_{0e}}{8g^2} \sum_{F=1}^{N-1} F \left(\frac{\Omega_Z^{(F)}}{N - F} \right)^2, \quad (7.60)$$

$$\Gamma_{\text{GHZ} \rightarrow \text{GHZ}_-, \gamma_1, Z\pm}^{(F \neq n_1)} = \sum_{F=1}^{N-1} \sum_{a=1}^N |\langle \text{GHZ}_- | L_{\gamma_1, a, Z\pm}^{(F \neq n_1)} | \text{GHZ} \rangle|^2 \approx \frac{N \gamma_{1e}}{16g^2} \sum_{F=1}^{N-1} F \left(\frac{\Omega_Z^{(F)}}{N - F} \right)^2. \quad (7.61)$$

We neglect the gain of population in $|\text{GHZ}\rangle$ from $|\text{GHZ}_-\rangle$. Furthermore, we note that due to its scaling with N^2 , loss from $|\text{GHZ}\rangle$ by oscillator decay should be avoided. In addition, effective oscillator decay is not useful for the ‘Z’ pumping

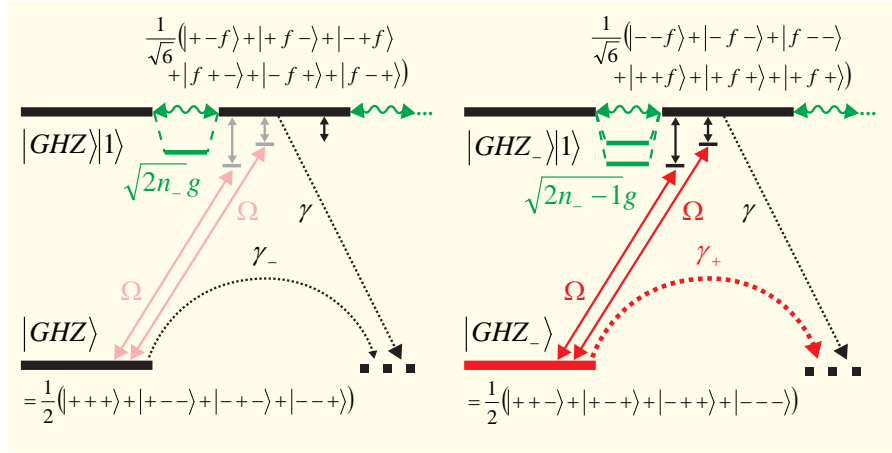


FIGURE 7.6: Second dissipative mechanism for GHZ preparation, shown for $N = 3$ qubits. Depumping of $|\text{GHZ}_-\rangle$ (“X pumping”), is achieved using the coupling configuration shown in Fig. 7.4 b). $|\text{GHZ}\rangle$ is a superposition of states with only even numbers n_- of atoms in $|-\rangle$, while n_- is odd for $|\text{GHZ}_-\rangle$. The atom-excited states to which $|\text{GHZ}\rangle$ ($|\text{GHZ}_-\rangle$) is coupled by weak driving, form dressed states with other atom- and oscillator-excited states at $\sqrt{n_-}g$ with even (odd) n_- . We depump $|\text{GHZ}_-\rangle$ by applying fields with detunings $\Delta_X^{(F)} = \sqrt{F}g$ where $F = 1, 3, 5, \dots \leq N$. Population pumped out by this process is again pumped to $|0\rangle^{\otimes N}$ by the ‘Z’ pumping process in Sec. 7.3.2.

process. As we will see below, this is also the case for X pumping. Therefore, we will generally choose to work with $\kappa_{a/b} = 0$ for the GHZ protocol (a weak cooling $\kappa \ll \Omega$ may nevertheless be used to counteract heating). The overall loss rate from $|\text{GHZ}\rangle$ due to off-resonant Z pumping is then given by

$$\Gamma_{\text{GHZ} \rightarrow ?, Z} \approx \frac{N(2\gamma_{0e} + \gamma_{1e})}{8g^2} \sum_{F=1}^{N-1} F \left(\frac{\Omega_Z^{(F)}}{N-F} \right)^2. \quad (7.62)$$

Here, the question mark stands for any potential final state; in the scaling analysis we will typically consider the worst state possible. For the reasonable assumption of $\gamma_{0e} = \gamma_{1e} = \frac{\gamma_e}{2}$ we obtain

$$\Gamma_{\text{GHZ} \rightarrow ?, Z} \approx \frac{3\gamma_e N}{16g^2} \sum_{F=1}^{N-1} F \left(\frac{\Omega_Z^{(F)}}{N-F} \right)^2. \quad (7.63)$$

We conclude that for $g \gg \gamma, \kappa$, the rates from Z pumping, ultimately leading to $|0\rangle^{\otimes N}$, and thus to $|\text{GHZ}\rangle$, are much stronger than the loss rates from $|\text{GHZ}\rangle$. The derived rates will be used further to analyze the error and preparation time of the protocol in Sec. 7.4.

7.3.3 Emptying $|\text{GHZ}_-\rangle$: the X pumping

To achieve the second process (ii) in Sec. 7.1 for the dissipative preparation of a GHZ state we engineer the depumping of the undesired state $|\text{GHZ}_-\rangle$, the so-called “X pumping”, which is illustrated in Fig. 7.6. Here, we choose to express the system state in terms of the σ_x -eigenstates, $|\pm\rangle = \frac{1}{\sqrt{2}}(|0\rangle \pm |1\rangle)$. Expressed

in this basis, $|\text{GHZ}_-\rangle$ is a superposition of states with odd numbers of qubits in $|-\rangle$, n_- , while $|\text{GHZ}\rangle$ only contains states with an even n_- ,

$$|\text{GHZ}_-\rangle = \frac{1}{\sqrt{2^{N-1}}} ((|+\dots+-\rangle + |+\dots-+-\rangle + \dots) + \dots), \quad (7.64)$$

$$|\text{GHZ}\rangle = \frac{1}{\sqrt{2^{N-1}}} (|+\dots+\rangle + (|+\dots++--\rangle + |+\dots+- -+\rangle + \dots) + \dots).$$

In order to depump $|\text{GHZ}_-\rangle$ we therefore need to distinguish whether n_- is even or odd. We do this in a way similar to the Z pumping above, using the X coupling configuration described in Sec. 7.3.1. Here, the transition from the excited level $|f\rangle$ to $|-\rangle$ is coherently coupled to the harmonic oscillator b by an atom-oscillator coupling $H_{\text{int},X}$, and coherently excited by the drive $H_{\text{drive},X}$. Applying fields with detunings $\Delta_{X\pm}^{(F)} = \pm\sqrt{F}g$ with $F = 1, 3, 5, \dots \leq N$ thus excites the state $|\text{GHZ}_-\rangle$ and makes it decay to random states by spontaneous emission, as shown in Fig. 7.6 for $N = 3$. On the other hand, $|\text{GHZ}\rangle$ remains unaffected by this process. After decay out of $|\text{GHZ}_-\rangle$ the resulting states are again subjected to the Z pumping and then transferred back to $|0\rangle^{\otimes N}$. The combination of both processes thus dissipatively prepares $|\text{GHZ}\rangle$ over time and stabilizes it as the unique steady state of the dissipative dynamics. However, since the X pumping disturbs the Z pumping, it has to be sufficiently weak so that the Z pumping has a sizeable probability of reaching the final state $|0\rangle^{\otimes N}$ before being subject to X pumping; this requirement does not, however, slow down the preparation process significantly, as we will see in Sec. 7.4. We derive the effective operators and decay rates for the X pumping below.

Effective operators for the X configuration

The derivation of the effective operators for the X configuration is carried out in App. D. We obtain for the effective Lindblad operators

$$L_{\kappa,X}^{(F)} = \sum_{n_-=0}^N \frac{\sqrt{\kappa_b}\Omega_X^{(F)}}{2\tilde{g}_{X,n_-}^{(F)}} P_{n_-}, \quad (7.65)$$

$$L_{\gamma 0,a,X}^{(F)} = \sum_{n_-=0}^N \frac{\sqrt{\gamma 0_f}\Omega_X^{(F)}}{2\tilde{\Delta}_{X,n_-}^{(F)}} |0\rangle_a \langle -| P_{n_-}, \quad (7.66)$$

$$L_{\gamma 1,a,X}^{(F)} = \sum_{n_-=0}^N \frac{\sqrt{\gamma 1_f}\Omega_X^{(F)}}{2\tilde{\Delta}_{X,n_-}^{(F)}} |1\rangle_a \langle -| P_{n_-}. \quad (7.67)$$

In analogy to P_{n_+} , P_{n_-} is defined as the projector on all ground states with n_- atoms in $|-\rangle$. Furthermore, we use the effective detunings

$$\tilde{\Delta}_{X,n_-}^{(F)} = \tilde{\Delta}_X^{(F)} - \frac{n_-g^2}{\tilde{\delta}_X^{(F)}}, \quad (7.68)$$

$$\tilde{g}_{X,n_-}^{(F)} = g - \frac{\tilde{\Delta}_X^{(F)}\tilde{\delta}_X^{(F)}}{n_-g}, \quad (7.69)$$

and generalize the real detunings in Eq. (7.17) to complex ones,

$$\tilde{\Delta}_X^{(F)} = \omega_f - \omega_X^{(F)} - \frac{i\gamma_f}{2} = \Delta_X^{(F)} - \frac{i\gamma_f}{2}, \quad (7.70)$$

$$\tilde{\delta}_X^{(F)} = \omega_b - \omega_X^{(F)} - \frac{i\kappa_b}{2} = \delta_X^{(F)} - \frac{i\kappa_b}{2}. \quad (7.71)$$

The effective decay rates are found to be

$$\kappa_{X,n_-}^{(F)} = \frac{\kappa_b(\Omega_X^{(F)})^2}{4|\tilde{\delta}_{X,n_-}^{(F)}|^2}, \quad (7.72)$$

$$\gamma_{0,X,n_-}^{(F)} = \frac{\gamma_{0f}(\Omega_X^{(F)})^2}{4|\tilde{\Delta}_{X,n_-}^{(F)}|^2}, \quad (7.73)$$

$$\gamma_{1,X,n_-}^{(F)} = \frac{\gamma_{1f}(\Omega_X^{(F)})^2}{4|\tilde{\Delta}_{X,n_-}^{(F)}|^2}. \quad (7.74)$$

We engineer these rates by the choice of the detunings of the drive.

Engineered operators for the X configuration

To depump the $|\text{GHZ}_-\rangle$ state without affecting $|\text{GHZ}\rangle$ we apply again red- and blue-detuned laser fields $\Omega_{X\pm}^{(F)} = \Omega_X^{(F)}$ with detunings $\Delta_{X\pm}^{(F)} = \pm\sqrt{F}g$, but including only odd field indices $F = 1, 3, 5, \dots, (F \leq N)$, whereas for even $F = 2, 4, \dots$ we use $\Omega_X^{(F)} = 0$. From Eqs. (7.68)–(7.69) we find for the effective detunings for resonant ($F = n_-$) and off-resonant ($F \neq n_-$) excitation

$$\tilde{\Delta}_{X\pm,n_-}^{(F=n_-)} = \tilde{\Delta}_{X\pm}^{(F)} - \frac{n_-g^2}{\tilde{\delta}_{X\pm}^{(F)}} \approx -\frac{i}{2}(\gamma_f + \kappa_b), \quad \tilde{\Delta}_{X\pm,n_-}^{(F \neq n_-)} \approx \pm \frac{F - n_-}{\sqrt{F}}g, \quad (7.75)$$

$$\tilde{\delta}_{X\pm,n_-}^{(F=n_-)} = g - \frac{\tilde{\Delta}_{X\pm}^{(F)} \tilde{\delta}_{X\pm}^{(F)}}{n_-g} \approx \frac{i}{2} \frac{\gamma_f + \kappa_b}{\sqrt{n_-}}, \quad \tilde{\delta}_{X\pm,n_-}^{(F \neq n_-)} \approx \frac{n_- - F}{n_-}g. \quad (7.76)$$

For the effective decay rates we find from Eqs. (7.72)–(7.74),

$$\kappa_{X\pm,n_-}^{(F=n_-)} = \frac{n_- \kappa_b (\Omega_X^{(F)})^2}{(\gamma_f + \kappa_b)^2}, \quad \kappa_{X,n_-}^{(F \neq n_-)} = \frac{\kappa_b n_-^2 (\Omega_X^{(F)})^2}{4(n_- - F)^2 g^2}. \quad (7.77)$$

$$\gamma_{0,X\pm,n_-}^{(F=n_-)} = \frac{\gamma_{0f} (\Omega_X^{(F)})^2}{(\gamma_f + \kappa_b)^2}, \quad \gamma_{0,X\pm,n_-}^{(F \neq n_-)} = \frac{\gamma_{0f} F (\Omega_X^{(F)})^2}{4(F - n_-)^2 g^2}, \quad (7.78)$$

$$\gamma_{1,X\pm,n_-}^{(F=n_-)} = \frac{\gamma_{1f} (\Omega_X^{(F)})^2}{(\gamma_f + \kappa_b)^2}, \quad \gamma_{1,X\pm,n_-}^{(F \neq n_-)} = \frac{\gamma_{1f} F (\Omega_X^{(F)})^2}{4(F - n_-)^2 g^2}, \quad (7.79)$$

for resonant excitation ($F = n_-$) and for off-resonant ($F \neq n_-$) excitation. With these rates and Eqs. (7.65)–(7.67) we obtain the effective Lindblad operators

$$L_{\kappa, X_{\pm}}^{(F)} = \sum_{\text{odd } n_-} \left[\sqrt{\kappa_{X_{\pm}, n_-}^{(F=n_-)}} + \mathcal{O}\left(\frac{1}{g^2}\right) \right] P_{n_-} \quad (7.80)$$

$$+ \sum_{\text{even } n_-} \sqrt{\kappa_{X_{\pm}, n_-}^{(F \neq n_-)}} P_{n_-}, \quad (F = 1, 3, 5, \dots, (F \leq N)), \quad (7.81)$$

$$L_{\gamma_{0,a}, X_{\pm}}^{(F)} = \sum_{\text{odd } n_-} \left[\sqrt{\gamma_{0, X_{\pm}, n_-}^{(F=n_-)}} |0\rangle_a \langle -| P_{n_-} + \mathcal{O}\left(\frac{1}{g^2}\right) \right] \quad (7.82)$$

$$+ \sum_{\text{even } n_-} \sqrt{\gamma_{0, X_{\pm}, n_-}^{(F \neq n_-)}} |0\rangle_a \langle -| P_{n_-}, \quad (F = 1, 3, 5, \dots, (F \leq N)), \quad (7.83)$$

$$L_{\gamma_{1,a}, X_{\pm}}^{(F)} = \sum_{\text{odd } n_-} \left[\sqrt{\gamma_{1, X_{\pm}, n_-}^{(F=n_-)}} |1\rangle_a \langle -| P_{n_-} + \mathcal{O}\left(\frac{1}{g^2}\right) \right] \quad (7.84)$$

$$+ \sum_{\text{even } n_-} \sqrt{\gamma_{1, X_{\pm}, n_-}^{(n_- \neq F)}} |1\rangle_a \langle -| P_{n_-}, \quad (F = 1, 3, 5, \dots, (F \leq N)). \quad (7.85)$$

Again, we separate the effective Lindblad operators by the frequencies of the resonances, this time depending on n_- . We obtain similar Lindblad operators as for Z pumping, with enhanced terms to zeroth order in g ,

$$L_{\kappa, X_{\pm}}^{(F=n_-)} = \sqrt{\kappa_{X_{\pm}, n_-}^{(F=n_-)}} P_{n_-}, \quad (F = 1, 3, 5, \dots, (F \leq N)), \quad (7.86)$$

$$L_{\gamma_{0,a}, X_{\pm}}^{(F=n_-)} = \sqrt{\gamma_{0, X_{\pm}, n_-}^{(F=n_-)}} |0\rangle_a \langle -| P_{n_-}, \quad (F = 1, 3, 5, \dots, (F \leq N)), \quad (7.87)$$

$$L_{\gamma_{1,a}, X_{\pm}}^{(F=n_-)} = \sqrt{\gamma_{1, X_{\pm}, n_-}^{(F=n_-)}} |1\rangle_a \langle -| P_{n_-}, \quad (F = 1, 3, 5, \dots, (F \leq N)), \quad (7.88)$$

and suppressed terms acting on the target state

$$L_{\kappa, X_{\pm}}^{(F \neq n_-)} = \sqrt{\kappa_{X_{\pm}, n_-}^{(F \neq n_-)}} P_{n_-}, \quad (\text{even } n_-, \text{ odd } F), \quad (7.89)$$

$$L_{\gamma_{0,a}, X_{\pm}}^{(F \neq n_-)} = \sqrt{\gamma_{0, X_{\pm}, n_-}^{(F \neq n_-)}} |0\rangle_a \langle -| P_{n_-}, \quad (\text{even } n_-, \text{ odd } F), \quad (7.90)$$

$$L_{\gamma_{1,a}, X_{\pm}}^{(F \neq n_-)} = \sqrt{\gamma_{1, X_{\pm}, n_-}^{(F \neq n_-)}} |1\rangle_a \langle -| P_{n_-}, \quad (\text{even } n_-, \text{ odd } F). \quad (7.91)$$

As can be seen more clearly from the section below, these operators make $|\text{GHZ}_-\rangle$ (with only odd n_-) decay rapidly, while loss from $|\text{GHZ}\rangle$ (with only even n_-) is suppressed. In addition, the effective Hamiltonian is compensated by the red- and blue-detuned fields,

$$H_{\text{eff}, X} \approx H_{\text{eff}, X_+} + H_{\text{eff}, X_-} \approx 0. \quad (7.92)$$

We can therefore describe the dynamics in terms of rates.

Engineered decay rates for the X configuration

With the effective operators from Eqs. (7.86)–(7.88) we find the decay rates from $|\text{GHZ}_-\rangle$,

$$\Gamma_{\text{GHZ}_-\rightarrow?,\gamma_0,X\pm} \approx \frac{\gamma_{0f}}{(\gamma_f + \kappa_b)^2} \sum_{F=1,3,\dots}^N \binom{N}{F} \frac{F(\Omega_X^{(F)})^2}{2^{N-1}}, \quad (7.93)$$

$$\Gamma_{\text{GHZ}_-\rightarrow?,\gamma_1,X\pm} \approx \frac{\gamma_{1f}}{(\gamma_f + \kappa_b)^2} \sum_{F=1,3,\dots}^N \binom{N}{F} \frac{F(\Omega_X^{(F)})^2}{2^{N-1}}. \quad (7.94)$$

For the reasonable assumption of $\gamma_{0f} = \gamma_{1f} = \frac{\gamma_f}{2}$ the total rate is therefore given by

$$\Gamma_{\text{GHZ}_-\rightarrow?,X} \approx \frac{2\gamma_f}{(\gamma_f + \kappa_b)^2} \sum_{F=1,3,\dots}^N \binom{N}{F} \frac{F(\Omega_X^{(F)})^2}{2^{N-1}}. \quad (7.95)$$

The expression in Eq. (7.95) is the total decay rate from the $|\text{GHZ}_-\rangle$ state which is approximately given by the sum of all enhanced decay rates, weighted with the number of states with the same excitation. We conclude that the X pumping causes rapid depumping of $|\text{GHZ}_-\rangle$; the population of $|\text{GHZ}_-\rangle$ is then distributed over all other states. The losses from $|\text{GHZ}\rangle$ are only caused by the off-resonant drives with $F \neq n_-$. Using Eqs. (7.89)–(7.91) and ignoring negligible gain processes we obtain the loss rates

$$\Gamma_{\text{GHZ}\rightarrow?,\gamma_0,X\pm} \approx \frac{\gamma_{0f}}{4g^2} \sum_{n_-=0,2,\dots} \binom{N}{n_-} \frac{n_-}{2^{N-1}} \sum_{F=1,3,\dots} F \left(\frac{\Omega_X^{(F)}}{F - n_-} \right)^2 \quad (7.96)$$

$$\Gamma_{\text{GHZ}\rightarrow?,\gamma_1,X\pm} \approx \frac{\gamma_{1f}}{4g^2} \sum_{n_-=0,2,\dots} \binom{N}{n_-} \frac{n_-}{2^{N-1}} \sum_{F=1,3,\dots} F \left(\frac{\Omega_X^{(F)}}{F - n_-} \right)^2 \quad (7.97)$$

Here, the binomial coefficients originate from the number of states with the same number of atoms in $|-\rangle$. For the total loss rate from $|\text{GHZ}\rangle$ through X pumping with both red- ($X+$) and blue-detuned ($X-$) fields we approximately find

$$\Gamma_{\text{GHZ}\rightarrow?,\gamma,X} \approx \frac{\gamma_f}{2g^2} \sum_{n_-=0,2,\dots} \binom{N}{n_-} \frac{n_-}{2^{N-1}} \sum_{F=1,3,\dots} F \left(\frac{\Omega_X^{(F)}}{F - n_-} \right)^2 \quad (7.98)$$

From this expression we see that the loss terms from $|\text{GHZ}\rangle$ due to X pumping are of second order in g^{-1} and thus suppressed for $g \gg \gamma, \kappa$. Beside decay out of $|\text{GHZ}_-\rangle$ the X pumping also causes losses from states with odd n_- which have an overlap with states with $1 \leq n_1 \leq N - 1$ in the Z basis. This affects the transport from $n_1 = N - 1$ to $n_1 = 0$ by the Z pumping and thus to $|\text{GHZ}\rangle$ by imposing a loss rate

$$\Gamma_{n_1 \rightarrow ?, \gamma, X} \approx \frac{\gamma_f}{(\gamma_f + \kappa_b)^2} \sum_{F=1,3,\dots}^N \binom{N}{F} \frac{F(\Omega_X^{(F)})^2}{2^{N-1}}. \quad (7.99)$$

We will refer to this process as “X toss” below. As we will find out this does not, however, have a significant effect on the scaling of the preparation time and the error, if the strength of the X process is chosen properly.

We conclude the analytical discussion of the effective operators and engineered decay rates of the GHZ scheme by stating that the combination of Z and X pumping results in the preparation of a GHZ state from any initial state. For $g \gg \gamma, \kappa$ the gain rates are engineered to be strong, while the loss rates from $|\text{GHZ}\rangle$ are suppressed. We therefore expect the preparation of a GHZ state with high fidelity within a short preparation time. These questions are addressed in the section below, where we investigate the performance of the GHZ protocol.

7.4 Performance of the GHZ protocol

In the preceding section we have presented a scheme for the realization of the GHZ protocol described in Sec. 7.1. Our analysis of the effective operators and engineered decay rates of these processes has lead to the conclusion that our scheme allows for the dissipative preparation of a steady GHZ state regardless of the initial state of the system.

We now address the performance of the scheme. Here, we derive the scaling of the preparation time of a desired fidelity of the target state with the number of qubits and optimize it both analytically and numerically. We start out by an analysis for weak driving in Sec. 7.4.1. Since it is desirable to operate the scheme as fast as possible, we investigate potential strong driving effects in Sec. 7.4.2. Based on these, we present an analysis of the GHZ scheme for strong driving in Sec. 7.4.3. In Sec. 7.4.4 we assess the performance of the scheme numerically and compare the outcome with the analytical result.

7.4.1 Scaling analysis for weak driving

In the following, we present the results from the analysis of the performance of the protocol for weak driving. The full derivation is found in App. E.

To begin with, we describe the dynamics of the system using compartments defined by the number of atoms in $|1\rangle$, n_1 . This is done for $0 < n_1 < N$, whereas for $n_1 = 0$ and $n_1 = N$ we consider the compartments consisting of $|\text{GHZ}\rangle$ and $|\text{GHZ}_-\rangle$. The rates between these compartments have been derived in Sec. 7.3 using the effective operators which assume weak driving. An illustration of the compartment model is given in Fig. E.1 in App. E.

The preparation time of the GHZ states is the most important quantity. It is derived from the individual rates of the Z pumping which reduce n_1 stepwise down to $n_1 = 0$, which overlaps with the GHZ state. Adding up the times for the individual jumps and assuming that we start from the worst initial state with

$n_1 = N - 1$, we obtain for the preparation time of $|\text{GHZ}\rangle$ due to Z pumping

$$\tau_{n_1=1 \rightarrow \text{GHZ}} = 2\tau_{n_1=N-1 \rightarrow n_1=0} = \sum_{n_1=1}^{N-1} \tau_{n_1 \rightarrow n_1-1, \gamma, Z} = \sum_{n_1=1}^{N-1} \Gamma_{n \rightarrow n_1-1, \gamma, Z}^{-1} \quad (7.100)$$

$$= \frac{(\gamma_e + \kappa_a)^2}{\gamma_{0e}} \sum_{n_1=1}^{N-1} \frac{1}{n_1 (\Omega_Z^{(F=n_1)})^2}. \quad (7.101)$$

The error due to Z pumping, on the other hand, is given by Eq. (7.63),

$$\Gamma_{\text{GHZ} \rightarrow ?, \gamma, Z} \approx \frac{3\gamma_e N}{16g^2} \sum_{F=1}^{N-1} F \left(\frac{\Omega_Z^{(F)}}{N-F} \right)^2 \quad (7.102)$$

Both these expressions depend on the Rabi frequencies $\Omega_Z^{(F)}$ of the multi-tone drive $H_{\text{drive}, Z}$ and the decay rate γ_e of level $|e\rangle$; recall that $\gamma_e = \gamma_{0e} + \gamma_{1e}$. In a first step, we use the Lagrange multiplier method to minimize the error rate for a given preparation time by choosing the relative strength of the tones of the driving field. Then, in a second step, we adjust γ_e such as to achieve a desired error of the protocol, independent of the number of qubits N . The details are presented in App. E.1. The treatment of the X pumping is found in App. E.2.

In brief, we find that the steady state fidelity F is determined by the ratio of the decay out of the GHZ state at a rate $\Gamma_- \sim \frac{N\Omega^2}{\gamma}$, and the effective preparation rate $\Gamma_+ \sim \frac{N\gamma\Omega^2}{g^2}$, giving a steady state error $E \approx 1 - F = \frac{\Gamma_-}{\Gamma_+} \sim \frac{N\gamma^2}{g^2}$. With a suitably chosen low decay rate $\gamma \sim \frac{g\sqrt{E}}{\sqrt{N}}$ we can prepare a GHZ state with a desired fidelity F , independent of the number of atoms. Such an adjustable decay rate can, e.g., be achieved by taking $|e\rangle$ and $|f\rangle$ to be metastable states in an atom and driving them to an excited state (see Sec. 7.7). With suitably chosen Rabi frequencies $\Omega_Z^{(F)}$, $\Omega_X^{(F)}$ and a sufficiently low decay rate $\gamma \sim \frac{g}{\sqrt{EN}}$ we can then prepare a state with an error E within a preparation time

$$\tau_{\text{GHZ}} \propto \frac{\sqrt{N} \log^2 N}{\alpha^2 g \sqrt{E}}. \quad (7.103)$$

Here, α denotes the relation between the maximum Rabi frequency Ω and the decay rate γ . This dependency cannot be derived using the effective operators for weak driving used so far. However, on reasonable grounds which will become more clear in the next section, we can assume that α is limited by the effect of power broadening. Assuming that this effect grows quadratic with the driving, we use $\alpha \propto \frac{1}{\sqrt{N}}$. With this we obtain for the scaling of the preparation time

$$\tau_{\text{GHZ}} \propto \frac{N^{3/2} \log^2(N)}{g \sqrt{E}}. \quad (7.104)$$

While here, for the assumption of weak driving, it is not possible to derive an optimal driving strength, in Sec. 7.4.3 our considerations are turned into a more rigorous upper bound for the scaling of the preparation time, taking into account strong driving effects which allow us to derive an optimal Ω . We address these effects in Sec. 7.4.2 below.

7.4.2 Strong driving effects

The operator formalism used to derive effective couplings of the ground states in the system is built on the assumption of a perturbative drive much smaller than the couplings, decay, or detunings of the excited states, $\Omega \ll \gamma, \kappa, g, \Delta, \delta$. Effects from saturating the excited states that could possibly slow down the preparation process are thus not included in the rates derived so far. On the contrary, the dependency of all decay rates on the drives $\propto \Omega^2$ suggests that the optimal Rabi frequencies Ω of the drives are infinitely strong and thereby outside the perturbative regime. Thus, a proper assessment of the driving strength Ω requires the inclusion of strong driving effects which begin to play a role for $\Omega \lesssim \gamma, \kappa$.

In the following, we include such effects in the dynamics in an approximate way. Here, we discuss power broadening and population of the excited states and adjust the rates derived from the effective operators to account for power broadening. They will later be used to analytically derive the optimal Rabi frequencies Ω and the scaling of the protocols for strong driving. In addition, in our numerical simulations we will use effective operators where we have included the power broadening terms manually. While this treatment is not rigorous, it provides a convenient tool for rapidly determining the optimal parameters. These will be used to simulate the effective dynamics of the system beyond the regime of weak driving and to match it with the simulations describing a larger Hilbert space including excitations. In addition, we take into account the effect of population of the excited states in our numerics.

Power broadening

We first address the effect of power broadening (or ‘line’ broadening) in a simple model situation: A ground state $|0\rangle$ is resonantly coupled by a field with a Rabi frequency Ω to an excited level $|e\rangle$. In total, $|e\rangle$ decays at a rate $\gamma = \gamma_0 + \gamma_1$, where γ_1 is the decay rate into $|1\rangle$. We perform adiabatic elimination by setting the derivative of the density matrix to zero, $\dot{\rho} \approx 0$. In the weak driving regime, where the broadening of the excited level can be neglected, this yields an excited population of $\rho_{ee} = \frac{\Omega^2}{\gamma^2} \rho_{00}$ and thus an effective decay rate from $|0\rangle$ into $|1\rangle$ of $\gamma_{\text{eff}} = \frac{\Omega^2}{2\gamma}$. The population gain of state $|1\rangle$ is then given by

$$\dot{\rho}_{11} \approx \gamma_1 \rho_{ee} \approx \gamma_{\text{eff}} \rho_{00} \approx \frac{\Omega^2}{2\gamma} \rho_{00} \quad (7.105)$$

The same result is obtained when using the effective operators. Performing adiabatic elimination with a stronger drive we need to take into account the population of the excited level. This yields an excited population of $\rho_{ee} = \frac{\Omega^2}{\gamma^2 + \Omega^2} \rho_{00}$. Then, as the coupling of the ground state $|0\rangle$ to $|e\rangle$ is increased, we take into account the population of the coupled subspace of $|0\rangle$ and $|e\rangle$ rather than of state $|0\rangle$ only. This leads to

$$\dot{\rho}_{11} \approx \frac{\gamma_1 \rho_{00}}{(\rho_{00} + \rho_{ee})} (\rho_{00} + \rho_{ee}) \approx \frac{\gamma_1 \Omega^2}{\gamma^2 + 2\Omega^2} (\rho_{00} + \rho_{ee}) \quad (7.106)$$

For weak driving $\Omega^2 \ll \gamma^2$, this new decay rate $\gamma_{\text{eff}} = \frac{\gamma\Omega^2}{2(\gamma^2+2\Omega^2)}$ matches the previous result. The decay rate for strong driving can thus be obtained from the rate which was originally derived from the effective operators by “broadening” the natural line width of the excited state, $\gamma^2 \rightarrow \gamma^2 + 2\Omega^2$. In the limit of strong driving, $\Omega \rightarrow \infty$, the population is found in $|e\rangle$ with a probability of $\frac{1}{2}$ such that here γ_{eff} approaches the constant value of $\frac{\gamma}{2}$. Therefore, the effective decay rate from $|0\rangle$ to $|1\rangle$ cannot be increased to more than half of the line width of the level mediating it.

More generally, we now seek to include power broadening in the effective operators. This is done by replacing all complex effective detunings, e.g. $\tilde{\Delta}_{Z,n_1}^{(F)}$, here generally denoted as $\tilde{\Delta}_{\text{eff}}$ and \tilde{g}_{eff} , by “power broadened” ones. The replacements are made such that the rates obtained from the effective operators agree with the ones derived by adiabatic elimination. To this end, we make the replacements of $|\tilde{\Delta}_{\text{eff}}|^2 \rightarrow |\tilde{\Delta}_{\text{eff}}|^2 + n\Omega^2$ and $|\tilde{g}_{\text{eff}}|^2 \rightarrow |\tilde{g}_{\text{eff}}|^2 + n\Omega^2$, where n is the number of atoms that can be excited by the drive. However, as it turns out from numerical simulations, the action of power broadening needs to be doubled in the effective operators for ‘Z’ and ‘X’ to achieve agreement between the evolution due to the effective master equation (7.18) and the more complete master equation in (7.3). This can be attributed to interference between the blue- and red-detuned drives. Indeed, considering coherent excitation of a bright state consisting of both the blue- and the red-shifted dressed state suggests an increase of the broadening by a factor of two and thus the effective detunings $|\tilde{\Delta}_{\text{eff}}|^2 \rightarrow |\tilde{\Delta}_{\text{eff}}|^2 + 2n\Omega^2$ and $|\tilde{g}_{\text{eff}}|^2 \rightarrow |\tilde{g}_{\text{eff}}|^2 + 2n\Omega^2$. While these replacements are not rigorous, they are supported by our numerical simulations: It can be seen further down in Sec. 7.4.3 and 7.6.3 that (1) the analytical scalings derived using the strong driving operators comprise upper bounds to the numerically obtained scalings and that (2) the effective operators for strong driving agree well with simulations of the more complete master equation. Following this reasoning, the power broadened decay rate for the Z pumping from n_1 to $n_1 - 1$ is found to be

$$\Gamma_{n_1 \rightarrow n_1 - 1, \gamma_{0,Z}} \approx \frac{2n_1 \gamma_{0e} (\Omega_Z^{(F=n_1)})^2}{(\gamma_e + \kappa_a)^2 + 2n_1 (\Omega_Z^{(F=n_1)})^2}. \quad (7.107)$$

For the X depumping of $|\text{GHZ}_-\rangle$ we have

$$\Gamma_{\text{GHZ}_- \rightarrow ?, \gamma, X} \approx \sum_{F=1,3,\dots}^N \frac{2\gamma_f}{(\gamma_f + \kappa_b)^2 + 2n_- (\Omega_X^{(F=n_-)})^2} \binom{N}{n_-} \frac{n_- (\Omega_X^{(F=n_-)})^2}{2^{N-1}} \quad (7.108)$$

and for the X toss rate

$$\Gamma_{n_1 \rightarrow ?, \gamma, X} \approx \sum_{F=1,3,\dots}^N \frac{\gamma_f}{(\gamma_f + \kappa_b)^2 + 2F (\Omega_X^{(F=n_-)})^2} \binom{N}{F} \frac{n_- (\Omega_X^{(F=n_-)})^2}{2^{N-1}}. \quad (7.109)$$

As a consequence of the inclusion of terms for power broadening, increasing the driving strengths in the desired processes also increases the effect of power

broadening in the desired decay rates. In the off-resonant decay rates $\gamma_{\text{eff}} \propto \frac{\gamma\Omega}{g^2}$ the effect of power broadening is, on the other hand, negligible (given that $\Omega^2 \ll g^2$). The detrimental rates thus still increase for a growing Ω while the desired rates saturate. This is the limiting factor for the drive Ω which we will use to derive Ω further down.

Population of the excited states

An additional reduction in the fidelity for strong driving comes from the population of the excited induced by the drive. In the following, we investigate this effect:

The GHZ state, through its contribution from $|1\rangle^{\otimes N}$, is coupled to an excited state $|\psi_e\rangle = \frac{1}{\sqrt{N}}(|1..1e\rangle + |1..e1\rangle + \dots + |e..11\rangle)$ by $H_{\text{drive},Z}$. Despite being off-resonance, all tones of the driving field couple to the transition from $|\text{GHZ}\rangle$ to the dressed states of $|\psi_e\rangle$ and $|1\rangle^{\otimes N}|1\rangle$, with driving strengths of $\Omega_Z^{(F)} = \sqrt{\frac{N}{2}}\Omega_Z^{(F)}$ and detunings $\Delta_{Z\pm}^{(F)} = \pm\sqrt{N}g + \Delta_Z^{(F)} = (\pm\sqrt{N} \pm \sqrt{F})g$. For each tone the excited population is approximately given by

$$P_{\text{excited},Z\pm}^{(F)} \approx \frac{N\Omega_Z^{(F)}}{8(\sqrt{N} + \sqrt{F})^2g^2} + \frac{N\Omega_Z^{(F)}}{8(\sqrt{N} - \sqrt{F})^2g^2} \quad (7.110)$$

We also consider the excited population caused by X pumping. This requires representing the GHZ state in the X basis as in Eq. (7.64) and leads to an expression

$$P_{\text{excited},X\pm}^{(F)} \approx \sum_{n_-=2,4,\dots}^N \binom{N}{n_-} \left(\frac{n_-\Omega_X^{(F)}}{4(\sqrt{n_-} + \sqrt{F})^2g^2} + \frac{n_-\Omega_X^{(F)}}{4(\sqrt{n_-} - \sqrt{F})^2g^2} \right) \quad (7.111)$$

These expressions are included in our numerical simulations of the effective dynamics in the strong driving regime and provide another limitation on Ω . Our analytical derivation of the scaling involves, however, upper bounds to certain error processes and turns out to take place in a parameter regime where the population of the excited states is not significant. Therefore, in the analytical considerations below we leave out its effect.

7.4.3 Scaling analysis for strong driving

We use the results of the previous section to analyze the scaling of the preparation time for strong driving. As opposed to the analysis for weak driving in Sec. 7.4.1 we now also include the effect of power broadening. This enables us to optimize the Rabi frequencies of the drives. While here we present a summary of our analysis, the details are found in App. E.5. There, with the power broadened rates in Eq. (7.107), the preparation time is found to be given by

$$\tau_{n_1=N-1 \rightarrow \text{GHZ}} = 2\tau_{n_1=N-1 \rightarrow n_1=0} = 2 \sum_{n_1=1}^{N-1} (\Gamma_{n_1 \rightarrow n_1-1, \gamma_{0,Z}})^{-1} \quad (7.112)$$

$$= 2 \sum_{F=1}^{N-1} \left(\frac{\gamma_e}{F(\Omega_Z^{(F)})^2} + \frac{2}{\gamma_e} \right) = \frac{4(N-1)}{\gamma_e} + \sum_{F=1}^{N-1} \frac{2\gamma_e}{F(\Omega_Z^{(F)})^2} \quad (7.113)$$

It can be seen that the preparation rate increases with the strength of the driving Ω , but for too strong driving the fidelity becomes limited by power broadening, decreasing the preparation rate in Eq. (7.107), and thus, increasing the preparation time. On the other hand, the error rate in Eq. (E.9) remains unchanged

$$\Gamma_{\text{GHZ} \rightarrow ? , \gamma, Z} = \frac{3\gamma_e}{16g^2} N \sum_{F=1}^{N-1} \frac{F(\Omega_Z^{(F)})^2}{(N-F)^2}. \quad (7.114)$$

Normally, a reduced preparation time at constant error rate would result in an increased error of the protocol. As shown in App. E, these detrimental effects can be suppressed with suitable decay rates and driving strengths, decreasing polynomially with the number of qubits,

$$\gamma_e = 0.42 \cdot \frac{g\sqrt{E}}{\sqrt{N} \log N}, \quad (7.115)$$

$$\Omega_Z^{(F)} = 0.42 \cdot \frac{g\sqrt{E}}{N\sqrt{\log N}} \sqrt{\frac{N-F}{F}} \quad (\text{for } F = 1, \dots, N-1), \quad (7.116)$$

$$\gamma_f = 0.80 \cdot \frac{gE^{1/2}}{N^{1/2}} \quad (7.117)$$

$$\Omega_X^{(F)} = 0.24 \cdot \frac{gE^{1/2}}{N^{3/2}(\log N)^{1/2}} \quad (\text{for } F = 1, 3, 5 \leq N). \quad (7.118)$$

With these parameter choices we achieve for the preparation time

$$\tau_{\text{GHZ}} \approx 66 \frac{N^{3/2} \log N}{g\sqrt{E}}, \quad (7.119)$$

which agrees with the scaling of Eq. (7.104) up to a logarithm. It thereby confirms the previous result and constitutes a more rigorous upper bound for the preparation time at strong driving.

Note that in the above equations, E is meant to be the static error of the protocol which is attained in the limit of infinite time. For the “dynamical” error \mathcal{E} as the error that is reached within a finite time τ_{GHZ} one should everywhere set $E = 0.62\mathcal{E}$ for $\mathcal{E} = 0.1$ (or $E = 0.70\mathcal{E}$ for $\mathcal{E} = 0.03$). The GHZ preparation time is then also prolonged by an additional factor of $\sim \log(1/\mathcal{E})$. The details are found in App. E.4–E.5.

7.4.4 Numerical analysis and comparison

In the following, we verify our analytical results numerically. To this end, we simulate the time evolution by numerically solving the master equation. In Fig. 7.7 we plot the evolution due to the effective master equation, Eq. (7.18), containing the effective operators in Eqs. (7.19)–(7.21) and (7.65)–(7.67), including the terms for strong driving discussed in Sec. 7.4.2. We compare these curves with the evolution due to the more complete master equation, Eq. (7.3), truncated to one or two excitations. For the effective dynamics we use a Trotter-like ansatz, simulating the evolution under the Z and X pumping in an interchanging manner, performing base transformations between the eigenbases of σ_z and

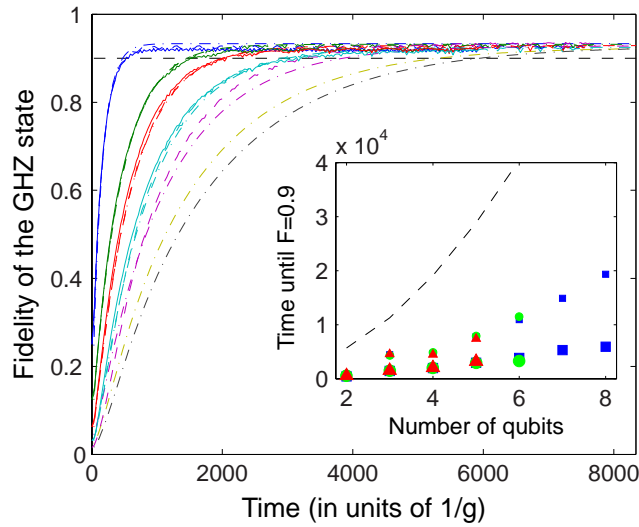


FIGURE 7.7: Evolution towards a steady many-body GHZ state. We numerically simulate the effective master equation of the protocol for dissipative preparation of a GHZ state, starting from an initially fully mixed state. The curves show the evolution for two to eight qubits (different colors) and are obtained by numerically optimizing all available parameters to reach a fidelity of $F = 0.9$ of the desired state within an as short as possible preparation time. The insets show the scaling of the preparation time with the number of qubits. In the curves and in the insets, we show different degrees of truncation of the Hilbert space: dash-dots/blue squares – effective dynamics after adiabatic elimination, solid lines/green circles – one excitation, red dashes/triangles – two excitations). In the insets, small symbols stand for analytically optimized parameters and large symbols for numerically optimized parameters. We find a favorable polynomial scaling of the preparation time with the number of qubits, which is in agreement with our analytical bound (black dash).

σ_x . The resulting time evolution towards a steady GHZ state for qubit numbers $N = 2, \dots, 8$ is shown in Fig. 7.7. The curves are obtained by simulating the effective master equation, after numerical optimization of the available system parameters to achieve a desired fidelity of $F_{\text{GHZ}} = 0.9$ in minimal time. The inset shows the time required to reach this fidelity when starting from an initially fully mixed state, as a function of the system size. It can be seen that the desired fidelity of $F = 0.9$ is indeed attained within shorter preparation time than given by our analytical upper bound in Eq. (7.119). The scaling of the points in the inset, which mark our numerical results, is similar to the analytical curves and supports a scaling of the preparation time which is less than quadratic in the qubit number. We therefore conclude that our GHZ protocol has a favorable polynomial scaling with the number of qubits.

7.5 Realization of the W protocol

We now demonstrate how the protocol for W preparation proposed in Sec. 7.1 can be realized in the physical system described in Sec. 7.2. In Sec. 7.5.1 we present a suitable setup. As mechanisms we again use the Z pumping of Sec. 7.3.2, discussed in Sec. 7.5.2, together with two more mechanisms, ‘A’ and ‘W’,

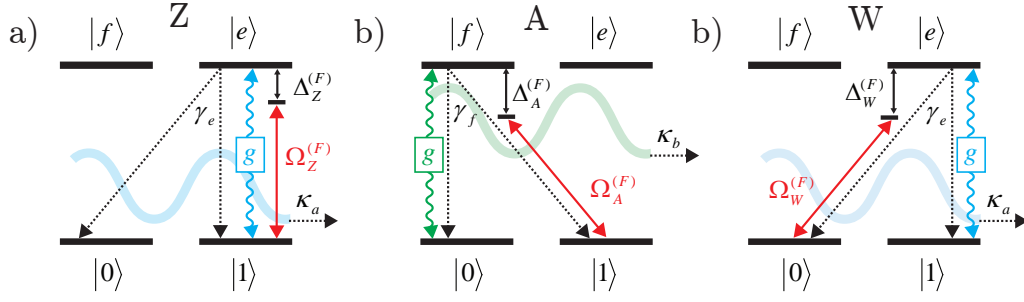


FIGURE 7.8: Setup for W state preparation. For the dissipative preparation of W states in the system presented in Sec. 7.2 we combine three coupling configurations, ‘Z’, ‘W’, and ‘A’, each consisting of an atom-oscillator coupling and a weak coherent drive. (a) The Z configuration consists of a coupling of the transition from $|e\rangle$ to $|1\rangle$ to the harmonic oscillator a with a coupling constant g . A multi-tone drive with individual Rabi frequencies $\Omega_Z^{(F)}$ and detunings $\Delta_Z^{(F)}$ for the tones F acts on the same transition. (b) In the A configuration the harmonic oscillator b couples to the transition from $|f\rangle$ to $|0\rangle$, whereas a single-tone drive with Ω_A and Δ_A acts on the transition from $|1\rangle$ to $|f\rangle$. (c) The W configuration is opposite to the A configuration: Here, we use the atom-oscillator coupling of the Z configuration on the transition from $|e\rangle$ to $|1\rangle$ and a two-tone drive with Ω_W and Δ_W on the transition from $|e\rangle$ to $|1\rangle$.

discussed in Sec. 7.5.3 and 7.5.4. In Sec. 7.6, we study the performance of the scheme.

7.5.1 Setup

For the preparation of W states we consider the coupling configurations shown in Fig. 7.8, which consist of atom-oscillator couplings and classical drives. The atom-oscillator couplings are modeled by the interaction Hamiltonian $H_{\text{int}} = H_{\text{int},Z/W} + H_{\text{int},A}$ with

$$H_{\text{int},Z/W} = g \left(a^\dagger J_{1e} + a J_{1e}^\dagger \right), \quad (7.120)$$

$$H_{\text{int},A} = g \left(b^\dagger J_{0f} + b J_{0f}^\dagger \right), \quad (7.121)$$

The coupling configurations are denoted by ‘Z’, ‘W’ and ‘A’, the coupling constant of the atom-oscillator coupling is given by g . $H_{\text{int},Z/W}$ describes that an atomic excitation in $|e\rangle$ is exchanged with the oscillator a , leaving the atom in state $|1\rangle$. $H_{\text{int},A}$ couples the transition between the excited state $|f\rangle$ and the ground state $|0\rangle$ to the oscillator b . The coherent excitation of the atoms by classical driving fields is given by the drive Hamiltonian $H_{\text{drive}} = H_{\text{drive},Z} + H_{\text{drive},A} + H_{\text{drive},W}$ with

$$H_{\text{drive},Z} = \frac{1}{2} \sum_F \Omega_Z^{(F)} e^{-i\omega_Z^{(F)} t} J_{e1} + H.c., \quad (7.122)$$

$$H_{\text{drive},W} = \frac{1}{2} \Omega_W^{(F)} e^{-i\omega_W t} J_{e0} + H.c., \quad (7.123)$$

$$H_{\text{drive},A} = \frac{1}{2} \Omega_A^{(F)} e^{-i\omega_A t} J_{f1} + H.c. \quad (7.124)$$

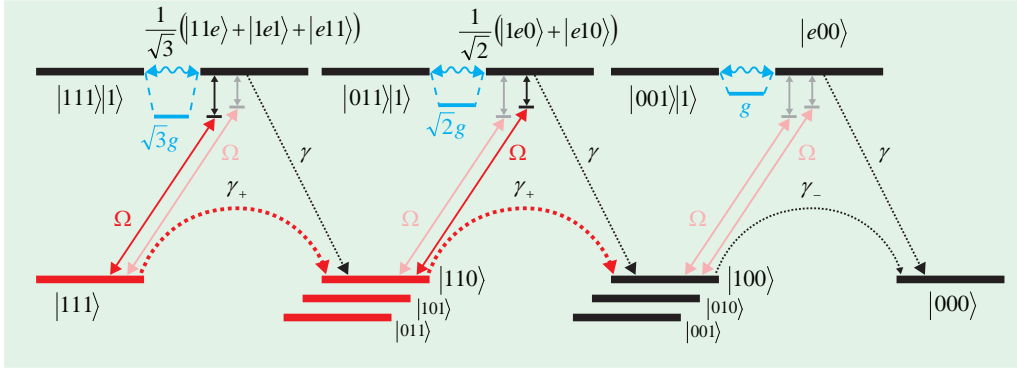


FIGURE 7.9: First dissipative mechanism for W state generation, shown for $N = 3$ qubits. Pumping of all states with $n_1 \geq 2$ atoms in $|1\rangle$ to $n_1 \leq 1$, is achieved using Z pumping in the coupling configuration shown in Fig. 7.4 a). Ground states are coupled to atom-excited states by weak driving. Dependent on the number of atoms in $|1\rangle$, n_1 , the excited states form dressed states with oscillator-excited states at energies $\pm\sqrt{n_1}g$. We apply fields with detunings $\Delta_Z^{(F)} = \sqrt{F}g$ for $2 \leq F \leq N$, by which all states with $n_1 \geq 2$ are pumped towards $n_1 \leq 1$.

For the Z drive, we generally allow for several field tones F with Rabi frequencies $\Omega_Z^{(F)}$ and frequencies $\omega_{Z/W/A}^{(F)}$. For further discussion we define the detunings

$$\Delta_Z^{(F)} = \omega_e - \omega_Z^{(F)}, \quad \delta_Z^{(F)} = \omega_a - \omega_Z^{(F)}, \quad (7.125)$$

$$\Delta_A = \omega_f - \omega_A, \quad \delta_A = \omega_b - \omega_A^{(F)}, \quad (7.126)$$

$$\Delta_W = \omega_e - \omega_W, \quad \delta_W = \omega_a - \omega_W. \quad (7.127)$$

We will again use these detunings to engineer certain effective decay processes to be strong and others to be weak.

7.5.2 Transferring states to $n_1 \leq 1$ by the Z pumping

We adapt the Z pumping mechanism, previously discussed in Sec. 7.3.2 for the GHZ scheme, to the preparation of W states. The respective ‘Z’ coupling configuration is shown in Fig. 7.8 a). This time, we apply Z fields with detunings $\Delta_{Z\pm}^{(F)} = \pm\sqrt{F}g$ with $2 \leq F \leq N$ to pump states with $n_1 \geq 2$ to the subspace with $n_1 \leq 1$. This subspace contains $|W\rangle$, $|0\rangle^{\otimes N}$ and the antisymmetric states with $n_1 = 1$. As can be seen from Fig. 7.9, the Z pumping here is similar to the one used for GHZ preparation above, with the difference that we choose fields with detunings $\Delta_{Z\pm\pm}^{(F)} = \pm\sqrt{F}g$ and $2 \leq F \leq N$ to pump the population to $n_1 \leq 1$ and $n_1 = 0$ as previously. The general effective operators for the Z configuration have already been discussed in Sec. 7.3.2. Below we therefore focus on the engineered operators and effective transfer rates for the Z pumping used in the W protocol.

Engineered operators for the Z pumping

We analyze Z pumping from states with $n_1 \geq 2$ to those with $n_1 \leq 1$. To do so, we insert the detunings $\Delta_{Z\pm}^{(F)} = \pm\sqrt{F}g$ for $2 \leq F \leq N$ into the expressions for

the effective detunings in Eqs. (7.22)–(7.23) and decay rates in Eqs. (7.26)–(7.28). This allows us to compute the Lindblad operators in Eqs. (7.19)–(7.21) for this parameter choice. For the enhanced processes ($n_1 = F$) we find

$$L_{\kappa,Z\pm}^{(F=n_1)} \approx \sqrt{\kappa_{Z\pm,n_1}^{(F=n_1)}} P_{n_1}, \quad (2 \leq F \leq N), \quad (7.128)$$

$$L_{\gamma_{0,a},Z\pm}^{(F=n_1)} \approx \sqrt{\gamma_{0,Z\pm,n_1}^{(F=n_1)}} |0\rangle_a \langle 1| P_{n_1}, \quad (2 \leq F \leq N), \quad (7.129)$$

$$L_{\gamma_{1,a},Z\pm}^{(F=n_1)} \approx \sqrt{\gamma_{1,Z\pm,n_1}^{(F=n_1)}} |1\rangle_a \langle 1| P_{n_1}, \quad (2 \leq F \leq N). \quad (7.130)$$

In addition, there are weak decay processes that affect $|W\rangle$ described by

$$L_{\kappa,Z\pm}^{(F \neq 1)} \approx \sqrt{\kappa_{Z\pm,n_1}^{(F \neq 1)}} P_{n_1=1}, \quad (2 \leq F \leq N), \quad (7.131)$$

$$L_{\gamma_{0,a},Z\pm}^{(F \neq 1)} \approx \sqrt{\gamma_{0,Z\pm,n_1}^{(F \neq 1)}} |0\rangle_a \langle 1| P_{n_1=1}, \quad (2 \leq F \leq N), \quad (7.132)$$

$$L_{\gamma_{1,a},Z\pm}^{(F \neq 1)} \approx \sqrt{\gamma_{1,Z\pm,n_1}^{(F \neq 1)}} |1\rangle_a \langle 1| P_{n_1=1}, \quad (2 \leq F \leq N). \quad (7.133)$$

The effective Hamiltonian is again compensated by choosing drives with both blue and red detunings (cf. Eq. (7.55)) so that we can turn to a description using rate equations.

Engineered decay rates for the Z pumping

We first calculate the rates for the desired mechanism consisting of several enhanced processes and then the loss rates. These rates will be needed to derive the time it takes to reach $|W\rangle$.

The decay rate leading from $n_1 = 2$ into $n_1 = 1$ constitutes an upper bound for the decay rate from $n_1 = 2$ to the antisymmetric subspace (from now on denoted by “as”), which contains all states with $n_1 = 1$ except the W state. This rate is given by

$$\Gamma_{2 \rightarrow \text{as}, \gamma_{0,Z}} \lesssim \Gamma_{2 \rightarrow 1, \gamma_{0,Z}} \approx \sum_{a=1}^N \sum_j |\langle \psi_j | P_1 L_{\gamma_{0,a,Z}}^{(F=n_1)} P_2 | \psi_k \rangle|^2 \approx \frac{2\gamma_{0e} (\Omega_Z^{(F=2)})^2}{(\gamma_e + \kappa_a)^2}. \quad (7.134)$$

Generally, the rate for Z pumping from a subspace with n_1 atoms in $|1\rangle$ to one with $n_1 - 1$ is found to be

$$\Gamma_{n_1 \rightarrow n_1-1, \gamma_{0,Z}} \approx \sum_{a=1}^N \sum_{j \neq k} |\langle \psi_j | P_{n_1-1} L_{\gamma_{0,a,Z}}^{(F=n_1)} P_{n_1} | \psi_k \rangle|^2 \approx \frac{2n_1 \gamma_{0e} (\Omega_Z^{(F=n_1)})^2}{(\gamma_e + \kappa_a)^2}. \quad (7.135)$$

We now turn to the effective decay processes from $|W\rangle$. Here, we find for the losses due to Z pumping

$$\Gamma_{W \rightarrow 0, \gamma_{0,Z}} = \sum_a \sum_F |\langle 0 |^{\otimes N} L_{\gamma_{0,a,Z}}^{(F=n_1)} |W\rangle|^2 \approx \frac{\gamma_{0e}}{2g^2} \sum_{F=2}^N F \left(\frac{\Omega_Z^{(F)}}{F-1} \right)^2 \quad (7.136)$$

$$\Gamma_{W \rightarrow \text{as}, \gamma_{1,Z}} \lesssim \Gamma_{W \rightarrow 1, \gamma_{1,Z}} = \sum_{k=1}^N \sum_{a=1}^N \sum_{F=2}^N |\langle 1_k | L_{\gamma_{1,a,Z}}^{(F=n_1)} |W\rangle|^2, \approx \frac{\gamma_{1e}}{2g^2} \sum_{F=2}^N F \left(\frac{\Omega_Z^{(F)}}{F-1} \right)^2. \quad (7.137)$$

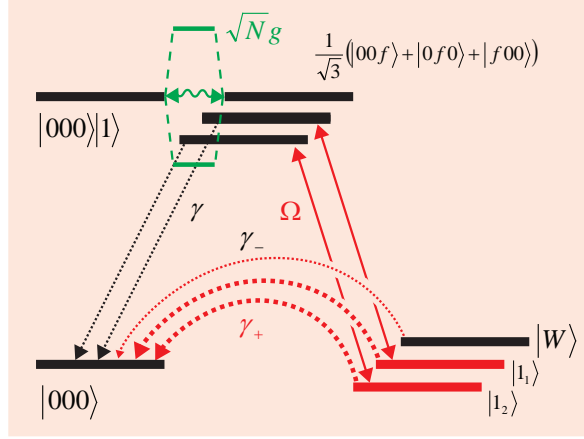


FIGURE 7.10: Second dissipative mechanism for W state generation, shown for $N = 3$ qubits: States with $n_1 = 1$ atom in state $|1\rangle$ with a symmetry differing from $|W\rangle$ are emptied by a process called “A pumping”, using the coupling situation shown in Fig. 7.8 (b). While the atom-excited state to which $|W\rangle$ is coupled by a single-tone drive forms dressed states with $|0\rangle^{\otimes N}|1\rangle$ at energies of $\pm\sqrt{N}g$, the atom-excited states to which the antisymmetric states $|1_{k\neq 0}\rangle$ are coupled are dark states of the oscillator coupling. They are thus in resonance with the drive ($\Delta_A = 0$) and pumped to $|0\rangle^{\otimes N}$. $|W\rangle$ is prepared from $|0\rangle^{\otimes N}$ as carried out in Sec. 7.5.4.

As can be seen from Eq. (7.135), the decay rates of the Z process depend on the number of atoms in $|1\rangle$ of a state, and not on its symmetry. To empty the antisymmetric states we therefore need an additional process, which we introduce below.

7.5.3 Emptying antisymmetric states: the A pumping

Since the Z pumping does not distinguish between the symmetry of the states with $n_1 = 1$, an additional process is needed to empty all states except for $|W\rangle$. Here, it is helpful to recognize that, while $|W\rangle$ is completely symmetric under permutation, the other $N - 1$ states with $n_1 = 1$ are antisymmetric under permutation. A basis for the antisymmetric states is given by

$$|1_k\rangle = \sum_{a=1}^N e^{2\pi i a k / N} \sigma_a^+ |0\rangle^{\otimes N}, \quad (1 \leq k \leq N - 1), \quad (7.138)$$

where $\sigma_a^+ = |1\rangle_a \langle 0|$. Note that $|1_0\rangle = |1_N\rangle = |W\rangle$ is the W state, or first Dicke state. The second Dicke state

$$|2_0\rangle = \sum_{a=1}^N (\sigma_a^+)^2 |0\rangle^{\otimes N} = \frac{1}{\sqrt{N(N-1)}} (|110..0\rangle + |1010..0\rangle + \dots + |0..011\rangle) \quad (7.139)$$

is the symmetric superposition of all states with two atoms in $|1\rangle$. To empty the antisymmetric states, we apply the coupling configuration shown in Fig. 7.8 b) with a single-tone drive resonant to the transition from $|1\rangle$ to $|f\rangle$, $\Delta_A = 0$, and

an oscillator coupling on the transition from $|f\rangle$ to $|0\rangle$. The ground states in the $n_1 = 1$ manifold are then driven to atom-excited states of the form

$$|0_k^f\rangle = \frac{1}{\sqrt{N}} \left((-1)^{\frac{2k}{N}} |0..0f\rangle + (-1)^{\frac{4k}{N}} |0..f0\rangle + \dots + (-1)^{2k} |f..00\rangle \right). \quad (7.140)$$

Here, the permutation symmetric atom-excited state $|0_0^f\rangle$, to which $|W\rangle$ is excited by the drive, is coupled to the state $|0\rangle^{\otimes N} |1\rangle_b$, which has an excitation of the oscillator b , with a coupling strength of $\sqrt{N}g$. Because of their strong coupling, these states form dressed states at energies $\pm\sqrt{N}g$, as is illustrated in Fig. 7.10. Excited states of other symmetries, to which the antisymmetric states are coupled, are dark states of the oscillator coupling. They are thus in resonance with the drive, if no detuning is applied, $\Delta_A = 0$. The antisymmetric ground states are then excited rapidly to the corresponding atom-excited states from where they decay to $|0\rangle^{\otimes N}$ by spontaneous emission. The W state, on the other hand, remains unaffected due to the resonant detuning of the corresponding dressed states.

As we will discuss in Sec. 7.5.4, a third mechanism is applied to prepare $|W\rangle$ from $|0\rangle^{\otimes N}$. We now turn to the effective operators and engineered rates for the A pumping.

Effective operators for the A configuration

The situation for the A configuration, and, as we will see below, also for the W configuration is different from the previous cases of Z and X in the sense that the drive and the atom-oscillator coupling act on different transitions. In App. D we obtain for the effective operators for the A configuration

$$L_{\kappa,A}^{(F)} = \sum_{n_1=0}^N \frac{\sqrt{\kappa_b} \Omega_A^{(F)}}{2\tilde{g}_{A,n_1}^{(F)}} J_{01} P_{n_1} \equiv \sum_{n_1} \sqrt{\kappa_{A,n_1}^{(F)}} J_{01} P_{n_1} \quad (7.141)$$

$$L_{\gamma_{0,a},A}^{(F)} = \sum_{n_1=0}^N \frac{\sqrt{\gamma_{0f}} \Omega_A^{(F)}}{2\tilde{\Delta}_A^{(F)}} \left[|0\rangle_a \langle 1| - (\tilde{n}_{A,n_1}^{(F)})^{-1} |0\rangle_a \langle 0| J_{01} \right] P_{n_1} \quad (7.142)$$

$$L_{\gamma_{1,a},A}^{(F)} = \sum_{n_1=0}^N \frac{\sqrt{\gamma_{1f}} \Omega_A^{(F)}}{2\tilde{\Delta}_A^{(F)}} \left[|1\rangle_a \langle 1| - (\tilde{n}_{A,n_1}^{(F)})^{-1} |1\rangle_a \langle 0| J_{01} \right] P_{n_1} \quad (7.143)$$

$$H_A^{(F)} = -\frac{(\Omega_A^{(F)})^2}{8\tilde{\Delta}_A^{(F)}} \sum_{n_1=0}^N \left[n_1 - (\tilde{n}_{A,n_1}^{(F)})^{-1} J_{10} J_{01} \right] P_{n_1} + H.c. \quad (7.144)$$

Here, we have the effective detunings

$$\tilde{g}_{A,n_1}^{(F)} = (N - n_1 + 1)g - \frac{\tilde{\Delta}_A^{(F)} \tilde{\delta}_A^{(F)}}{g}, \quad (7.145)$$

$$\tilde{n}_{A,n_1}^{(F)} = (N - n_1 + 1) - \frac{\tilde{\Delta}_A^{(F)} \tilde{\delta}_A^{(F)}}{g^2} = \frac{\tilde{g}_{A,n_1}^{(F)}}{g}, \quad (7.146)$$

where we have generalized the terms in Eq. (7.126) to complex detunings,

$$\tilde{\Delta}_A^{(F)} = \omega_f - \omega_A^{(F)} - \frac{i\gamma_f}{2} = \Delta_A^{(F)} - \frac{i\gamma_f}{2}, \quad (7.147)$$

$$\tilde{\delta}_A^{(F)} = \omega_b - \omega_A^{(F)} - \frac{i\kappa_b}{2} = \delta_A^{(F)} - \frac{i\kappa_b}{2}. \quad (7.148)$$

It can be seen that for the A configuration – and, as we will see below, also for the W configuration – we typically do not reach a compact expression for the effective operators. However, as we will see below, these expressions simplify considerably for the most states relevant in the scheme, in particular for the dark states of J_{10} .

Engineered operators for the A configuration

The A mechanism is meant to pump the antisymmetric states to $|0\rangle^{\otimes N}$, while ideally leaving $|W\rangle$ unaffected. To achieve this we use the A configuration with a resonant single-tone field, $\Delta_A = \delta_A = 0$. The decay of the oscillator mode b is assumed to be negligible, $\kappa_b = 0$. With this we obtain for the Lindblad operators in Eqs. (7.141)–(7.143) in the manifold $n_1 \leq 1$

$$L_{\kappa,A}^{(F=0)} P_{n_1 \leq 1} \approx \sqrt{\kappa_{A,n_1}^{(F=0,W)}} |0\rangle^{\otimes N} \langle W| \approx 0 \quad (7.149)$$

$$L_{\gamma_{0,a},A}^{(F=0)} P_{n_1 \leq 1} \approx \sqrt{\gamma_{0,A,n_1}^{(F=0,as)}} |0\rangle_a \langle 1| P_{n_1=1,as} + \sqrt{\gamma_{0,A,n_1}^{(F=0,W)}} |0\rangle_a \langle 1| P_W \quad (7.150)$$

$$L_{\gamma_{1,a},A}^{(F=0)} P_{n_1 \leq 1} \approx \sqrt{\gamma_{1,A,n_1}^{(F=0,as)}} |1\rangle_a \langle 1| P_{n_1=1,as} + \sqrt{\gamma_{1,A,n_1}^{(F=0,W)}} |1\rangle_a \langle 1| P_W \quad (7.151)$$

Here, we have defined a projector $P_{n_1=1,as} = \sum_{k=1}^{N-1} |1_k\rangle \langle 1_k|$ onto all antisymmetric states in $n_1 = 1$ and a projector onto the W state, $P_W = |W\rangle \langle W|$, and the effective decay rates

$$\kappa_{A,n_1}^{(F=0,as)} = 0, \quad \kappa_{A,n_1}^{(F=0,W)} = \frac{\kappa_b \Omega_A^2}{4g^2} = 0, \quad (7.152)$$

$$\gamma_{0,A,n_1}^{(F=0,as)} = \frac{\gamma_{0f} \Omega_A^2}{\gamma_f^2}, \quad \gamma_{0,A}^{(F=0,W)} = \frac{\gamma_{0f} \kappa_b \Omega_A^2}{16N^3 g^2} = 0, \quad (7.153)$$

$$\gamma_{1,A,n_1}^{(F=0,as)} = \frac{\gamma_{1f} \Omega_A^2}{\gamma_f^2}, \quad \gamma_{1,A}^{(F=0,W)} = \frac{\gamma_{1f} \kappa_b \Omega_A^2}{16N^3 g^2} = 0. \quad (7.154)$$

It can be seen that the effective spontaneous emission from antisymmetric states with $n_1 = 1$ is only limited by the line width γ_f and thus very rapid compared to the loss terms with g in the denominator. These losses from $|W\rangle$ are suppressed by a detuning growing with the qubit number and are switched off completely for $\kappa_b = 0$. The effective Hamiltonian of the A mechanism acting on the $n_1 = 1$ manifold is zero due to the absence of a detuning of the driving field,

$$H_A \approx 0 \quad (7.155)$$

so that we describe the A pumping by rates.

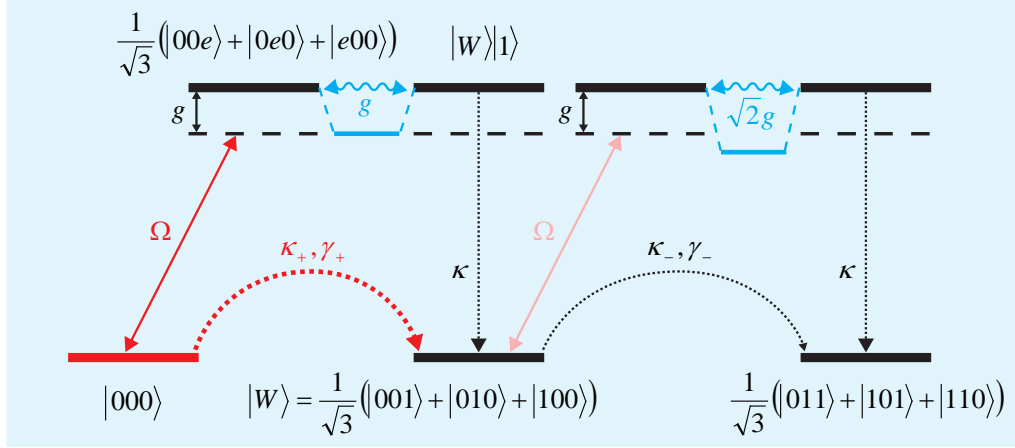


FIGURE 7.11: Third dissipative mechanism for W state generation, shown for $N = 3$ qubits: $|W\rangle$ is prepared from $|0\rangle^{\otimes N}$ using the coupling situation shown in Fig. 7.8 (c). $|0\rangle^{\otimes N}$ is coupled to an excited state by a two-tone drive with detunings $\Delta_{W\pm} = \pm g$. The atom-oscillator coupling with g causes $|0_0^e\rangle$ and $|W\rangle|1\rangle$ to form dressed states which are each in resonance with one tone of the drive (shown for red detuning). Effective oscillator decay from $|0\rangle^{\otimes N}$ leads to the desired state $|W\rangle$. Excitation of $|W\rangle$ is suppressed as the excitation of the corresponding dressed states would require a drive tone with a detuning of $\pm\sqrt{2}g$.

Engineered decay rates for the A pumping

The depumping rate for antisymmetric states (“as”) is given by

$$\Gamma_{\text{as}\rightarrow 0, \gamma_0, A} = \sum_a |\langle 0 |^{\otimes N} L_{\gamma_0, a, A}^{(F=0)} |1_{k\neq 0}\rangle|^2 \approx \frac{\gamma_0 f \Omega_A^2}{\gamma_f^2}. \quad (7.156)$$

The loss rates from $|W\rangle$ are, on the other hand, found to be small,

$$\Gamma_{W\rightarrow 0, \kappa, A} = |\langle 0 |^{\otimes N} L_{\kappa, A}^{(F=0)} |W\rangle|^2 \approx \frac{\kappa_b \Omega_A^2}{4Ng^2} \approx 0, \quad (7.157)$$

$$\Gamma_{W\rightarrow 0, \gamma_0, A} = \sum_a |\langle 0 |^{\otimes N} L_{\gamma_0, a, A}^{(F=0)} |W\rangle|^2 \approx \frac{\gamma_0 f \kappa_b^2 \Omega_A^2}{16N^2 g^4} \approx 0, \quad (7.158)$$

$$\Gamma_{W\rightarrow \text{as}, \gamma_1, A} = \sum_{k=1}^N \sum_{a=1}^N |\langle 1_k | L_{\gamma_1, a, A}^{(F=0)} |W\rangle|^2 \approx \frac{\gamma_1 f \kappa_b^2 \Omega_A^2}{16N^2 g^4} \approx 0. \quad (7.159)$$

The A pumping is found to be limited only by the more or less freely adjustable decay rate γ_f of the excited level $|f\rangle$. The depumping of the antisymmetric states to $|0\rangle^{\otimes N}$ is thus a very efficient process. Preparation of the $|W\rangle$ state from $|0\rangle^{\otimes N}$ requires an additional, third process, which is the ‘W’ mechanism discussed in the following section.

7.5.4 Preparation of $|W\rangle$ from $|0\rangle^{\otimes N}$: the W pumping

After all population with $n_1 \geq 2$ has been transferred to $n_1 \leq 1$, the A pumping discussed in the previous section pumps all states except for $|W\rangle$ to $|0\rangle^{\otimes N}$.

The actual preparation of $|W\rangle$ from $|0\rangle^{\otimes N}$ is realized by a third process, the so-called “W pumping”. This is achieved by an effective decay (or “cooling”) of the harmonic oscillator, realized by the coupling configuration in Fig. 7.8 c). To achieve this process, we apply a two-tone drive with detunings $\Delta_{W\pm} = \pm g$ on the transition from $|0\rangle$ to $|e\rangle$ and use the oscillator coupling on the transition from $|e\rangle$ to $|1\rangle$. The state $|0\rangle^{\otimes N}$ is then excited by the drive to a symmetric atom-excited superposition state, from where the atomic excitation is transferred to the oscillator, yielding state $|W\rangle|1\rangle$. As the latter two states form dressed states at energies of $\pm g$, the chosen detunings ensure that $|0\rangle^{\otimes N}$ is excited resonantly. Oscillator decay then transfers the system to the $|W\rangle$ state. Due to the specific detuning, leakage of population from $|W\rangle$ to higher Dicke states does not occur, as this would require detunings $\Delta = \pm\sqrt{n_1}g$ with $n_1 > 1$.

Instead of oscillator decay, the W mechanism can also be realized by spontaneous emission at the cost of a factor $\sim \sqrt{N}$ in the preparation time. This is due to the fact that the involved atom-excited state does not only decay into $|W\rangle$, but also to the $N - 1$ other states with $n_1 = 1$. We now turn to the effective operators and decay rates for W pumping.

Effective operators for the W configuration

We derive the effective operators for the W configuration in App. D. Using n_0 to denote the number of atoms in $|0\rangle$ we obtain

$$L_{\kappa,W}^{(F)} = \sum_{n_0=0}^N \frac{\sqrt{\kappa_a}\Omega_W^{(F)}}{2\tilde{g}_{W,n_0}^{(F)}} J_{10} P_{n_0} \equiv \sum_{n_0=0}^N \sqrt{\kappa_{W,n_0}^{(F)}} J_{10} P_{n_0}, \quad (7.160)$$

$$L_{\gamma_{0,a},W}^{(F)} = \sum_{n_0=0}^N \frac{\sqrt{\gamma_{0e}}\Omega_W^{(F)}}{2\tilde{\Delta}_W^{(F)}} \left[|0\rangle_a \langle 0| - (\tilde{n}_{W,n_0}^{(F)})^{-1} |0\rangle_a \langle 1| J_{10} \right] P_{n_0}, \quad (7.161)$$

$$L_{\gamma_{1,a},W}^{(F)} = \sum_{n_0=0}^N \frac{\sqrt{\gamma_{1e}}\Omega_W^{(F)}}{2\tilde{\Delta}_W^{(F)}} \left[|1\rangle_a \langle 0| - (\tilde{n}_{W,n_0}^{(F)})^{-1} |1\rangle_a \langle 1| J_{10} \right] P_{n_0}, \quad (7.162)$$

$$H_W^{(F)} = -\frac{(\Omega_W^{(F)})^2}{8\tilde{\Delta}_W^{(F)}} \sum_{n_0=0}^N \left[n_0 - (\tilde{n}_{W,n_0}^{(F)})^{-1} J_{01} J_{10} \right] P_{n_0} + H.c. \quad (7.163)$$

Here, we use the effective detunings

$$\tilde{g}_{W,n_0}^{(F)} = (N - n_0 + 1)g - \frac{\tilde{\Delta}_W^{(F)}\tilde{\delta}_W^{(F)}}{g}, \quad (7.164)$$

$$\tilde{n}_{W,n_0}^{(F)} = (N - n_0 + 1) - \frac{\tilde{\Delta}_W^{(F)}\tilde{\delta}_W^{(F)}}{g^2} = \frac{\tilde{g}_{W,n_0}^{(F)}}{g}, \quad (7.165)$$

with complex energies generalized from Eq. (7.127),

$$\tilde{\Delta}_W^{(F)} = \omega_e - \omega_W^{(F)} - \frac{i\gamma_e}{2} = \Delta_W^{(F)} - \frac{i\gamma_e}{2}, \quad (7.166)$$

$$\tilde{\delta}_W^{(F)} = \omega_a - \omega_W^{(F)} - \frac{i\kappa_a}{2} = \delta_W^{(F)} - \frac{i\kappa_a}{2}. \quad (7.167)$$

As in the case of the A configuration, we do not reach compact expressions for all of the effective operators. The expressions will, however, simplify below,

where we discuss the engineering of the effective operators inserting the actual parameters.

Engineered operators for the W pumping

For the W mechanism we use a field with a single red and a single blue detuning, $\Delta_{W\pm} = \pm g = \delta_{W\pm}$. By this condition we transfer population from $|0\rangle^{\otimes N}$ ($n_1 = 0$) rapidly and directly to $|W\rangle$ ($n_1 = 1$) by collective decay, while loss from $|W\rangle$ is effectively suppressed by different resonance conditions. Preparation of anti-symmetric states $|1_{k\neq 0}\rangle$ is also avoided unless spontaneous emission dominates over oscillator decay, $\gamma_e \gg \kappa_a$, in which case a modified scheme for W preparation with a different scaling is obtained. We find for the effective operators of Eqs. (7.160)–(7.162) in the manifold $n_1 \leq 2$,

$$L_{\kappa,W\pm}^{(F=1)} P_{n_1 \leq 2} \approx \sqrt{\kappa_{W\pm,n_0}^{(F=1,0)}} |W\rangle \langle 0|^{\otimes N} + \sum_{n_0 \geq 1} \sqrt{\kappa_{W\pm,n_0}^{(F=1,W)}} |2_0\rangle \langle W|, \quad (7.168)$$

$$L_{\gamma_0,W\pm}^{(F=1)} P_{n_1 \leq 2} \approx \sqrt{\gamma_{0,W\pm,n_0}^{(F=1,0)}} |0\rangle_a \langle 1| P_{n_1=0} + \sum_{n_0 \geq 1} \sqrt{\gamma_{0,W\pm,n_0}^{(F=1,W)}} |0\rangle_a \langle 0| P_{n_0=1}, \quad (7.169)$$

$$L_{\gamma_1,W\pm}^{(F=1)} P_{n_1 \leq 2} \approx \sqrt{\gamma_{1,W\pm,n_0}^{(F=1,0)}} |1\rangle_a \langle 1| P_{n_1=0} + \sum_{n_0 \geq 1} \sqrt{\gamma_{1,W\pm,n_0}^{(F=1,W)}} |1\rangle_a \langle 0| P_{n_0=1}. \quad (7.170)$$

Here, we have introduced the effective decay rates

$$\kappa_{W\pm,n_0}^{(F=1,0)} = N \frac{\kappa_a \Omega_{W\pm}^2}{(\kappa_a + \gamma_e)^2}, \quad \kappa_{W\pm,n_0}^{(F=1,W)} = (N-1) \frac{\kappa_a \Omega_{W\pm}^2}{4g^2}, \quad (7.171)$$

$$\gamma_{0,W\pm,n_0}^{(F=1,0)} = N \frac{\gamma_{0e} \Omega_{W\pm}^2}{(\kappa_a + \gamma_e)^2}, \quad \gamma_{0,W\pm,n_0}^{(F=1,W)} = (N-1) \frac{\gamma_{0e} \Omega_{W\pm}^2}{4g^2}, \quad (7.172)$$

$$\gamma_{1,W\pm,n_0}^{(F=1,0)} = N \frac{\gamma_{1e} \Omega_{W\pm}^2}{(\kappa_a + \gamma_e)^2}, \quad \gamma_{1,W\pm,n_0}^{(F=1,W)} = (N-1) \frac{\gamma_{1e} \Omega_{W\pm}^2}{4g^2}, \quad (7.173)$$

with effective couplings for the drive acting resonantly on $|0\rangle^{\otimes N}$ ($F = 1, 0$), or off-resonantly on $|W\rangle$ ($F = 1, W$),

$$\tilde{g}_{W\pm,n_0}^{(F=1,0)} = \tilde{n}_{W\pm,n_0}^{(F=1,0)} g = \frac{i}{2} (\kappa_a + \gamma_e), \quad (7.174)$$

$$\tilde{g}_{W\pm,n_0}^{(F=1,W)} = \tilde{n}_{W\pm,n_0}^{(F=1,W)} g = g. \quad (7.175)$$

Again, the effective Hamiltonian processes are compensated by the use of fields with opposite detunings,

$$H_W \approx H_{W+} + H_{W-} \approx 0, \quad (7.176)$$

so that we can restrict the discussion to gain and loss rates.

Engineered decay rates for the W pumping

Using the engineered operators above we find the preparation rate of $|W\rangle$,

$$\Gamma_{0 \rightarrow W,\kappa,W} \equiv |\langle W | L_{\kappa,W,n_0}^{(F=1)} |0\rangle^{\otimes N}|^2 \approx \frac{2N\kappa_a \Omega_{W\pm}^2}{(\kappa_a + \gamma_e)^2} \quad (7.177)$$

In addition, there are enhanced decay processes from $|0\rangle^{\otimes N}$ to states with $n_1 = 1$ by spontaneous emission

$$\Gamma_{0 \rightarrow W, \gamma_1, W} \equiv |\langle W | L_{\gamma_1, W, n_0}^{(F=1)} | 0 \rangle^{\otimes N}|^2 \approx \frac{2\gamma_1 e \Omega_W^2}{(\kappa_a + \gamma_e)^2} \quad (7.178)$$

$$\Gamma_{0 \rightarrow \text{as}, \gamma_1, W} \equiv \left| \sum_{k=1}^{N-1} \langle 1_k | L_{\gamma_1, W, n_0}^{(F=1)} | 0 \rangle^{\otimes N} \right|^2 \approx \frac{2(N-1)\gamma_1 e \Omega_W^2}{(\kappa_a + \gamma_e)^2} \quad (7.179)$$

The first of these processes can be used to build an alternative W preparation scheme which works in the absence of oscillator decay, $\kappa_a = 0$. Here, population pumped to “as” by the rate above is transferred back to $|0\rangle^{\otimes N}$ by the A mechanism. The less directed preparation mechanism results, however, in a different scaling. For the loss rates from $|W\rangle$ due to the W process we obtain

$$\Gamma_{W \rightarrow 2, \kappa, W} \equiv \sum_{a=1}^N |\langle 2_0 | L_{\kappa, W}^{(F=1)} | W \rangle|^2 \approx (N-1) \frac{\kappa_a \Omega_W^2}{g^2}, \quad (7.180)$$

$$\Gamma_{W \rightarrow 2, \gamma_1, W} \equiv \sum_{j=1}^N \sum_{a=1}^N |\langle \psi_j | L_{\gamma_1, a, W}^{(F=1)} | W \rangle|^2 \approx (N-1) \frac{\gamma_1 e \Omega_W^2}{g^2}, \quad (7.181)$$

$$\Gamma_{W \rightarrow \text{as}, \gamma_0, W} \lesssim \Gamma_{W \rightarrow 1, \gamma_0, W} \equiv \sum_{j=1}^N \sum_{a=1}^N |\langle \psi_j | L_{\gamma_0, a, W}^{(F=1)} | W \rangle|^2 \approx (N-1) \frac{\gamma_0 e \Omega_W^2}{g^2}. \quad (7.182)$$

We find that all loss rates from the target state $|W\rangle$ scale with $1/g^2$, while the gain terms are only limited by the decay rates γ and κ . We therefore conclude from our analytical discussion of the effective operators of the W scheme that the combination of the three presented mechanisms allows for the dissipative preparation of a W state. Since all states in the system eventually end up in the W state, $|W\rangle$ is attained as the unique steady state of the dynamics, independent of the initial state. Since for $g \gg \gamma, \kappa$ the gain rates are much larger than the loss rates from $|W\rangle$ the preparation of the W state is likely to take place within short time and to yield a high fidelity. We investigate these questions further in the section below, where we use the derived rates to analyze the scaling and speed of the protocol.

7.6 Performance of the W protocol

In the previous section we have presented a scheme for realizing the W protocol presented in Sec. 7.1. Using the effective operator formalism to derive engineered decay rates we have shown that the W state is indeed prepared as the steady state. We now study the performance of the scheme, in view of the error and the speed of the protocol. We begin with an analysis for weak driving in Sec. 7.6.1, and then present an analysis for strong driving in Sec. 7.6.2, taking into account strong driving effects discussed in Sec. 7.6.3. We compare our analytical results with numerical ones in Sec. 7.6.4.

7.6.1 Scaling analysis for weak driving

We perform the scaling analysis of the presented protocol in the same manner as for the GHZ protocol in Sec. 7.4.1. The details are found in App. F.1. Here, we

again use a rate equation model with compartments defined by n_1 (for $n_1 \geq 2$). For $n_1 \leq 1$ we use one compartment containing the antisymmetric states defined in (7.138), one for the W state, and one for $|0\rangle^{\otimes N}$. The rates between these compartments have been derived in Sec. 7.5 above, the model is illustrated in Fig. F.1 in App. F.1. Optimizing available parameters, we find for the preparation time of a W state with an error E in the limit of large qubit numbers

$$\tau_W \propto \frac{N (\log N)^{3/2}}{g\sqrt{E}} \quad (7.183)$$

Similar to Sec. 7.4.1, we have not derived the optimal Rabi frequencies of the drives. Instead, we have assumed relations between driving strengths and the corresponding decay rates of the kind $\Omega = \alpha\gamma$. For the result in Eq. (7.183) we have used our previous assumption of $\alpha \propto \frac{1}{\sqrt{N}}$ (cf. App. F.1). As in Sec. 7.4.1, this assumption is motivated by power broadening as the dominating strong driving effect. In Sec. 7.6.3, we will conduct a proper analysis of the scaling of the W protocol for strong driving, after deriving suitable expressions for the decay rates in this regime in Sec. 7.6.2 below.

7.6.2 Strong driving effects

In a similar manner as in Sec. 7.4.2 for the GHZ scheme, we now address strong driving effects that play a role in the W scheme, but are not accounted for by the effective operators discussed in Sec. 7.5. We investigate power broadening and population of the excited states as two such effects and manually include terms for power broadening in the engineered decay rates derived in Sec. 7.5. This permits us to analyze the optimal Rabi frequencies of the drives and to take the generation of W states to its limits.

Power broadening

Similarly as for the GHZ scheme above, we find for the W scheme the “power-broadened” collective decay rate from $|0\rangle^{\otimes N}$ to $|W\rangle$,

$$\Gamma_{0 \rightarrow W, \kappa, W} \approx \frac{2N\kappa_a\Omega_W^2}{(\kappa_a + \gamma_e)^2 + 2N\Omega_W^2}. \quad (7.184)$$

For the individual decay process from $|0\rangle^{\otimes N}$ to $|W\rangle$ we have

$$\Gamma_{0 \rightarrow W, \gamma_{1e}, W} \approx \frac{2\gamma_{1e}\Omega_W^2}{(\kappa_a + \gamma_e)^2 + 2N\Omega_W^2}. \quad (7.185)$$

and for the individual decay process from $|0\rangle^{\otimes N}$ to “as”

$$\Gamma_{0 \rightarrow W, \kappa, W} \approx \frac{2(N-1)\gamma_{1e}\Omega_W^2}{(\kappa_a + \gamma_e)^2 + 2N\Omega_W^2}. \quad (7.186)$$

Pumping of antisymmetric states with $n_1 = 1$ (“as”) to $|0\rangle^{\otimes N}$, using only a single, resonant field, becomes

$$\Gamma_{\text{as} \rightarrow 0, \gamma_0, A} \approx \frac{\gamma_{0f}\Omega_A^2}{\gamma_f^2 + \Omega_A^2} \quad (7.187)$$

Note that, other than for Z, X, and W, for A the replacements $|\tilde{\Delta}_{\text{eff}}|^2 \rightarrow |\tilde{\Delta}_{\text{eff}}|^2 + n\Omega^2$ and $|\tilde{g}_{\text{eff}}|^2 \rightarrow |\tilde{g}_{\text{eff}}|^2 + n\Omega^2$ are sufficient. An additional factor of two due to a constructive interference of blue- and red-detuning drives is not required, since the A configuration uses only a single, resonant drive.

We will use the rates above to address the scaling of the preparation time in the strongly driven regime and to derive the optimal Rabi frequencies in Sec. 7.6.3.

Population of the excited states

The population of the excited states due to W and A pumping is found to be

$$P_{\text{excited},W\pm} \approx \frac{N\Omega_W}{2(\sqrt{2} + \sqrt{1})^2 g^2} + \frac{N\Omega_W}{2(\sqrt{2} - \sqrt{1})^2 g^2} \quad (7.188)$$

$$P_{\text{excited},A\pm} \approx \frac{(N-1)\Omega_A}{2Ng^2} \quad (7.189)$$

We include these expressions in our numerical simulations of the effective dynamics in the strong driving regime in Sec. 7.6.4.

7.6.3 Scaling analysis for strong driving

We use the power broadened rates from the previous section to analyze the W scheme for weak driving. Again, we choose the parameters such that, for given N , they minimize the preparation time of the W state. The details of the optimization are found in App. F.2. Here, a compact and close-to-optimal result is reached by setting the decay rate to

$$\gamma = \sqrt{\frac{2}{7}} \frac{g\sqrt{E}}{\sqrt{\log N}}. \quad (7.190)$$

assuming $\gamma_e = \gamma_f = \kappa_a = \gamma$, $\kappa_b = 0$, $\gamma_{0e} = \gamma_{1e} = \gamma_{0f} = \gamma_{1f} = \gamma/2$, and by choosing the driving strengths to be

$$\Omega_W = \frac{\gamma}{\sqrt{N}}, \quad (7.191)$$

$$\Omega_A = \gamma, \quad (7.192)$$

$$\Omega_Z^{(F)} = \gamma \sqrt{\frac{F-1}{F}}, \quad (F = 2, 3, \dots, N). \quad (7.193)$$

Then, for given stationary error E , the preparation time of the W state becomes, for large N ,

$$\tau_W \approx \sqrt{14} \frac{N(\log N)^{1/2}}{g\sqrt{E}}. \quad (7.194)$$

Other than Eq. (7.183) this result includes strong driving effects and should therefore be seen as the correct upper bound for the preparation time. It should, however, be noted that the scaling in Eqs. (7.183) and (7.194) is predominantly due to the long time to pump from a completely mixed state to $n_1 \leq 2$. Starting from $|0\rangle^{\otimes N}$ may therefore result in a scaling which is only logarithmic.

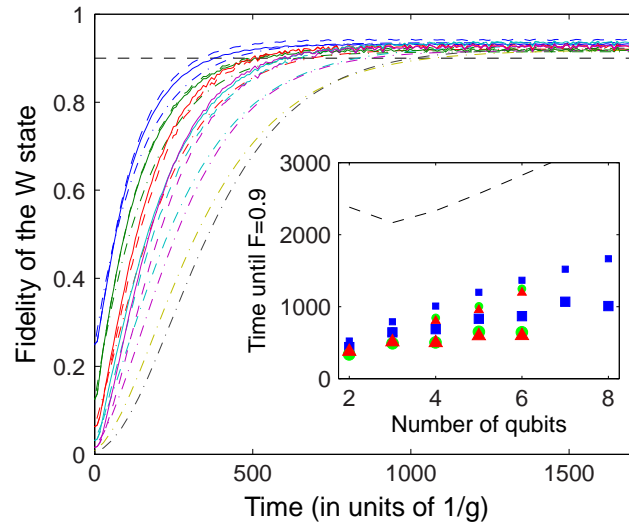


FIGURE 7.12: Evolution towards a steady many-body W state. We numerically simulate the effective master equation of the protocol for dissipative preparation of a W state, starting from an initially fully mixed state. The curves show the evolution for two to eight qubits (different colors) and are obtained by numerically optimizing all available parameters to reach a fidelity of $F = 0.9$ of the desired state within an as short as possible preparation time. The insets show the scaling of the preparation time with the number of qubits. In the curves and in the insets, we show different degrees of truncation of the Hilbert space: dash-dots/blue squares – effective dynamics after adiabatic elimination, solid lines/green circles – one excitation, red dashes/triangles – two excitations). In the insets, small symbols stand for analytically optimized parameters and large symbols for numerically optimized parameters. We find a favorable polynomial scaling of the preparation time with the number of qubits, which is in agreement with our analytical bounds (black dashed line).

Similar to GHZ (cf. Sec. 7.4.3), the static error E is related the dynamical error \mathcal{E} by $E = 0.62\mathcal{E}$ for $\mathcal{E} = 0.1$. Also the corresponding preparation time is prolonged by an additional factor of $\sim \log(1/\mathcal{E})$. The details are found in App. E.5.

7.6.4 Numerical analysis and comparison

In Fig. 7.12 b) we address the scaling of the preparation time of the W protocol numerically. To this end, we simulate the effective master equation in Eq. (7.18), using the operators in Eqs. (7.19)–(7.21), Eqs. (7.141)–(7.143) and Eqs. (7.160)–(7.162) with terms for strong driving (cf. Sec. 7.6.2). Here, we again optimize the available parameters to achieve a fidelity of $F = 0.9$ in minimal time and compare the resulting curves with the evolution due to the master equation in Eq. (7.3) with one or two excitations. The resulting evolution towards a W state is shown in Fig. 7.12 for $N = 2, \dots, 8$ qubits. In Fig. 7.12 b) we plot the time required to reach the desired fidelity of $F = 0.9$ when starting from an initially fully mixed state, against the number of qubits. Similar to the analytical result in (7.194), the numerical points in the inset of Fig. 7.12 support a close-to-linear scaling of the preparation time with the system size. The analytical curve is found to constitute an upper bound for the numerical points. We thus conclude

that also our W protocol exhibits a favorable polynomial scaling with the number of qubits.

7.7 Implementation in a system of trapped ions

All the necessary ingredients for our scheme are present in trapped ion experiments: A suitable setup can consist of a chain of N trapped ions, with two (meta-) stable ground levels $|0\rangle$ and $|1\rangle$ and two auxiliary levels, $|e\rangle$ and $|f\rangle$. Two phononic modes, cooled to the ground state, e.g. by sympathetic cooling of auxiliary ions, and coupled to the sidebands of the ions' transitions, can be used as harmonic oscillators. Tunable decay of the auxiliary levels by spontaneous emission can, e.g., be achieved by taking $|e\rangle$ and $|f\rangle$ to be metastable states in an atom and driving them to an excited state by a repumper [105]. An alternative stroboscopic implementation requires only a single auxiliary level with a repumper, interchanging between taking the role of $|e\rangle$ and $|f\rangle$ in the assumed coupling configurations, and a single phononic mode, interchanging between a and b .

7.8 Summary

In conclusion, we have shown that dissipative state preparation can be extended to the generation of many body entanglement. This is achieved by generating complex multi-particle Lindblad operators. Using this technique, we develop protocols for the dissipative preparation of GHZ and W states which exhibit favorable polynomial scalings with the qubit number. Our approach may be realized in realistic physical systems such as trapped ions where the basic ingredients of the scheme have already been implemented [105]. We have chosen to exemplify the procedures by preparing W and GHZ states, which are the standard examples of multi-particle entangled states, but the developed techniques are applicable to a range of other tasks. Particularly interesting examples would be the construction of error correction codes, where the dissipation constantly pumps entropy out of the system to stabilize the encoded information [163], or the observation of exotic phase transitions [20, 121] induced by many particle dissipation.

Conclusion and Outlook

In this thesis, we have presented protocols for the dissipative preparation of entanglement. Considering concrete physical systems we have designed schemes that can produce two-particle and multi-particle entangled steady states. To analyze our schemes we have developed a set of methods, in particular an **effective operator formalism** for open quantum systems (Chapter 3).

This technique has allowed us to greatly reduce the complexity of the physical systems considered throughout this work, as has been seen in Chapter 4 – 7. Here, our formalism has provided an understanding of the quantum dynamics and helped us to identify the effective coherent and dissipative interactions. In addition, it has allowed us to engineer effective decay processes to prepare certain desired states. The effective operator concept has thus proven useful for the development of physical schemes for dissipative state preparation.

Since its presentation, our effective operator formalism has been applied in various settings outside dissipative state preparation and dissipative quantum computation, such as cooling, photon switching, and distribution of entanglement, and is inspiring further development of effective descriptions. It may also play a constructive role in quantum simulation in the still novel field of dissipative phase transitions, and in advanced cooling schemes, e.g. involving optomechanical systems. However, in particular in the cooling context, an extension of the effective operator formalism to warm open systems seems necessary.

In Chapter 4 we have presented a scheme for the preparation of a two-particle entangled state in a cavity QED system. There we have shown that, using the sources of noise which naturally occur in a cavity QED system for our protocol, a maximally entangled state of two Λ -atoms in an optical cavity can be prepared and maintained as the steady state of the evolution. As an important result, we have found that our dissipative protocols exhibit a favorable scaling of the error which is linear in the cooperativity of the cavity. The error scaling has thus been improved as compared to previous, in particular unitary protocols for entanglement preparation.

The protocols we have proposed are suitable for various experimental settings. In particular, we have considered schemes which work in the absence of trapping of the atoms in the cavity in the transversal direction, and with cavity driving. Our detailed study may therefore be helpful for the demonstration of

entanglement by dissipation in today's cavity QED experiments. In addition, the thorough understanding of dissipative preparation mechanisms has helped our studies in Chapter 5 – 7.

In Chapter 5, we have considered an entangling task similar to Chapter 4, but implemented it in a superconducting system. Even though superconducting qubits coupled to a common resonator, so-called circuit QED, are made such as to mimic atomic systems, a number of difficulties had to be overcome to make a dissipative entangling scheme work in this system. Here, in particular a two-photon drive needed to be engineered and the preparation mechanism had to be made faster than the qubit decoherence present in the system. It has, however, been possible to develop mechanisms for the dissipative preparation of the desired maximally entangled singlet state of two transmons. Our analysis of the scheme showed that high fidelity with the singlet state can be reached within favorable time for state-of-the-art superconducting systems. As in Chapter 4, we have studied the effect of experimental imperfections to support a potential experimental realization of our scheme.

Meanwhile, dissipatively prepared entanglement of superconducting qubits has been achieved experimentally [116] based on a different theoretical scheme [114]. Compared to this work, we consider our scheme to be more relevant for the generation of high-fidelity steady-state entanglement in superconducting systems.

As another, highly attractive system that has found extensive application in quantum information, we have considered trapped ions in Chapter 6. There, we have presented a scheme for the dissipative preparation of an entangled steady state of two trapped ions, together with its experimental implementation. The scheme takes advantage of the properties of the system and of an added tunable decay process. Its successful experimental realization has shown that dissipation can indeed be turned from an adversary into a resource and that the dissipative approach is viable in practice. Our theoretical analysis of the experiment has explained the remaining sources of error and has shown how these can be reduced. Further adjustment of ion trap setups to the needs of dissipative protocols may thus allow for higher fidelities of the steady state in the future.

In Chapter 7, we have extended the dissipative preparation of entanglement to multi-particle entangled states. Assuming a generic physical system we have shown that dissipative many-body mechanisms can be engineered which produce GHZ and W states. The resulting entangling schemes were found to have favorable polynomial scalings of the preparation time with the qubit number. Our schemes can be experimentally realized in a trapped ion setting.

We believe that dissipatively prepared multi-particle states may be a precious resource in quantum information processing protocols, such as in error correction schemes, and for quantum metrology schemes, where large entangled states can be used to improve the measurement accuracy below the Heisenberg limit.

For the many-body protocols presented in this work, the action of the operators was more important than their actual form. Future works will also focus on the latter, performing “dissipative operator engineering” rather than “dissipative state engineering”. This may allow for the dissipative preparation of broader classes of states, such as graph states [19], and thereby open up the way for

dissipation-aided quantum computation schemes. Here, for example one-way quantum computation schemes [164] could be considered, where a large entangled state (“pad”) is initially prepared as a steady state, using the advantages of dissipative state preparation. In a similar manner, operators could be built that correct the action of specific sources of noise, in error correction schemes (see, e.g., Ref. [163]). Beside quantum computation, noise is found to trigger dissipative phase transitions [20, 121]. Engineering non-trivial noise may thus be of great potential for both quantum simulation of open systems and for the understanding of phenomena of dissipative many-body systems.

Wang-Schirmer scheme generalized to Λ -atoms

In the following, we generalize the scheme of Wang and Schirmer [86], originally proposed for two two-level atoms, to Λ -type atoms. In contrast to the schemes presented so far, the ground state $|1\rangle$ of the two atoms is shifted asymmetrically for the two atoms so that a coherent coupling is created between $|S\rangle$ and $|T\rangle$. This means that a pure singlet state $|S\rangle$ can, even in the absence of spontaneous emission, no longer be reached as the steady state of the time evolution. However, an engineered cavity decay process between the triplet states $|00\rangle \rightarrow |T\rangle \rightarrow |11\rangle$ is used to prepare a steady state which has a minor overlap with $|11\rangle$ and a high fidelity with the singlet.

By elimination of the excited states we will reduce the coupled Λ -atom systems to an effective system of two coupled qubits described by the master equation of Ref. [86] and, subsequently, derive the error scaling of the preparation of the entangled state with the cavity parameters.

The coherent interactions are given by the Hamiltonian of the system as in Eqs. (4.6)–(4.9). Here, we use a ground-state Hamiltonian \hat{H}_g

$$\hat{H}_g = \sum_{j=1,2} \left(\beta + (-1)^j b \right) |1\rangle_j \langle 1| + \Omega_{\text{MW}} (|0\rangle_j \langle 1| + |1\rangle_j \langle 0|), \quad (\text{A.1})$$

where a static magnetic field b has been introduced that results in a shift of ground state $|1\rangle$ with opposite signs for the two atoms. The driving fields for both atoms exhibit the same phase ($\phi = 0$) so that the general effective Lindblad operators are the same as for the $|T\rangle$ schemes. The effective Hamiltonian consists of shifts of the ground states

$$\begin{aligned} \hat{H}_{\text{eff}} = & -\text{Re} \left[\frac{\Omega^2}{2\tilde{\Delta}_{1,\text{eff}}} \right] |00\rangle \langle 00| - \text{Re} \left[\frac{\Omega^2}{4\tilde{\Delta}_{2,\text{eff}}} \right] |T\rangle \langle T| \\ & - \text{Re} \left[\frac{\Omega^2}{4\tilde{\Delta}_{0,\text{eff}}} \right] |S\rangle \langle S| + \hat{H}_g. \end{aligned} \quad (\text{A.2})$$

A parameter choice of $\delta = 0$, $\Delta \gg g \gg (\gamma, \kappa, \Omega, \Omega_{\text{MW}}, \beta, b)$ and $\Delta\kappa \gg g^2$, allows for an adiabatic elimination of the excited atomic levels $|e\rangle$. In this limit,

all propagators $\tilde{\Delta}_{n,\text{eff}}^{-1}$ are simply determined by the shifts of the atomic excited levels Δ ,

$$\tilde{\Delta}_{n,\text{eff}}^{-1} \approx \Delta^{-1}. \quad (\text{A.3})$$

We then obtain the effective Lindblad operators

$$\hat{L}_{\text{eff}}^\kappa = -i\sqrt{\kappa_{\text{eff}}}|11\rangle\langle T| - i\sqrt{\kappa_{\text{eff}}}|T\rangle\langle 00|, \quad (\text{A.4})$$

$$\begin{aligned} \hat{L}_{\text{eff}}^{\gamma,0,\{1,2\}} &= +\sqrt{2\gamma_{\text{eff}}}|00\rangle\langle 00| + \sqrt{\gamma_{\text{eff}}/2}(|T\rangle\langle T| \pm |T\rangle\langle S|) \\ &\quad + \sqrt{\gamma_{\text{eff}}/2}(\pm |S\rangle\langle T| + |S\rangle\langle S|), \end{aligned} \quad (\text{A.5})$$

$$\begin{aligned} \hat{L}_{\text{eff}}^{\gamma,1,\{1,2\}} &= +\sqrt{\gamma_{\text{eff}}}(\mp |S\rangle\langle 00| + |T\rangle\langle 00|) \pm \sqrt{\gamma_{\text{eff}}}|11\rangle\langle S| \\ &\quad + \sqrt{\gamma_{\text{eff}}}|11\rangle\langle T|, \end{aligned} \quad (\text{A.6})$$

where $\kappa_{\text{eff}} = \frac{2g^2\Omega^2}{\Delta^2\kappa}$ and $\gamma_{\text{eff}} = \frac{\gamma\Omega^2}{16\Delta^2}$. The effective Hamiltonian is given by

$$\begin{aligned} \hat{H}_{\text{eff}} &= -\frac{\Omega^2}{2\Delta}|00\rangle\langle 00| + 2\beta|11\rangle\langle 11| \\ &\quad + \left(\beta - \frac{\Omega^2}{4\Delta}\right)|T\rangle\langle T| + \left(\beta - \frac{\Omega^2}{4\Delta}\right)|S\rangle\langle S| \\ &\quad - b(|S\rangle\langle T| + |T\rangle\langle S|) + \Omega_{\text{MW}}(|00\rangle\langle T| + |T\rangle\langle 11| + H.c.). \end{aligned} \quad (\text{A.7})$$

The corresponding effective couplings are shown in Fig. A.1 a).

In order to match the master equation of Ref. [86], we compensate the shifts in the effective Hamiltonian in Eq. (A.7); i.e. we set the (symmetric) detuning of $|1\rangle$ to $\beta = -\frac{\Omega^2}{4\Delta}$. We then obtain the effective Hamiltonian and the effective cavity decay

$$\hat{H}_{\text{eff}} = -b(|S\rangle\langle T| + |T\rangle\langle S|) + \Omega_{\text{MW}}(|00\rangle\langle T| + |T\rangle\langle 11| + H.c.) \quad (\text{A.8})$$

$$\hat{L}_{\text{eff}}^\kappa = \sqrt{\kappa_{\text{eff}}}(|11\rangle\langle T| + |T\rangle\langle 00|). \quad (\text{A.9})$$

From here we construct the Dicke-type master equation along the lines of Ref. [86]. In contrast to Ref. [86], however, we analytically take the (for this scheme) undesired but unavoidable spontaneous emission into account and write

$$\dot{\rho} = -i[\hat{H}_{\text{eff}}, \rho] + \mathcal{D}[\hat{L}_{\text{eff}}^\kappa] + \sum_k \mathcal{D}[\hat{L}_{\text{eff}}^{\gamma,k}] \quad (\text{A.10})$$

with \hat{L}_κ as the engineered decay and \hat{L}_k^γ as the undesirable spontaneous emission processes. In order to analyze the scheme we note that

$$|\psi_S\rangle = \frac{1}{\sqrt{\Omega_{\text{MW}}^2 + b^2}}(b|11\rangle + \Omega_{\text{MW}}|S\rangle) \quad (\text{A.11})$$

is a steady state of the Hamiltonian of Eq. (A.4) and also of the Liouvillian of Eq. (A.10) in the absence of spontaneous emission. To understand the dissipative state preparation mechanism we change into a basis consisting of $|\psi_S\rangle$ and the orthogonal state

$$|\psi_1\rangle = \frac{1}{\sqrt{\Omega_{\text{MW}}^2 + b^2}}(\Omega_{\text{MW}}|11\rangle - b|S\rangle). \quad (\text{A.12})$$

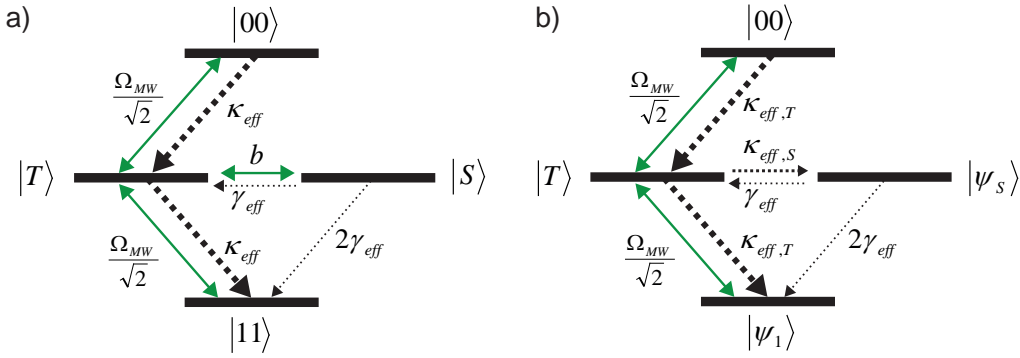


FIGURE A.1: Effective processes of the Wang-Schirmer scheme adapted to Λ -atoms. (a) In the shuffling picture, the triplet states are coupled by a microwave or Raman field Ω_{MW} and decay by an effective cavity decay κ_{eff} . The singlet $|S\rangle$ is coherently coupled to $|T\rangle$ by the level shift b . (b) In the steady-state picture, the desired steady state $|\psi_S\rangle$ is no longer coherently coupled, but dissipatively prepared from $|T\rangle$ at a rate $\kappa_{eff,S}$. Population in $|\psi_S\rangle$ is lost by spontaneous emission γ_{eff} .

As can be seen from Fig. A.1 b), the singlet-like steady state $|\psi_S\rangle$ is prepared at a rate $\kappa_{eff,S} \equiv |\langle \psi_S | \hat{L}_{eff}^\kappa | T \rangle|^2 = \frac{4b^2 g^2 \Omega^2}{\Delta^2 \kappa (2b^2 + \Omega_{MW}^2)}$, ($\kappa_{eff,S} \ll \kappa_{eff}$) and decays only by spontaneous emission.

For the derivation of the error scaling we use a rate argument to compare the decay rates into and out of the steady state ($\dot{P} = 0$, $P_{\psi_S} \approx 1$)

$$(1 - F_{\psi_S}) \approx 3P_T \approx \frac{3\Gamma_{\psi_S \rightarrow} P_S}{\Gamma_{\rightarrow \psi_S}} \approx \frac{3\gamma\kappa (4b^2 + 3\Omega_{MW}^2) \Omega_{MW}^2}{64g^2 (2b^2 + \Omega_{MW}^2) b^2}, \quad (\text{A.13})$$

where we have used the strong coupling condition, and the assumption that the populations of the three undesired states are well-shuffled by Ω_{MW} so that they have a similar population. In contrast to the previously presented schemes, the static error of the protocol incorporates a second term that determines the preset compromise in the fidelity of the steady state due to the asymmetry b so that

$$\begin{aligned} (1 - F_S) &= (1 - F_{\psi_S}) + (1 - |\langle \psi_S | S \rangle|^2) \\ &= \frac{3\gamma\kappa (4b^2 + 3\Omega_{MW}^2) \Omega_{MW}^2}{64g^2 (2b^2 + \Omega_{MW}^2) b^2} + \frac{2b^2}{2b^2 + \Omega_{MW}^2}. \end{aligned} \quad (\text{A.14})$$

The minimal overall error is reached for a trade-off at which these terms are equal. This compromise between establishing the steady state by the asymmetry, and at the same time avoiding the decrease in its fidelity by the asymmetry, is the cause of the different scaling of the error and speed discussed in Sec. 4.6. For the parameter b we obtain the condition

$$b_{opt} = \frac{\sqrt{3}\Omega_{MW}}{\sqrt[4]{2^5}} \sqrt[4]{\frac{\gamma\kappa}{g^2}}. \quad (\text{A.15})$$

Inserting this yields the effective decay rate into $|\psi_S\rangle$

$$\kappa_{eff,S} = \frac{4g^2\Omega^2}{\Delta^2\kappa \left(2 + \frac{3}{\sqrt{32C}}\right)} \approx \frac{2g^2\Omega^2}{\Delta^2\kappa} \quad (\text{A.16})$$

and the error of the protocol

$$(1 - F_S)_{\text{WS}} = \frac{3\gamma\kappa (8g + \sqrt{2}\sqrt{\gamma\kappa})}{4g (3\gamma\kappa + 4\sqrt{2}g\sqrt{\gamma\kappa})} \approx \frac{3}{2\sqrt{2C}}. \quad (\text{A.17})$$

Thus, we find that for the WS protocol the fidelity of the steady state with the maximally entangled singlet state exhibits a scaling with one over the square root of the cooperativity of the cavity. As in the $|S_1\rangle$ scheme, we have one prominent decay process to prepare the singlet from the three dressed ground states. With b_{opt} the spectral gap is then given by

$$\lambda_{\text{WS}} = \frac{\kappa_{\text{eff},S}}{3} = \frac{2g^2\Omega^2}{3\Delta^2\kappa}. \quad (\text{A.18})$$

A numerical comparison with the other schemes is given in Sec. 4.6.

Effects from imperfect coupling of the atoms to the cavity

Experimental realization of a scheme for dissipative state preparation requires an understanding of the effects originating from the imperfect couplings of the atoms to the cavity mode. In state-of-the-art cavity QED systems, such as Ref. [41], longitudinal confinement prevents fluctuation of the atomic positions along the cavity axis. Still, a static difference in the couplings of the two atoms is possible. Expressing these couplings as $g_1 = g(1 + \alpha)$ and $g_2 = g(1 - \alpha)$ the above analyses can still be carried out for the mean coupling of $g = \frac{1}{2}(g_1 + g_2)$. From the asymmetry α an additional source of error emerges. Below, we exemplarily derive this asymmetry error for the $|S_1\rangle$ scheme. In case of a static, asymmetric coupling of the two atoms to the cavity the atom-cavity coupling can be written as

$$\begin{aligned}\hat{H}_{\text{ac}} &= \hat{a} (g_1|e\rangle_1\langle 1| + g_2|e\rangle_2\langle 1|) + H.c. \\ &= \hat{a}g ((1 + \alpha)|e\rangle_1\langle 1| + (1 - \alpha)|e\rangle_2\langle 1|) + H.c.,\end{aligned}\tag{B.1}$$

The asymmetry error affects both the dynamics of the populations and the coherences so that we use the effective Liouvillian \mathcal{L}_{eff} to derive the steady state, after having excluded other sources of error beforehand ($\kappa_{\text{eff}} \rightarrow 0$). For weak driving and strong coupling $g \gg (\gamma, \kappa) \gg (\Omega, \Omega_{\text{MW}}, \beta)$ the asymmetry error α can be effectively decoupled from both the static error ($\propto C^{-1}$) and the dynamic error ($\propto \Omega^2$) and we obtain

$$(1 - F_S)_\alpha \approx 3\alpha^2.\tag{B.2}$$

The result is plotted in Fig. B.1 using the parameters of Ref. [41]. The effect of an asymmetric coupling is found to be rather small as compared to other sources of errors. For $|\alpha| \approx 0.1$ the loss of fidelity through asymmetry is as small as $\approx 2\%$. In this case, with $\frac{g_1}{g_2} \approx 1.22$, fidelities of about 90% are still achievable.

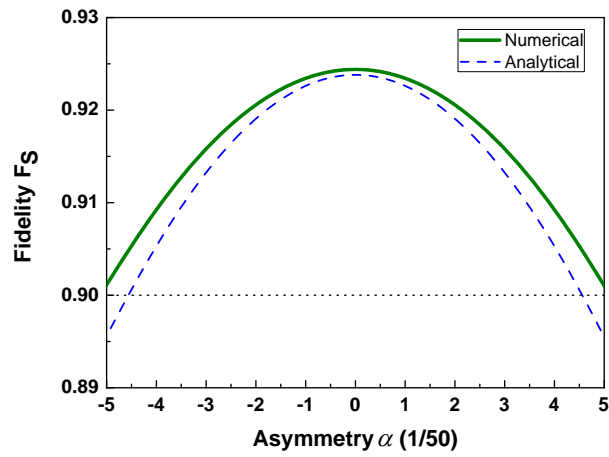


FIGURE B.1: Fidelity under asymmetric coupling to the cavity. Numerical results from the full Liouvillian (solid green) are well-approximated by the analytic findings (blue dash). High fidelities of about 90% are achieved up to $|\alpha| \approx 0.1$, where $\frac{g_1}{g_2} \approx 1.22$.

Spin-state fidelity measurement

In the following, we discuss the technique used in the experiment described in Chapter 6 to determine the state of the system.

To detect the populations of the $|S\rangle$, $|T\rangle$, $|\uparrow\uparrow\rangle$, and $|\downarrow\downarrow\rangle$ states, we need to obtain the relevant elements of the density matrix ρ describing the state of the two ${}^9\text{Be}^+$ ions during the experiment. Since each ion may be found in any of the three ground states $|\uparrow\rangle$, $|\downarrow\rangle$, $|a\rangle$ (Fig. 6.1) the density matrix has dimensions 9×9 . The singlet-state population is given by $\frac{1}{2}(\rho_{\uparrow\downarrow,\uparrow\downarrow} + \rho_{\downarrow\uparrow,\downarrow\uparrow}) - \text{Re}(\rho_{\uparrow\downarrow,\downarrow\uparrow})$ and the triplet-state population is given by $\frac{1}{2}(\rho_{\uparrow\downarrow,\uparrow\downarrow} + \rho_{\downarrow\uparrow,\downarrow\uparrow}) + \text{Re}(\rho_{\uparrow\downarrow,\downarrow\uparrow})$. The fidelity of the target entangled state, F , is equal to the singlet-state population. For the steady state fidelity, we report the average fidelity measured between 6 and 12 ms for the continuous case and between 35 and 59 steps in the stepwise case. We first measure the populations of the $|\downarrow\rangle$ state by collecting fluorescence photons from the laser-induced cycling transition $|\downarrow\rangle \leftrightarrow 2p \ ^2P_{3/2}|3,3\rangle$ of both ${}^9\text{Be}^+$ ions together. We apply this detection beam for 250 μs and collect photon counts with a photo-multiplier tube (approximately 30 counts are registered per ion in the $|\downarrow\rangle$ state). We repeat the experiment and detection 400 times to obtain a histogram. We fit the histogram of counts to a Poisson distribution to obtain the probabilities to measure both ions, one ion, and zero ions in the $|\downarrow\rangle$ state denoted by P_2 , P_1 , and P_0 , respectively. Specifically, these probabilities are related to the density matrix as follows: $P_2 = \rho_{\downarrow\downarrow,\downarrow\downarrow}$, $P_1 = \rho_{\downarrow\uparrow,\downarrow\uparrow} + \rho_{\uparrow\downarrow,\uparrow\downarrow} + \rho_{a\downarrow,a\downarrow} + \rho_{\downarrow a,\downarrow a}$, and $P_0 = \rho_{\uparrow\uparrow,\uparrow\uparrow} + \rho_{a\uparrow,a\uparrow} + \rho_{\uparrow a,\uparrow a} + \rho_{aa,aa}$. We repeat the entanglement preparation scheme and perform a microwave π pulse on the $|\downarrow\rangle \leftrightarrow |\uparrow\rangle$ followed by the same detection procedure to obtain: $P_{2,\pi} = \rho_{\uparrow\uparrow,\uparrow\uparrow}$, $P_{1,\pi} = \rho_{\uparrow\downarrow,\uparrow\downarrow} + \rho_{\downarrow\uparrow,\downarrow\uparrow} + \rho_{a\uparrow,a\uparrow} + \rho_{\uparrow a,\uparrow a}$, and $P_{0,\pi} = \rho_{\downarrow\downarrow,\downarrow\downarrow} + \rho_{a\downarrow,a\downarrow} + \rho_{\downarrow a,\downarrow a} + \rho_{aa,aa}$. Thus, assuming the population of the $|aa\rangle$ state is negligible (see below), we have $\rho_{\uparrow\downarrow,\uparrow\downarrow} + \rho_{\downarrow\uparrow,\downarrow\uparrow} = P_1 - (P_{0,\pi} - P_2)$. To obtain the off-diagonal elements we perform the same experiment but with a microwave $\pi/2$ pulse on the $|\downarrow\rangle \leftrightarrow |\uparrow\rangle$ transition prior to the detection to obtain $P_{2,\pi/2}$, $P_{1,\pi/2}$, and $P_{0,\pi/2}$. The phase of the microwave is randomized in each experiment. It can be shown that $\text{Re}(\rho_{\uparrow\downarrow,\downarrow\uparrow}) = -1/2 + 2P_{0,\pi/2} + \frac{1}{2}(P_2 - P_0) + \frac{1}{2}(P_{2,\pi} - P_{0,\pi})$, which gives the last piece of information needed to obtain the populations of the $|S\rangle$ and $|T\rangle$ states.

Due to spontaneous Raman scattering caused by the sideband laser beams it is

possible that the ${}^9\text{Be}^+$ ions can be transferred to a hyperfine state outside the $|\uparrow\rangle, |\downarrow\rangle, |a\rangle$ manifold. However, this detection procedure does not distinguish these states from the $|a\rangle$ state. Our model predicts that the probability to find at least one ion outside the three-state manifold is at most 5% for the data in Fig. 6.3 and 3% for the data in Fig. 6.4. In future experiments, this population could be brought back to the three-state manifold with additional repump beams.

To calculate the singlet fidelity above, we assumed that the probability to find both atoms outside the $|\uparrow\rangle, |\downarrow\rangle$ qubit manifold was negligible. For the data in figures 6.3 and 6.4 we measured the probability to find at least one ion outside the qubit manifold state, given by $P_0 + P_{0,\pi} - (P_2 + P_{2,\pi})$, to be 7(5)% and 2(2)% respectively for the steady state. We expect the probability to find both ions outside the qubit manifold to be on order of the square of the probability to find one ion outside the qubit manifold, which is therefore small. Furthermore, our theoretical model predicts the probability of finding both ions outside the qubit manifold to be at most 1% for the continuous implementation and 0.05% for the stepwise implementation.

Derivation of the effective operators for the many-body schemes

In the following, we derive the effective dynamics for each of the four coupling configurations used to prepare GHZ and W states by dissipation in Chapter 7.

As can be seen from Sec. 7.2 the dissipation only affects the excited levels $|e\rangle$ and $|f\rangle$ and the oscillator modes a and b . We can thus, based on the assumption of weak driving, adiabatically eliminate these decaying degrees of freedom from the master equation. This is done using the effective operator formalism presented in Chapter 3, by which the dynamics of the master equation in Eq. (7.3) are reduced to effective couplings between the ground states of the system, described by an effective master equation

$$\dot{\rho} = -i[H_{\text{eff}}, \rho] + \sum_k L_{k,\text{eff}}\rho(L_{k,\text{eff}})^\dagger - \frac{1}{2} \left((L_{k,\text{eff}})^\dagger L_{k,\text{eff}}\rho + \rho(L_{k,\text{eff}})^\dagger L_{k,\text{eff}} \right), \quad (\text{D.1})$$

Since we are dealing with multiple field tones F that give rise to the effective couplings, we use the extended formalism of Sec. 3.3.6 with

$$H_{\text{eff}} = -\frac{1}{2}V_- \sum_F \left(H_{\text{NH}}^{(F)} \right)^{-1} V_+^{(F)} + H.c., \quad (\text{D.2})$$

$$L_{k,\text{eff}} = L_k \sum_F \left(H_{\text{NH}}^{(F)} \right)^{-1} V_+^{(F)}, \quad (\text{D.3})$$

$$H_{\text{NH}}^{(F)} = H_{\text{free}} + H_{\text{int}} - \frac{i}{2} \sum_k L_k^\dagger L_k - \omega^{(F)}. \quad (\text{D.4})$$

Here, $V_+^{(F)}$ denotes the exciting part and $V_-^{(F)}$ the deexciting part of the drive $V^{(F)}$ ($V_\pm = \sum_F V_\pm^{(F)}$). The non-Hermitian Hamiltonian $H_{\text{NH}}^{(F)}$, which contains the frequency $\omega^{(F)}$ of the respective field tone F , describes the time evolution of the excited states. The drives are regarded as perturbations and thus denoted by “ V ”; they are defined by the drive Hamiltonians H_{drive} in Sec. 7.3.1 and 7.5.1 so

that we use $V = H_{\text{drive}}$ for each configuration below. Based on the assumption of a weak excitation V we restrict our discussion to the states which have at most one atomic or oscillator excitation. H_{NH} then contains the energies and couplings of the excited states. Since H_{NH} needs to be inverted to compute the effective operators, we will, for each coupling situation, start out by discussing this entity.

Z configuration

We begin with the Z coupling configuration, which is similar to the X configuration. Both are required for the generation of GHZ states. We use $H_{\text{int,Z}}$ and $H_{\text{drive,Z}}$ from Sec. 7.3.1 and the Lindblad operators of Eqs. (7.6)–(7.11) to set up the non-Hermitian Hamiltonian

$$H_{\text{NH,Z}}^{(F)} = \tilde{\Delta}_Z^{(F)} J_{ee} + \tilde{\delta}_Z^{(F)} a^\dagger a + g \left(a^\dagger J_{1e} + a J_{1e}^\dagger \right). \quad (\text{D.5})$$

Here, we have introduced complex detunings $\tilde{\Delta}_Z^{(F)} = \omega_e - \omega_Z^{(F)} - \frac{i\gamma_e}{2}$ and $\tilde{\delta}_Z^{(F)} = \omega_a - \omega_Z^{(F)} - \frac{i\kappa_a}{2}$, where F denotes the particular tone of the driving field. Furthermore, we have changed into a frame rotating with the frequency of the drive $\omega_Z^{(F)}$. For the derivation of the effective operators we will for simplicity drop the sub- and superscripts denoting the coupling configurations and field tones. To invert the non-Hermitian Hamiltonian we divide it into four blocks

$$H_{\text{NH}} = A + B + C + D, \quad (\text{D.6})$$

$$A = \tilde{\delta} a^\dagger a, \quad B = g a^\dagger J_{1e}, \quad C = g a J_{1e}^\dagger, \quad D = \tilde{\Delta} J_{ee}. \quad (\text{D.7})$$

After this separation we can formally invert the Hamiltonian H_{NH} , using Banachiewicz' theorem [165] for the blockwise inversion of a square matrix,

$$H_{\text{NH}}^{-1} = a + b + c + d, \quad (\text{D.8})$$

$$d = \left(D - CA^{-1}B \right)^{-1}, \quad (\text{D.9})$$

$$a = A^{-1} + A^{-1}B d CA^{-1}, \quad (\text{D.10})$$

$$b = -A^{-1}B d, \quad (\text{D.11})$$

$$c = B^T = -d CA^{-1} \quad (\text{D.12})$$

We now need to compute d to obtain any of the above elements. As we shall see, it is possible to simplify the calculation and to obtain closed expressions for the decay rates if we separate the involved operators by the number of atoms in state $|1\rangle$. This is done by introducing projection operators P_{n_1} which project on the states with the same number n_1 (from now on, n) of atoms in $|1\rangle$. For the Z and X configurations discussed here, n_1 (or n_- for X) is conserved under the couplings by the coherent interactions H_{int} and V , but can be changed by the dissipative jump processes L_k , e.g. from n_1 to $n_1 - 1$ in the case of Z. Using the projectors we can split the non-Hermitian Hamiltonian of the excited states and its four blocks by n ,

$$H_{\text{NH}} = \sum_{n=0}^N H_{\text{NH},n} P_n = \sum_{n=0}^N A_n + B_n + C_n + D_n. \quad (\text{D.13})$$

The inverse of the non-Hermitian Hamiltonian for each n is then found to be

$$H_{\text{NH},n}^{-1} = a_n + b_n + c_n + d_n. \quad (\text{D.14})$$

With that the effective operators of Eqs. (D.2)–(D.3) are formally given by

$$L_{\kappa,\text{eff}} = \sum_n \sqrt{\kappa} a b_n V P_n \quad (\text{D.15})$$

$$L_{\gamma_0,a,\text{eff}} = \sum_n \sqrt{\gamma_0} |0\rangle_a \langle e| d_n V P_n \quad (\text{D.16})$$

$$L_{\gamma_1,a,\text{eff}} = \sum_n \sqrt{\gamma_1} |1\rangle_a \langle e| d_n V P_n \quad (\text{D.17})$$

$$H_{\text{eff}} = -\frac{1}{2} V \sum_n d_n V P_n + H.c. \quad (\text{D.18})$$

To obtain the effective Lindblad operators and the effective Hamiltonian it is thus sufficient to compute the blocks d_n and b_n of the inverse non-Hermitian Hamiltonian. Using the identities $a(a^\dagger a)^{-1} a^\dagger = \mathbb{1}$ and $P_g J_{1e} J_{ee} = P_g J_{1e}$ (where P_g is the projector onto the ground states) we obtain

$$d_n = \frac{1}{\tilde{\Delta}} \left[J_{ee} - \left(n - \frac{\tilde{\Delta} \tilde{\delta}}{g^2} \right)^{-1} J_{1e}^\dagger J_{1e} \right], \quad (\text{D.19})$$

$$b_n = \frac{g}{\tilde{\Delta} \tilde{\delta}} a^\dagger J_{1e} \left[J_{ee} - \left(n - \frac{\tilde{\Delta} \tilde{\delta}}{g^2} \right)^{-1} J_{1e}^\dagger J_{1e} \right]. \quad (\text{D.20})$$

With this, and readopting the sub- and superscripts for the configuration and the field, and changing to a more detailed notation for the effective Lindblad operators we find

$$L_{\kappa_a,Z} = \sum_{n_1,F} \frac{\sqrt{\kappa_a} \Omega_Z^{(F)}}{2} e^{-i\omega_Z^{(F)} t} \left(g - \frac{\tilde{\Delta}_Z^{(F)} \tilde{\delta}_Z^{(F)}}{n_1 g} \right)^{-1} P_{n_1} \quad (\text{D.21})$$

$$\equiv \sum_{n_1,F} \frac{\sqrt{\kappa_a} \Omega_Z^{(F)}}{2 \tilde{g}_{Z,n_1}^{(F)}} e^{-i\omega_Z^{(F)} t} P_{n_1}, \quad (\text{D.22})$$

$$L_{\gamma_0,a,Z} = \sum_{n_1,F} \frac{\sqrt{\gamma_0 e} \Omega_Z^{(F)}}{2} e^{-i\omega_Z^{(F)} t} \left(\tilde{\Delta}_Z^{(F)} - \frac{n_1 g^2}{\tilde{\delta}_Z^{(F)}} \right)^{-1} |0\rangle_a \langle 1| P_{n_1} \quad (\text{D.23})$$

$$\equiv \sum_{n_1,F} \frac{\sqrt{\gamma_0 e} \Omega_Z^{(F)}}{2 \tilde{\Delta}_{Z,n_1}^{(F)}} e^{-i\omega_Z^{(F)} t} |0\rangle_a \langle 1| P_{n_1}, \quad (\text{D.24})$$

$$L_{\gamma_1,a,Z} = \sum_{n_1,F} \frac{\sqrt{\gamma_1 e} \Omega_Z^{(F)}}{2} e^{-i\omega_Z^{(F)} t} \left(\tilde{\Delta}_Z^{(F)} - \frac{n_1 g^2}{\tilde{\delta}_Z^{(F)}} \right)^{-1} |1\rangle_a \langle 1| P_{n_1} \quad (\text{D.25})$$

$$\equiv \sum_{n_1,F} \frac{\sqrt{\gamma_1 e} \Omega_Z^{(F)}}{2 \tilde{\Delta}_{Z,n_1}^{(F)}} e^{-i\omega_Z^{(F)} t} |1\rangle_a \langle 1| P_{n_1}. \quad (\text{D.26})$$

To obtain this we have used the identities $P_g J_{1e} J_{e1} P_g = P_g J_{11} P_g$, $J_{11} P_{n_1} = n_1 P_{n_1}$, and $J_{ee} J_{e1} P_g = J_{e1} P_g$. In the last expression we have introduced the effective

detunings $\tilde{\Delta}_{Z,n_1}$ and the effective couplings \tilde{g}_{Z,n_1} with

$$\tilde{\Delta}_{Z,n_1}^{(F)} = \tilde{\Delta}_Z^{(F)} - \frac{n_1 g^2}{\tilde{\delta}_Z^{(F)}}, \quad (\text{D.27})$$

$$\tilde{g}_{Z,n_1}^{(F)} = g - \frac{\tilde{\Delta}_Z^{(F)} \tilde{\delta}_Z^{(F)}}{n_1 g}. \quad (\text{D.28})$$

As can be seen from Eqs. (D.22)–(D.26), dealing with multiple frequencies in the drive leads a priori to an sum over terms for all fields in the effective Lindblad operators. However, as the frequencies of these fields are well-distinguishable, we separate the Lindblad operators by their driving field F . Given the quadratic appearance of the Lindblad operators in the master equation, we can also drop the exponential phase factors. For the effective Lindblad operators for the fields F we then obtain

$$L_{\kappa_a,Z}^{(F)} = \sum_{n_1=0}^N \frac{\sqrt{\kappa_a} \Omega_Z^{(F)}}{2 \tilde{g}_{Z,n_1}^{(F)}} P_{n_1}, \quad (\text{D.29})$$

$$L_{\gamma_{0e},a,Z}^{(F)} = \sum_{n_1=0}^N \frac{\sqrt{\gamma_{0e}} \Omega_Z^{(F)}}{2 \tilde{\Delta}_{Z,n_1}^{(F)}} |0\rangle_a \langle 1| P_{n_1}, \quad (\text{D.30})$$

$$L_{\gamma_{1e},a,Z}^{(F)} = \sum_{n_1=0}^N \frac{\sqrt{\gamma_{1e}} \Omega_Z^{(F)}}{2 \tilde{\Delta}_{Z,n_1}^{(F)}} |1\rangle_a \langle 1| P_{n_1}. \quad (\text{D.31})$$

We also define the corresponding effective decay rates

$$\kappa_{a,Z,n_1}^{(F)} = \frac{\kappa_a (\Omega_Z^{(F)})^2}{4 |\tilde{g}_{Z,n_1}^{(F)}|^2}, \quad (\text{D.32})$$

$$\gamma_{0,Z,n_1}^{(F)} = \frac{\gamma_{0e} (\Omega_Z^{(F)})^2}{4 |\tilde{\Delta}_{Z,n_1}^{(F)}|^2}, \quad (\text{D.33})$$

$$\gamma_{1,Z,n_1}^{(F)} = \frac{\gamma_{1e} (\Omega_Z^{(F)})^2}{4 |\tilde{\Delta}_{Z,n_1}^{(F)}|^2}. \quad (\text{D.34})$$

The operators in Eqs. (D.29)–(D.31) are then the effective Lindblad operators for the Z configuration. As can be seen from the expressions in Eqs. (D.27)–(D.28), the effective detunings $\tilde{\Delta}_{Z,n}^{(F)}$ can be engineered to be very small by a suitable choice of the frequencies ω_F of the fields F which can be used to engineer the rates $\gamma_{0,Z,n_1}^{(F)}$ and $\gamma_{1,Z,n_1}^{(F)}$ of the effective decay processes. The engineering of the effective decay process that prepare GHZ and W states will be the subject of Sec. 7.3 and 7.5.

The effective Hamiltonian is computed from Eq. (D.2). Other than for the effective Lindblad operators, introducing a multi-tone driving field results in cross terms between different fields, here denoted by F and G ,

$$H_Z = - \sum_{n_1=0}^N \sum_{F,G} \text{Re} \left(\frac{n_1 \Omega_Z^{(F)} \Omega_Z^{(G)}}{4 \tilde{\Delta}_{Z,n_1}^{(F)}} e^{-i(\omega_Z^{(F)} - \omega_Z^{(G)})t} \right) P_{n_1} \quad (\text{D.35})$$

Here, all terms $F \neq G$ have fast rotating exponential phase factors. Restricting the treatment to $F = G$ where these terms cancel, we obtain the main contribution

$$H_Z \approx - \sum_{n_1=0}^N \sum_F \operatorname{Re} \left(\frac{n_1 (\Omega_Z^{(F)})^2}{4\tilde{\Delta}_{Z,n_1}^{(F)}} \right) P_{n_1} \equiv \sum_{n_1=0}^N \sum_F s_{Z,n_1}^{(F)} P_{n_1}. \quad (\text{D.36})$$

We thus find that the main effective Hamiltonian processes are AC Stark shifts with a magnitude

$$s_{Z,n_1}^{(F)} = -\operatorname{Re} \left(\frac{n_1 (\Omega_Z^{(F)})^2}{4\tilde{\Delta}_{Z,n_1}^{(F)}} \right) \quad (\text{D.37})$$

As we will see in Chapter 7, our choice of the field tones will make these Hamiltonian terms compensate each other.

X configuration

We perform an analogous treatment for the X pumping mediated by the excited level $|f\rangle$ and the oscillator mode b . The effective operators are obtained in the same way as for the Z configuration, using the non-Hermitian Hamiltonian

$$H_{\text{NH},X}^{(F)} = \tilde{\Delta}_X^{(F)} J_{ff} + \tilde{\delta}_X^{(F)} a^\dagger a + g a^\dagger J_{-f} + g a J_{-f}^\dagger \quad (\text{D.38})$$

with the complex energies $\tilde{\Delta}_X^{(F)} = \omega_f - \omega_X^{(F)} - \frac{i\gamma_f}{2}$ and $\tilde{\delta} = \omega_b - \omega_X^{(F)} - \frac{i\kappa_b}{2}$. Carrying out the derivation in the same manner as above for Z, we obtain for the effective Lindblad operators

$$L_{\kappa,X}^{(F)} = \sum_{n_-=0}^N \frac{\sqrt{\kappa_b} \Omega_X^{(F)}}{2\tilde{g}_{X,n_-}^{(F)}} P_{n_-} \quad (\text{D.39})$$

$$L_{\gamma_{0,a},X}^{(F)} = \sum_{n_-=0}^N \frac{\sqrt{\gamma_{0f}} \Omega_X^{(F)}}{2\tilde{\Delta}_{X,n_-}^{(F)}} |0\rangle_a \langle -| P_{n_-} \quad (\text{D.40})$$

$$L_{\gamma_{1,a},X}^{(F)} = \sum_{n_-=0}^N \frac{\sqrt{\gamma_{1f}} \Omega_X^{(F)}}{2\tilde{\Delta}_{X,n_-}^{(F)}} |1\rangle_a \langle -| P_{n_-}. \quad (\text{D.41})$$

with the effective detunings

$$\tilde{\Delta}_{X,n_-}^{(F)} = \tilde{\Delta}_X^{(F)} - \frac{n_- g^2}{\tilde{\delta}_X^{(F)}}, \quad (\text{D.42})$$

$$\tilde{g}_{X,n_-}^{(F)} = g - \frac{\tilde{\Delta}_X^{(F)} \tilde{\delta}_X^{(F)}}{n_- g}. \quad (\text{D.43})$$

The effective decay rates can be written as

$$\kappa_{X,n_-}^{(F)} = \frac{\kappa_b(\Omega_X^{(F)})^2}{4|\tilde{\delta}_{X,n_-}^{(F)}|^2}, \quad (\text{D.44})$$

$$\gamma_{0,X,n_-}^{(F)} = \frac{\gamma_{0f}(\Omega_X^{(F)})^2}{4|\tilde{\Delta}_{X,n_-}^{(F)}|^2}, \quad (\text{D.45})$$

$$\gamma_{1,X,n_-}^{(F)} = \frac{\gamma_{1f}(\Omega_X^{(F)})^2}{4|\tilde{\Delta}_{X,n_-}^{(F)}|^2}. \quad (\text{D.46})$$

These operators resemble the ones for Z pumping in Eqs. (D.29)–(D.31) when $|1\rangle$ is replaced by $|-\rangle$. The difference is that spontaneous emission is still assumed to lead to the final states $|0\rangle$ and $|1\rangle$.

W configuration

We now turn to the other two coupling situations, W and A, which are required for preparing the $|W\rangle$ state. The situation for W and A is different from the previous cases of Z and X in the sense that V and H act on different transitions. Here, we first consider W and, in the next section, A. To find d we consider H_{NH} in blocks of coupled states with $n_1 = N - n_0 + 1$ atoms in $|1\rangle$, where n_0 denotes the number of atoms in state $|0\rangle$ that can be excited by the drive,

$$H_{\text{NH},W}^{(F)} = \tilde{\Delta}_W^{(F)} J_{ee} + \tilde{\delta}_W^{(F)} a^\dagger a + g a^\dagger J_{1e} + g a J_{1e}^\dagger, \quad (\text{D.47})$$

using $\tilde{\Delta}_W^{(F)} = \omega_e - \omega_W^{(F)} - \frac{i\gamma_e}{2}$ and $\tilde{\delta}_W^{(F)} = \omega_a - \omega_W^{(F)} - \frac{i\kappa_a}{2}$. Inversion yields the expressions

$$d_{W,n_0}^{(F)} = \frac{1}{\tilde{\Delta}} \left[J_{ee} - \left((N - n_0 + 1) - \frac{\tilde{\Delta}_W^{(F)} \tilde{\delta}_W^{(F)}}{g^2} \right)^{-1} J_{e1} J_{1e} \right] \equiv \frac{1}{\tilde{\Delta}} \left[J_{ee} - \tilde{n}_{W,n_0}^{-1} J_{e1} J_{1e} \right] \quad (\text{D.48})$$

$$b_{W,n_0}^{(F)} = \left[(N - n_0 + 1) g - \frac{\tilde{\Delta}_W^{(F)} \tilde{\delta}_W^{(F)}}{g} \right]^{-1} (a^\dagger a)^{-1} a^\dagger J_{1e} \equiv \tilde{g}_{W,n_0}^{-1} (a^\dagger a)^{-1} a^\dagger J_{1e}, \quad (\text{D.49})$$

where we have defined the effective couplings

$$\tilde{g}_{W,n_0}^{(F)} = (N - n_0 + 1) g - \frac{\tilde{\Delta}_W^{(F)} \tilde{\delta}_W^{(F)}}{g} \quad (\text{D.50})$$

$$\tilde{n}_{W,n_0}^{(F)} = (N - n_0 + 1) - \frac{\tilde{\Delta}_W^{(F)} \tilde{\delta}_W^{(F)}}{g^2} = \frac{\tilde{g}_{W,n_0}^{(F)}}{g}. \quad (\text{D.51})$$

With the identity $P_g J_{1e} J_{e0} P_g = P_g J_{10} P_g$ this yields the effective operators for W,

$$L_{\kappa,W}^{(F)} = \sum_{n_0=0}^N \frac{\sqrt{\kappa_a} \Omega_W^{(F)}}{2\tilde{g}_{W,n_0}^{(F)}} J_{10} P_{n_0} \equiv \sum_{n_0=0}^N \sqrt{\kappa_{W,n_0}^{(F)}} J_{10} P_{n_0}, \quad (\text{D.52})$$

$$L_{\gamma_{0,a},W}^{(F)} = \sum_{n_0=0}^N \frac{\sqrt{\gamma_{0e}} \Omega_W^{(F)}}{2\tilde{\Delta}_W^{(F)}} \left[|0\rangle_a \langle 0| - (\tilde{n}_{W,n_0}^{(F)})^{-1} |0\rangle_a \langle 1| J_{10} \right] P_{n_0}, \quad (\text{D.53})$$

$$L_{\gamma_{1,a},W}^{(F)} = \sum_{n_0=0}^N \frac{\sqrt{\gamma_{1e}} \Omega_W^{(F)}}{2\tilde{\Delta}_W^{(F)}} \left[|1\rangle_a \langle 0| - (\tilde{n}_{W,n_0}^{(F)})^{-1} |1\rangle_a \langle 1| J_{10} \right] P_{n_0}, \quad (\text{D.54})$$

$$H_W^{(F)} = -\frac{(\Omega_W^{(F)})^2}{8\tilde{\Delta}_W^{(F)}} \sum_{n_0=0}^N \left[n_0 - (\tilde{n}_{W,n_0}^{(F)})^{-1} J_{01} J_{10} \right] P_{n_0} + H.c. \quad (\text{D.55})$$

It can be seen that for the W configuration – and, as we will see below, also for A – we typically do not reach a compact expression for the effective operators. However, as we will see in Sec. 7.5, these expressions simplify considerably for most of the states which are relevant to the scheme, in particular for the dark states of J_{10} .

A configuration

The effective operators for A are found by making the replacements $0 \leftrightarrow 1$, $e \leftrightarrow f$ and $n_0 \leftrightarrow n_1$ in the terms for W above. We then obtain

$$L_{\kappa,A}^{(F)} = \sum_{n_1=0}^N \frac{\sqrt{\kappa_b} \Omega_A^{(F)}}{2\tilde{g}_{A,n_1}^{(F)}} J_{01} P_{n_1} \equiv \sum_n \sqrt{\kappa_{A,n_1}^{(F)}} J_{01} P_{n_1} \quad (\text{D.56})$$

$$L_{\gamma_{0,a},A}^{(F)} = \sum_{n_1=0}^N \frac{\sqrt{\gamma_{0e}} \Omega_A^{(F)}}{2\tilde{\Delta}_A^{(F)}} \left[|0\rangle_a \langle 1| - (\tilde{n}_{A,n_1}^{(F)})^{-1} |0\rangle_a \langle 0| J_{01} \right] P_{n_1} \quad (\text{D.57})$$

$$L_{\gamma_{1,a},A}^{(F)} = \sum_{n_1=0}^N \frac{\sqrt{\gamma_{1e}} \Omega_A^{(F)}}{2\tilde{\Delta}_A^{(F)}} \left[|1\rangle_a \langle 1| - (\tilde{n}_{A,n_1}^{(F)})^{-1} |1\rangle_a \langle 0| J_{01} \right] P_{n_1} \quad (\text{D.58})$$

$$H_A^{(F)} = -\frac{(\Omega_A^{(F)})^2}{8\tilde{\Delta}_A^{(F)}} \sum_{n_1=0}^N \left[n_1 - (\tilde{n}_{A,n_1}^{(F)})^{-1} J_{10} J_{01} \right] P_{n_1} + H.c. \quad (\text{D.59})$$

The above operators are used in Chapter 7 to engineer effective decay processes.

Scaling analysis of the GHZ protocol

In the following, we provide an analytical study of the scaling of the GHZ scheme¹. We derive an expression for the preparation time and optimize it by the choice of the parameters. The analysis is performed both for weak driving, beginning in Sec. E.1, and for strong driving in Sec. E.5.

E.1 Optimization of the parameters for Z pumping alone

The different schemes presented in Chapter 7 have in common that the population of a nearly exponential number of states is pumped to subspaces with a polynomial number of states in a number of steps linear in the size of the system. For GHZ we have engineered strong decay processes from $N - 1 \geq n_1 \geq 2$ for W from $N \geq n_1 \geq 2$. The decay is achieved using the Z pumping which is only sensitive to n_1 and reduces this to $n_1 - 1$, finally leading to $n_1 = 0$ for GHZ and $n_1 \leq 1$ for W state preparation. In order to assess the performance of the scheme it is thus important to know the time for a concatenated process consisting of many consecutive Z processes. The rate of each individual decay is given by (see Eq. (7.56)):

$$\Gamma_{n_1 \rightarrow n_1-1, \gamma 0, Z}^{(F=n_1)} = \sum_{a=1}^N \sum_k |\langle \psi_k | P_{n_1-1} L_{\gamma 0, a, Z}^{(F=n_1)} P_{n_1} | \psi_j \rangle|^2 \approx \frac{2n_1 \gamma 0_e (\Omega_Z^{(F=n_1)})^2}{(\gamma_e + \kappa_a)^2} \quad (\text{E.1})$$

The average time for this decay to occur is given by the inverse decay rate,

$$\tau_{n_1 \rightarrow n_1-1, \gamma 0, Z} = \Gamma_{n_1 \rightarrow n_1-1, \gamma 0, Z}^{-1} \quad (\text{E.2})$$

For the total time required for pumping from an n_1 to an n'_1 we add the average times for the intermediate steps

$$\tau_{n_1 \rightarrow n'_1} = \sum_{n=n'_1+1}^{n_1} \tau_{n \rightarrow n-1, \gamma 0, Z} = \sum_{n=n'_1+1}^{n_1} \Gamma_{n \rightarrow n-1, \gamma 0, Z}^{-1} = \frac{(\gamma_e + \kappa_a)^2}{2\gamma 0_e} \sum_{n=n'_1+1}^{n_1} \frac{1}{n (\Omega_Z^{(F=n)})^2} \quad (\text{E.3})$$

¹The analysis has been performed in collaboration with D. Reeb.

We can also assign a total decay rate from an initial state with n_1 to a final state with n'_1 , $\Gamma_{n_1 \rightarrow n'_1} = \frac{1}{\tau}$. It is, however, more useful to use the total preparation time and to minimize it by the choice of available parameters. Here, in particular the Rabi frequencies $\Omega_Z^{(F)}$ of individual field tones F can be chosen, as well as the tunable decay rate γ_e .

Since the pumping occurs from a maximal n_1 of $N - 1$ to $n_1 - 1$, the worst case preparation time for Z pumping is (using Eq. (E.3)) found to be given by

$$\tau_{n_1=N-1 \rightarrow n_1=0} = \frac{(\gamma_e + \kappa_a)^2}{2\gamma_{0e}} \sum_{n_1=1}^{N-1} \frac{1}{n_1 (\Omega_Z^{(F=n_1)})^2} \quad (\text{E.4})$$

The time from $n_1 = 1$ to $|\text{GHZ}\rangle$ differs from that to $n_1 = 0$ by a factor of 2. This is due to the fact that only half of the population is pumped to $|\text{GHZ}\rangle$ and the other half to $|\text{GHZ}_-\rangle$, which is continuously depumped by the X pumping discussed below. Therefore, on average two attempts are required so that the preparation time is doubled,

$$\tau_{n_1=N-1 \rightarrow \text{GHZ}} = 2\tau_{n_1=N-1 \rightarrow n_1=0} = \frac{(\gamma_e + \kappa_a)^2}{\gamma_{0e}} \sum_{n_1=1}^{N-1} \frac{1}{n_1 (\Omega_Z^{(F=n_1)})^2} \quad (\text{E.5})$$

For the analysis of the GHZ preparation we will from now on choose the parameter values $\kappa_a = \kappa_b = 0$, $\gamma_{0e} = \gamma_{1e} = \gamma_e/2$, and abbreviate $\gamma_e \equiv \gamma$. In order to obtain dimensionless optimization variables, we will furthermore write $\Omega_Z^{(F=n_1)} =: A_F \Omega$ (for $F = 1, 2, \dots, N - 1$) with nonnegative dimensionless variables A_F . The quantity Ω is a dimensionful frequency parameter, whose size has been chosen such that (for the weak driving calculation) all $\Omega_Z^{(F=n_1)}$ have to satisfy $\Omega_Z^{(F=n_1)} \leq \Omega$, i.e. such that the dimensionless parameters A_F satisfy $A_F \in [0, 1]$. In this notation, the above GHZ preparation time reads:

$$\tau_{n_1=N-1 \rightarrow \text{GHZ}} = \frac{2\gamma}{\Omega^2} \sum_{F=1}^{N-1} \frac{1}{FA_F^2} = \frac{2\gamma}{\Omega^2} H(\{A_F\}), \quad (\text{E.6})$$

where we have defined the function

$$H(\{A_F\}) := \sum_{F=1}^{N-1} \frac{1}{FA_F^2}. \quad (\text{E.7})$$

With the same abbreviations, the error rate from Z pumping alone reads, from Eq. (7.63):

$$\Gamma_{\text{GHZ} \rightarrow ?; \gamma, Z} = \frac{3\gamma_e N}{16g^2} \sum_{F=1}^{N-1} F \left(\frac{\Omega_Z^{(F)}}{N-F} \right)^2 = \frac{3\gamma\Omega^2}{16g^2} N \sum_{F=1}^{N-1} \frac{FA_F^2}{(N-F)^2} \quad (\text{E.8})$$

$$= \frac{3\gamma\Omega^2}{16g^2} NG(\{A_F\}), \quad (\text{E.9})$$

where

$$G(\{A_F\}) := \sum_{F=1}^{N-1} \frac{FA_F^2}{(N-F)^2}. \quad (\text{E.10})$$

Our goal for now is to find parameters $\{A_F\}$ that minimize the Z-error for any given value of the GHZ preparation time (or, equivalently, minimize the GHZ preparation time for any fixed error value). Minimizing $G(\{A_F\})$ under the constraint $H(\{A_F\}) \equiv \tilde{H} \equiv \text{const}$ by the method of Lagrange multipliers leads to

$$A_F^2 = \eta \frac{N-F}{F}, \quad \text{with } \eta > 0 \text{ such that } \frac{1}{\eta} \sum_{F=1}^{N-1} \frac{1}{N-F} = \tilde{H}. \quad (\text{E.11})$$

Approximating the latter harmonic sum gives roughly $\eta \approx (\log N)/\tilde{H}$, and we would have $A_F > 1$ for some F (in particular for $F = 1$) if $\eta > 1/(N-1)$, i.e. if $\tilde{H} \lesssim (N-1) \log N$.

However, one can still find the optimal assignment $\{A_F\}$ minimizing $G(\{A_F\})$ while obeying $0 \leq A_F \leq 1$ and $H(\{A_F\}) \leq \tilde{H}$:

$$A_F^2 = \left[\eta \frac{N-F}{F} \right]^1, \quad (\text{E.12})$$

where we defined the ‘‘ceil-1’’ function

$$[x]^1 := \begin{cases} 1 & \text{if } x > 1 \\ x & \text{if } x \leq 1 \end{cases}, \quad (\text{E.13})$$

and η needs to be adjusted such that $H(\{A_F\}) = \tilde{H}$. The assignment (E.12) means that $A_F^2 = 1$ for $F < N/(1+1/\eta)$ and $A_F^2 = \eta(N-F)/F$ for $F \geq N/(1+1/\eta)$. That (E.12) is the unique optimal solution can be checked by the Karush-Kuhn-Tucker (KKT) conditions [166, Sec. 5.3.3], using that the function $G(\{A_F\})$ to be minimized and the constraint function $H(\{A_F\})$ are both strictly convex in their arguments.

For $\eta \in [1/(N-1), N-1]$ (such that the selection between the two cases in (E.13) happens at some $F \in [1, N-1]$) one can thus compute:

$$H(\{A_F\}) = \sum_{F=1}^{N-1} \frac{1}{A_F^2 F} \approx \sum_{F=1}^{N/(1+1/\eta)} \frac{1}{F} + \sum_{F=N/(1+1/\eta)}^{N-1} \frac{1}{\eta(N-F)} \quad (\text{E.14})$$

$$\approx \log \frac{N}{1+1/\eta} + \frac{1}{\eta} \log N \left(1 - \frac{1}{1+1/\eta} \right) \quad (\text{E.15})$$

$$\approx \left(1 + \frac{1}{\eta} \right) \log N + \frac{1}{\eta} \log \frac{1}{\eta} - \left(1 + \frac{1}{\eta} \right) \log \left(1 + \frac{1}{\eta} \right) \quad (\text{E.16})$$

$$\approx \left(1 + \frac{1}{\eta} \right) \log N, \quad (\text{E.17})$$

and

$$G(\{A_F\}) = \sum_{F=1}^{N-1} \frac{A_F^2 F}{(N-F)^2} \approx \sum_{F=N/(1+1/\eta)}^{N-1} \frac{\eta}{N-F} + \sum_{F=1}^{N/(1+1/\eta)} \frac{F}{(N-F)^2} \quad (\text{E.18})$$

$$\approx \eta \log N \left(1 - \frac{1}{1+1/\eta} \right) + \eta + \log \left(1 - \frac{1}{1+1/\eta} \right) \quad (\text{E.19})$$

$$\approx \eta \log N + \eta - (\eta + 1) \log(\eta + 1) \quad (\text{E.20})$$

$$\approx \eta \log N. \quad (\text{E.21})$$

For $\eta = \text{const} > 0$, the error in both estimates is $\mathcal{O}(1)$ as $N \rightarrow \infty$ and thus irrelevant compared to the $\log N$ terms. In particular, if one wants the numerical factor H in the preparation time (E.6) to scale like $\log N$ (like optical pumping), then one needs $\eta \geq \mathcal{O}(1)$, which we achieve by letting $\eta = \text{const}$ as $N \rightarrow \infty$.

The error E can generally be obtained by comparing the preparation time of the desired state of the protocol and the loss rate out of it. Using Eqs. (E.6) and (E.9), the error E is found to be given by

$$E := (\tau_{n_1=N-1 \rightarrow \text{GHZ}})(\Gamma_{\text{GHZ} \rightarrow ?,\gamma,Z}) = \frac{3\gamma^2}{8g^2} N G(\{A_F\}) H(\{A_F\}). \quad (\text{E.22})$$

Thus, to achieve a desired error E (which may be N -dependent, i.e. $E = E(N)$), one can adjust γ appropriately. If we assume a relation $\Omega = \alpha\gamma$ in order to limit Ω to the weak driving regime (and where the number α may or may not depend on N , i.e. $\alpha = \alpha(N)$), we can plug this back into the worst-case preparation time (E.6) to obtain

$$\tau_{n_1=N-1 \rightarrow \text{GHZ}} = \frac{2\gamma}{\Omega^2} H = \frac{2}{\alpha^2\gamma} H = \sqrt{\frac{3}{2}} \frac{1}{\sqrt{E\alpha^2g}} \sqrt{N G H^3} \quad (\text{E.23})$$

$$\approx \eta^{1/2} \left(1 + \frac{1}{\eta}\right)^{3/2} \frac{\sqrt{3/2}}{\sqrt{E\alpha^2g}} N^{1/2} \log^2 N, \quad (\text{E.24})$$

where the last estimate holds for $\eta = \text{const}$ as $N \rightarrow \infty$ and we have neglected lower-order terms in N . The prefactor is minimized for $\eta = 2$, leading to a minimal preparation time (for the desired error E):

$$\tau_{n_1=N-1 \rightarrow \text{GHZ}} \approx \frac{9}{2\sqrt{2}} \frac{1}{\sqrt{E\alpha^2g}} N^{1/2} \log^2 N \approx \frac{3.2}{\sqrt{E\alpha^2g}} N^{1/2} \log^2 N. \quad (\text{E.25})$$

To summarize the optimal parameter choices for the scenario considered here:

- The A_F for $1 \leq F \leq N-1$ have to be chosen as follows (cf. Eq. (E.12) with the optimal choice $\eta = 2$):

$$A_F = \sqrt{[2(N-F)/F]^1}, \quad (\text{E.26})$$

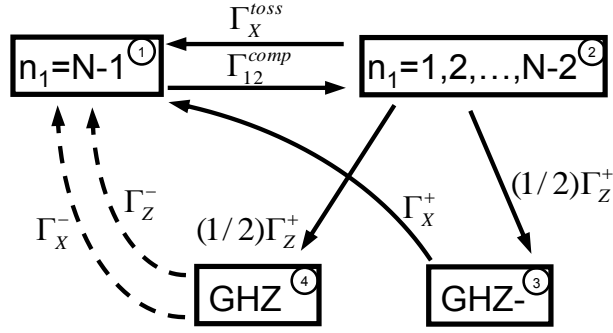
i.e. $A_F = 1$ for $1 \leq F \leq 2N/3$, and $A_F = \sqrt{2(N-F)/F}$ for $2N/3 < F \leq N-1$. This leads to:

$$H(\{A_F\}) = \frac{3}{2} \log N + \mathcal{O}(1), \quad (\text{E.27})$$

$$G(\{A_F\}) = 2 \log N + \mathcal{O}(1). \quad (\text{E.28})$$

- The choice of $\gamma \equiv \gamma_e$, and consequently of $\Omega \equiv \alpha\gamma$ and $\gamma_{0e} = \gamma_{1e} = \gamma/2$, is given by:

$$\gamma = \frac{2\sqrt{2}}{3} \frac{g\sqrt{E}}{\sqrt{N \log N}}. \quad (\text{E.29})$$

FIGURE E.1: Four-compartment-model of the process creating $|\text{GHZ}\rangle$.

We also set $\kappa_a = \kappa_b = 0$. This leads to:

$$\tau_{n_1=N-1 \rightarrow \text{GHZ}} = \frac{9}{2\sqrt{2}} \frac{1}{\sqrt{E}\alpha^2 g} N^{1/2} \log^2 N. \quad (\text{E.30})$$

The appearance of $N^{1/2}$ in the scaling of $\tau_{n_1=N-1 \rightarrow \text{GHZ}}$ can be traced back to the fact that the noise Γ_- acts on each of the N atoms (i.e. the prefactor of N in Eq. (7.63)).

E.2 Compartment model and effective rates

While so far we have only discussed the Z pumping, we will now make a simplified model of both processes, Z and X, that create the $|\text{GHZ}\rangle$ state. This model is more pessimistic w.r.t. the preparation time and the error treatment than the actual (Lindbladian) dynamics described in Sec. 7.3.2. Nevertheless, this model will still yield a scaling of the preparation time as $\tau_{\text{GHZ}} \sim (N^{1/2} \log^2 N) / \sqrt{E}$ with the number of qubits N and the error E , just like Eq. (E.25), which thus shows that this is indeed the best achievable scaling.

Our simplified model is shown in Fig. E.1 and consists of four compartments as we explain now. We split the 2^N -dimensional Hilbert space into the subspaces with $n_1 = 1, 2, \dots, N-1$, counting the number of $|1\rangle$ -states appearing in a computational basis state (as in Sec. 7.3.2). All states with $n_1 = N-1$ are put into compartment 1, as they are furthest away (in pumping time) from the GHZ states; the states with $n_1 = 1, \dots, N-2$ are then put into compartment 2. The two Hilbert space dimensions belonging to $n_1 = 0$ and to $n_1 = N$ are split into the compartments 3 and 4 of Fig. E.1, corresponding to the $|\text{GHZ}_-\rangle$ and the $|\text{GHZ}_+\rangle$ states, respectively. The “good” Z pumping process creates each of those GHZ states with equal rate $\frac{1}{2}\Gamma_Z^+$ out of compartment 2 where using Eq. (E.3) we find

$$\Gamma_Z^+ = (\tau_{n_1=N-2 \rightarrow n_1=0})^{-1} = \left(\frac{\gamma}{\Omega^2} \sum_{F=1}^{N-2} \frac{1}{FA_F^2} \right)^{-1} = \left(\frac{3\gamma}{2\Omega^2} \log N \right)^{-1} = \frac{\Omega^2}{\gamma} \frac{2}{3 \log N}. \quad (\text{E.31})$$

Here, we have again plugged in $\gamma_{0e} = \gamma/2$, $\kappa_a = 0$ and the optimal A_j from Eq. (E.26) and followed the same computation as for (E.17), neglecting lower-order

terms. Similarly, the rate from compartment 1 to compartment 2 is given by Eq. (E.1):

$$\Gamma_{12}^{comp} = \Gamma_{n_1=N-1 \rightarrow n_1=N-2, \gamma, 0, Z}^{(F=N-1)} \approx \frac{2(N-1)\gamma_{0e}(\Omega_Z^{(F=N-1)})^2}{(\gamma_e + \kappa_a)^2} = \frac{2\Omega^2}{\gamma}. \quad (\text{E.32})$$

As compartment 1 is the furthest away from the desired GHZ state, we pessimistically model the X-toss (i.e. the action of the X process on the states other than $|\text{GHZ}_\pm\rangle$, see Eq. (7.99)) to throw any state back to the $n_1 = N - 1$ compartment, with a rate Γ_X^{toss} to be computed below. Similarly, we model the errors Γ_Z^- and Γ_X^- affecting $|\text{GHZ}\rangle$ such that they move the $|\text{GHZ}\rangle$ -state back to compartment 1. By the same rationale, even the “good” X process Γ_X^+ is modelled to take the un-wanted state $|\text{GHZ}_-\rangle$ back to compartment 1.

The detrimental Z rate for the compartment model as computed with the parameters from the previous subsection, Eq. (E.26) (see also Eqs. (E.9), (E.10), and (E.21) with the optimal $\eta = 2$) is

$$\Gamma_Z^- = \Gamma_{\text{GHZ} \rightarrow ?, \gamma, Z} = \frac{3\gamma\Omega^2}{16g^2} NG(\{A_f\}) = \frac{\gamma\Omega^2}{g^2} \frac{3N \log N}{8}. \quad (\text{E.33})$$

For the X rates, it was found in Sec. 7.3.3 that only the Rabi oscillations $\Omega_X^{(F)}$ with *odd* index F should be turned on. Similar to Sec. E.1, we write $\Omega_X^{(F)} = A_X^{(F)}\Omega$ with the dimensionless parameters $A_X^{(F)}$ which we discuss below. The “good” X rate Γ_X^+ for the compartment model of Fig. E.1 is then given by Eq. (7.95):

$$\Gamma_X^+ = \Gamma_{\text{GHZ} \rightarrow ?, X} \approx \frac{2\gamma_f}{(\gamma_f + \kappa_b)^2} \sum_{F=1,3,\dots}^N \binom{N}{F} \frac{F(\Omega_X^{(F)})^2}{2^{N-1}} \quad (\text{E.34})$$

$$= \frac{2\Omega^2}{\gamma} \sum_{F=1,3,\dots}^N \frac{1}{2^{N-1}} \binom{N}{F} F(A_X^{(F)})^2. \quad (\text{E.35})$$

Since the (normalized) probability distribution $\{\binom{N}{F}/2^{N-1}\}_{F=1,3,\dots}^N$ is strongly peaked around the values $F \sim N/2$ (similar to the full binomial distribution), the exact functional choice of the X coefficients $A_X^{(F)}$ (for odd F) does not really matter in the limit of large N , as long as it is not exponentially fine tuned. Since a similar binomial distribution occurs in the X error rates below as well and as the same reasoning applies, we can take all $A_X^{(F)}$ to be equal as a very good approximation:

$$A_X^{(F=1)} = A_X^{(F=3)} = A_X^{(F=5)} = \dots \equiv A_X. \quad (\text{E.36})$$

With this, the rate Γ_X^+ evaluates to (with exponentially good accuracy for large N):

$$\Gamma_X^+ = \frac{2\Omega^2}{\gamma} \frac{N}{2} A_X^2 = \frac{\Omega^2}{\gamma} N A_X^2, \quad (\text{E.37})$$

As we will see below, with this choice the error induced by the X error rate is smaller than the one from the Z process and thus not a major limitation to the preparation of the entangled state.

The X error rate Γ_X^- is given by (7.98), and we simplify it again with our above parameter choices, making approximations of the binomial distribution and the other sum which are good in the large- N limit:

$$\Gamma_X^- = \Gamma_{\text{GHZ} \rightarrow ? , \gamma, X} \approx \frac{\gamma_f}{2g^2} \sum_{n=0,2,\dots} \frac{1}{2^{N-1}} \binom{N}{n_-} n_- \sum_{F=1,3,\dots} F \left(\frac{\Omega_X^{(F)}}{F - n_-} \right)^2 \quad (\text{E.38})$$

$$\approx \frac{\gamma \Omega^2 A_X^2}{2g^2} \frac{N}{2} \sum_{F=1,3,\dots} \frac{F}{(F - [N/2]_{\text{even}})^2}. \quad (\text{E.39})$$

In the expression above, $[N/2]_{\text{even}}$ denotes the next higher integer number of $N/2$. Having the limit of large N in mind, we evaluate the last sum as follows:

$$\begin{aligned} & \sum_{F=1,3,\dots} \frac{F}{(F - [N/2]_{\text{even}})^2} \quad (\text{E.40}) \\ &= \sum_{1 \leq F \leq [N/2]_{\text{even}} - 1}^{\text{Fodd}} \frac{F}{(F - [N/2]_{\text{even}})^2} + \sum_{[N/2]_{\text{even}} + 1 \leq F \leq N}^{\text{Fodd}} \frac{F}{(F - [N/2]_{\text{even}})^2} \\ &= \sum_{1 \leq F \leq [N/2]_{\text{even}} - 1}^{\text{Fodd}} \frac{[N/2]_{\text{even}}}{(F - [N/2]_{\text{even}})^2} + \sum_{1 \leq F \leq [N/2]_{\text{even}} - 1}^{\text{Fodd}} \frac{F - [N/2]_{\text{even}}}{(F - [N/2]_{\text{even}})^2} \\ & \quad + \sum_{[N/2]_{\text{even}} + 1 \leq F \leq N}^{\text{Fodd}} \frac{[N/2]_{\text{even}}}{(F - [N/2]_{\text{even}})^2} + \sum_{[N/2]_{\text{even}} + 1 \leq F \leq N}^{\text{Fodd}} \frac{F - [N/2]_{\text{even}}}{(F - [N/2]_{\text{even}})^2} \\ &= [N/2]_{\text{even}} \left(\frac{1}{1^2} + \frac{1}{3^2} + \dots + \frac{1}{([N/2]_{\text{even}} - 1)^2} \right) \\ & \quad - \left(\frac{1}{1} + \frac{1}{3} + \dots + \frac{1}{([N/2]_{\text{even}} - 1)} \right) \\ & \quad + [N/2]_{\text{even}} \left(\frac{1}{1^2} + \frac{1}{3^2} + \dots + \frac{1}{(N - [N/2]_{\text{even}} - 1)^2} \right) \\ & \quad + \left(\frac{1}{1} + \frac{1}{3} + \dots + \frac{1}{(N - [N/2]_{\text{even}} - 1)} \right) \\ & \approx 2 \cdot \frac{N}{2} \sum_{n=1,3,5,\dots}^{\infty} \frac{1}{n^2} = 2 \cdot \frac{N}{2} \cdot \frac{3}{4} \sum_{n=1,2,3,4,\dots}^{\infty} \frac{1}{n^2} = N \frac{3\pi^2}{4 \cdot 6} \approx 1.23N \approx \frac{5N}{4}, \end{aligned}$$

neglecting subleading terms in N . This finally gives:

$$\Gamma_X^- = \frac{\gamma \Omega^2}{g^2} \frac{5N^2 A_X^2}{16}. \quad (\text{E.41})$$

Finally, the X toss rate Γ_X^{toss} in Fig. E.1 is given by Eq. (7.99), which with our parameter choices becomes [note that (7.99) is half of the “good” rate (7.95), which we have computed in Eq. (E.37) already]:

$$\Gamma_X^{\text{toss}} = \frac{\Omega^2}{\gamma} \frac{N A_X^2}{2}. \quad (\text{E.42})$$

From the process in Fig. E.1 one can see that the optimal parameters A_X have to be chosen such that the good X-process and the good Z-process have about the

same rate: If the X pumping rate Γ_X^+ is too weak, population will accumulate in $|\text{GHZ}_-\rangle$ by the Z pumping (Γ_Z^+). On the other hand, a too strong X pumping will hinder the preparation mechanism through the X toss effect. We thus set the rates for the desired processes, Z pumping and X depumping to be equal,

$$\Gamma_X^+ = \Gamma_Z^+. \quad (\text{E.43})$$

This results in:

$$A_X^2 = \frac{2}{3N \log N} \quad (\text{E.44})$$

(note that, for all $N \geq 2$, this choice is consistent with the requirement $A_X \leq 1$ for the weak-driving analysis).

With these choices made, we summarize the parameters and effective rates for the four-compartment model of Fig. E.1 found so far:

- For the Z-pumping, we make the choice of parameters found to be optimal in Eq. (E.26):

$$A_Z^{(F)} = \begin{cases} 1 & \text{for } F \leq 2N/3, \\ \sqrt{2 \frac{N-F}{F}} & \text{for } F \geq 2N/3, \end{cases} \quad (\text{E.45})$$

meaning that $\Omega_Z^{(F)} = \Omega A_Z^{(F)}$.

- For the X-pumping we take (see Eq. (E.44)):

$$A_X^{(F=\text{odd})} = \sqrt{\frac{2}{3} \frac{1}{N \log N}}, \quad A_X^{(F=\text{even})} = 0. \quad (\text{E.46})$$

- Then one obtains for the effective rates in Fig. E.1:

$$\Gamma_Z^+ = \Gamma_X^+ = \frac{\Omega^2}{\gamma} \frac{2}{3 \log N}, \quad (\text{E.47})$$

$$\Gamma_{12}^{\text{comp}} = \frac{\Omega^2}{\gamma} \cdot 2 = \Gamma_Z^+ \cdot 3 \log N, \quad (\text{E.48})$$

$$\Gamma_X^{\text{toss}} = \frac{\Omega^2}{\gamma} \frac{1}{3 \log N} = \frac{1}{2} \Gamma_Z^+, \quad (\text{E.49})$$

$$\Gamma_Z^- = \frac{\gamma \Omega^2}{g^2} \frac{3N \log N}{8}, \quad (\text{E.50})$$

$$\Gamma_X^- = \frac{\gamma \Omega^2}{g^2} \frac{5N}{24 \log N}. \quad (\text{E.51})$$

- The total error rate (leading from compartment 4 to compartment 1) is thus

$$\Gamma_- := \Gamma_Z^- + \Gamma_X^- = \frac{\gamma \Omega^2}{g^2} \frac{3N \log N}{8} \left(1 + \frac{5}{9 \log^2 N} \right) \quad (\text{E.52})$$

$$= \Gamma_Z^+ \cdot \frac{\gamma^2}{g^2} \frac{9N \log^2 N}{16} \left(1 + \frac{5}{9 \log^2 N} \right). \quad (\text{E.53})$$

E.3 Transition matrix, stationary error, and GHZ preparation time

The transition matrix for the 4-compartment model of Fig. E.1 is:

$$T = \begin{pmatrix} -\Gamma_{12}^{comp} & \Gamma_X^{toss} & \Gamma_X^+ & \Gamma_- \\ \Gamma_{12}^{comp} & -(\Gamma_X^{toss} + \Gamma_Z^+) & 0 & 0 \\ 0 & \frac{1}{2}\Gamma_Z^+ & -\Gamma_X^+ & 0 \\ 0 & \frac{1}{2}\Gamma_Z^+ & 0 & -\Gamma_- \end{pmatrix} \quad (\text{E.54})$$

$$= \Gamma_Z^+ \begin{pmatrix} -3 \log N & \frac{1}{2} & 1 & \Gamma_- / \Gamma_Z^+ \\ 3 \log N & -\frac{3}{2} & 0 & 0 \\ 0 & \frac{1}{2} & -1 & 0 \\ 0 & \frac{1}{2} & 0 & -\Gamma_- / \Gamma_Z^+ \end{pmatrix}. \quad (\text{E.55})$$

The steady-state population $p_\infty := (P_1(\infty), P_2(\infty), P_3(\infty), P_4(\infty))$ is given as the solution (normalized to the sum of entries being 1) of the equation $Tp_\infty = 0$. This gives:

$$p_\infty = \begin{pmatrix} P_1(\infty) \\ P_2(\infty) \\ P_3(\infty) \\ P_4(\infty) \end{pmatrix} = \begin{pmatrix} 1 / \log N \\ 2 \\ 1 \\ \Gamma_Z^+ / \Gamma_- \end{pmatrix} \cdot \frac{1}{3 + \frac{1}{\log N} + \frac{\Gamma_-}{\Gamma_Z^+}}. \quad (\text{E.56})$$

The *steady-state fidelity* is just $F = P_4(\infty)$, and the *error* is thus

$$\begin{aligned} E &= 1 - F = 1 - P_4(\infty) = 1 - \frac{1}{1 + \frac{\Gamma_-}{\Gamma_Z^+} \left(3 + \frac{1}{\log N}\right)} \\ &\approx \frac{\Gamma_-}{\Gamma_Z^+} \left(3 + \frac{1}{\log N}\right) = \frac{\gamma^2 27N \log^2 N}{g^2 16} \left(1 + \frac{5}{9 \log^2 N}\right) \left(1 + \frac{1}{3 \log N}\right). \end{aligned} \quad (\text{E.57})$$

(Here, the approximation in the second line was made for analytical convenience and gives a slightly pessimistic bound.) In the scaling with large N , this expression for E agrees with the one implied by Eq. (E.29) that was found by other means before, and the prefactor is similar. Thus, to achieve a desired stationary error E , we need to adjust γ such that:

$$\gamma = g\sqrt{E} \left[\frac{27N \log^2 N}{16} \left(1 + \frac{5}{9 \log^2 N}\right) \left(1 + \frac{1}{3 \log N}\right) \right]^{-1/2}. \quad (\text{E.58})$$

Below we will use this expression instead of the results obtained in (E.29) which were derived by considered only the Z pumping.

So far, we have discussed the Z pumping separately from the X pumping, deriving an individual characteristic time $\tau_{n_1=N-1 \rightarrow \text{GHZ}}$. It now remains to derive an analytical expression for the total GHZ pumping time that is obtained in the presence of X pumping, using the parameters (E.59) and (E.26). In order to factor

out the dependence of the stationary error E and to obtain a tractable analytical expression, we make (for the computation of the GHZ preparation time) an approximation to the transition matrix (E.54) by dropping the small terms leading out of the GHZ state (these terms vanish in the limit of $E \rightarrow 0$). That is, we set the fourth column in (E.54) to zero:

$$T_+ = \Gamma_Z^+ \begin{pmatrix} -3 \log N & \frac{1}{2} & 1 & 0 \\ 3 \log N & -\frac{3}{2} & 0 & 0 \\ 0 & \frac{1}{2} & -1 & 0 \\ 0 & \frac{1}{2} & 0 & 0 \end{pmatrix}. \quad (\text{E.60})$$

For the initial population vector $(P_1(0), P_2(0), P_3(0), P_4(0)) = (0, 0, 1, 0)$, which corresponds to the whole population being in the worst state $|\text{GHZ}_-\rangle$ of Fig. E.1, we have the following evolution:

$$\begin{pmatrix} P_1(t) \\ P_2(t) \\ P_3(t) \\ P_4(t) \end{pmatrix} = e^{tT_+} \begin{pmatrix} P_1(0) \\ P_2(0) \\ P_3(0) \\ P_4(0) \end{pmatrix} = e^{(t\Gamma_Z^+)(T_+/\Gamma_Z^+)} \begin{pmatrix} 0 \\ 0 \\ 1 \\ 0 \end{pmatrix}. \quad (\text{E.61})$$

Thus, on time-scales larger than any fixed t_0 , the transition from the worst state $|\text{GHZ}_-\rangle$ to the desired state $|\text{GHZ}\rangle$ happens at least as fast as in an exponential decay process, with an approximation Γ_+ for the effective exponential rate computed as:

$$P_4(t_0) = 1 - e^{-\Gamma_+ t_0}, \quad \text{i.e.} \quad \Gamma_+ = \Gamma_Z^+ \frac{-\log(1 - P_4(t_0))}{\Gamma_Z^+ t_0}. \quad (\text{E.62})$$

Note that the fraction in the last expression will depend both on $(\Gamma_Z^+ t_0)$ and on N , since the N -dependence of the transition matrix T_+ in Eq. (E.60) cannot be factored out completely. To get a meaningful expression for the exponential rate, the timescale t_0 should be chosen comparable to the other relevant timescales of the process. For definiteness we will thus set $t_0 := 1/\Gamma_Z^+$ throughout.

The characteristic preparation time of $|\text{GHZ}\rangle$ in the sense of an exponential rate is then:

$$\tau_{\text{GHZ}} = \frac{1}{\Gamma_+} = \frac{1}{\Gamma_Z^+} \left(\frac{-\log(1 - P_4(t_0))}{\Gamma_Z^+ t_0} \right)^{-1} \quad (\text{E.63})$$

$$\stackrel{[\text{Eq. (E.47)}]}{=} \frac{3\gamma}{2\Omega^2} \log N \left(\frac{-\log(1 - P_4(t_0))}{\Gamma_Z^+ t_0} \right)^{-1} \quad (\text{E.64})$$

$$\stackrel{[\Omega=\alpha\gamma]}{=} \frac{3}{2\alpha^2\gamma} \log N \left(\frac{-\log(1 - P_4(t_0))}{\Gamma_Z^+ t_0} \right)^{-1} \quad (\text{E.65})$$

$$\stackrel{[\text{Eq. (E.59)}]}{=} \frac{N^{1/2} \log^2 N}{\alpha^2 g \sqrt{E}} \times \left[\frac{9\sqrt{3}}{8} \frac{\Gamma_Z^+ t_0}{-\log(1 - P_4(t_0))} \sqrt{\left(1 + \frac{5}{9 \log^2 N}\right) \left(1 + \frac{1}{3 \log N}\right)} \right]. \quad (\text{E.66})$$

In the limit of large N , the square root inside the bracketed expression will tend to 1. And also the fractional expression involving $P_4(t_0)$ will tend to a constant number independent of N , since large values of the first column in the matrix in (E.60) mean that the transition time out of the first compartment is insignificant compared to the other transition times, which are all *independent* of N . This is also easily seen numerically.

In the following table, we evaluate the factor in square brackets (which we call $b(N)$) in Eq. (E.66) for different values of N :

N	2	3	4	6	8	10	20	50	100	10^3	10^4	10^5	10^6
$b(N)$	55	33	27	23	21	20	18	17	16	15	14.6	14.3	14.1

The GHZ preparation time is then:

$$\tau_{\text{GHZ}} = b(N) \frac{\sqrt{N} \log^2 N}{\alpha^2 g \sqrt{E}}, \quad (\text{E.67})$$

where $b(N)$ tends to about 13 as $N \rightarrow \infty$ (see table above). The parameter choices for this can be found in Eqs. (E.45), (E.46), and (E.59) together with $\Omega = \alpha\gamma$, $\gamma_{0e} = \gamma_{1e} = \gamma$, $\kappa_a = \kappa_b = 0$.

E.4 Analysis of the “dynamical problem”

Here, we analyze the “dynamical problem”. This means that, for a certain exponential form of the time-evolution of the GHZ error $E(t)$ (or, equivalently, of the GHZ fidelity $F(t) = 1 - E(t)$) in an effective model, we compute and minimize the time t it takes to achieve a desired target error \mathcal{E} . The main result will be that, up to an additional factor of $\log(1/\mathcal{E})$, the scaling of the preparation time with the particle number N and with the error \mathcal{E} is the same as in the previous analytical approaches, see e.g. Eqs. (E.30) and (E.67) (with E replaced by \mathcal{E}).

In the following, we write again $\Omega = \alpha\gamma$ to be able to limit our treatment to the weak-driving regime by suitable choices of the number α . Furthermore, to keep the main derivation as general as possible, we write the rates into and out of the desired GHZ state as

$$\Gamma = \frac{\Omega^2}{\gamma} f(N) = \alpha^2 \gamma f(N), \quad (\text{E.68})$$

$$\Gamma_- = \frac{\gamma \Omega^2}{g^2} h(N) \quad (\text{E.69})$$

with functions $f \equiv f(N)$ and $h \equiv h(N)$. Later, we will evaluate our results for the functions

$$h(N) = \frac{3N \log N}{8} \left(1 + \frac{5}{9 \log^2 N} \right), \quad (\text{E.70})$$

which is motivated by Eq. (E.53), and

$$f(N) = \frac{2}{3 + 9 \log N}, \quad (\text{E.71})$$

which is chosen such that the ratio Γ_-/Γ yields the stationary error from Eq. (E.58).

Finally, we make the following basic ansatz for the time evolution of the error:

$$E(t) = \frac{\Gamma_-}{\Gamma} + \left(1 - \frac{\Gamma_-}{\Gamma}\right) e^{-t\kappa\Gamma}. \quad (\text{E.72})$$

Note that in the limit of $t \rightarrow \infty$ the error indeed converges to Γ_-/Γ with an exponential rate given by $\kappa\Gamma$, where $\kappa > 0$ can be a dimensionless constant to adjust the effective decay rate in a model where the effective decay rate $\kappa\Gamma$ does not match with the steady state error Γ_-/Γ (see Eqn. (E.98) and below). Since we are interested in the regime of small stationary error Γ_-/Γ , we can approximate and continue:

$$E(t) \approx \frac{\Gamma_-}{\Gamma} + e^{-t\kappa\Gamma} = \frac{\gamma^2}{g^2} \frac{h(N)}{f(N)} + \exp[-\gamma t\kappa\alpha^2 f(N)] \quad (\text{E.73})$$

$$= \left(\frac{\gamma}{g} \frac{\sqrt{h(N)}}{\sqrt{f(N)}}\right)^2 + \exp\left[-\left(\frac{\gamma}{g} \frac{\sqrt{h(N)}}{\sqrt{f(N)}}\right) \left(t\kappa g\alpha^2 \frac{f(N)^{3/2}}{h(N)^{1/2}}\right)\right] \quad (\text{E.74})$$

$$= c^2 + e^{-c\tau}, \quad (\text{E.75})$$

where we abbreviate with a constant c and a “rescaled time” τ as follows:

$$c := \frac{\gamma}{g} \frac{\sqrt{h(N)}}{\sqrt{f(N)}}, \quad (\text{E.76})$$

$$\tau := t\kappa g\alpha^2 \frac{f(N)^{3/2}}{h(N)^{1/2}}. \quad (\text{E.77})$$

We can treat c as a free optimization variable, since γ is a freely adjustable parameter, and thus we can adjust c to any non-negative real number by choosing γ appropriately (even if g and $h(N)$ and $f(N)$ are fixed). Furthermore, τ is essentially the same as the physical time t , but rescaled by a fixed number (which in particular depends on N and g).

Now the dynamical problem is as follows: Given any fixed *target error* $\mathcal{E} \in (0, 1)$, we would like to find $c > 0$ such that the time τ needed to achieve this error by Eqn. (E.75) is minimized. Obviously, from (E.75), any such suitable c satisfies $c \in (0, \sqrt{\mathcal{E}})$. Thus, we can explicitly solve Eqn. (E.75) for τ given c and \mathcal{E} :

$$\tau = \tau(c) = \frac{-\log(\mathcal{E} - c^2)}{c} \quad (c \in (0, \sqrt{\mathcal{E}})). \quad (\text{E.78})$$

To minimize this (rescaled) time $\tau = \tau(c)$, we set its derivative equal to zero (note that a minimum exists since $\lim_{c \rightarrow 0} \tau(c) = \lim_{c \rightarrow \sqrt{\mathcal{E}}} \tau(c) = +\infty$):

$$\frac{d\tau(c)}{dc} = \frac{2}{\mathcal{E} - c^2} + \frac{\log(\mathcal{E} - c^2)}{c^2} = 0 \quad (\text{E.79})$$

$$\Leftrightarrow -\log(\mathcal{E} - c^2) = -2 + \frac{2\mathcal{E}}{\mathcal{E} - c^2} \quad (\text{E.80})$$

$$\Leftrightarrow \frac{1}{\mathcal{E} - c^2} = \exp\left[-2 + \frac{2\mathcal{E}}{\mathcal{E} - c^2}\right] \quad (\text{E.81})$$

$$\Leftrightarrow \frac{-2\mathcal{E}}{\mathcal{E} - c^2} \exp\left[-\frac{2\mathcal{E}}{\mathcal{E} - c^2}\right] = -2\mathcal{E}e^{-2} \quad (\text{E.82})$$

$$\Leftrightarrow \frac{-2\mathcal{E}}{\mathcal{E} - c^2} = W(-2\mathcal{E}/e^2), \quad (\text{E.83})$$

where W is (a branch of) the *Lambert W function* [167], which satisfies $W(z)e^{W(z)} = z$ (W is defined to be a solution to this equation for every $z \in \mathbb{C}$). Now we have to identify the correct branch of $W(z)$ for our purposes: First, since $\mathcal{E} \in (0, 1)$, the argument $-2\mathcal{E}/e^2$ in (E.83) satisfies $-2\mathcal{E}/e^2 \in (-2/e^2, 0) \subseteq [-1/e, 0)$; secondly, since $c \in (0, \sqrt{\mathcal{E}})$, the image in Eq. (E.83) satisfies $-2\mathcal{E}/(\mathcal{E} - c^2) \in (-\infty, -2)$. Both these things together mean that the correct branch (solution) of the function $W(z)$ in our problem is the branch $W_{-1} : [-1/e, 0) \rightarrow (-\infty, -1]$, $z \mapsto W_{-1}(z)$. Then we can continue from (E.83), and solve explicitly for the time-optimal c :

$$c = \sqrt{\mathcal{E}} \sqrt{1 + \frac{2}{W_{-1}(-2\mathcal{E}/e^2)}}. \quad (\text{E.84})$$

The optimal time τ can be obtained by plugging this expression into (E.78) and simplifying the expression, but there is a less direct and somewhat easier way: Observe from Eqs. (E.78) and (E.79) that

$$\tau = \frac{2c}{\mathcal{E} - c^2} = \frac{c}{\mathcal{E}} \frac{2\mathcal{E}}{\mathcal{E} - c^2} \stackrel{[\text{Eq. (E.83)}]}{=} \frac{-W_{-1}(-2\mathcal{E}/e^2)}{\mathcal{E}} c \stackrel{[\text{Eq. (E.84)}]}{=} \quad (\text{E.85})$$

$$= \frac{1}{\sqrt{\mathcal{E}}} \sqrt{W_{-1}(-2\mathcal{E}/e^2)^2 + 2W_{-1}(-2\mathcal{E}/e^2)} \quad (\text{E.86})$$

$$\approx \frac{1}{\sqrt{\mathcal{E}}} \log \frac{1}{\mathcal{E}} \quad (\text{as } \mathcal{E} \rightarrow 0), \quad (\text{E.87})$$

where in the last step we used the asymptotic approximation of our branch of the Lambert W function [167]: $W_{-1}(x) = \log(-x) - \log(-\log(-x)) + \mathcal{O}(1)$ as $x \rightarrow 0$. This is justified when we are interested in the case of very small or asymptotically vanishing error $\mathcal{E} \rightarrow 0$.

Finally, we can use the above expressions to solve Eqs. (E.76) and (E.77) for the physically interesting optimal parameters $\gamma = \gamma(N, \mathcal{E})$ and $t_{\text{GHZ}} = t(N, \mathcal{E})$ using the values given in Eqs. (E.84) and (E.86). When we use the choices for $f(N)$ and

$h(N)$ given in Eqs. (E.70) and (E.71), we obtain:

$$\gamma = g c \frac{f(N)^{1/2}}{h(N)^{1/2}} = \frac{4}{3\sqrt{3}} \frac{g\sqrt{\mathcal{E}}}{\sqrt{N} \log N} \sqrt{1 + \frac{2}{W_{-1}(-2\mathcal{E}/e^2)}} \quad (\text{E.88})$$

$$\times \left(1 + \frac{5}{9 \log^2 N}\right)^{-1/2} \left(1 + \frac{1}{3 \log N}\right)^{-1/2} \quad (\text{E.89})$$

$$\approx \frac{4}{3\sqrt{3}} \frac{g\sqrt{\mathcal{E}}}{\sqrt{N} \log N} \quad (\text{as } N \rightarrow \infty, \mathcal{E} \rightarrow 0), \quad (\text{E.90})$$

Note that for small dynamical error \mathcal{E} we have $W_{-1} \rightarrow 0$, such that Eq. (E.90) approaches the previous result in Eq. (E.59). This is due to the fact that for small \mathcal{E} the stationary part of the error dominates. The GHZ preparation time (defined as the time to reach a GHZ error of value \mathcal{E}) is:

$$t_{\text{GHZ}} = \frac{\tau}{g\kappa\alpha^2} \frac{h(N)^{1/2}}{f(N)^{3/2}} \quad (\text{E.91})$$

$$= \frac{27\sqrt{3}}{8\kappa} \frac{\sqrt{N} \log^2 N}{\alpha^2 g \sqrt{\mathcal{E}}} \sqrt{W_{-1}^2 \left(-\frac{2\mathcal{E}}{e^2}\right) + 2W_{-1} \left(-\frac{2\mathcal{E}}{e^2}\right)} \quad (\text{E.92})$$

$$\times \left(1 + \frac{5}{9 \log^2 N}\right)^{1/2} \left(1 + \frac{1}{3 \log N}\right)^{3/2} \quad (\text{E.93})$$

$$\approx \frac{27\sqrt{3}}{8\kappa} \frac{\sqrt{N} \log^2 N}{\alpha^2 g \sqrt{\mathcal{E}}} \log \frac{1}{\mathcal{E}} \quad (\text{as } N \rightarrow \infty, \mathcal{E} \rightarrow 0). \quad (\text{E.94})$$

The approximations of the Lambert-W-function used above, i.e. $\sqrt{1 + 2/W_{-1}} \rightarrow 1$ and $\sqrt{W_{-1}^2 + 2W_{-1}} \rightarrow \log(1/\mathcal{E})$, are good only for quite small \mathcal{E} . For $\mathcal{E} = 0.1$, one should instead use the exact value $W_{-1}(-2\mathcal{E}/e^2) = -5.27$, leading to $\sqrt{1 + 2/W_{-1}} = 0.788$ and $\sqrt{W_{-1}^2 + 2W_{-1}} = 4.15$, which makes that Eq. (E.94) is by a factor 1.8 lower than Eq. (E.93). For $\mathcal{E} = 0.03$ the corresponding value is $W_{-1}(-2\mathcal{E}/e^2) = -6.72$, leading to $\sqrt{1 + 2/W_{-1}} = 0.838$ and $\sqrt{W_{-1}^2 + 2W_{-1}} = 5.63$, which makes that Eq. (E.94) is by a factor 1.6 lower than Eq. (E.93). We can also find the relation between the stationary error $E = \Gamma_-/\Gamma$ (from Eq. (E.72)) and the dynamical error \mathcal{E} :

$$\frac{E}{\mathcal{E}} = \frac{\Gamma_-}{\mathcal{E}\Gamma} \quad (\text{E.95})$$

$$\stackrel{[\text{Eqs. (E.68)-(E.71)}]}{=} \frac{\gamma^2}{\mathcal{E} g^2} \frac{3N \log N}{8} \left(1 + \frac{5}{9 \log^2 N}\right) \frac{9 \log N}{2} \left(1 + \frac{1}{3 \log N}\right) \quad (\text{E.96})$$

$$\stackrel{[\text{Eq. (E.89)}]}{=} 1 + \frac{2}{W_{-1}(-2\mathcal{E}/e^2)}, \quad (\text{E.97})$$

which is independent of N . Thus, using the above values, for $\mathcal{E} = 0.1$ we get for the stationary error at the optimal parameters $E = 0.62\mathcal{E}$, whereas for $\mathcal{E} = 0.03$ we get $E = 0.70\mathcal{E}$.

It now remains to fix the value of κ (appearing in (E.93)–(E.94)) in an appropriate way, namely such that the model (E.72) matches the GHZ preparation process from Sections E.2 and E.3 as well as possible. For this, note that the effective GHZ preparation rate Γ_{GHZ} from Sec. E.3 can be inferred from Eq. (E.63):

$$\kappa\Gamma \stackrel{!}{=} \Gamma_{\text{GHZ}} \equiv \frac{1}{\tau_{\text{GHZ}}} = \frac{\Omega^2}{\gamma} \frac{2}{3 \log N} \frac{-\log(1 - P_4(t_0))}{\Gamma_Z^+ t_0}. \quad (\text{E.98})$$

Using the value of Γ from Eqs. (E.68) and (E.71), we can solve for κ :

$$\kappa = 3 \left(\frac{-\log(1 - P_4(t_0))}{\Gamma_Z^+ t_0} \right) \left(1 + \frac{1}{3 \log N} \right). \quad (\text{E.99})$$

Evaluating this as in Sec. E.3, we get the following table:

N	2	3	4	5	6	7	8	10	20	50	100
κ	0.28	0.32	0.34	0.35	0.36	0.36	0.37	0.38	0.39	0.40	0.41

E.5 GHZ scaling analysis for strong driving

When taking power broadening into account (see Sec. 7.4.2), then instead of Eq. (E.1) from the weak driving scenario, the favorable transition rates of the Z process are now given by Eq. (7.107) (for $n_1 = 1, 2, \dots, N - 1$):

$$\Gamma_{n_1 \rightarrow n_1-1, \gamma_0, Z} = \frac{2n_1 \gamma_{0e} (\Omega_Z^{(F=n_1)})^2}{(\gamma_e + \kappa_a)^2 + 2n_1 (\Omega_Z^{(F=n_1)})^2} = \frac{\gamma F \Omega_F^2}{\gamma^2 + 2F \Omega_F^2}, \quad (\text{E.100})$$

where we have again used the parameter values and abbreviations $\gamma_e \equiv \gamma$, $\gamma_{0e} = \gamma/2$, $\Omega_Z^{(F=n_1)} = \Omega_F$ as in Sec. E.1. Thus, instead of (E.5), the Z pumping time is now:

$$\tau_{n_1=N-1 \rightarrow \text{GHZ}} = 2\tau_{n_1=N-1 \rightarrow n_1=0} = 2 \sum_{n_1=1}^{N-1} (\Gamma_{n_1 \rightarrow n_1-1, \gamma_0, Z})^{-1} \quad (\text{E.101})$$

$$= 2 \sum_{F=1}^{N-1} \left(\frac{\gamma}{\Omega_F^2 F} + \frac{2}{\gamma} \right) = \frac{4(N-1)}{\gamma} + \sum_{F=1}^{N-1} \frac{2\gamma}{F \Omega_F^2}. \quad (\text{E.102})$$

The error rate from (E.9) remains unchanged:

$$\Gamma_{\text{GHZ} \rightarrow ?, \gamma, Z} = \frac{3\gamma}{16g^2} N \sum_{F=1}^{N-1} \frac{F \Omega_F^2}{(N-F)^2}. \quad (\text{E.103})$$

As below (E.10), we now minimize $\Gamma_{\text{GHZ} \rightarrow ?, \gamma, Z}$ (as a function of the variables $\{\Omega_f\}$) while keeping $\tau_{n_1=N-1 \rightarrow \text{GHZ}}$ constant. This leads, by the method of Lagrange multipliers, to:

$$\Omega_F^2 = \lambda \frac{N-F}{F} \quad (\text{for } F = 1, 2, \dots, N-1), \quad (\text{E.104})$$

where λ is a Lagrange multiplier (that has units of frequency²), which we will determine later. Plugging this back into (E.102) and (E.103), we get:

$$\tau_{N-1 \rightarrow \text{GHZ}} = \frac{4(N-1)}{\gamma} + \frac{2\gamma}{\lambda} \sum_{F=1}^{N-1} \frac{1}{N-F} \simeq \frac{4(N-1)}{\gamma} + \frac{2\gamma}{\lambda} \log N, \quad (\text{E.105})$$

$$\Gamma_{\text{GHZ} \rightarrow ?, \gamma, Z} = \frac{3\gamma\lambda}{16g^2} N \log N. \quad (\text{E.106})$$

Thus, the stationary Z error is (cf. (E.22)):

$$E_Z = (\Gamma_{\text{GHZ} \rightarrow ?, \gamma, Z})(\tau_{N-1 \rightarrow \text{GHZ}}) = \frac{3\lambda}{4g^2} (N-1)N \log N + \frac{3\gamma^2}{8g^2} N \log^2 N. \quad (\text{E.107})$$

Thus, when the desired stationary Z error E_Z is given, then λ and γ are determined by each other (since g and N are fixed):

$$\lambda = \frac{8g^2 E_Z - 3\gamma^2 N \log^2 N}{6(N-1)N \log N} \quad \left(\text{for } \gamma^2 \in \left[0, \frac{8g^2 E_Z}{3N \log^2 N} \right] \right). \quad (\text{E.108})$$

Plugging this back into (E.105), we get:

$$\tau_{N-1 \rightarrow \text{GHZ}} = 4(N-1) \left[\frac{1}{\gamma} + \frac{\gamma}{\frac{8g^2 E_Z}{3N \log^2 N} - \gamma^2} \right]. \quad (\text{E.109})$$

For fixed N , g , E_Z , and γ , this is the minimal Z pumping time (i.e. minimized over all choices of pumping rates $\{\Omega_f\}$). Since we do not want to fix γ a priori, we minimize the last expression over γ , finding that the optimal choice is

$$\gamma = \sqrt{\frac{8g^2 E_Z}{9N \log^2 N}}. \quad (\text{E.110})$$

The corresponding pumping strengths can now be computed from (E.104) and (E.108):

$$\Omega_F = \sqrt{\frac{8g^2 E_Z}{9N(N-1) \log N} \frac{N-F}{F}} \quad (\text{for } F = 1, \dots, N-1), \quad (\text{E.111})$$

and the optimal Z pumping time for given N , g , E_Z is then (compare to (E.25) without power broadening):

$$\tau_{N-1 \rightarrow \text{GHZ}} = \frac{9}{\sqrt{2}} \frac{(N-1)\sqrt{N} \log N}{g\sqrt{E_Z}} \simeq \frac{9}{\sqrt{2}} \frac{N^{3/2} \log N}{g\sqrt{E_Z}}. \quad (\text{E.112})$$

From now on we set $(N-1) \simeq N$, as this neglects only subleading terms.

We also take power broadening into account for the desired X rate (see (7.108)) and for the X toss rate (see (7.99)), which we both compute as in (E.34)–(E.37) and (E.42), and we take the detrimental X rate from (E.41):

$$\Gamma_X^+ = \sum_{n_-=1,3,\dots}^N \frac{1}{2^{N-1}} \binom{N}{n_-} \frac{2\gamma_f}{(\gamma_f + \kappa_b)^2 + 2n_-(\Omega_X^{(F=n_-)})^2} n_-(\Omega_X^{(F=n_-)})^2 \quad (\text{E.113})$$

$$\simeq \frac{2\gamma_f}{\gamma_f^2 + 2(N/2)\Omega^2} \frac{N}{2} \Omega^2 = N \frac{\gamma_f \Omega^2}{\gamma_f^2 + N\Omega^2}, \quad (\text{E.114})$$

$$\Gamma_X^{\text{toss}} = \frac{1}{2} \Gamma_X^+ \simeq \frac{N}{2} \frac{\gamma_f \Omega^2}{\gamma_f^2 + N\Omega_X^2}, \quad (\text{E.115})$$

$$\Gamma_X^- = \frac{\gamma_f \Omega^2}{g^2} \frac{5N^2}{16}. \quad (\text{E.116})$$

Now we adjust the X parameters Ω and γ_f such that the X rates agree with the corresponding Z rates (cf. Sec. E.2), i.e. $\Gamma_X^+ \equiv 2\Gamma_X^{\text{toss}} = \Gamma_Z^+ := 1/(\tau_{N-1 \rightarrow \text{GHZ}}) = \frac{\sqrt{2}}{9} \frac{g\sqrt{E_Z}}{N^{3/2} \log N}$ and $\Gamma_X^- = \Gamma_{\text{GHZ} \rightarrow ?}^- = \frac{\sqrt{2}}{9} \frac{gE_Z^{3/2}}{N^{3/2} \log N}$. To solve this for γ_f and Ω exactly, one would have to solve a cubic equation. As this is quite cumbersome and uninformative, we are looking for solutions which satisfy the following scaling ansatz: $\gamma_f \simeq N^\alpha (\log N)^\beta$ and $\Omega \simeq N^\phi (\log N)^\psi$. Then, one finds actually *two* possible solutions for Ω and γ_f , which lead to the desired scaling of Γ_X^+ and Γ_X^- (as N becomes large). One solution is:

$$\Omega = \frac{2^{5/4}}{3 \cdot 5^{1/4}} \frac{gE_Z^{1/2}}{N^{3/2} (\log N)^{1/2}} \quad (\text{E.117})$$

$$\gamma_f = \frac{4}{\sqrt{5}} \frac{gE_Z^{1/2}}{N^{1/2}}, \quad (\text{E.118})$$

Formally, another solution exists, but this is in the extremely saturated regime where our effective operators do not apply.

Finally, we need to find the relation between the above rate $\Gamma_Z^+ := (\tau_{N-1 \rightarrow \text{GHZ}, Z})^{-1}$ and the total GHZ preparation time $\tau_{\text{GHZ}} \equiv 1/\Gamma_+$ (which includes the errors and X toss) and the total stationary error E , just as in Sec. E.3. For this, we consider a simplified 3-compartment model which constitutes a very good approximation in the large- N -limit, in which the parameters (E.117) were computed in the first place. Here, compartment A comprises the states with $n_1 = 1, 2, \dots, N-1$, compartment B is the state $|\text{GHZ}_-\rangle$ and compartment C the state $|\text{GHZ}\rangle$. Then the transition matrix is (cf. (E.54) and Fig. E.1):

$$T = \begin{pmatrix} -2\Gamma_Z^+ - \Gamma_X^{\text{toss}} & \Gamma_X^+ & \Gamma_- \\ \Gamma_Z^+ + \Gamma_X^{\text{toss}} & -\Gamma_X^+ & 0 \\ \Gamma_Z^+ & 0 & -\Gamma_- \end{pmatrix} = \Gamma_Z^+ \begin{pmatrix} -5/2 & 1 & \Gamma_-/\Gamma_Z^+ \\ 3/2 & -1 & 0 \\ 1 & 0 & -\Gamma_-/\Gamma_Z^+ \end{pmatrix}, \quad (\text{E.119})$$

again with $\Gamma_- = \Gamma_X^- + \Gamma_Z^-$, and again as in Sec. E.3 we denote by T_+ the transition matrix without the “bad” rates Γ_- . From the stationary vector p_∞ satisfying

$Tp_\infty = 0$ we can again compute the total stationary error E :

$$E = 1 - \frac{1}{1 + \frac{5}{2} \frac{\Gamma_-}{\Gamma_+^+}} \simeq \frac{5}{2} \frac{\Gamma_-}{\Gamma_+^+} = 5E_Z. \quad (\text{E.120})$$

We therefore have to set $E_Z = E/5$ in all previous expressions. The relation between Γ_Z^+ and $\Gamma_+ \equiv 1/\tau_{\text{GHZ}}$ is similar to Eq. (E.62):

$$\Gamma_+ = \Gamma_Z^+ \frac{-\log(1 - P_C(t_0))}{\Gamma_Z^+ t_0}, \quad (\text{E.121})$$

where again P_C denotes the population in the GHZ state when starting from the GHZ- state. Computing this for the above transition matrix and plugging in the values for Γ_Z^+ and E from above, we obtain:

$$\Gamma_+ = 0.216 \cdot \Gamma_Z^+ = 0.0339 \cdot \frac{g\sqrt{E_Z}}{N^{3/2} \log N} = 0.0152 \cdot \frac{g\sqrt{E}}{N^{3/2} \log N}. \quad (\text{E.122})$$

Thus, in the large- N limit, the final GHZ preparation time τ_{GHZ} is:

$$\tau_{\text{GHZ}} = \frac{1}{\Gamma_+} \simeq 66 \frac{N^{3/2} \log N}{g\sqrt{E}}. \quad (\text{E.123})$$

This is achieved by the following parameter choices in terms of g , N , E :

$$\gamma = 0.42 \cdot \frac{g\sqrt{E}}{\sqrt{N} \log N} \quad (\text{this is the } \gamma\text{-rate for } Z \text{ pumping}), \quad (\text{E.124})$$

$$\Omega_F = 0.42 \cdot \frac{g\sqrt{E}}{N\sqrt{\log N}} \sqrt{\frac{N-F}{F}} \quad (\text{for } F = 1, \dots, N-1), \quad (\text{E.125})$$

$$\Omega = 0.24 \cdot \frac{gE^{1/2}}{N^{3/2}(\log N)^{1/2}} \quad (\text{E.126})$$

$$\gamma_f = 0.80 \cdot \frac{gE^{1/2}}{N^{1/2}}. \quad (\text{E.127})$$

Again, as in Eq. (E.97), if one is interested in the dynamical error \mathcal{E} instead of the static error E , one should everywhere set $E = 0.62\mathcal{E}$ for $\mathcal{E} = 0.1$ (or $E = 0.70\mathcal{E}$ for $\mathcal{E} = 0.03$). Furthermore, the GHZ preparation time is then prolonged by an additional factor of $\log(1/\mathcal{E})$ (see Eq. (E.94)).

Scaling analysis of the W protocol

Similar to our scaling analysis of the GHZ preparation time in App. E, we analyze the scaling of the W preparation time¹ in the following. As already anticipated from the transition rates computed in Sections 7.5 and 7.6.2, we will again employ a transition rate model, now consisting of five compartments as shown in Fig. F.1.

F.1 Weak driving analysis

Compartment 5 encompasses all states with $n_1 \geq 3$ excitations. As can be seen from Sec. 7.5, none of the error processes leads into this compartment, such that this compartment is continually emptied. As can be seen from Fig. F.1, the time to reach the W state (compartment 1) is longest time when starting from $n_1 = N$, which we will henceforth assume as the worst case. Thus, the transition rate Γ_{54}^+ from compartment 5 into compartment 4 (consisting of the states with $n_1 = 2$ excitations) is computed from the $N - 2$ individual transitions $N \rightarrow (N - 1) \rightarrow \dots \rightarrow 3 \rightarrow 2$. With Eq. (7.135) and following the rule of inverse addition of decay rates we get:

$$\Gamma_{54}^+ = \left(\sum_{n_1=3}^N (\Gamma_{n_1 \rightarrow j-1, \gamma_{0,Z}})^{-1} \right)^{-1} = \left(\sum_{F=3}^N \frac{1}{F} \right)^{-1} \cdot \frac{2\gamma_{0e}(\Omega_Z^{(F \geq 3)})^2}{(\gamma_e + \kappa_a)^2}, \quad (\text{F.1})$$

where we have made the parameter choice that all $\Omega_Z^{(F=n_1)}$ for $n_1 = 3, \dots, N$ are equal to each other and we call their value $\Omega_Z^{(F \geq 3)}$. The inverse of the sum on the right-hand-side equals $(\log N)^{-1}$, up to a correction that is smaller than $(\log N)^{-2}$, i.e. of lower order.

As physically and implementationally reasonable parameter choices (see also

¹The analysis has been performed in collaboration with D. Reeb.

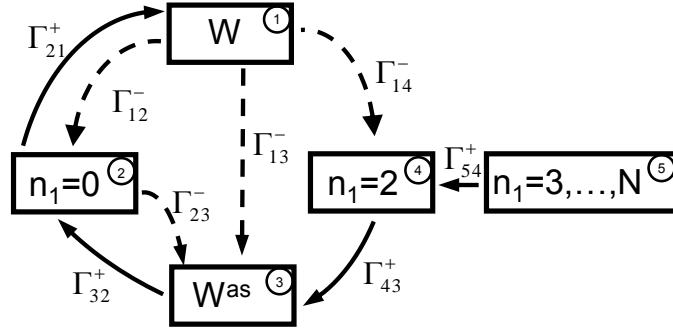


FIGURE F.1: 5-compartment-model of the W process. The “good” transition rates are shown as bold lines with arrows, whereas the error processes are shown with dashed lines.

Sec. 7.5), we will throughout set

$$\gamma_{0e} = \gamma_{1e} = \frac{1}{2}\gamma_e, \quad (\text{F.2})$$

$$\gamma_{0f} = \gamma_{1f} = \frac{1}{2}\gamma_f. \quad (\text{F.3})$$

Furthermore, we introduce a dimensionless constant β to write κ_a as:

$$\kappa_a = \beta\gamma_e. \quad (\text{F.4})$$

Later on, it will be seen that β is to be chosen as a constant (of order 1) in order to obtain an optimal scaling of the W preparation time. From Eq. (7.135) it can be seen that the desirable decay rate saturates for too strong drives since the transition is saturated. Hence, driving stronger than $\Omega_Z^{(F \geq 3)} \approx \gamma_e + \kappa_a = \gamma_e(1 + \beta)$ does not significantly increase the preparation rate, but only the loss rates. We thus re-parametrize $\Omega_Z^{(F \geq 3)}$ with a dimensionless constant α_n :

$$\Omega_Z^{(F \geq 3)} = \alpha_n \gamma_e \quad (\text{F.5})$$

With these substitutions and assumptions, the transition rate Γ_{54}^+ from (F.1) reads:

$$\Gamma_{54}^+ = \gamma_e \cdot \frac{\alpha_n^2}{(1 + \beta)^2} \cdot \frac{1}{\log N}. \quad (\text{F.6})$$

With the same substitutions, Eq. (7.134) yields the transition rate from compartment 4 to compartment 3 (consisting of the states with $n_1 = 1$ excitation and outside of the sector with permutation symmetry, i.e. the “antisymmetric” $n_1 = 1$ states):

$$\Gamma_{43}^+ = \gamma_e \cdot \frac{2\alpha_Z^2}{(1 + \beta)^2}, \quad (\text{F.7})$$

where the dimensionless constant α_Z (potentially different from α_n) has been introduced:

$$\Omega_Z^{(F=2)} = \alpha_Z \gamma_e \quad (\text{F.8})$$

Here, we have made the worst case assumption that decay from states with $n_1 = 2$ leads to the antisymmetric states in $n_1 = 1$.

The favorable transition rate from compartment 3 to compartment 2 (consisting of the $n_1 = 0$ state) is given by Eq. (7.156). As the parameter Ω_A does not appear in the loss rates (Eqs. (7.157)–(7.159)) in the present approximation, it will clearly be best to choose it as large as possible. However, when we include power broadening, the decay rate saturates at around

$$\Gamma_{32}^+ = \gamma_f \cdot \frac{1}{2}. \quad (\text{F.9})$$

Finally, the transition rate from compartment 2 to compartment 1 (the desired W state) is given by Eq. (7.177). Again due to the restrictions set by power broadening, we must have $\Omega_W \leq \gamma_e + \kappa_a = (1 + \beta)\gamma_e$. We reparametrize with a dimensionless parameter α_W :

$$\Omega_W = \frac{\alpha_W}{\sqrt{N}} \gamma_e \quad (\text{F.10})$$

(Note, here we take the factor \sqrt{N} into the parametrization for notational convenience, since in both the good rates and the loss rates the parameter Ω_W always appears in the combination $N\Omega_W^2$, see Sections 7.5.4 and 7.6.2). Thus, we get from Eq. (7.177):

$$\Gamma_{21}^+ = \Gamma_{0 \rightarrow W, \kappa, W} = \gamma_e \cdot \frac{2\alpha_W^2 \beta}{(1 + \beta)^2}. \quad (\text{F.11})$$

For the full W preparation time τ_W , we get from Eqs. (F.6), (F.7), (F.9), (F.11) and the rule of the inverse addition of decay rates:

$$\begin{aligned} \tau_W &= \tau_W(N, \alpha_n, \alpha_Z, \alpha_W, \beta, \gamma_e, \gamma_f) = \frac{1}{\Gamma_{54}^+} + \frac{1}{\Gamma_{43}^+} + \frac{1}{\Gamma_{32}^+} + \frac{1}{\Gamma_{21}^+} \\ &= \frac{1}{\gamma_e} \cdot \left[\frac{\log N}{\alpha_n^2} \cdot (1 + \beta)^2 + \frac{1}{\alpha_Z^2} \cdot \frac{(1 + \beta)^2}{2} + 2 \left(\frac{\gamma_e}{\gamma_f} \right) + \frac{1}{\alpha_W^2} \cdot \frac{(1 + \beta)^2}{2\beta} \right]. \end{aligned} \quad (\text{F.12})$$

$$(\text{F.13})$$

Next we compute the loss rates from the W state, i.e. the rates corresponding to the dashed lines in Fig. F.1. For this, observe that the parameter κ_b occurs only in the loss rates (Sec. 7.5.3), but not in the gain rates; thus, it will be optimal to set

$$\kappa_b = 0. \quad (\text{F.14})$$

Also note that there is no loss from the W state into compartment 5, i.e. $\Gamma_{15}^- = 0$.

The loss rate Γ_{14}^- is given by the sum of Eqs. (7.180) and (7.181), where we approximate the factor $(N - 1)$ by N :

$$\Gamma_{14}^- = \frac{N(\kappa_a + \gamma_{1e})\Omega_W^2}{g^2} = \frac{\gamma_e^3}{g^2} \cdot \frac{\alpha_W^2(1 + 2\beta)}{2}, \quad (\text{F.15})$$

where we have simply used the substitutions Eqs. (F.2), (F.4), and (F.10) from above.

The loss rate Γ_{13}^- is given by the sum of Eqs. (7.182) and (7.137):

$$\Gamma_{13}^- = \frac{N\gamma_{0e}\Omega_W^2}{g^2} + \frac{\gamma_{1e}}{2g^2} \cdot 2 \left(\frac{\Omega_Z^{(F=2)}}{2-1} \right)^2 + \frac{\gamma_{1e}}{2g^2} \sum_{F=3}^N F \left(\frac{\Omega_Z^{(F \geq 3)}}{F-1} \right)^2 \quad (\text{F.16})$$

$$= \frac{\gamma_e^3}{g^2} \left[\frac{\alpha_W^2}{2} + \frac{\alpha_Z^2}{2} + \frac{\alpha_n^2 \log N}{4} \right], \quad (\text{F.17})$$

where we have simply plugged in the substitutions from Eqs. (F.2), (F.5), (F.8), (F.10), and used that $\sum_{F=3}^N F/(F-1)^2 = \sum_{n=2}^{N-1} (1/n + 1/n^2) = (\log N) + \mathcal{O}(1)$, which equals $\log N$ up to subleading terms.

The loss rate Γ_{12}^- is given by Eq. (7.136), and follows in the same way as (F.16)–(F.17):

$$\Gamma_{12}^- = \frac{\gamma_{0e}}{2g^2} \cdot 2 \left(\frac{\Omega_Z^{(F=2)}}{2-1} \right)^2 + \frac{\gamma_{0e}}{2g^2} \sum_{F=3}^N F \left(\frac{\Omega_Z^{(F \geq 3)}}{F-1} \right)^2 \quad (\text{F.18})$$

$$= \frac{\gamma_e^3}{g^2} \left[\frac{\alpha_Z^2}{2} + \frac{\alpha_n^2 \log N}{4} \right]. \quad (\text{F.19})$$

Finally, we take into account the error rate from the 0 state to the antisymmetric $n_1 = 1$ states, given in Eq. (7.179):

$$\Gamma_{23}^- = \frac{2N\gamma_{1e}\Omega_W^2}{(\kappa_a + \gamma_e)^2} = \gamma_e \cdot \frac{\alpha_W^2}{(1 + \beta)^2}, \quad (\text{F.20})$$

which again follows from the substitutions (F.2), (F.4), and (F.10). Given the gain and loss rates just computed, the intensity matrix (Markov transition kernel) for the compartment model of Fig. F.1 is:

$$T = \begin{pmatrix} -(\Gamma_{12}^- + \Gamma_{13}^- + \Gamma_{14}^-) & \Gamma_{21}^+ & 0 & 0 & 0 \\ \Gamma_{12}^- & -\Gamma_{21}^+ - \Gamma_{23}^- & \Gamma_{32}^+ & 0 & 0 \\ \Gamma_{13}^- & \Gamma_{23}^- & -\Gamma_{32}^+ & \Gamma_{43}^+ & 0 \\ \Gamma_{14}^- & 0 & 0 & -\Gamma_{43}^+ & \Gamma_{54}^+ \\ 0 & 0 & 0 & 0 & -\Gamma_{54}^+ \end{pmatrix}. \quad (\text{F.21})$$

It is easy to see that the stationary vector \vec{p}_∞ (satisfying $T\vec{p}_\infty = \vec{0}$, and containing the steady state populations of each compartment) is given by

$$\vec{p}_\infty = \frac{1}{1 + p_2 + p_3 + p_4} \begin{pmatrix} 1 \\ p_2 \\ p_3 \\ p_4 \\ 0 \end{pmatrix}, \quad (\text{F.22})$$

where the numbers p_2, p_3, p_4 are, using the above expressions, given by :

$$p_2 = \frac{\Gamma_{12}^- + \Gamma_{13}^- + \Gamma_{14}^-}{\Gamma_{21}^+} = \frac{\gamma_e^2}{g^2} \left[\frac{(1+\beta)^3}{2\beta} + \frac{\alpha_Z^2}{\alpha_W^2} \cdot \frac{(1+\beta)^2}{2\beta} + \frac{\alpha_n^2 \log N}{\alpha_W^2} \cdot \frac{(1+\beta)^2}{4\beta} \right], \quad (\text{F.23})$$

$$\begin{aligned} p_3 &= \frac{\Gamma_{13}^- + \Gamma_{14}^-}{\Gamma_{32}^+} + p_2 \frac{\Gamma_{23}^-}{\Gamma_{32}^+} \\ &= \frac{\gamma_e^2}{g^2} \left(\frac{\gamma_e}{\gamma_f} \right) \left[\alpha_W^2 \cdot \frac{(1+\beta)(1+2\beta)}{\beta} + \alpha_Z^2 \cdot \frac{1+\beta}{\beta} + \alpha_n^2 \log N \cdot \frac{1+\beta}{2\beta} \right], \end{aligned} \quad (\text{F.24})$$

$$p_4 = \frac{\Gamma_{14}^-}{\Gamma_{43}^+} = \frac{\gamma_e^2}{g^2} \left[\frac{\alpha_W^2}{\alpha_Z^2} \cdot \frac{(1+\beta)^2(1+2\beta)}{4} \right]. \quad (\text{F.26})$$

The steady-state error E equals $1 - (\vec{p}_\infty)_0$, where $(\vec{p}_\infty)_0$ is the steady-state fidelity that can be read off from (F.22). Thus:

$$E = 1 - \frac{1}{1 + p_2 + p_3 + p_4} \approx p_2 + p_3 + p_4, \quad (\text{F.27})$$

where the last approximation is very good in the regime of small error ($E \lesssim 10\%$) we are interested in. We shall employ this approximation from now on. As can be seen from Eqs. (F.23)–(F.27), the stationary error will decrease as $\gamma_f/\gamma_e \rightarrow \infty$, which furthermore *reduces* the W preparation time (see Eq. (F.13)).

It will thus, within the current approximation, be optimal to choose $\gamma_f \rightarrow \infty$. Note, however, that the current derivation assumes that g is the largest coupling in the system, invalidating this limit for γ_f . However, even for a γ_f of the order of γ_e , other terms will dominate the error and preparation rate. We will thus in the following assume a

$$r = \frac{\gamma_e}{\gamma_f} \quad (\text{F.28})$$

between the decay rates that is independent of N and has a value $r \sim 1$. With this substitution, the stationary error becomes:

$$\begin{aligned} E \approx p_2 + p_3 + p_4 &= \frac{\gamma_e^2}{g^2} \left[\frac{(1+\beta)^3}{2\beta} + \frac{\alpha_Z^2}{\alpha_W^2} \cdot \frac{(1+\beta)^2}{2\beta} + \frac{\alpha_n^2 \log N}{\alpha_W^2} \cdot \frac{(1+\beta)^2}{4\beta} \right] \\ &+ \frac{\gamma_e^2}{g^2} \left[\alpha_W^2 \cdot \frac{r(1+\beta)(1+2\beta)}{\beta} + \alpha_Z^2 \cdot \frac{r(1+\beta)}{\beta} \right] \\ &+ \frac{\gamma_e^2}{g^2} \left[\alpha_n^2 \log N \cdot \frac{r(1+\beta)}{2\beta} + \frac{\alpha_W^2}{\alpha_Z^2} \cdot \frac{(1+\beta)^2(1+2\beta)}{4} \right]. \end{aligned} \quad (\text{F.29})$$

Note that the expression in the square brackets is dimensionless, as are all parameters occurring in it. We also assume that g is fixed from the beginning. Thus, for any given scaling of the dimensionless parameters (which we will determine below), we must choose a small enough γ_e in order to achieve the stationary error E . To get E , we must choose

$$\gamma_e = \frac{g\sqrt{E}}{\sqrt{[\text{brackets}]}} \quad (\text{F.30})$$

where [brackets] denotes the expression in square brackets in Eq. (F.29). Plugging this into the W preparation time (F.13) (using (F.28), so that all quantities except γ_e are dimensionless), we obtain:

$$\tau_W = \frac{1}{g\sqrt{E}} \cdot \left[\frac{\log N}{\alpha_n^2} \cdot (1+\beta)^2 + \frac{1}{\alpha_Z^2} \cdot \frac{(1+\beta)^2}{2} + 2r + \frac{1}{\alpha_W^2} \cdot \frac{(1+\beta)^2}{2\beta} \right] \cdot \sqrt{\frac{(1+\beta)^3}{2\beta} + \frac{\alpha_Z^2}{\alpha_W^2} \cdot \frac{(1+\beta)^2}{2\beta} + \frac{\alpha_n^2 \log N}{\alpha_W^2} \cdot \frac{(1+\beta)^2}{4\beta} + \alpha_W^2 \cdot \frac{r(1+\beta)(1+2\beta)}{\beta} + \alpha_Z^2 \cdot \frac{r(1+\beta)}{\beta} + \alpha_n^2 \log N \cdot \frac{r(1+\beta)}{2\beta} + \frac{\alpha_W^2}{\alpha_Z^2} \cdot \frac{(1+\beta)^2(1+2\beta)}{4}} \quad (\text{F.31})$$

Here, there are terms $\log(N)$ which grow with the qubit number, while the terms with r are constant and can thus be omitted for large N . Given that α_n , α_Z and α_W enter in the same way, we can assume that there is little gain in having them different. We thus set them equal to each other. We then obtain for the preparation time

$$\tau_W \stackrel{[N \text{ large}]}{\simeq} \frac{(\log N)^{3/2}}{\alpha^2 g \sqrt{E}} \cdot \frac{(1+\beta)^3}{2\sqrt{\beta}} \stackrel{[N \text{ large}, \beta=1]}{\simeq} 4 \frac{(\log N)^{3/2}}{\alpha^2 g \sqrt{E}} \quad (\text{F.32})$$

Eq. (F.32) identifies the resulting scaling in the weak driving regime. Similar to the result for GHZ it goes as the inverse of the strength of the driving, parametrized by α . To investigate the true scaling we thus have to perform a strong driving analysis. This is done below, but in short we find that the main limitation comes from α_n . This is due to the fact that α_n enters in Γ_{54}^+ which describes the rate at which we can depump the manifold with $n_1 \geq 2$. It necessarily involves $\mathcal{O}(N)$ decays and a resulting time $\mathcal{O}\left(\frac{N}{\gamma}\right)$. Comparing to Eq. (F.6) we see that this puts a restriction $\alpha_n \sim \frac{1}{\sqrt{N}}$. Inserting this in Eq. (F.32) gives us the scaling which only differs from the result obtained below by logarithmic corrections.

F.2 W scaling analysis for strong driving

We will analyze here the scaling of the W preparation time using effective operators accounting for the power broadening effect (Sec. 7.6.2). As in Sec. F.1, we employ again the transition rate model from Fig. F.1. To keep the analysis manageable, we will again assume simple and physically well-motivated relations between the decay rates and express all of them in terms of a single parameter, which we call γ throughout (cf. also Sec. F.1):

$$\gamma_e = \gamma_f = \kappa_a \equiv \gamma, \quad (\text{F.33})$$

$$\gamma_{0e} = \gamma_{1e} = \frac{1}{2}\gamma_e = \frac{1}{2}\gamma, \quad (\text{F.34})$$

$$\gamma_{0f} = \gamma_{1f} = \frac{1}{2}\gamma_f = \frac{1}{2}\gamma, \quad (\text{F.35})$$

$$\kappa_b = 0. \quad (\text{F.36})$$

From Eq. (7.107), we get for the rates of the Z pumping (for $n_1 = 2, 3, \dots, N$):

$$\Gamma_{n_1 \rightarrow n_1 - 1} = \Gamma_{n_1 \rightarrow n_1 - 1, \gamma 0, Z} = \frac{2F\gamma_{0e}\Omega_F^2}{(\gamma_e + \kappa_a)^2 + 2F\Omega_F^2} = \frac{\gamma F\Omega_F^2}{4\gamma^2 + 2F\Omega_F^2} \quad (\text{F.37})$$

where we denote the different pumping strengths for the optical Z pumping by Ω_F with $F = 2, 3, \dots, N$. By the law of inverse addition of decay rates, we thus obtain the following ‘‘good’’ rates Γ_{54}^+ and Γ_{43}^+ (cf. Fig. F.1):

$$\Gamma_{54}^+ = \left(\sum_{n_1=3}^N (\Gamma_{n_1 \rightarrow n_1 - 1})^{-1} \right)^{-1} = \left(\sum_{F=3}^N \frac{2}{\gamma} + \frac{4\gamma}{F\Omega_F^2} \right)^{-1} \quad (\text{F.38})$$

$$= \left(\frac{2(N-2)}{\gamma} + 4\gamma \sum_{F=3}^N \frac{1}{F\Omega_F^2} \right)^{-1}, \quad (\text{F.39})$$

$$\Gamma_{43}^+ = \Gamma_{n_1=2 \rightarrow \text{as}} \approx \Gamma_{2 \rightarrow 1, \gamma 0, Z} = \frac{\gamma\Omega_2^2}{2\gamma^2 + 2\Omega_2^2}. \quad (\text{F.40})$$

The only errors caused by the Z pumping rates Ω_F are, by Eqs. (7.136) and (7.137):

$$\Gamma_{W \rightarrow 0, \gamma 0, Z} = \Gamma_{W \rightarrow \text{as}, \gamma 1, Z} = \frac{\gamma}{4g^2} \sum_{F=2}^N \frac{F\Omega_F^2}{(F-1)^2}. \quad (\text{F.41})$$

Besides in these errors, the Z pumping drives Ω_F appear in the preparation time $\tau_W = (\Gamma_{54}^+)^{-1} + (\Gamma_{43}^+)^{-1} + (\Gamma_{32}^+)^{-1} + (\Gamma_{21}^+)^{-1}$ (see below and also e.g. Eq. (F.12)), and they appear only in the combination $(\Gamma_{54}^+)^{-1} + (\Gamma_{43}^+)^{-1} = \frac{2(N-1)}{\gamma} + 4\gamma \sum_{F=2}^N \frac{1}{F\Omega_F^2}$. To find the optimal choice of $\{\Omega_F\}_{F=2}^N$, we therefore want to minimize the total Ω_F -error in Eq. (F.41) for each constant value of $(\Gamma_{54}^+)^{-1} + (\Gamma_{43}^+)^{-1}$, or equivalently, for each constant value of $\sum_{F=2}^N \frac{1}{F\Omega_F^2}$. The method of Lagrange multipliers thus leads us to consider the following Lagrangian:

$$\mathcal{L}(\{\Omega_F\}_{F=2}^N, \lambda) := \sum_{F=2}^N \frac{F\Omega_F^2}{(F-1)^2} + \lambda^2 \sum_{F=2}^N \frac{1}{F\Omega_F^2}, \quad (\text{F.42})$$

where λ is a Lagrange multiplier that has dimensions of [frequency]². Solving the minimizer conditions $\frac{d\mathcal{L}}{d\Omega_F} = 0$ for all $F = 2, \dots, N$, we get the solutions

$$\Omega_F^2 = \lambda \frac{F-1}{F} \quad (F = 2, 3, \dots, N). \quad (\text{F.43})$$

Thus, the optimal choice for the $(N-1)$ parameters $\{\Omega_F\}$ depends on only one parameter λ , which we will choose below in the optimal way. Plugging (F.43) back into (F.40), into $(\Gamma_{54}^+)^{-1} + (\Gamma_{43}^+)^{-1}$, and into the error rates (F.41), we get:

$$\Gamma_{43}^+ = \frac{\lambda\gamma}{4\gamma^2 + 2\lambda}, \quad (\text{F.44})$$

$$(\Gamma_{54}^+)^{-1} + (\Gamma_{43}^+)^{-1} = \frac{2(N-1)}{\gamma} + 4\gamma \sum_{F=2}^N \frac{1}{\lambda(F-1)} \simeq \frac{2(N-1)}{\gamma} + \frac{4\gamma \log N}{\lambda}, \quad (\text{F.45})$$

$$\Gamma_{W \rightarrow 0, \gamma 0, Z} = \Gamma_{W \rightarrow \text{as}, \gamma 1, Z} = \frac{\gamma}{4g^2} \sum_{F=2}^N \frac{\lambda}{F-1} \simeq \frac{\lambda\gamma \log N}{4g^2}. \quad (\text{F.46})$$

The good rate Γ_{32}^+ is, from Eq. (7.109):

$$\Gamma_{32}^+ = \Gamma_{\text{as} \rightarrow 0, \gamma_0, A} = \frac{\gamma \Omega_A^2}{2\gamma^2 + 2\Omega_A^2}. \quad (\text{F.47})$$

Due to the choice $\kappa_b = 0$, the parameter Ω_A appears only in this good rate, but not in any error rate (see Sec. 7.5.3). Thus, Ω_A should be chosen in such a way as to maximize Γ_{32}^+ , which happens for $\Omega_A \gg \gamma_f$. As we have assumed g to be the largest parameter in our derivation, we set, however, $\Omega_A = \gamma_f$. We thus have:

$$\Gamma_{32}^+ = \frac{\gamma}{4}. \quad (\text{F.48})$$

By Eq. (7.184), the rate Γ_{21}^+ (with collective decay) is:

$$\Gamma_{21}^+ = \Gamma_{0 \rightarrow W, \kappa, W} = 2 \cdot \frac{\gamma N \Omega_W^2}{4\gamma^2 + 2N\Omega_W^2} = \frac{\gamma N \Omega_W^2}{2\gamma^2 + N\Omega_W^2}. \quad (\text{F.49})$$

The only free parameters (for any fixed values of N and g) in the above rates are now γ , λ and Ω_W , and we will optimize over those later (also taking the error into account). For convenience, we want to optimize over dimensionless parameters, and thus we write λ and Ω_W as dimensionless multiples of appropriate powers of the dimensionful quantity γ :

$$N\Omega_W^2 = \alpha\gamma^2, \quad (\text{F.50})$$

$$\lambda = \beta\gamma^2. \quad (\text{F.51})$$

With this notation, the total preparation time becomes:

$$\tau_W = \frac{1}{\Gamma_{54}^+} + \frac{1}{\Gamma_{43}^+} + \frac{1}{\Gamma_{32}^+} + \frac{1}{\Gamma_{21}^+} = \quad (\text{F.52})$$

$$= \frac{2(N-1)}{\gamma} + \frac{4\gamma \log N}{\lambda} + \frac{4}{\gamma} + \frac{2\gamma^2 + N\Omega_W^2}{\gamma N \Omega_W^2} = \quad (\text{F.53})$$

$$= \frac{2}{\gamma} \left(N + \frac{3}{2} + \frac{2 \log N}{\beta} + \frac{1}{\alpha} \right). \quad (\text{F.54})$$

Now we compute the stationary error E in terms of the above protocol parameters (see the dashed lines in Fig. F.1). From Eqs. (F.15), (F.16) (see also (F.46)), (F.18), and (7.186), we get the error rates:

$$\Gamma_{14}^- = \Gamma_{W \rightarrow 2}^- = \frac{(\kappa_a + \gamma_{1e})N\Omega_W^2}{g^2} = \frac{3\gamma N \Omega_W^2}{2g^2} = \frac{3\alpha\gamma^3}{2g^2}, \quad (\text{F.55})$$

$$\Gamma_{13}^- = \Gamma_{W \rightarrow \text{as}}^- = \frac{\gamma_{0e}N\Omega_W^2}{g^2} + \frac{\lambda\gamma \log N}{4g^2} = \frac{\alpha\gamma^3}{2g^2} + \frac{\beta\gamma^3 \log N}{4g^2}, \quad (\text{F.56})$$

$$\Gamma_{12}^- = \Gamma_{W \rightarrow 0}^- = \frac{\lambda\gamma \log N}{4g^2} = \frac{\beta\gamma^3 \log N}{4g^2}, \quad (\text{F.57})$$

$$\Gamma_{23}^- = \Gamma_{0 \rightarrow \text{as}}^- = \frac{2N\gamma_{1e}\Omega_W^2}{(\kappa_a + \gamma_e)^2 + 2N\Omega_W^2} = \frac{\alpha\gamma}{4 + 2\alpha}. \quad (\text{F.58})$$

In terms of these gain and loss rates, the Markov transition matrix and the stationary state vector \vec{p}_∞ look like Eqs. (F.21) and (F.22), where now p_2, p_3, p_4 are given by:

$$p_2 = \frac{\Gamma_{12}^- + \Gamma_{13}^- + \Gamma_{14}^-}{\Gamma_{21}^+} = \frac{\gamma^2}{g^2} \left(4 + 2\alpha + \frac{\beta \log N}{2} + \frac{\beta \log N}{\alpha} \right), \quad (\text{F.59})$$

$$p_3 = \frac{\Gamma_{13}^- + \Gamma_{14}^-}{\Gamma_{32}^+} + p_2 \frac{\Gamma_{23}^-}{\Gamma_{32}^+} = \frac{\gamma^2}{g^2} (12\alpha + 2\beta \log N), \quad (\text{F.60})$$

$$p_4 = \frac{\Gamma_{14}^-}{\Gamma_{43}^+} = \frac{\gamma^2}{g^2} \left(3\alpha + \frac{6\alpha}{\beta} \right). \quad (\text{F.61})$$

Again, the steady-state error E equals $1 - (\vec{p}_\infty)_0$:

$$E = 1 - \frac{1}{1 + p_2 + p_3 + p_4} \approx p_2 + p_3 + p_4, \quad (\text{F.62})$$

where the last approximation is very good in the regime of small error ($E \lesssim 10\%$), which we are interested in, so that we employ this approximation from now on. Thus:

$$E = \frac{\gamma^2}{g^2} \left[4 + 17\alpha + \frac{5\beta \log N}{2} + \frac{\beta \log N}{\alpha} + \frac{6\alpha}{\beta} \right]. \quad (\text{F.63})$$

Therefore, if the desired stationary error E is given, we have to choose γ in the following way:

$$\gamma = \frac{g\sqrt{E}}{\sqrt{4 + 17\alpha + \frac{5\beta \log N}{2} + \frac{\beta \log N}{\alpha} + \frac{6\alpha}{\beta}}}. \quad (\text{F.64})$$

Therefore, for given stationary error E , the W preparation time is from (F.54):

$$\tau_W = \frac{2}{\gamma} \left(N + \frac{3}{2} + \frac{2 \log N}{\beta} + \frac{1}{\alpha} \right) \quad (\text{F.65})$$

$$= \frac{1}{g\sqrt{E}} \left[2N + 3 + \frac{4 \log N}{\beta} + \frac{2}{\alpha} \right] \sqrt{4 + 17\alpha + \frac{5\beta \log N}{2} + \frac{\beta \log N}{\alpha} + \frac{6\alpha}{\beta}}. \quad (\text{F.66})$$

Now, to find the optimal W -preparation time τ_W for any given N , we simply have to minimize this expression over all choices of dimensionless parameters $\alpha, \beta > 0$. We do this using MATHEMATICA for small values of N , and obtain the following results:

N	α	β	τ_W from (F.66)
2	0.77	2.62	$54.1/(g\sqrt{E})$
3	0.75	2.33	$72.3/(g\sqrt{E})$
4	0.72	2.12	$89.4/(g\sqrt{E})$
5	0.69	1.96	$105.6/(g\sqrt{E})$
6	0.66	1.82	$121.3/(g\sqrt{E})$
7	0.63	1.70	$136.7/(g\sqrt{E})$
8	0.61	1.61	$151.6/(g\sqrt{E})$
9	0.59	1.52	$166.3/(g\sqrt{E})$
10	0.58	1.45	$180.7/(g\sqrt{E})$

We examine now the exact optimal N -scaling in the asymptotic regime. Note that the expression under the square root in (F.66) satisfies:

expression under square root (F.67)

$$\geq \frac{\beta \log N}{\alpha} + \frac{6\alpha}{\beta} - 2 \cdot \sqrt{\frac{\beta \log N}{\alpha}} \cdot \sqrt{\frac{6\alpha}{\beta}} + 2 \cdot \sqrt{\frac{\beta \log N}{\alpha}} \cdot \sqrt{\frac{6\alpha}{\beta}} \quad (\text{F.68})$$

$$= \left(\sqrt{\frac{\beta \log N}{\alpha}} - \sqrt{\frac{6\alpha}{\beta}} \right)^2 + 2 \cdot \sqrt{\frac{\beta \log N}{\alpha}} \cdot \sqrt{\frac{6\alpha}{\beta}} \quad (\text{F.69})$$

$$\geq 2 \cdot \sqrt{\frac{\beta \log N}{\alpha}} \cdot \sqrt{\frac{6\alpha}{\beta}} = 2\sqrt{6}(\log N)^{1/2}. \quad (\text{F.70})$$

Thus, the preparation time τ_W in (F.66) satisfies:

$$\tau_W \geq \frac{\sqrt{8\sqrt{6}}}{g\sqrt{E}} N(\log N)^{1/4}. \quad (\text{F.71})$$

And indeed, such a N -scaling like $N(\log N)^{1/4}$ can be achieved in (F.66) by choosing $\alpha = \alpha_0$ and $\beta = \beta_0/(\log N)^{1/2}$ with positive constants α_0 and β_0 . Then the overall asymptotic prefactor is minimized for $\alpha_0 = \beta_0/\sqrt{6}$ and small positive constant β_0 . Note that, due to the log-term in Eq. (F.66), the limit $\beta_0 \rightarrow 0$ is not, however, sensible for any finite N . For this reason, and since the numerical prefactor can never become smaller than $\sqrt{8\sqrt{6}} = 4.42$ anyway, we may for example want to choose $\beta = 1/(\log N)^{1/2}$ and $\alpha = 1/\sqrt{6}$, in which case the asymptotic W preparation time is:

$$\tau_W = 5.44 \frac{N(\log N)^{1/4}}{g\sqrt{E}} \quad \text{as } N \rightarrow \infty \quad (\text{for } \alpha = 1/\sqrt{6}, \beta = (\log N)^{-1/2}). \quad (\text{F.72})$$

For the simpler choice $\alpha = \beta = 1$, the scaling becomes only a little worse:

$$\tau_W = \sqrt{14} \frac{N(\log N)^{1/2}}{g\sqrt{E}} \quad \text{as } N \rightarrow \infty \quad (\text{for } \alpha = \beta = 1). \quad (\text{F.73})$$

Note that, due to the log-terms, the *asymptotic* N -scaling of the preparation time (F.66) is relevant only for rather large N (e.g. only when $2\sqrt{6}(\log N)^{1/2} > (4 + 17\alpha)$), and one should rather use the parameter values provided in the preceding table. For realistic (small) values of N , these parameter choices lead to somewhat better τ_W than any of the choices that led to Eqs. (F.72) and (F.73).

To conclude, we summarize the above parameter choices:

- choose the dimensionless parameters α, β such that, for the given N , they minimize the expression (F.66), as done in the above table for $N = 2, \dots, 10$. (Alternatively, choose for example $\alpha = \beta = 1$).
- set $\gamma_e = \gamma_f = \kappa_a = \gamma, \kappa_b = 0, \gamma_{0e} = \gamma_{1e} = \gamma_{0f} = \gamma_{1f} = \gamma/2$, where

$$\gamma = \frac{g\sqrt{E}}{\sqrt{4 + 17\alpha + \frac{5\beta \log N}{2} + \frac{\beta \log N}{\alpha} + \frac{6\alpha}{\beta}}}. \quad (\text{F.74})$$

- set the pumping rates to be:

$$\Omega_W = \frac{\sqrt{\alpha}\gamma}{\sqrt{N}}, \quad (\text{F.75})$$

$$\Omega_A = \gamma, \quad (\text{F.76})$$

$$\Omega_F = \sqrt{\beta}\gamma\sqrt{\frac{F-1}{F}} \quad (F = 2, 3, \dots, N). \quad (\text{F.77})$$

- then the τ_W preparation time is given by (F.66).

Similar as in the GHZ scheme, the dynamical error \mathcal{E} is obtained by multiplying the static error E with a factor (cf. Eq. (E.97), e.g. $E = 0.62\mathcal{E}$ for $\mathcal{E} = 0.1$ or $E = 0.70\mathcal{E}$ for $\mathcal{E} = 0.03$). The W preparation time is then prolonged by an additional factor of $\log(1/\mathcal{E})$ (see Eq. (E.94)).

Bibliography

- [1] J. J. Sakurai and J. Napolitano. *Modern Quantum Mechanics*. Addison-Wesley, 2011.
- [2] E. Schrödinger. Die gegenwärtige Situation der Quantenmechanik. *Naturwissenschaften*, 23:807, 1935.
- [3] A. Einstein, B. Podolsky, and N. Rosen. Can quantum-mechanical description of physical reality be considered complete? *Phys. Rev.*, 47:777, 1935.
- [4] A. Aspect, P. Grangier, and G. Roger. Experimental realization of Einstein-Podolsky-Rosen-Bohm Gedankenexperiment: a new violation of Bell's inequalities. *Phys. Rev. Lett.*, 49:91, 1982.
- [5] C. E. Shannon. A Mathematical Theory of Communication. *Bell System Technical Journal*, 27:379, 1948.
- [6] M. A. Nielsen and I. L. Chuang. *Quantum computation and quantum information*. Cambridge University Press, Cambridge, 2000.
- [7] T. D. Ladd, F. Jelezko, R. Laflamme, Y. Nakamura, C. Monroe, and J. L. O'Brien. Quantum computers. *Nature*, 464:45, 2010.
- [8] L. K. Grover. Quantum Mechanics Helps in Searching for a Needle in a Haystack. *Phys. Rev. Lett.*, 79:325, 1997.
- [9] P. W. Shor. Polynomial-Time Algorithms for Prime Factorization and Discrete Logarithms on a Quantum Computer. *SIAM J. Comput.*, 26:1484, 1997.
- [10] N. Gisin, G. Ribordy, W. Tittel, and H. Zbinden. Quantum cryptography. *Rev. Mod. Phys.*, 74:145, 2002.
- [11] V. Giovannetti, S. Lloyd, and L. Maccone. Quantum-enhanced measurements: beating the standard quantum limit. *Science*, 306:1330, 2004.
- [12] L. M. K. Vandersypen, M. Steffen, and G. Breyta. Experimental realization of Shor's quantum factoring algorithm using nuclear magnetic resonance. *Nature*, 412:883, 2001.

- [13] J. Chiaverini, D. Leibfried, T. Schaetz, M. D. Barrett, R. B. Blakestad, J. Britton, W. M. Itano, J. D. Jost, E. Knill, C. Langer, R. Ozeri, and D. J. Wineland. Realization of quantum error correction. *Nature*, 432:2, 2004.
- [14] M. D. Reed, L. DiCarlo, S. E. Nigg, L. Sun, L. Frunzio, S. M. Girvin, and R. J. Schoelkopf. Realization of three-qubit quantum error correction with superconducting circuits. *Nature*, 482:382, 2012.
- [15] C. Gardiner and P. Zoller. *Quantum Noise: A Handbook of Markovian and Non-Markovian Quantum Stochastic Methods with Applications to Quantum Optics*. Springer, 2010.
- [16] M. Schlosshauer. Decoherence, the measurement problem, and interpretations of quantum mechanics. *Rev. Mod. Phys.*, 76:1267, 2004.
- [17] D. P. DiVincenzo. Topics in Quantum Computers. *NATO ASI Series*, 345:657, 1997.
- [18] J. F. Poyatos, J. I. Cirac, and P. Zoller. Quantum reservoir engineering with laser cooled trapped ions. *Phys. Rev. Lett.*, 77:4728, 1996.
- [19] B. Kraus, H. P. Büchler, S. Diehl, A. Kantian, A. Micheli, and P. Zoller. Preparation of entangled states by quantum Markov processes. *Phys. Rev. A*, 78:042307, 2008.
- [20] F. Verstraete, M. M. Wolf, and J. I. Cirac. Quantum computation and quantum-state engineering driven by dissipation. *Nature Phys.*, 5:633, 2009.
- [21] For an amazing Bronze Age hat that displays a lunisolar calendar, see http://en.wikipedia.org/wiki/Golden_Hat.
- [22] J. S. Bell. On the Einstein-Podolsky-Rosen Paradox. *Physics*, 1:195, 1964.
- [23] J.-W. Pan, D. Bouwmeester, M. Daniell, H. Weinfurter, and A. Zeilinger. Experimental test of quantum nonlocality in three-photon Greenberger-Horne-Zeilinger entanglement. *Nature*, 403:515, 2000.
- [24] W. Dür, G. Vidal, and J. I. Cirac. Three qubits can be entangled in two inequivalent ways. *Phys. Rev. A*, 62:1, 2000.
- [25] D. Bouwmeester, J.-W. Pan, K. Mattle, M. Eibl, H. Weinfurter, and A. Zeilinger. Experimental Quantum Teleportation. *Nature*, 390:575, 1997.
- [26] M. Fleischhauer and M. D. Lukin. Quantum memory for photons: Dark-state polaritons. *Phys. Rev. A*, 65:022314, 2002.
- [27] P. W. Shor. Scheme for reducing decoherence in quantum computer memory. *Phys. Rev. A*, 52:2493, 1995.
- [28] A. Steane. Multiple-Particle Interference and Quantum Error Correction. *Proc. Roy. Soc. Lond. A*, 452:2551.
- [29] H. Carmichael. *An Open Systems Approach to Quantum Optics*. Springer-Verlag, 1993.

- [30] H. P. Breuer and F. Petruccione. *The Theory of Open Quantum Systems*. OUP Oxford, 2007.
- [31] G. Lindblad. On the generators of quantum dynamical semigroups. *Communications in Mathematical Physics*, 130:119, 1976.
- [32] J. I. Cirac and P. Zoller. Quantum computations with cold trapped ions. *Phys. Rev. Lett.*, 74:4091, 1995.
- [33] A. Sørensen and K. Mølmer. Quantum Computation with Ions in Thermal Motion. *Phys. Rev. Lett.*, 82:1971, 1999.
- [34] C. Monroe, D. M. Meekhof, B. E. King, S. R. Jefferts, W. M. Itano, D. J. Wineland, and P. Gould. Resolved-sideband raman cooling of a bound atom to the 3D zero-point energy. *Phys. Rev. Lett.*, 75:4011, 1995.
- [35] F. Schmidt-Kaler, H. Häffner, M. Riebe, S. Gulde, G. P. T. Lancaster, T. Deuschle, C. Becher, C. F. Roos, J. Eschner, and R. Blatt. Realization of the Cirac-Zoller controlled-NOT quantum gate. *Nature*, 422:408, 2003.
- [36] C. A. Sackett, D. Kielpinski, B. E. King, and C. Langer. Experimental entanglement of four particles. *Nature*, 404, 2000.
- [37] R. Miller, T. E. Northup, K. M. Birnbaum, A. Boca, A. D. Boozer, and H. J. Kimble. Trapped atoms in cavity QED: coupling quantized light and matter. *J. Phys. B: At. Mol. Opt. Phys.*, 38:S551, 2005.
- [38] A. D. Boozer, A. Boca, R. Miller, T. E. Northup, and H. J. Kimble. Cooling to the Ground State of Axial Motion for One Atom Strongly Coupled to an Optical Cavity. *Phys. Rev. Lett.*, 97:083602, 2006.
- [39] A. D. Boozer, A. Boca, R. Miller, T. E. Northup, and H. J. Kimble. Reversible State Transfer between Light and a Single Trapped Atom. *Phys. Rev. Lett.*, 98:193601, 2007.
- [40] A. Kubanek, A. Ourjoumtsev, and I. Schuster. Two-photon gateway in one-atom cavity quantum electrodynamics. *Phys. Rev. Lett.*, 101:203602, 2008.
- [41] A. Kubanek, M. Koch, C. Sames, A. Ourjoumtsev, P. W. H. Pinkse, K. Murr, and G. Rempe. Photon-by-photon feedback control of a single-atom trajectory. *Nature*, 462:898, 2009.
- [42] M. Koch, C. Sames, A. Kubanek, M. Apel, M. Balbach, A. Ourjoumtsev, P. W. H. Pinkse, and G. Rempe. Feedback Cooling of a Single Neutral Atom. *Phys. Rev. Lett.*, 105:173003, 2010.
- [43] P. Domokos, J. M. Raimond, M. Brune, and S. Haroche. Simple cavity-QED two-bit universal quantum logic gate: The principle and expected performances. *Phys. Rev. A*, 52:3554, 1995.
- [44] T. Pellizzari, S. Gardiner, J. Cirac, and P. Zoller. Decoherence and Continuous Observation and Quantum Computing: A Cavity QED Model. *Phys. Rev. Lett.*, 75:3788, 1995.

- [45] M. B. Plenio, S. F. Huelga, A. Beige, and P. L. Knight. Cavity-loss-induced generation of entangled atoms. *Phys. Rev. A*, 59:2468, 1999.
- [46] A. Beige, D. Braun, B. Tregenna, and P. L. Knight. Quantum computing using dissipation to remain in a decoherence-free subspace. *Phys. Rev. Lett.*, 85:8, 2000.
- [47] S.-B. Zheng and G.-C. Guo. Efficient Scheme for Two-Atom Entanglement and Quantum Information Processing in Cavity QED. *Phys. Rev. Lett.*, 85:2392, 2000.
- [48] J. Pachos and H. Walther. Quantum Computation with Trapped Ions in an Optical Cavity. *Phys. Rev. Lett.*, 89:187903, 2002.
- [49] A. S. Sørensen and K. Mølmer. Measurement induced entanglement and quantum computation with atoms in optical cavities. *Phys. Rev. Lett.*, 91:097905, 2003.
- [50] A. Rauschenbeutel, G. Nogues, S. Osnaghi, P. Bertet, M. Brune, J.-M. Raimond, and S. Haroche. Step-by-Step Engineered Multiparticle Entanglement. *Science*, 288:2024, 2000.
- [51] L. DiCarlo, M. D. Reed, L. Sun, B. R. Johnson, J. M. Chow, J. M. Gambetta, L. Frunzio, S. M. Girvin, M. H. Devoret, and R. J. Schoelkopf. Preparation and measurement of three-qubit entanglement in a superconducting circuit. *Nature*, 467:574, 2010.
- [52] A. Sørensen and K. Mølmer. Entanglement and quantum computation with ions in thermal motion. *Phys. Rev. A*, 62:022311, 2000.
- [53] D. Leibfried, E. Knill, S. Seidelin, J. Britton, R. B. Blakestad, J. Chiaverini, D. B. Hume, W. M. Itano, J. D. Jost, C. Langer, R. Ozeri, R. Reichle, and D. J. Wineland. Creation of a six-atom 'Schrödinger cat' state. *Nature*, 438:639, 2005.
- [54] T. Monz, P. Schindler, J. T. Barreiro, M. Chwalla, D. Nigg, W. A. Coish, M. Harlander, W. Hänsel, M. Hennrich, and R. Blatt. 14-qubit entanglement: Creation and coherence. *Physical Review Letters*, 106:130506, 2011.
- [55] B. P. Lanyon, C. Hempel, D. Nigg, M. Müller, R. Gerritsma, F. Zähringer, P. Schindler, J. T. Barreiro, M. Rambach, G. Kirchmair, M. Hennrich, P. Zoller, R. Blatt, and C. F. Roos. Universal digital quantum simulation with trapped ions. *Science*, 334:57, 2011.
- [56] D. Hanneke, J. P. Home, J. D. Jost, J. M. Amini, D. Leibfried, and D. J. Wineland. Realization of a programmable two-qubit quantum processor. *Nature Phys.*, 6:13, 2010.
- [57] H. Häffner, W. Hänsel, C. F. Roos, J. Benhelm, D. Chek-al-kar, M. Chwalla, T. Körber, U. D. Rapol, M. Riebe, P. O. Schmidt, C. Becher, O. Gühne, W. Dür, and R. Blatt. Scalable multiparticle entanglement of trapped ions. *Nature*, 438:643, 2005.

- [58] R. J. Schoelkopf and S. M. Girvin. Wiring up quantum systems. *Nature*, 451:664, 2008.
- [59] J. Koch, T. M. Yu, J. Gambetta, A. A. Houck, D. I. Schuster, J. Majer, A. Blais, M. H. Devoret, S. M. Girvin, and R. J. Schoelkopf. Charge-insensitive qubit design derived from the Cooper pair box. *Phys. Rev. A*, 76:042319, 2007.
- [60] A. A. Houck, J. Koch, M. H. Devoret, S. M. Girvin, and R. J. Schoelkopf. Life after charge noise: recent results with transmon qubits. *Quantum Inf. Process.*, 8:105, 2009.
- [61] J. M. Chow, J. M. Gambetta, A. D. Corcoles, S. T. Merkel, J. A. Smolin, C. Rigetti, S. Poletto, G. A. Keefe, M. B. Rothwell, J. R. Rozen, M. B. Ketchen, and M. Steffen. Universal Quantum Gate Set Approaching Fault-Tolerant Thresholds with Superconducting Qubits. *Phys. Rev. Lett.*, 109:060501, 2012.
- [62] C. Rigetti, J. M. Gambetta, S. Poletto, B. L. T. Plourde, J. M. Chow, A. D. Corcoles, J. A. Smolin, S. T. Merkel, J. R. Rozen, G. A. Keefe, M. B. Rothwell, M. B. Ketchen, and M. Steffen. Superconducting qubit in waveguide cavity with coherence time approaching 0.1 ms. *Phys. Rev. B*, 86:100506, 2012.
- [63] S. Poletto, J. M. Gambetta, S. T. Merkel, J. A. Smolin, J. M. Chow, A. D. Corcoles, G. A. Keefe, M. B. Rothwell, J. R. Rozen, D. W. Abraham, C. Rigetti, and M. Steffen. Entanglement of Two Superconducting Qubits in a Waveguide Cavity via Monochromatic Two-Photon Excitation. *Phys. Rev. Lett.*, 109:240505, 2012.
- [64] H. Paik, D. I. Schuster, L. S. Bishop, G. Kirchmair, G. Catelani, A. P. Sears, B. R. Johnson, M. J. Reagor, L. Frunzio, L. I. Glazman, S. M. Girvin, M. H. Devoret, and R. J. Schoelkopf. Observation of High Coherence in Josephson Junction Qubits Measured in a Three-Dimensional Circuit QED Architecture. *Phys. Rev. Lett.*, 107:240501, 2011.
- [65] A. P. Sears, A. Petrenko, G. Catelani, L. Sun, H. Paik, G. Kirchmair, L. Frunzio, L. I. Glazman, S. M. Girvin, and R. J. Schoelkopf. Photon shot noise dephasing in the strong-dispersive limit of circuit QED. *Phys. Rev. B*, 86:180504, 2012.
- [66] M. Neeley, R. C. Bialczak, M. Lenander, E. Lucero, M. Mariantoni, A. D. O'Connell, D. Sank, H. Wang, M. Weides, J. Wenner, Y. Yin, T. Yamamoto, A. N. Cleland, and J. M. Martinis. Generation of Three-Qubit Entangled States using Superconducting Phase Qubits. *Nature*, 467:570, 2010.
- [67] A. Fedorov, L. Steffen, M. Baur, M. P. da Silva, and A. Wallraff. Implementation of a Toffoli gate with superconducting circuits. *Nature*, 481:170, 2012.
- [68] D. E. Chang, A. S. Sørensen, P. R. Hemmer, and M. D. Lukin. Quantum Optics with Surface Plasmons. *Phys. Rev. Lett.*, 97:053002, 2006.

- [69] D. E. Chang, A. S. Sørensen, E. A. Demler, and M. D. Lukin. A single-photon transistor using nanoscale surface plasmons. *Nature Phys.*, 2:807, 2007.
- [70] L.-M. Duan and H. Kimble. Scalable Photonic Quantum Computation through Cavity-Assisted Interactions. *Phys. Rev. Lett.*, 92:127902, 2004.
- [71] J. L. O'Brien. Optical quantum computing. *Science*, 318:1567, 2007.
- [72] M. Saffman, T. G. Walker, and K. Mølmer. Quantum information with Rydberg atoms. *Rev. Mod. Phys.*, 82, 2010.
- [73] E. Knill. Resilient Quantum Computation. *Science*, 279:342, 1998.
- [74] W. Happer. Optical pumping. *Rev. Mod. Phys.*, 44:160, 1972.
- [75] A. Aspect, E. Arimondo, R. Kaiser, N. Vansteenkiste, and C. Cohen-Tannoudji. Laser Cooling below the One-Photon Recoil Energy by Velocity-Selective Coherent Population Trapping. *Phys. Rev. Lett.*, 61:826, 1988.
- [76] D. Kienzler, H.-Y. Lo, B. Keitch, L. de Clercq, F. Leupold, F. Lindenefser, M. Marinelli, V. Negnevitsky, and J. P. Home. Quantum harmonic oscillator state synthesis by reservoir engineering. *arXiv:1409.3032*, 2014.
- [77] M. S. Kim, J. Lee, D. Ahn, and P. L. Knight. Entanglement induced by a single-mode heat environment. *Phys. Rev. A*, 65:040101, 2002.
- [78] S. Schneider and G. J. Milburn. Entanglement in the steady state of a collective-angular-momentum (Dicke) model. *Phys. Rev. A*, 65:042107, 2002.
- [79] A. M. Basharov. Decoherence and Entanglement in Radiative Decay of a Diatomic System. *J. Exp. Theor. Phys.*, 94:1070], 2002.
- [80] L. Jakóbczyk. Entangling two qubits by dissipation. *J. Phys. A*, 35:6383, 2002.
- [81] D. Braun. Creation of Entanglement by Interaction with a Common Heat Bath. *Phys. Rev. Lett.*, 89:277901, 2002.
- [82] F. Benatti, R. Floreanini, and U. Marzolin. Environment Induced Entanglement in Markovian Dissipative Dynamics. *Phys. Rev. Lett.*, 91:070402, 2003.
- [83] F. Benatti, R. Floreanini, and U. Marzolin. Entangling two unequal atoms through a common bath. *Phys. Rev. A*, 81:012105, 2010.
- [84] S. Clark, A. Peng, M. Gu, and S. Parkins. Unconditional Preparation of Entanglement between Atoms in Cascaded Optical Cavities. *Phys. Rev. Lett.*, 91:177901, 2003.
- [85] G. Vacanti and A. Beige. Cooling atoms into entangled states. *New. J. Phys.*, 11:083008, 2009.

- [86] X. T. Wang and S. G. Schirmer. Generating maximal entanglement between non-interacting atoms by collective decay and symmetry breaking. *arXiv:1005.2114*, 2011.
- [87] J. Cho, S. Bose, and M. S. Kim. Optical Pumping into Many-Body Entanglement. *Phys. Rev. Lett.*, 106:020504, 2011.
- [88] A. Gonzalez-Tudela, D. Martín-Cano, E. Moreno, L. Martín-Moreno, C. Tejedor, and F. J. García-Vidal. Entanglement of Two Qubits Mediated by One-Dimensional Plasmonic Waveguides. *Phys. Rev. Lett.*, 106:020501, 2011.
- [89] D. Martín-Cano, Alejandro González-Tudela, L. Martín-Moreno, F. J. García-Vidal, C. Tejedor, and E. Moreno. Dissipation-driven generation of two-qubit entanglement mediated by plasmonic waveguides. *Phys. Rev. B*, 84:235306, 2011.
- [90] J. Busch, S. De, S. S. Ivanov, B. T. Torosov, T. P. Spiller, and A. Beige. Cooling atom-cavity systems into entangled states. *Phys. Rev. A*, 84:022316, 2011.
- [91] J. T. Barreiro, M. Müller, P. Schindler, D. Nigg, T. Monz, M. Chwalla, M. Hennrich, C. F. Roos, P. Zoller, and R. Blatt. An open-system quantum simulator with trapped ions. *Nature*, 470:486, 2011.
- [92] M. Müller, K. Hammerer, Y. L. Zhou, C. F. Roos, and P. Zoller. Simulating open quantum systems: from many-body interactions to stabilizer pumping. *New J. Phys.*, 13:085007, 2011.
- [93] M. Gullans, T. G. Tiecke, D. E. Chang, J. Feist, J. D. Thompson, J. I. Cirac, P. Zoller, and M. D. Lukin. Nanoplasmonic Lattices for Ultracold Atoms. *Phys. Rev. Lett.*, 109:235309, 2012.
- [94] A. González-Tudela and D. Porras. Mesoscopic Entanglement Induced by Spontaneous Emission in Solid-State Quantum Optics. *Phys. Rev. Lett.*, 110:080502, 2013.
- [95] M. Kiffner, U. Dorner, and D. Jaksch. Dissipative quantum-light-field engineering. *Phys. Rev. A*, 85:023812, 2012.
- [96] M. Foss-Feig, A. J. Daley, J. K. Thompson, and A. M. Rey. Steady-state many-body entanglement of hot reactive fermions. *Phys. Rev. Lett.*, 109:230501, 2012.
- [97] A. S. Parkins, E. Solano, and J. I. Cirac. Unconditional Two-Mode Squeezing of Separated Atomic Ensembles. *Phys. Rev. Lett.*, 96:053602, 2006.
- [98] C. A. Muschik, E. S. Polzik, and J. I. Cirac. Dissipatively driven entanglement of two macroscopic atomic ensembles. *Phys. Rev. A*, 83:052312, 2011.

- [99] H. Krauter, C. A. Muschik, K. Jensen, W. Wasilewski, J. M. Petersen, J. I. Cirac, and E. S. Polzik. Entanglement Generated by Dissipation and Steady State Entanglement of Two Macroscopic Objects. *Phys. Rev. Lett.*, 107:080503, 2011.
- [100] E. G. Dalla Torre, J. Otterbach, E. Demler, V. Vuletic, and M. D. Lukin. Dissipative Preparation of Spin Squeezed Atomic Ensembles in a Steady State. *Phys. Rev. Lett.*, 110:120402, 2013.
- [101] F. Reiter, M. J. Kastoryano, and A. S. Sørensen. Driving two atoms in an optical cavity into an entangled steady state using engineered decay. *New J. Phys.*, 14:053022, 2012.
- [102] M. J. Kastoryano, F. Reiter, and A. S. Sørensen. Dissipative Preparation of Entanglement in Optical Cavities. *Phys. Rev. Lett.*, 106:090502, 2011.
- [103] A. Bermudez, T. Schaetz, and M. B. Plenio. Dissipation-assisted quantum information processing with trapped ions. *Phys. Rev. Lett.*, 110:110502, 2013.
- [104] C. Cormick, A. Bermudez, S. F. Huelga, and M. B. Plenio. Dissipative ground-state preparation of a spin chain by a structured environment. *New J. Phys.*, 15:073027, 2013.
- [105] Y. Lin, J. P. Gaebler, F. Reiter, T. R. Tan, R. Bowler, A. S. Sørensen, D. Leibfried, and D. J. Wineland. Dissipative production of a maximally entangled steady state of two quantum bits. *Nature*, 504:415, 2013.
- [106] A. W. Carr and M. Saffman. Preparation of Entangled and Antiferromagnetic States by Dissipative Rydberg Pumping. *Phys. Rev. Lett.*, 111:033607, 2013.
- [107] D. D. B. Rao and K. Mølmer. Dark Entangled Steady States of Interacting Rydberg Atoms. *Phys. Rev. Lett.*, 111:033606, 2013.
- [108] D. D. B. Rao and K. Mølmer. Deterministic entanglement of Rydberg ensembles by engineered dissipation. *arXiv:1407.1228*, 2014.
- [109] P. B. Li, S. Y. Gao, H. R. Li, S. L. Ma, and F. L. Li. Dissipative preparation of entangled states between two spatially separated nitrogen-vacancy centers. *Phys. Rev. A*, 85:042306, 2012.
- [110] J. Zhang, Y. Liu, C.-W. Li, T.-J. Tarn, and F. Nori. Generating stationary entangled states in superconducting qubits. *Phys. Rev. A*, 79:052308, 2009.
- [111] P.-B. Li, S.-Y. Gao, and F.-L. Li. Engineering two-mode entangled states between two superconducting resonators by dissipation. *Phys. Rev. A*, 86:012318, 2012.
- [112] K. Xia, M. Macovei, and J. Evers. Stationary entanglement in strongly coupled qubits. *Phys. Rev. B*, 84:184510, 2011.

- [113] K. W. Murch, U. Vool, D. Zhou, S. J. Weber, S. M. Girvin, and I. Siddiqi. Cavity-assisted quantum bath engineering. *Phys. Rev. Lett.*, 109:183602, 2012.
- [114] Z. Leghtas, U. Vool, S. Shankar, M. Hatridge, S. M. Girvin, M. H. Devoret, and M. Mirrahimi. Stabilizing a Bell state of two superconducting qubits by dissipation engineering. *Phys. Rev. A*, 87:042315, 2013.
- [115] F. Reiter, L. Tornberg, G. Johansson, and A. S. Sørensen. Steady-state entanglement of two superconducting qubits engineered by dissipation. *Phys. Rev. A*, 88:032317, 2013.
- [116] S. Shankar, M. Hatridge, Z. Leghtas, K. M. Sliwa, A. Narla, U. Vool, S. M. Girvin, L. Frunzio, M. Mirrahimi, and M. H. Devoret. Autonomously stabilized entanglement between two superconducting quantum bits. *Nature*, 504:419, 2013.
- [117] M. Fannes, B. Nachtergaele, and R. F. Werner. Finitely correlated states on quantum spin chains. *Comm. Math. Phys.*, 144:443, 1992.
- [118] F. Verstraete and J. I. Cirac. Renormalization algorithms for quantum-many body systems in two and higher dimensions. *arXiv:cond-mat/0407066*, 2004.
- [119] F. Pastawski, L. Clemente, and J. I. Cirac. Quantum memories based on engineered dissipation. *Phys. Rev. A*, 83:012304, 2011.
- [120] K.G.H. Vollbrecht, C. A. Muschik, and J. I. Cirac. Entanglement distillation by dissipation and continuous quantum repeaters. *Phys. Rev. Lett.*, 107:120502, 2011.
- [121] S. Diehl, A. Micheli, A. Kantian, B. Kraus, H. P. Büchler, and P. Zoller. Quantum States and Phases in Driven Open Quantum Systems with Cold Atoms. *Nature Phys.*, 4:878, 2008.
- [122] E. Brion, L. H. Pedersen, and K. Mølmer. Adiabatic elimination in a lambda system. *J. Phys. A*, 40:1033, 2007.
- [123] D. F. V. James and J. Jerke. Effective Hamiltonian theory and its applications in quantum information. *Can. J. Phys.*, 85:625, 2007.
- [124] O. Gamel and D. F. V. James. Time-averaged quantum dynamics and the validity of the effective Hamiltonian model. *Phys. Rev. A*, 82:052106, 2010.
- [125] G. Gamow. Zur Quantentheorie des Atomkernes. *Z. Phys.*, 51:204, 1928.
- [126] J. Dalibard, Y. Castin, and K. Mølmer. Wave-function approach to dissipative processes in quantum optics. *Phys. Rev. Lett.*, 68:580, 1992.
- [127] H. J. Carmichael. Quantum trajectory theory for cascaded open systems. *Phys. Rev. Lett.*, 70:2273, 1993.

- [128] E. Persson, I. Rotter, H.-J. Stöckmann, and M. Barth. Observation of resonance trapping in an open microwave cavity. *Phys. Rev. Lett.*, 85:2478, 2000.
- [129] A. Volya and V. Zelevinsky. Non-Hermitian effective Hamiltonian and continuum shell model. *Phys. Rev. C*, 67:054322, 2003.
- [130] Y. Alhassid, Y. V. Fyodorov, T. Gorin, W. Ihra, and B. Mehlig. Fano interference and cross-section fluctuations in molecular photodissociation. *Phys. Rev. A*, 73:042711, 2006.
- [131] H. Feshbach. Unified Theory of Nuclear Reactions. *Ann. Phys.*, 5:357, 1958.
- [132] C. Mahaux and H. A. Weidenmüller. *Shell-Model Approach to Nuclear Reactions*. North-Holland Publishing Co., Amsterdam, 1969.
- [133] I. Rotter. A non-Hermitian Hamilton operator and the physics of open quantum systems. *J. Phys. A*, 42:153001, 2009.
- [134] F. Reiter and A. S. Sørensen. Effective operator formalism for open quantum systems. *Phys. Rev. A*, 85:032111, 2012.
- [135] M. M. Wolf and D. Perez-Garcia. The inverse eigenvalue problem for quantum channels. *arXiv:1005.4545*, 2010.
- [136] F. C. A. Kerling. Dissipative preparation of entanglement of two emitters coupled to a one-dimensional quantum wire. Master thesis, Radboud University Nijmegen, 2014.
- [137] Y. Yin, Y. Chen, D. Sank, P. J. J. O'Malley, T. C. White, R. Barends, J. Kelly, E. Lucero, M. Mariantoni, A. Megrant, C. Neill, A. Vainsenchr, J. Wenner, A. N. Korotkov, A. N. Cleland, and J. M. Martinis. Catch and release of microwave photon states. *Phys. Rev. Lett.*, 110:107001, 2013.
- [138] W. Kelly, Z. Dutton, J. Schlafer, B. Mookerji, T. A. Ohki, J. S. Kline, and D. P. Pappas. Direct Observation of Coherent Population Trapping in a Superconducting Artificial Atom. *Phys. Rev. Lett.*, 104:163601, 2010.
- [139] P. C. de Groot, J. Lisenfeld, R. N. Schouten, S. Ashhab, A. Lupascu, C. J. P. M. Harmans, and J. E. Mooij. Selective darkening of degenerate transitions demonstrated with two superconducting quantum bits. *Nature Phys.*, 6:763, 2010.
- [140] J. M. Chow, A. D. Corcoles, J. M. Gambetta, C. Rigetti, B. R. Johnson, J. A. Smolin, J. R. Rozen, G. A. Keefe, M. B. Rothwell, M. B. Ketchen, and M. Steffen. Simple All-Microwave Entangling Gate for Fixed-Frequency Superconducting Qubits. *Phys. Rev. Lett.*, 107:080502, 2011.
- [141] S. Filipp, A. F. van Loo, M. Baur, L. Steffen, and A. Wallraff. Preparation of subradiant states using local qubit control in circuit QED. *Phys. Rev. A*, 84:061805, 2011.

- [142] J. R. Johansson, P. D. Nation, and F. Nori. QuTiP 2: A Python framework for the dynamics of open quantum systems. *Comput. Phys. Commun.*, 184:1234, 2013.
- [143] J. R. Johansson, P. D. Nation, and F. Nori. QuTiP: An open-source Python framework for the dynamics of open quantum systems. *Comput. Phys. Commun.*, 183:1760, 2012.
- [144] C. Sayrin, I. Dotsenko, X. Zhou, B. Peaudecerf, T. Rybarczyk, S. Gleyzes, P. Rouchon, M. Mirrahimi, H. Amini, M. Brune, J.-M. Raimond, and S. Haroche. Real-time quantum feedback prepares and stabilizes photon number states. *Nature*, 477:73, 2011.
- [145] R. Vijay, C. Macklin, D. H. Slichter, S. J. Weber, K. W. Murch, R. Naik, A. N. Korotkov, and I. Siddiqi. Stabilizing Rabi oscillations in a superconducting qubit using quantum feedback. *Nature*, 490:77, 2012.
- [146] D. Ristè, C. C. Bultink, K. W. Lehnert, and L. DiCarlo. Feedback control of a solid-state qubit using high-fidelity projective measurement. *Phys. Rev. Lett.*, 109:240502, 2012.
- [147] S. Brakhane, W. Alt, T. Kampschulte, M. Martinez-Dorantes, R. Reimann, S. Yoon, A. Widera, and D. Meschede. Bayesian feedback control of a two-atom spin-state in an atom-cavity system. *Phys. Rev. Lett.*, 109:173601, 2012.
- [148] P. Schindler, M. Müller, D. Nigg, J. T. Barreiro, E. A. Martinez, M. Hennrich, T. Monz, S. Diehl, P. Zoller, and R. Blatt. Quantum simulation of dynamical maps with trapped ions. *Nature Phys.*, 9:361, 2013.
- [149] P. Campagne-Ibarcq, E. Flurin, N. Roch, D. Darson, P. Morfin, M. Mirrahimi, M. H. Devoret, F. Mallet, and B. Huard. Persistent Control of a Superconducting Qubit by Stroboscopic Measurement Feedback. *Phys. Rev. X*, 3:021008, 2013.
- [150] D. Ristè, M. Dukalski, C. A. Watson, G. de Lange, M. J. Tiggelman, Ya. M. Blanter, K. W. Lehnert, R. N. Schouten, and L. DiCarlo. Deterministic entanglement of superconducting qubits by parity measurement and feedback. *Nature*, 502:350, 2013.
- [151] M. D. Barrett, B. DeMarco, T. Schaetz, V. Meyer, D. Leibfried, J. Britton, J. Chiaverini, W. M. Itano, B. Jelenković, J. E. Jost, C. Langer, T. Rosenband, and D. J. Wineland. Sympathetic cooling of ${}^9\text{Be}^+$ and ${}^{24}\text{Mg}^+$ for quantum logic. *Phys. Rev. A*, 68:042302, 2003.
- [152] J. D. Jost, J. P. Home, J. M. Amini, D. Hanneke, R. Ozeri, C. Langer, J. J. Bollinger, D. Leibfried, and D. J. Wineland. Entangled mechanical oscillators. *Nature*, 459:683, 2009.
- [153] C. Monroe, D. M. Meekhof, B. E. King, W. M. Itano, and D. J. Wineland. Demonstration of a fundamental quantum logic gate. *Phys. Rev. Lett.*, 75:4714, 1995.

- [154] R. Ozeri, W. M. Itano, R. B. Blakestad, J. Britton, J. Chiaverini, J. D. Jost, C. Langer, D. Leibfried, R. Reichle, S. Seidelin, J. H. Wesenberg, and D. J. Wineland. Errors in trapped-ion quantum gates due to spontaneous photon scattering. *Phys. Rev. A*, 75:042329, 2007.
- [155] H. Uys, M. J. Biercuk, A. P. VanDevender, C. Ospelkaus, D. Meiser, R. Ozeri, and J. J. Bollinger. Decoherence due to elastic rayleigh scattering. *Phys. Rev. Lett.*, 105:200401, 2010.
- [156] S. M. Tan. A computation toolbox for quantum and atomic optics. *J. Opt. B*, 1:424, 1999.
- [157] C. Ospelkaus, C. E. Langer, J. M. Amini, K. R. Brown, D. Leibfried, and D. J. Wineland. Trapped-ion quantum logic gates based on oscillating magnetic fields. *Phys. Rev. Lett.*, 101:090502, 2008.
- [158] C. Ospelkaus, U. Warring, Y. Colombe, K. R. Brown, J. M. Amini, D. Leibfried, and D. J. Wineland. Microwave quantum logic gates for trapped ions. *Nature*, 476:181, 2011.
- [159] D. J. Wineland, C. Monroe, W. M. Itano, D. Leibfried, B. E. King, and D. M. Meekhof. Experimental issues in coherent quantum-state manipulation of trapped atomic ions. *J. Res. Natl. Inst. Stand. Technol.*, 103:259, 1998.
- [160] D. A. Hite, Y. Colomb, A. C. Wilson, K. R. Brown, U. Warring, R. Jördens, J. D. Jost, K. S. McKay, D. P. Pappas, D. Leibfried, and D. J. Wineland. 100-fold reduction of electric-field noise in an ion trap cleaned with *in situ* argon-ion-beam bombardment. *Phys. Rev. Lett.*, 109:103001, 2012.
- [161] R. N. Stevenson, J. J. Hope, and A. R. R. Carvalho. Engineering steady states using jump-based feedback for multipartite entanglement generation. *Phys. Rev. A*, 84:022332, 2011.
- [162] S. K. Lee, J. Cho, and K. S. Choi. Emergence of stationary many-body entanglement in driven-dissipative Rydberg lattice gases. *arXiv:1401.0028*, 2013.
- [163] E. Kapit, J. T. Chalker, and S. H. Simon. Passive correction of quantum logical errors in a driven, dissipative system: a blueprint for an analog quantum code fabric. *arXiv:1408.0959*, 2014.
- [164] R. Raussendorf, D. E. Browne, and H. J. Briegel. Measurement based Quantum Computation on Cluster States. *Phys. Rev. A*, 68:02231, 2003.
- [165] S. Puntanen and G. Styan. *The Schur Complement and Its Applications*, (F. Zhang, ed.). Springer, 2005.
- [166] S. Boyd and L. Vandenberghe. *Convex Optimization*. Cambridge University Press, online available at <http://stanford.edu/~boyd/cvxbook/>, 2004.
- [167] see e.g. http://en.wikipedia.org/wiki/Lambert_W_function.